ETDE-CH--9901

PAUL SCHERRER INSTITUT

ISSN 1423-7342
March 1999

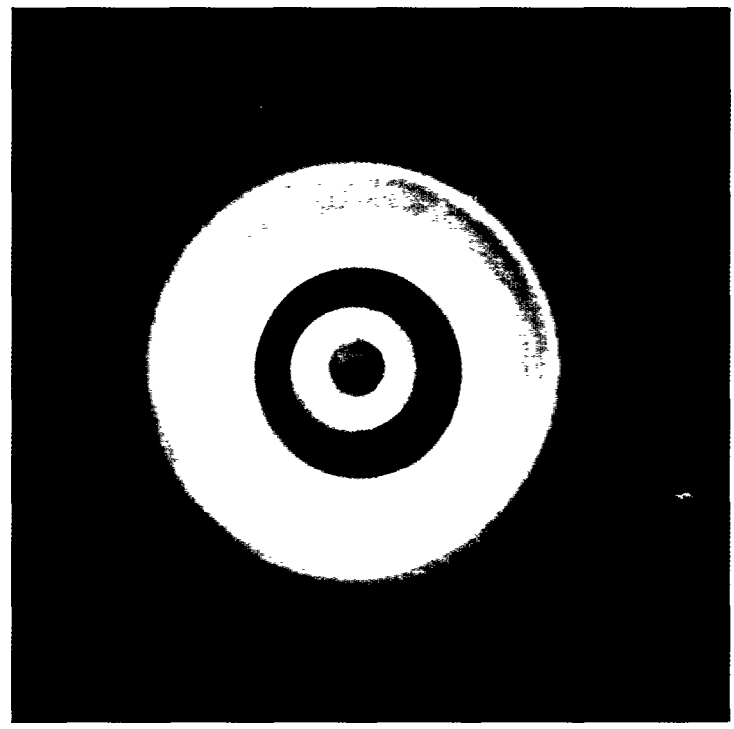

PSI • Scientific Report 1998 / Volume V

General Energy

Cover Photo

View along the tubing system of a prototype Condensation Interface which was developed for the on-line measurement of heavy metal concentrations in hot gases.

See article by Ch. Ludwig, S. Stucki and A.J. Schuler

Photo: Armin Müller, PSI

PAUL SCHERRER INSTITUT

ISSN 1423-7342
March 1999

Scientific Report 1998

Volume V

General Energy

ed. by: Christina Daum and Jakob Leuenberger

CH-5232 Villigen PSI
Switzerland
Phone: 056 / 310 21 11
Telefax: 056 / 310 21 99
http://www1.psi.ch/www_f5_hn/f5_home.html

DISCLAIMER

Portions of this document may be illegible in electronic image products. Images are produced from the best available original document.

TABLE OF CONTENTS

INTRODUCTION

A. Wokaun

In 1998, the necessity of reducing global greenhouse gas emissions in view of imminent global changes was again in the focus of worldwide discussions involving politicians, stakeholders, and the society at large. In view of a growing world population and a desirable economic development in many world regions, the reduction of CO_2 emissions represents an extremely challenging task.

In view of its mission to contribute towards the development of a globally more sustainable energy supply system, the General Energy Department is focusing on four topical areas:

- advancing technologies for the use of renewable energies
- investigating options for chemical and electrochemical energy storage on various time scales
- developing highly efficient converters for the low emission use of fossil and renewable fuels, including both combustion devices and fuel cells
- analyzing the consequences of energy use, and advancing scenarios for the development of the energy supply system.

Progress in these topical areas is described in the corresponding sections of this report. In the following paragraphs, a few key results achieved in 1998 will be highlighted.

RENEWABLE ENERGIES

Among the 'new renewables', the technological utilization of biomass is expected to provide the largest contribution towards global energy supply in the next century. Ecological balances must be carefully considered in energy crop production, but are clearly positive in waste utilization. The latter concept enhances competitiveness due to the valuation of the waste disposal function. We are therefore focusing on the influence of contaminants, such as metal salts, on the biomass gasification kinetics.

The synthesis gas produced may be used for the production of methanol, which is considered a prime candidate for synthetic liquid fuels from renewables. Methanol can be converted to dimethyl ether, a promising diesel substitute that can be burnt in compression ignition engines with practically no particulate matter emissions. We are exploring the option of producing DME from methanol on-board of vehicles by compact catalytic converters.

Technologies for solar energy utilization can rarely compete with today's low fossil energy prices, but hold a large potential when CO_2 reduction targets will be implemented. Solar chemistry aims at the production of solar fuels, i.e. storing solar energy in the form of chemicals with a high heating value, which may be stored and transported to the site of energy need (such as, again, in transport applications). As an example of this concept, we are presenting our strategy for the solar thermal production of zinc, together with an economic evaluation. Solar decarbonization of fossil fuels is another interesting greenhouse gas mitigation option.

TOWARDS A MORE SUSTAINABLE MOBILITY - DEVELOPMENT OF MATERIALS, ENERGY STORAGE DEVICES, AND EFFICIENT CONVERTERS

Renewable fuels hold a large potential on the route towards a more sustainable mobility. First, in agreement with international studies, our analysis shows that the power requirement of the vehicle may be reduced by more than 50 % by decreasing weight, air drag, and rolling resistance. Second, the greenhouse gas emissions are further cut by furnishing this vehicle with a power train based on fuel cells. Third, with the use of electric motors, braking energy may be recovered by regenerative braking and electrochemical storage in supercapacitors.

As present day's high performance low temperature fuel cells are fuelled by hydrogen, reformer technologies play a crucial role for providing the hydrogen aboard the vehicle from fuels such as methanol. Catalysts have therefore been developed for methanol partial oxidation, and the performance of the reformer / fuel cell system was evaluated.

Progress in the development of polymer electrolyte fuel cells (PEFCs) is reported along two lines. The performance of PSI's proton conducting membrane was further enhanced, among others by improving the mechanical specifications important for stack applications. Successful testing over a continuous operating time exceeding 10'000 hours, as reported in this volume, represents a milestone in demonstrating the competitive advantages of this material for fuel cells in transportation.

Experiments with segmented membranes have provided valuable insights on the water distribution and flow, an important issue for stack design. Besides demonstrating a 1 kW PEFC stack based exclusively on PSI components, a pilot series of fuel cell stacks has been made available for testing in various educational institutions.

Electrolytic double layer capacitors, termed supercapacitors, excel by very high capacities, and are developed for fast storage of the electrical energy generated during the regenerative braking process of a vehicle. Electrode material development is guided by advanced characterization techniques, such as small angle X-ray scattering. The performance of the device was demonstrated by successfully performing 100'000 charge / discharge cycles.

High power batteries continue to be important for transport applications, such as in hybrid vehicles. In this context, the zinc / air battery is explored in view of its high energy storage density; a 12 V / 20 Ah stack has been demonstrated. The lithium battery, on the other hand, is in high demand for meeting the power requirements of a large variety of portable devices. Development and advanced spectroscopic characterization of electrode materials are pursued in our lithium ion battery project.

COMBUSTION RESEARCH

An important milestone has been reached in our project aiming at reducing NO_x emissions under conditions that are typical of gas turbine combustion. The pressure dependence of NO_x formation under lean premix conditions was studied experimentally, and the desired pressure-induced NO_x reduction was accounted for by quantitative modeling. In catalytically stabilized combustion, which potentially features lowest NO_x emissions, the importance of establishing turbulent flow conditions for overcoming mass transfer limitations was investigated.

Powerful laser spectroscopic methods are being made available for the *in situ* characterization of technical combustion processes. The visualization of fuel oil mixing with air using laser induced fluorescence, and the quantification of soot formation are examples presented in this volume.

As mentioned above, the combustion properties of fuels from renewables are a subject of high interest. We have therefore embarked in a detailed study of the associated gas phase reaction mechanisms; the dissociation dynamics of the oxygenated fuel methylal is shown as an example.

CONSEQUENCES OF ENERGY USE FOR ATMOSPHERE AND CLIMATE

Alpine ecosystems are sensitive to traffic related pollutant emissions. From the measurement campaign performed in the Mesolcina valley, in which a quantitative budget of air mass and pollutant flows through various cross sections was obtained, we can show how ozone, hydrocarbons and NO_x are transported into the high Alpine regions by the valley wind systems. These investigations are supported by theoretical studies of pollutant dispersion and of atmospheric turbulence.

Scenario calculations have been performed to provide quantitative estimates of the regional impacts of energy related pollutant emissions on various ecosystems. In discussing the consequences of greenhouse gas emissions on a global scale, the expected changes in biomass induced by a global temperature increase have been analyzed. As a noteworthy result, we find that growth of biomass initially exerts a regulating and hence stabilizing influence on global temperature, whereas exceedingly high stress due to strong (greenhouse-gas induced) forcing may give rise to a rapid loss of biomass, thereby amplifying the temperature increase.

As CO_2 reduction targets have been adopted by the Kyoto and Buenos Aires Conferences of Parties, analyses of greenhouse gas reduction strategies become extremely important for choosing the most cost effective options of resource allocation. Cases studies of the benefits of joint implementation (JI) of reduction measures among industrialized countries, as well as partnerships with non-Annex I countries within the CDM (clean development mechanism) program, have been carried out. As a most remarkable result, the effect of technological progress is shown to have a major impact on the composition of future energy supply systems under sustainability constraints. Using the concept of learning curves, we show how advanced technologies may reduce their costs and penetrate the markets, as stimulated by the necessity of reaching CO_2 reduction goals.

These results provide us with a further incentive to pursue our technological research programs described above, aimed at promoting methods for the utilization of renewable energies, advancing chemical and electrochemical energy storage concepts, and using this energy in highly efficient, low emission converters. Finally, we are aware that progress towards a more sustainable energy system will occur only if these efforts are matched by corresponding, high yield actions aiming at reducing the per capita energy demand.

Renewable Energies and Materials Cycles

THE INFLUENCE OF CHLORINE ON THE FATE AND ACTIVITY OF ALKALI METALS DURING THE GASIFICATION OF WOOD

R. Struis, C. von Scala, A. Schuler, S. Stucki

Chlorine clearly inhibits the CO_2-gasification reaction of charcoal at 800 °C. From this and other observations the picture emerges that the reduction in the gasification reactivity of the charcoal is intimately related to the deactivation of the catalytically active alkali metals residing in the wood due to the formation of the chloride salt. It is argued that the heavy metal chlorides will likely transfer the chlorine to the indigenous alkali metals during the pyrolysis stage of the wood. The fate of the thus formed alkali metal chlorides can then be either their removal from the sample (evaporation), or, when present at the gasification stage, re-activation (i.e., de-chlorination) under our gasification conditions.

1 INTRODUCTION

In our earlier reports we addressed the influence of heavy metals (Pb, Zn, Cu), earth-alkali metals (Mg, Ca) and that of alkali metals (Na, K) on the gasification reactivity of wood when using CO_2 as the oxidising agent at 800 °C [1-3]. We conclude that in untreated wood mainly the indigenous alkali metals (K, Na) are catalysing the gasification reaction, whereas the other metals show no substantial activity. On the other hand we observe that the reactivity of wood impregnated with chloride containing species decreases, especially with $ZnCl_2$, $PbCl_2$, or, $CuCl_2$. In the present work we present experimental results underlying our view on the reactivity and fate of the alkali metals as invoked by chlorine.

Experimental details concerning the wood impregnation procedure and the separately performed wood pyrolysis and gasification of the resulting charcoals can be found in our earlier contributions [1-3] and in the ETH dissertation [4].

2 KEY EXPERIMENTS

Determination of the metal concentrations (ICP-AES) in charcoal from impregnated wood reveals that no cation exchange takes place between the naturally present alkali metals and the impregnation salts and that the volatile heavy metal chlorides themselves are not greatly removed from the charcoal. The latter observation is the more stunning for wood impregnated with $ZnCl_2$ seen the low melting (318 °C) and boiling point (731 °C) of this salt. Pure $ZnCl_2$ salt itself would certainly have evaporated completely under our pyrolysis conditions (viz., 2.5 hours at 600 °C under flowing argon gas). Occasional determination of the zinc content (ICP-AES) during the gasification of a $ZnCl_2$ enriched charcoal probe at 800 °C shows that zinc is only slowly removed form the charcoal with time. Only pyrolysis at 900 °C results in a rapid removal. These observations indicate that already during the pyrolysis stage itself $ZnCl_2$ must have been transformed in other, less volatile, zinc species (likely metallic zinc; T_{boil} = 907 °C). We also suspect that the released chlorine (as HCl or Cl_2) reacts with indigenous alkali carbonates, hereby forming more stable, but catalytically inactive, chloride salts. The chlorine transfer is likely promoted by the water produced during the wood pyrolysis, typically, between T = 300 - 450 °C, including the following reactions [4]:

$$MCl_2 + H_2O \rightarrow MO + 2\,HCl \quad \{M = Zn, Cu, Pb\} \qquad (1)$$

$$MO + C \rightarrow M + CO \qquad (2)$$

$$K_2CO_3 + 2\,HCl \rightarrow 2\,KCl + CO_2 + H_2O \qquad (3)$$

The thus formed alkali metal chlorides are quite stable themselves, but may eventually also evaporate from the charcoal under the pre- (2.5 h at 600 °C) or post-pyrolsis (20 min at 900 °C) conditions where we use argon as purge gas [4]. It is therefore reasonable to assume that the treated charcoals are poor in alkali metal content and consequently have a (much) lower initial gasification reactivity when compared to the untreated sample. Moreover, wood pyrolysis at 800 °C using an argon/HCl gas mixture as purging agent and a cold-finger positioned at the end of the furnace oven tube confirm the volatilisation of the alkali metals which are naturally present in the wood [4].

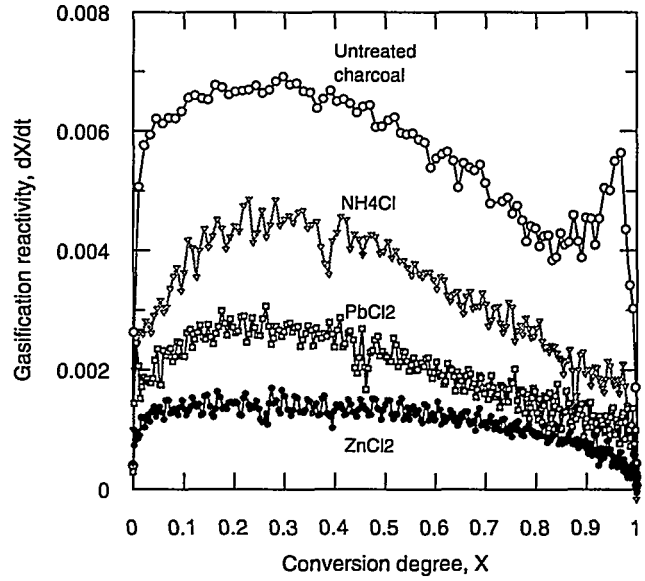

Fig. 1: Gasification reactivity, dX/dt, of chlorine enriched charcoals versus the conversion degree, X.

On the other hand, the course of reactivity with conversion degree is mainly determined by the structural

changes in the porous charcoal [3, 4]. Because the BET determination of the untreated and treated charcoals do not reveal any changes in the charcoal surface [4], we do not expect substantial changes in the shape of the reactivity course itself. These expectations are fully confirmed by our gasification experiments made with the Thermo-Gravimetric-Analyser (TGA) and are shown in Figure 1. With TGA one traces the charcoal weight, m, as a function of time. The reaction rate, or, reactivity, r is expressed as the time derivative of the conversion degree, viz., **r = dX / dt**, where the conversion degree, X, relates the carbon mass reacting at time t with the mass present at start as **X(t) = 1 - m(t) / m(0)**. The differences noticeable in Figure 1 towards the very end of the gasification are due to catalyst phenomena which are not considered in the structural reactivity models employed in the literature [3].

Another key experimental result is shown in Figure 2 where we plotted, respectively, the gasification reactivity course of untreated charcoal, charcoal enriched with Na_2CO_3, and with NaCl. We note that the catalytic activity of sodium resembles that of potassium, but it's concentration in untreated wood is ca. 10 times smaller than that of potassium.

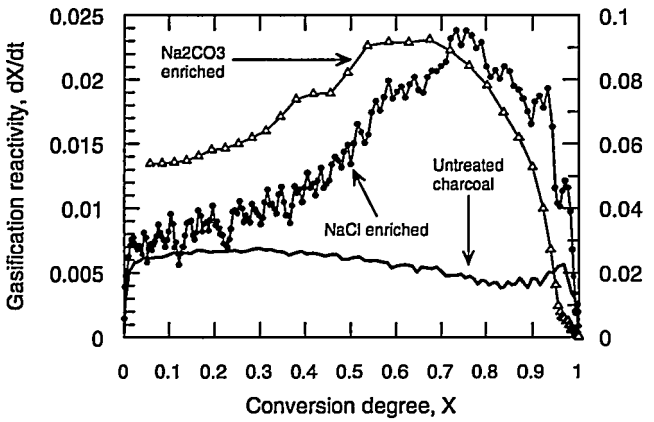

Fig. 2: Gasification reactivity of charcoals as a function of the conversion degree. Note: The values for the Na_2CO_3 enriched sample are given on the right-hand side axes.

From Figure 2 it is clearly seen that the initial reactivity of the NaCl enriched probe closely resembles that of untreated charcoal, and certainly not that of the Na_2CO_3 enriched sample which reacts ca. 10 times faster. On the other hand, the reactivity course of the Na_2CO_3 doped sample shows a marked maximum around $X \approx 0.6 - 0.7$. The position of this maximum strongly contrasts with the maximum found with untreated charcoal (Fig. 1) which typically lies around $X \approx 0.2 - 0.4$. This difference has already been noted by us and others [4] and, to our opinion, is intimately related with catalytic phenomena which are ignored by common, structurally based reactivity models. For the moment we point out that the NaCl doped sample also shows a marked maximum around $X \approx 0.8$, which means no less than that the amount of catalytically active (i.e., chlorine-free) sodium species must have increased during the gasification course. We conclude that the chlorine in NaCl has been superseded by the gasification agent CO_2.

To test our interpretation hypothesis, Figure 3 shows the initial gasification rate of untreated charcoal and of charcoals treated with various chlorine containing species as a function of the active, i.e., chlorine-free, alkali metal content determined with ICP-AES.

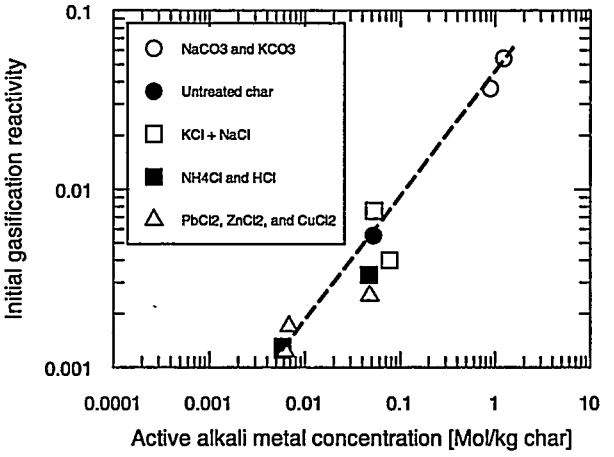

Fig. 3: Initial gasification rate, dX/dt, of various chlorine enriched charcoals (arbitrarily units) as a function of the concentration of *active* alkali metals.

With NaCl or KCl enriched wood we assume that a part may have evaporated from the charcoal during the pre- or post- pyrolysis stage, but that no chlorine transfer occurs between the added salts and the indigenous metals. The alkali metal content then refers to the indigenous, non-added alkali metal species. With the samples impregnated with heavy metal chlorides we assume that the chlorinated indigenous alkali metals are completely removed (evaporated) from the probe, so that the alkali metal content determined with ICP-AES refers only to the chlorine-free form.

Figure 3 depicts a clear, almost linear, correlation between the initial gasification reactivity and the active alkali metal content in the charcoal.

3 REFERENCES

[1] C. von Scala, R. Struis, S. Stucki, PSI Annual Report Annex V, 70-71 (1995).

[2] Ibid, PSI Annual Report Annex V, 6-7 (1996).

[3] R. Struis, C. von Scala, PSI Annual Report Annex V, 16-18 (1997).

[4] *The Influence of contaminants on the gasification of waste wood*, C. von Scala, Ph.D. Thesis, ETH-Zürich, Thesis Nr. 12665 (1998).

ON-BOARD CONVERSION OF METHANOL TO DIMETHYL ETHER AS AN ALTERNATIVE DIESEL FUEL

H. Armbruster, G. Heinzelmann, R. Struis, S. Stucki

The catalytic dehydration of methanol to dimethyl ether was investigated for application on-board a methanol fuelled vehicle. Several catalysts have been tested in a fixed bed reactor. Our approach is to develop a small and efficient reactor converting liquid MeOH under pressure and at low reaction temperatures.

1 INTRODUCTION

Dimethyl ether (DME) has received considerable attention as a diesel substitute fuel during the last years.

This is explained on one side by the fact that DME has excellent combustion properties, and that diesel engines require only minor modifications to run on this fuel. The major problems with conventional diesel fuel are soot, NOX and noise emissions. One opportunity to circumvent these problems is using an alternative fuel such as methanol or ethanol. But these fuels have a low cetane number (a measure of a fuel's ability to autoignite) in comparison to DME. The cetane number is an important characteristic for the combustion in diesel engines. DME has thus the potential to meet even the tightest emission regulations [1].

The state-of-the-art technology for the production of DME is the dehydration of MeOH over alumina catalysts. The direct synthesis from synthesis gas has been projected to be the most economical route for the DME production an a very large scale [2].

Today the price of DME is five times higher than the MeOH price. The reason for this is the small market for DME. It is used as an environmentally friendly propellant for spray cans, but the production and the demand are very small. One of the world leaders in MeOH synthesis technologies, Haldor Topsøe, extrapolates that direct synthesis of DME from synthesis gas could be competitive with current (untaxed) diesel prices. This extrapolation is made assuming "megaplants" which require very large investments and the economy of scale of which still needs to be proven [3,4].

But still unsolved are problems related to the further handling, storage and distribution of DME, which is a colourless, non-toxic gas under ambient condition. DME must therefore be handled, stored and distributed like e.g. LPG, which is liquid for pressures above 5 bar.

The existing infrastructure for automotive fuels is mainly based on liquid fuels.

2 ON-BOARD CONVERSION

With respect to environmental, operational aspects and economics we consider DME as an alternative diesel fuel on the basis of on-board MeOH conversion. Our approach is to develop a small and efficient reactor converting liquid MeOH under pressure and at low reaction temperatures.

The advantages of MeOH conversion in liquid phase are higher space-time-yields to match peak fuel input to the engine (ρ_{liquid} /ρ_{gas} ≈ 600), less compression work when the reaction mixture is liquid under the injection condition, and smaller dimensions of the reactor.

The catalyst should preferentially operate under low reaction temperatures, which is thermodynamically more favourable for the DME production and makes the start-up time shorter.

Further potential for this approach is the utilisation of other alcohols such as bio-ethanol. For heavy duty diesel engines, the fumigation of on-board produced ethers as a replacement for ignition-improver additives is another possible application.

3 CATALYSTS

Some potential catalyst candidates are known from MeOH dehydration in the gas phase. It is known that the acidic catalysts are used for the conversion of MeOH to DME. The most important catalysts for the industrial use are Al_2O_3 and $Al_6Si_2O_{13}$ (with or without promoters) [5].

In the production of lower olefins over zeolite, DME is obtained as a by-product. There is a possibility that under different conditions DME would be the main product. Another group are cation-exchange polymers such as Nafion and organic resins.

No catalysts are known for the liquid-phase application.

Conceivable problems in the liquid-phase application could be the loss of acidity with time in presence of water or MeOH. It is known that Nafion dissolves in liquid MeOH/H_2O mixtures. Another fact is that the cation-exchange polymers have only a moderate thermal stability which could be a problem.

4 PRELIMINARY RESULTS

For a liquid phase application we use a fixed bed reactor with which we test the catalysts' ability to convert MeOH to DME. Figure 1 shows the experimental setup.

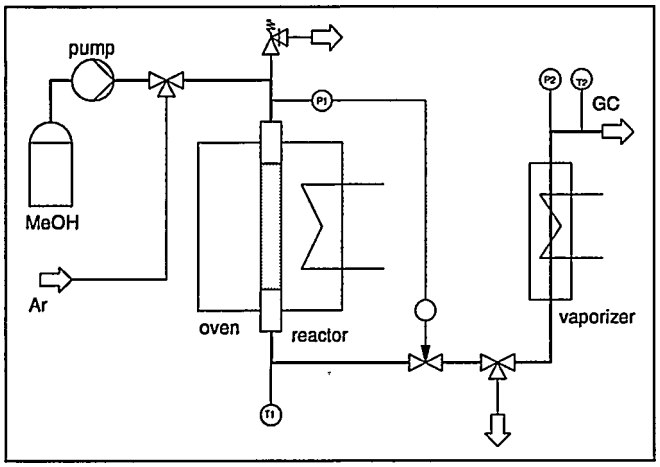

Fig. 1: Experimental set-up for testing catalysts.

The dehydration reaction of MeOH is carried out in a fixed-bed, plug-flow tube-reactor

$$2CH_3OH \leftrightarrow CH_3OCH_3 + H_2O.$$

The reactor, which is electrically heated, contains about 10 g of catalyst. MeOH is fed with a piston pump. The temperature is measured by means of a thermocouple in an axial thermowell running along the length of the reactor. Pressure is adjusted by a control valve connected with a pressure transmitter. The products are vaporised and then analysed by gas chromatography.

Figure 2 shows first results of experiments with an organic cation-exchanger resin.

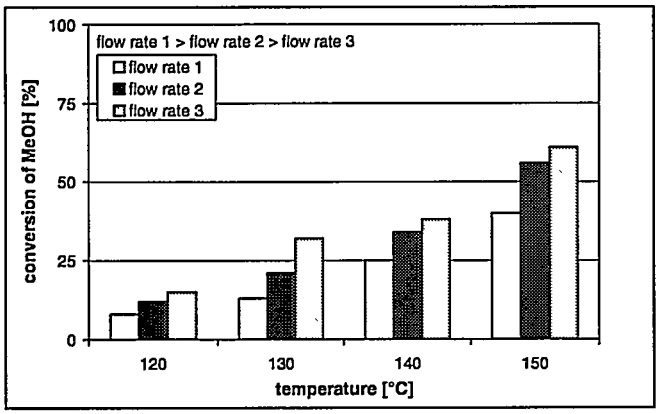

Fig. 2: MeOH conversion as a function of various temperatures and flow rates.

Without an explicit optimisation of reaction conditions the experiment shows that a conversion of MeOH above 50 % was achieved for the given experimental conditions at a temperature of 150 °C. This result implies that a catalyst bed of < 8 l could yield a fuel mixture of 25 % DME, 25 % H_2O, 50 % MeOH at a rate sufficient for a 90 $kW_{thermal}$ engine. The combustion properties of such a mixture in a diesel engine will have to be compared with unconverted methanol and 100 % DME operation.

For the future we focus on the conversion efficiencies and rates of other catalysts in the liquid phase, together with the long term behaviour of such catalysts.

It remains to be seen whether effects like reaction inhibition due to stagnation or absorption of water at the catalyst surface influence the reaction rate and the maximum achievable conversion.

Another important item is the phase behaviour of the ternary system MeOH/DME/H_2O as a function of composition, temperature and pressure. This is important with respect to the reaction, storage and the injection.

5 REFERENCES

[1] T. Fleisch et al., *A new clean diesel technology: Demonstration of ULEV emissions on an Navistar diesel engine fuelled with dimethyl ether,* SAE paper 950061.

[2] J. B. Hansen et al., *Large scale manufacture of dimethyl ether - a new alternative diesel fuel from natural gas,* SAE paper 950063.

[3] T. Fleisch, P. Meurer, *DME - The diesel fuel for the 21st century ?* AVL Conference "Engine and environment", Graz, Austria (1995).

[4] R. Verbeek, J. van der Weide, *Global assessment of dimethyl ether: comparison with other fuel,* SAE paper 971607.

[5] Ullman`s Encyclopedia of Industrial Chemistry 5th Ed., VCH Verlag, **A8**, 541-544.

SOLAR THERMAL PRODUCTION OF ZINC: PROGRAM STRATEGY

A. Steinfeld, A. Weidenkaff, S. Moeller, R. Palumbo

The solar thermal production of zinc is considered for the conversion of solar energy into storable and transportable chemical fuels. The ultimate objective is to develop a technically and economically viable technology that can produce solar zinc. The program strategy for achieving such a goal involves research on two paths: a direct path via the solar thermal splitting of ZnO in the absence of fossil fuels, and an indirect path via the solar carbothermal/CH_4-thermal reduction of ZnO, with fossil fuels (coke or NG) as chemical reducing agents. Both paths make use of concentrated solar energy for high-temperature process heat. The direct path brings us to the complete substitution of fossil fuels with solar fuels for a sustainable energy supply system. The indirect path creates a link between today's fossil-fuel-based technology and tomorrow's solar chemical technology and builds bridges between present and future energy economies.

1 INTRODUCTION

Zinc is a versatile metal: besides being a widely used commodity in the galvanizing and chemical industries, it is also a compact and safe-to-handle solid fuel that finds applications in Zn/air fuel cells and batteries. Zinc can also be reacted with water and form hydrogen that can be further processed for heat and electricity generation. The chemical product from these power generation processes is zinc oxide, which in turn needs to be reduced to zinc and recycled. However, the current industrial production of zinc carries severe environmental consequences. The commercial production techniques by electrolytic and smelting furnaces are characterized by their high energy consumption and their concomitant environmental pollution: the zinc world production amounts to about 7 million tonnes per year and discharges annually approximately 66 million tonnes of CO_2 to the atmosphere [1]. These emissions are derived mostly from the combustion of fossil fuels and could be substantially reduced or completely eliminated by using instead concentrated solar radiation as the energy source of high-temperature process heat.

The thermochemical path for producing zinc using high-temperature solar energy is further justified by thermodynamic arguments: the energy conversion efficiency can exceed 50% [2,3]. High efficiencies directly translate to lower solar collection area and associated costs of the heliostat field, which amount to 40-50% of the capital cost for the entire solar chemical plant [4]. Under these assumptions, a recent economic assessment for a large-scale chemical plant indicates that the solar thermal production of zinc might be competitive with other renewable technologies (e.g. solar electricity plus electrolysis of ZnO), and, under proper conditions, be competitive even with conventional fossil-fuel-based processes at current fossil fuel prices [4].

Solar-made zinc offers the possibility of storing and transporting solar energy. The conversion of solar energy into chemical energy carriers, that can be stored over long periods of time and transported over long distances, overcomes the principal drawbacks of solar energy, namely: being dilute, intermittent, and inconveniently distributed. Our ultimate objective is to develop a technically and economically viable technology for a solar thermal process that can produce zinc as a transportable chemical fuel for a sustainable energy supply system.

2 STRATEGY

The strategy for reaching our long-term objective involves research on two paths, as illustrated in Figure 1 [5]:

1) the *direct path* via the direct solar thermal splitting of ZnO, represented by:

$$ZnO \longrightarrow Zn + 1/2\ O_2 \qquad (1)$$

2) the *indirect path* via the solar carbothermal and CH_4-thermal reduction of ZnO, represented by:

$$ZnO + C(gr) \longrightarrow Zn + CO \qquad (2)$$

$$ZnO + CH_4 \longrightarrow Zn + 2H_2 + CO \qquad (3)$$

Reaction (1) proceeds at elevated temperatures (above about 2000 K) using solar process heat [2]. Such a high-temperature reaction requires the development of a completely novel process engineering technology and will take time before such technology will be ready for large-scale commercialization. It is clear that one should start developing now if one wishes to be ready in 30 years and avoid expensive and riddled-with-mistakes crash programs. This path requires supporting a continuous program of research, development, and demonstration. An overview of this research program is given in Ref. [6].

Reactions (2) and (3) make use of fossil fuels exclusively as chemical reducing agents (such as C(gr) from coal or CH_4 from natural gas (NG)). Process heat is supplied by solar energy and *not* by the combustion

of fossil fuels. The products of reactions (2) and (3) are cleaner fuels with a solar-upgraded energetic value because the solar input increases their energy content above the value of the fossil fuel. In the presence of a reducing agent, such as C(gr) and CH_4, the uptake of oxygen by the formation of CO brings about the thermal reduction of ZnO to Zn at much lower temperatures, above about 1300 K [7,8]. Thus, reactions (2) and (3) require more moderate and, presently, more technically-feasible temperatures. They use a combination of novel and conventional process technologies. Traditional materials and reactor concepts are thus possible for the mixed fuel/solar energy technology. With this path we hope to reduce the lead time for transferring important solar technology to industry. This route is an important intermediate solution toward a sustainable energy supply.

The chemical thermodynamics and kinetics of reactions (1) to (3) have been reported in previous publications [2-14]. Reactions (1) to (3) were effected at the solar furnaces of PSI, U. of Minnesota (USA), Weizmann Institute (Israel), and CNRS (France) [2, 7, 8, 11-15]. Based on these previous studies and on the constraints that the chemistry places on the engineering design of solar chemical reactors, we have proceeded with the development of solar reactors that can operate continuously and have the potential of being scaleable for large-scale industrial applications.

Pursuing R&D in both the *direct* and *indirect* path is a recommended strategy. The *direct path* brings us to the complete substitution of fossil fuels with solar fuels. The *indirect path* creates a link between today's fossil-fuel-based technology and tomorrow's solar chemical technology, and builds bridges between present and future energy economies. The transition from fossil to solar fuels can occur smoothly with the help of processes that mix fossil fuels and solar energy.

3 ACKNOWLEDGEMENTS

The financial support from the Swiss Federal Office of Energy and the Baugarten Foundation is gratefully acknowledged. We thank M. Brack, P. Haueter, A. Meier, and D. Wuillemin for their help in the design, construction, and testing of the solar reactors.

4 REFERENCES

[1] A. Steinfeld, *Energy* **22**, pp. 311-316, 1997.

[2] R. Palumbo *et al.*, *Chemical Engineering Science* **53**, 2503-2518 (1998).

[3] A. Steinfeld, C. Larson , R. Palumbo, M. Foley, *Energy* **21**, 205-222 (1996).

[4] A. Steinfeld, I. Spiewak, *Energy Conversion and Management* **39**, 1513-1518 (1998).

[5] A. Steinfeld, *Proc. 3rd. Sabin Conf. on Energy and the Environment*, Weizmann Institute, 33-42 (1996).

[6] R. Palumbo, S. Moeller, A. Steinfeld, *High Temperature Material Processes*, in press (1998).

[7] J. P. Murray, A. Steinfeld, E. A. Fletcher, *Energy* **20**, 695-704 (1995).

[8] A. Steinfeld, A. Frei, P. Kuhn, D. Wuillemin, *Int. J. Hydrogen Energy* **20**, 793-804 (1995).

[9] W. Hirschwald, F. Stolze, *Zeitschrift für Physikalische Chemie Neue Folge* **77**, 21-42 (1972).

[10] A. Weidenkaff, A. Steinfeld, A. Wokaun, B. Eichler, A. Reller, *Solar Energy* in press (1998).

[11] S. Möller, Diplomarbeit, Universität Dortmund (1996).

[12] E. Bilgen, M. Ducarroir, M. Foex, F. Sibieude, and F. Trombe, *Int. J. Hydrogen Energy* **2**, 251-257 (1977).

[13] M. Epstein, K. Ehrensberger, A. Yogev, *International Symposium on Solar Chemistry*, PSI, 6-8 Oct. (1997).

[14] O. Boutin, Diplome d'Etudes Approfondies, LSGC-ENSIC, Nancy-France (1996).

[15] A. Steinfeld, M. Brack, A. Meier, A. Weidenkaff, D. Wuillemin, *Energy* **23**, 803-814 (1998).

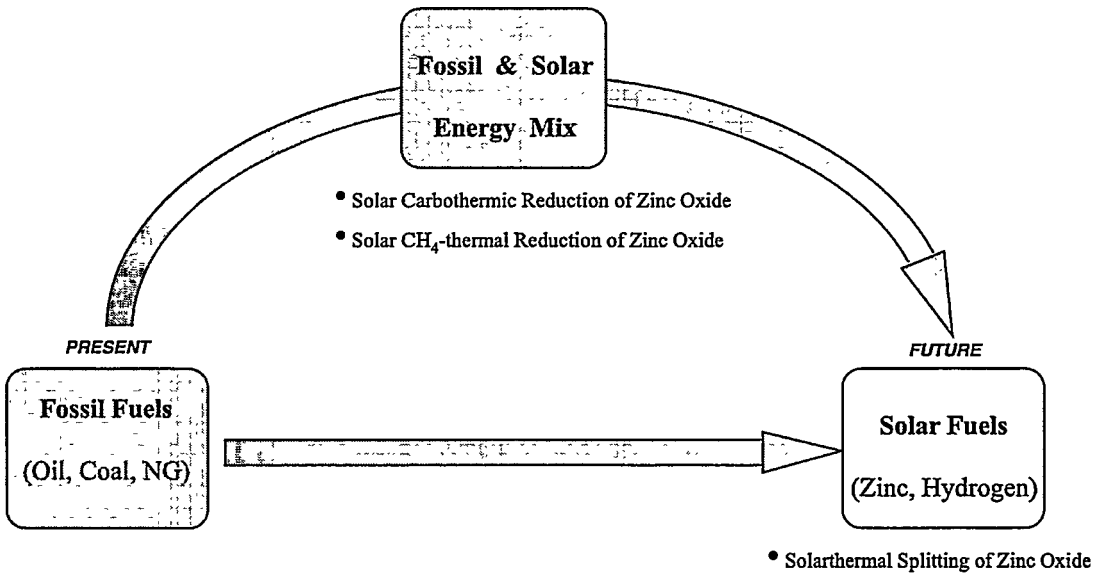

Fig. 1: Strategy for the substitution of fossil fuels with solar fuels (Zn and H_2) involves research on two paths: a *direct path* via the solar thermal splitting of ZnO and an *indirect path* via the solar carbothermal/CH_4-thermal reduction of ZnO.

ECONOMIC EVALUATION OF THE SOLAR THERMAL CO-PRODUCTION OF ZINC, SYNTHESIS GAS, AND HYDROGEN

A. Steinfeld, I. Spiewak (EC Joint Research Centre, Spain)

The use of concentrated solar energy for co-producing Zn and synthesis gas from ZnO and natural gas upgrades the calorific value of the initial reactants by 39% and, when compared to the traditional carbothermic reduction of ZnO, has the potential of reducing CO_2 emissions by up to 78%. An economic assessment for an industrial thermochemical plant, 30 to 51 MW solar input, indicates that the cost of solar production of zinc ranges between 89-133 $/t (excluding the cost of ZnO feed and credit for pollution abatement), and thus might be competitive with conventional fossil-fuel-based processes at current fuel prices. The cost of solar H_2, produced by splitting water with zinc, is estimated to be in the range 0.10-0.14 $/kWh, and it is a favorable long term prospect once the cost of energy will account for the environmental externalities from fossil fuel burning such as the costs for CO_2 mitigation and pollution abatement.

1 INTRODUCTION

The production of zinc and syngas are major consumers of energy and release vast amounts of greenhouse gases and pollutants to the environment. These emissions can be substantially reduced by replacing fossil fuels with concentrated solar energy as the source of high-temperature process heat. Zinc and syngas, besides being valuable commodities, are energy vectors for the storage and transportation of solar energy.

Using natural gas (NG) as the reducing agent of ZnO combines in a single process the reforming of CH_4 and the reduction of ZnO to co-produce zinc and syngas [1-5]. The overall reaction can be represented as:

$$ZnO + CH_4 \longrightarrow Zn + 2H_2 + CO \qquad (1)$$

This combined process has some positive features: (i) NG is reformed in the absence of catalysts and, with proper optimization, may be made to produce high quality syngas with an H_2:CO molar ratio of 2, which is especially suitable for the synthesis of methanol, a promising substitute of gasoline for fuelling cars; (ii) the evolved gases are sufficiently valuable commodities to justify their collection, eliminating inherent gas emissions to the environment; (iii) the integration of ZnO-reduction and NG-reforming into a single reactor improves energy efficiencies through concurrent high temperature reactions. The CO_2 mitigation potential, when compared to the traditional carbothermic reduction, is as high as 78%. Furthermore, the use of solar energy for supplying the reaction enthalpy upgrades the calorific value of the initial reactants by 39% [2].

The chemical thermodynamics and kinetics of reaction (1) have been reported in Refs. [1-3]. The reaction is highly endothermic and proceeds at temperatures above 1250 K. Technical feasibility has been demonstrated for a 5-kW solar reactor tested in a high-flux solar furnace [4]. This note presents an economic assessment of the costs of solar Zn and H_2, when produced via reaction (1) using solar process heat [5]. This analysis requires a definition of the material and energy flows and an estimation of the cost of the plant components, their operation, and maintenance.

2 MATERIAL AND ENERGY FLOWS

Figure 1 shows a model flow diagram for the proposed solar thermochemical process. It uses a solar reactor, a heat exchanger, a quenching device, a Zn/air fuel cell, a water-splitter reactor, a H_2/O_2 fuel cell, a water-gas shift reactor, and a heat engine.

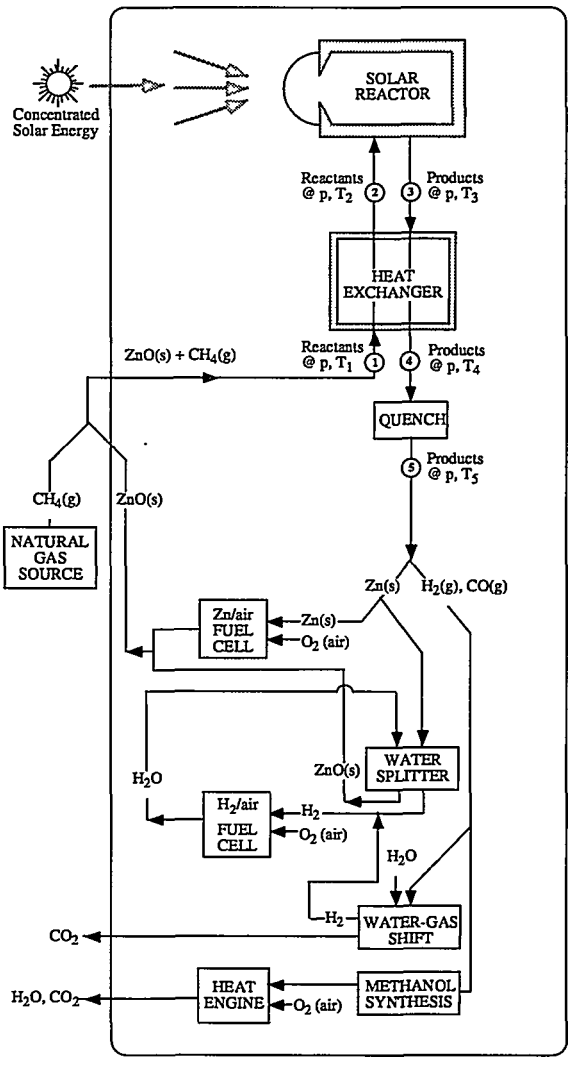

Fig. 1: Model flow diagram of the solar thermochemical process [5].

An equimolar mixture of ZnO(s) and CH_4(g) is fed into the process at 298 K and 1 atm. Table 1 summarizes the enthalpy changes for the solar process without heat recovery [5]. The reactants can be pre-heated in an adiabatic counter-current-flow heat exchanger where some portion of the sensible and latent heat of the products is transferred to the reactants. Without heat recovery the enthalpy change is 549 kJ/mol. The maximum possible heat recovery is 225 kJ/mol, reducing the solar requirement to 324 kJ/mol.

Step	*T [K]*	*$\Delta H°$ [kJ/mol]*
Heat ZnO	300 to 1250	+48
Heat CH_4	300 to 1250	+59
$ZnO+CH_4 \rightarrow Zn(g)+2H_2+CO$	1250	+442
Cool $Zn(g) + 2H_2 + CO$	1250 to 300	-237
$Zn(g) \rightarrow Zn(l)$	---	-116
$Zn(l) \rightarrow Zn(s)$	693	-7

Table 1: Standard enthalpy changes for effecting reaction (1).

3 ESTIMATED COSTS

Table 2 shows the cost breakdown of the solar chemical plant and the unit cost of zinc, for the case of no heat recovery. Included is also the unit cost of hydrogen for the case that zinc is further processed to hydrogen by means of a water-splitting reactor. Not included in the analysis is the cost of the ZnO feed, such as might be characteristic of ZnO-recycle from batteries. Government subsidies or any credit for CO_2 mitigation have also been excluded from consideration. Detailed cost estimation is found in Ref. [5].

The present market prices for zinc are about $1000/t. Its price is strongly influenced by the cost of energy required to produce it: assuming an energy consumption of 35-50 GJ/t and a fossil-fuel-based power cost of 0.05 $/kWh, the cost of energy represents between 40-70% of the market value of zinc. The estimated cost of solar Zn is between $89 and $133/t, neglecting the cost of ZnO feed and depending on the heat recovery efficiency. The cost of the solar collection system (heliostats, tower, tower reflector and secondary concentrators) represents about 50% of the total cost of the plant, while the reactor cost amounts to only 10% of the total cost. However, since the efficiency of the reactor dictates the size of the heliostat field, reaching high efficiencies will have a significant impact on reducing the cost of Zn.

As for hydrogen production, the solar technology is a favorable long term prospect once the cost of energy will account for the environmental externalities from fossil fuel burning such as the costs for CO_2 mitigation and pollution abatement. The weaknesses of this economic analysis are related principally to the early stage of process development. The technical feasibility of large-scale reactors and heat recovery techniques needs demonstration.

Assumptions	
Solar input [MW]	51
Solar input/year [MWh/yr]	117,300
Heliostat area [m^2]	105,000
Design ZnO feed [kg-mol/hr]	334
Zinc metal production [t/yr]	50,000
Syngas production [million-kWh/yr]	164
H_2 production [million-kWh/yr]	52
Fixed charge rate [%/yr]	15
Annual solar thermal efficiency* [%]	49
Capital cost [million $]	
Heliostat field [$150/$m^2$]	15.75
Tower	3.60
Tower reflector and CPCs	5.30
Solar receiver-reactor	6.00
H_2 chemical plant (hydrolyzer + storage)	5.00
Syngas compressor + storage	3.50
Balance of plant, indirects, contingency	15.00
TOTAL (for Zn)	49.15
TOTAL (for H_2)	54.15
Annual cost [million $]	
Capital cost (for Zn)	7.37
Capital cost (for H_2)	8.12
Operations and maintenance	1.08
NG cost [8.50 $/MWh]	1.46
Credit for syngas sale [20 $/MWh]	-3.28
TOTAL for Zn	6.63
TOTAL for H_2	7.38
Specific cost	
Unit cost of Zn [$/t]	133
Unit cost of H_2 [$/kWh]	0.14

* Annual solar thermal efficiency is defined as the fraction of annual solar radiation used for process heat. It is calculated, on a yearly basis, as the ratio of the enthalpy change of the reaction to the solar beam radiation incident over the heliostat area.

Table 2: Costs of solar Zn and H_2, without heat recovery.

4 ACKNOWLEDGEMENTS

We gratefully acknowledge the financial support of the Swiss Federal Office of Energy and the Baugarten Foundation.

5 REFERENCES

[1] A. Steinfeld, A. Frei, P. Kuhn, D. Wuillemin, *Int. J. Hydrogen Energy* **20**, 793-804 (1995).

[2] A. Steinfeld, *Energy* **22**, 311-316 (1997).

[3] A. Steinfeld, C. Larson , R. Palumbo, M. Foley, *Energy* **21**, 205-222 (1996).

[4] A. Steinfeld, M. Brack, A. Meier, A. Weidenkaff, D. Wuillemin, *Energy* **23**, 803-814 (1998).

[5] A. Steinfeld, I. Spiewak, *Energy Conversion and Management* **39**, 1513-1518 (1998).

SOLAR PRODUCTION OF CATALYTIC FILAMENTOUS CARBON BY THERMAL DECOMPOSITION OF HYDROCARBONS AND CARBON MONOXIDE

V.A. Kirillov, G.G. Kuvshinov, Yu.I. Mogilnykh (Boreskov Institute of Catalysis, Russia), A. Reller (University of Hamburg, Germany), A. Steinfeld, A. Weidenkaff, A. Meier

Concentrated solar radiation was used as the clean source of process heat for the production of Catalytic Filamentous Carbon (CFC) by thermal decomposition of gaseous hydrocarbons and by CO disproportionation in the presence of small metal catalyst particles. Depending on the catalyst, two different types of CFC, namely nanotubes and nanofibers, were obtained in solar experiments at the PSI solar furnace.

1 INTRODUCTION

Catalytic Filamentous Carbon (CFC) can be formed by thermal decomposition of hydrocarbons and by CO disproportionation in the presence of small catalyst particles containing group VIII metals [1,2]. These carbon materials exhibit unique properties which are of technical interest in various fields, e.g. in the reinforcement of composites, in energy storage devices, and in environmental pollution control.

The catalytic decomposition of hydrocarbons and the CO disproportionation proceed at temperatures above about 450°C when conducted at atmospheric pressure. The general stoichiometric reactions can be represented by

$$C_nH_m \leftrightarrow nC + \frac{m}{2}H_2$$

and

$$2CO \leftrightarrow C + CO_2,$$

respectively. Usually, the energy for these processes is supplied by electric heaters or by combusting some portion of the hydrocarbon containing gases. An attractive alternate approach is the use of concentrated solar radiation as a clean source of process heat [3]. We studied the influence of the direct solar radiation on the chemical reaction and on the morphology of the produced CFC. We examined the solar produced CFC samples for their capability to store hydrogen and for their suitability to special electrical and mechanical applications [4]. Furthermore, we determined the carbon mass produced per unit catalyst mass during the reaction time and the chemical conversion of methane to hydrogen [5]. Experiments were performed under direct solar irradiation using the high-flux solar furnace of the Paul Scherrer Institute (PSI) and under similar reaction conditions using an electric furnace with indirect heat transfer at the Boreskov Institute of Catalysis (BIC).

2 EXPERIMENTAL

The solar experiments were conducted in the PSI solar furnace. The experimental set-up has been described elsewhere [3]. Here, we summarise briefly the main features of the solar receiver/reactor. It consisted of a 2 cm diameter quartz tube containing a 5 cm high fluidized bed of inert material (Al_2O_3 grains) and on top of it a 5 mm high layer of fine catalyst granules (Ni/Al_2O_3 or Co/MgO). The inert material did not act as a catalyst support, but rather it was introduced to stabilise the temperature in the reaction zone, prevent sintering, and help fluidization. The tubular fluidized bed reactor was uniformly irradiated by concentrated sunlight using a silver-coated secondary reflector. A typical solar experiment consisted of two phases: (1) for the catalyst activation, the fluidized bed was solar-heated to temperatures of about 450 to 500°C under a flow of 10 vol% H_2 and 90 vol% N_2; (2) for the catalyst deactivation, the fluidized bed was subjected to a reacting gas flow according to various process operating conditions (see Table 1). The composition of the gaseous products was analysed by gas chromatography.

3 RESULTS

After activation of the catalyst particles (Ni/Al_2O_3, Co/MgO) with hydrogen, the catalytic carbon formation begins with the chemisorption and decomposition of hydrocarbons (CH_4, C_4H_{10}) or CO on the surface of each metal nanoparticle, followed by carbon diffusion through the catalyst nanoparticle and precipitation of carbon in the form of filamentous carbon on the opposite side of the nanoparticle [1].

Exp.	Catalyst	Mean Reactant Flow Rate [m³/hr]					$T_{average}$ [°C]
		N_2	H_2	CH_4	C_4H_{10}	CO	
1	Co/MgO	0.07		0.018			550
2	Co/MgO	0.10	0.011	0.015			550
3	Co/MgO	0.15				0.018	430
4	Ni/Al_2O_3	0.10				0.032	450
5	Ni/SiO_2	0.08		0.024			550
6	Ni/Al_2O_3	0.12	0.014	0.018			540
7	Ni/Al_2O_3	0.10	0.011		0.004		470

Table 1: Typical experimental conditions for the CFC production in the solar furnace.

High resolution transmission electron micrographs (HRTEM) of both the solar and the laboratory experiments show that two different types of filamentous carbon were obtained, namely nanotubes and nanofibers. The morphology of the produced CFC depends mainly on the catalyst. Carbon nanofibers without a hollow channel are obtained mainly on the Ni/Al_2O_3 catalyst that forms conical nuclei (growth centres) with the tip pointing in the direction of the filament growth (Figure 1). In contrast, nanotubes with long, parallel,

cylindrical walls containing the catalyst particle inside the hollow core are formed mainly on the rather spherical Co/MgO catalyst (Figure 2). The size of the produced filaments depends on the size of the catalyst particle.

The carbon textures of our solar-produced CFC samples were comparable to those obtained under similar experimental conditions in the laboratory. Typically, the following properties were determined by BET: the surface area is about 50 to 170 m^2/g, the micropore volume is between 0.002 and 0.008 cm^3/g, the average pore diameter ranges between 10 and 40 nm, and the pore volume is in the range of 0.4 to 0.8 cm^3/g. We found no significant influence of the reaction temperature (between 450 and 700°C) on the carbon surface area and on the average pore volume.

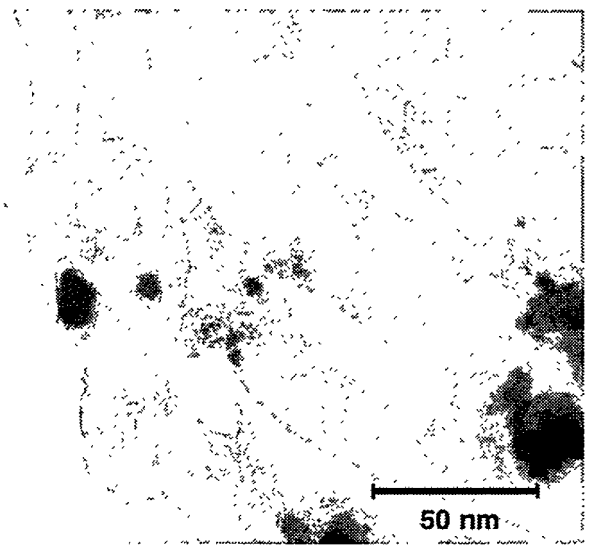

Fig. 1: HRTEM of solar-produced nanofibers on Ni/Al_2O_3 catalyst by decomposition of CH_4+H_2 (Exp.6).

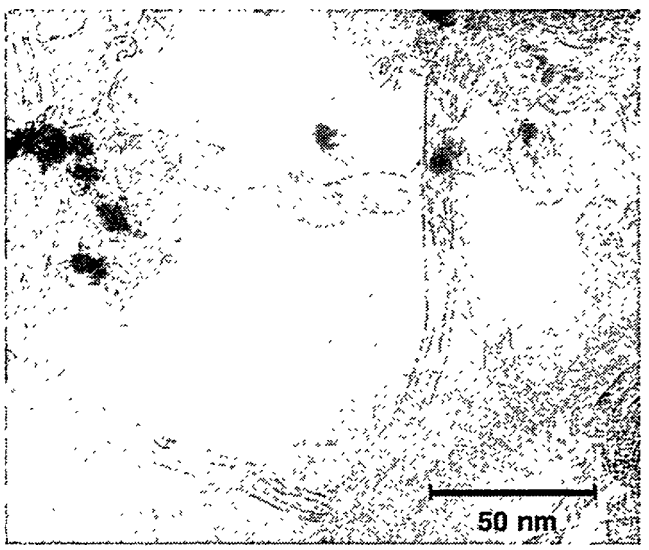

Fig. 2: HRTEM of solar-produced nanotubes on Co/MgO catalyst by CO disproportionation (Exp.3).

In a recent patent [6], the authors claimed that significant amounts of hydrogen could be stored in layered nanostructures by decomposing carbon-containing gases over a catalyst. However, these preliminary results have not been confirmed, and our solar and laboratory CFC samples did not show any H_2 storage capability [7]. This negative result can be partly explained by the fact that the pore size of our CFC samples seems to exceed the critical size suitable for H_2 storage (about 1 nm) [7].

4 CONCLUSION

From the CFC properties obtained by BET and from the inspection of HRTEM images we conclude that CFC with well defined morphology can be produced using direct solar radiation. We found that the different catalytic growth mechanisms depend on the type of the metal particles, the exposed crystal surface and the reacting gas. However, the influence of the reaction temperature on the carbon texture and the role of the different reacting gases need further investigation.

The appropriate choice of the relevant parameters responsible for the CFC texture should allow one to produce valuable chemical commodities of technical interest. The production of CFC by solar thermal decomposition of hydrocarbons and CO disproportionation is an interesting challenge for future research in materials science.

5 ACKNOWLEDGEMENTS

We gratefully acknowledge the financial support from the Swiss Federal Office of Energy (BFE). We thank A. Frei, F. Geiger, T. Schelling (PSI), R. Wessiken (ETH Zürich), A. Khassin (BIC), and M. Fröba (University of Hamburg) for technical support.

6 REFERENCES

[1] R.T.K. Baker, Carbon **27**(3), 315-323 (1989).

[2] V.A. Likholobov, V.B. Fenelov, L.G. Okkel, et al., React. Kinet. Catal. Lett. **54**(2), 381-411 (1995).

[3] A. Steinfeld, V. Kirillov, G. Kuvshinov, Y. Mogilnykh, A. Reller, Chem. Engng Sci. **52**, 3599-3603 (1997).

[4] A. Meier, V. Kirillov, G. Kuvshinov, et al., *Solar Thermal Decomposition of Hydrocarbons and Carbon Monoxide for the Production of Catalytic Filamentous Carbon*, Chem. Engng Sci., in press (1999).

[5] A. Meier, V. Kirillov, G. Kuvshinov, et al., *Production of Catalytic Filamentous Carbon by Solar Thermal Decomposition of Hydrocarbons*, Proc. 9th Int. Symp. Solar Thermal Concentrating Technologies, Odeillo, France, in press (1999).

[6] N.M. Rodriguez, R.T.K. Baker, US Patent No. 5,653,951, publ. 5.8.97 (1997).

[7] B. Meurant, E. Newson, PSI, private communication (1998).

DEVELOPMENT OF AN APPARATUS TO STUDY CHEMICAL REACTIONS AT HIGH TEMPERATURE – A PROGRESS REPORT

M. Sturzenegger, Th. Schelling, E. Steiner, D. Wuillemin

TREMPER is an apparatus that was devised to study kinetic and thermodynamic aspects of high-temperature reactions under concentrated solar irradiation. The design allows investigations on solid or liquid samples under inert or reactive atmospheres. The working temperature is adjustable; the upper limit that has yet been reached is about 1900 K. TREMPER will facilitate chemical reactivity studies on a temperature level that is difficult to access by other means. First experiments were conducted to study the decomposition of manganese oxide MnO_2. Chemical analysis of exposed samples confirmed that the parent MnO_2 was decomposed to mixtures of MnO and Mn_3O_4. The amount of MnO ranged from 60 mol-% in air to 86 mol-% under inert atmosphere.

1 INTRODUCTION

High-temperature reactions of metal oxides are attractive for converting concentrated solar radiation to chemical energy to eventually provide chemical fuels [1]. The completeness of the employed reaction has an immediate impact on the efficiency of the conversion. Furthermore, the kinetics of the reaction is an important parameter for choosing the appropriate process reactor concept and for designing the desired process reactor. However, experiments employing conventional techniques yield often thermodynamic and kinetic data for temperatures only up to 1800 K. The literature thus contains only few experimental data for temperatures above 1800 K. Most of these reported data were extrapolated from moderate temperatures over a range of several hundred degrees. The goal of this study was therefore the design of an apparatus that would allow to experimentally assess equilibrium compositions of condensed phase metal oxides under defined atmospheres at temperatures up to 2500 K and allow to establish the course of the reaction.

2 EXPERIMENTAL

The apparatus, TREMPER, is schematically represented in Figure 1. A 45° mirror (1) guides the concentrated solar radiation from the parabolic concentrator of the solar furnace onto the sample at position 2. The sample is placed in a shallow hole on a water-cooled support from copper to avoid reaction between the oxide and the support. Because the amount of incoming radiation energy greatly exceeds the reaction enthalpy the cold support has no impact on the maximum desired temperature. The course of the reaction can be derived from the evolution of gaseous products or from the chemical composition of the solid product. The gases are collected in situ just above the sample with a fused silica capillary (3) and are analysed in the mass spectrometer. The reaction is terminated by remotely releasing the hammer (4). The hot oxide will be rapidly cooled between the water-cooled sample support and the hammer, and the high-temperature composition is frozen by the quench. A gas flow is directed towards the mirror (position 5) to avoid deposition of volatilized metal oxides and to maintain a constant oxygen partial pressure above the sample. The entire apparatus is placed in a quartz tube (6) to ensure reproducible working conditions and to allow variations in the atmosphere's oxygen partial pressure.

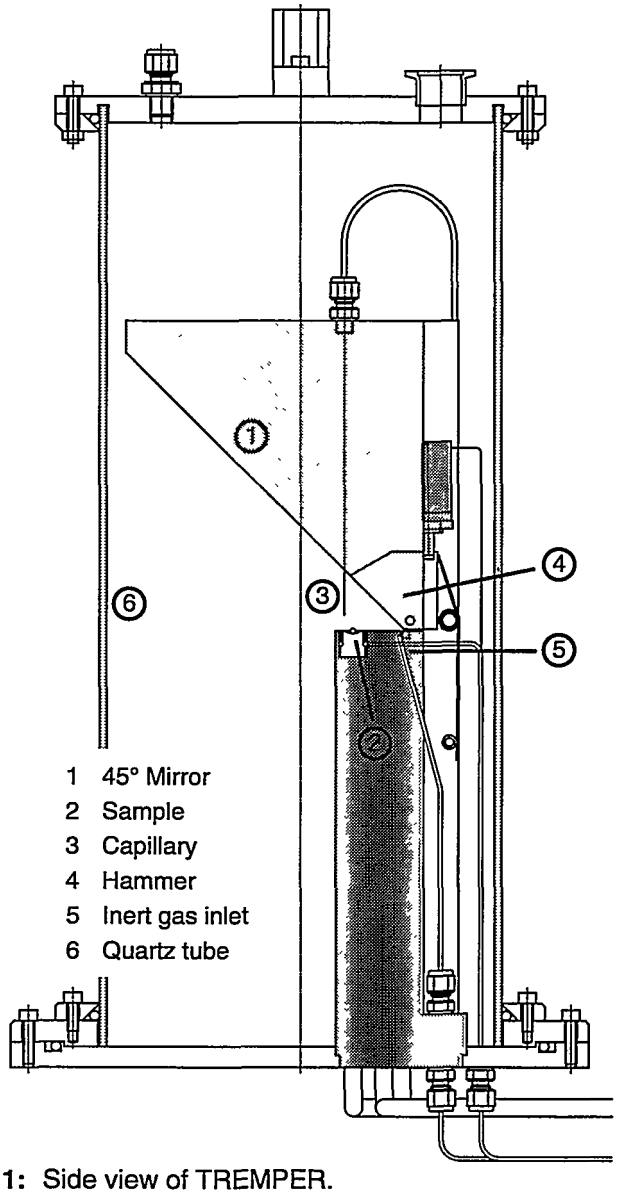

Fig. 1: Side view of TREMPER.

Group	Atmosphere	Exposure Time [s]	Quenched	MnO Content[a] [mol-%]	
				XRD	TG[b]
1	air	85	no	2	-
1	air	272	no	7	-
2	air	20	yes	30	38
2	air	180	yes	60	-
3	N_2	20	no	50	57
3	N_2	20	no	44	53
3	N_2	47	no	61	70
3	N_2	48	no	64	77
3	N_2	195	no	79	86

[a] The difference to 100 mol-% is Mn_3O_4. [b] The MnO content was derived from thermogravimetric reductions in H_2.

Table 1: MnO content of solar reduced MnO_2 samples.

The starting material was pure manganese(IV)oxide, MnO_2. The powder was pressed into pellets and pieces of them ($\approx$ 5 x 5 mm^2 with a weight of $\approx$ 200 mg) were placed on the sample holder.

Experiments were conducted at the 50 kW solar furnace at PSI. Incident irradiation varied between 710 and 915 Wm^{-2}, the corresponding flux densities on a Lambertian reference target ranged from 230 to 420 Wcm^{-2}. The peak flux densities in the plane of the sample were determined to be approximately 80 % of the flux density on the reference target. The gas flow at position 5 was 10 $l_N min^{-1}$.

Reacted samples were analysed by means of powder X-ray diffractometry and thermogravimetric analysis.

3 RESULTS

Exposure of MnO_2 pellets caused melting of the sample and the formation of droplets with diameters of $\approx$ 5 mm. The results of phase analysis and chemical analysis are listed in Table 1. It shows that decomposition reactions yielded Mn_3O_4-MnO mixtures under both inert atmosphere and under air. None of the samples contained Mn_2O_3, even samples decomposed under air and not quenched were free of Mn_2O_3.

4 DISCUSSION

The experiments had to objectives: On the one hand they were aimed at gaining information on the solar thermal reduction of MnO_2. On the other hand it needed to be verified whether TREMPER is suitable for systematic reactivity studies at high temperatures. Reliability and quench behaviour of the apparatus, as well as reproducibility of the experiments were therefore important aspects to be evaluated.

The results of the decomposition experiments in Table 1 indicate that MnO_2 can be decomposed at moderate flux densities with high yields. Under air and flux densities in the sample plane of 230 Wcm^{-2} MnO was obtained with yields up to 60 %. Under N_2 and flux densities of 400 Wm^{-2} samples with up to 86 mol-% were obtained. The results suggest that the formation of Mn_3O_4-MnO mixtures with only 5 mol-% MnO in earlier experiments [2] was due to specific reaction conditions and not because of thermodynamic constraints. The results further indicate that the sample must have reached temperatures close to 1900 K because otherwise no decomposition would have occurred in air.

A comparison of the results demonstrate the quench ability of TREMPER. Decomposition of MnO_2 under air without quenching (group 1) yielded only small amounts of MnO. In contrast, quenched samples from experiments under air (group 2) were much richer in MnO. Their content is comparable to those of experiments under N_2 (group 3). A calculation whether the observed difference between group 2 and 3 is only due to the different oxygen partial pressure needs to be conducted.

The repetition of decomposition experiments under nominally equal conditions yielded samples whose composition agreed within 10 %. Thus, reproducibility is sufficient to derive thermodynamic and kinetic information with good accuracy.

5 CONCLUSION

Experiments and results demonstrate the ability of TREMPER to conduct reactivity studies with condensed phase materials. High reliability and good reproducibility will allow an efficient acquiring of experimental data to assess equilibrium compositions as well as to derive kinetic parameters.

Information on the sample temperature has yet been deduced from the occurrence of chemical reactions. The actual temperature, however, is a crucial parameter in reactivity studies. The implementation of a temperature measurement technique will therefore be an important objective in the next step of development.

6 ACKNOWLEDGEMENTS

The authors wish to thank A. Frei for analysing the samples. Financial support from the Swiss Federal Office of Energy is gratefully acknowledged.

7 REFERENCES

[1] A. Steinfeld, P. Kuhn, A. Reller, R. Palumbo, J. Murray, Y. Tamaura, *Solar-Processed Metals as Clean Energy Carriers and Water-Splitters,* Proc. 11th World Hydrogen Energy Conference, Stuttgart/Germany, 601-609 (1996).

[2] J. Ganz, E. Steiner, M. Sturzenegger, *Powder Cloud Reactors – An Attractive Concept to Run Solar High-Temperature Reactions,* Proc. 9th International Symposium on Solar Thermal Concentrating Technologies, Odeillo/France, in press.

MONTE-CARLO RAY TRACING SIMULATION OF A FALLING PARTICLE RECEIVER IN CONNECTION WITH A CENTRAL RECEIVER FIELD

I. Alxneit

The program RAY was developed to perform Monte-Carlo simulations of the flux distribution in solar reactors in connection with an arbitrary heliostat field. The code accounts for the shading of the incoming rays from the sun due to the reactor supporting tower as well as for full blocking and shading of the heliostats among themselves. A simplified falling particle reactor (FPR) was evaluated. A central receiver field was used with a total area of 311 m^2 composed of 176 round, focusing heliostats. No attempt was undertaken to optimise either the geometry of the heliostat field nor the aiming strategy of the heliostats. The FPR was evaluated at two different geographic latitudes (-8.23W/47.542N; PSI and -8.23W/20.0N) and during the course of a day (May 30th). The incident power passing through the reactor aperture and the flux density distribution within the FPR was calculated.

1 INTRODUCTION

In an exploratory study on the feasibility of the solar calcination of limestone for solar assisted cement production the concept of a falling particle reactor was evaluated [1]. This concept relies on the direct absorption of the solar power by the falling particles. Monte-Carlo ray tracing simulations were performed to judge whether flux densities that are needed for the calcination can be achieved on the particle curtain.

The program RAY randomly defines rays coming from the sun and propagates them according to the laws of geometrical optics from the sun via the heliostats into the reactor. The subroutine rng-double_new.c [2] was used as high quality random number generator.

For the simulations a simplified model of a reactor was used (see Figure 1). The round, barrel-like reactor body was modelled as a hexagonal tube. For each simulation the flux densities were calculated for the nine targets contributing the model, i.e. six walls, ceiling, just before the entrance aperture (spot size), just after the entrance aperture (flux entering the reactor).

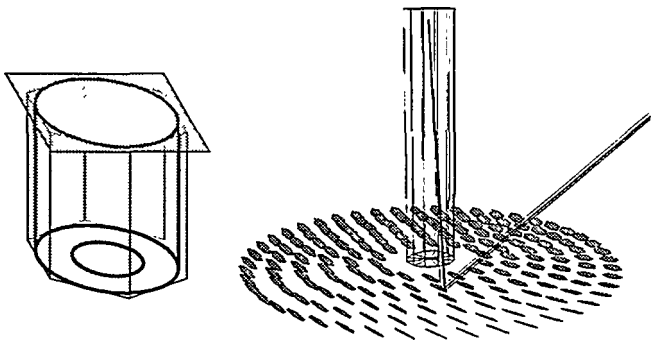

Fig. 1: Model of the reactor (left) and layout of the central receiver field (right).

The simple circular heliostat field of Figure 1 was used. Each of the heliostats aims at the centre of the reactor aperture. The reactor is situated face down on a tower at a height of 19 m. In these simulations the new concept of small focusing heliostats [3] was employed. Thus, each heliostat is a praraboloid, its focal length chosen to focus onto the aperture of the reactor. Generally all simulations were performed using 100000 rays per m^2 projected heliostat surface. This results in a total of 27.5 - 30.0 Mrays to be calculated for each of the nine targets defined above. RAY performs at about 100000 rays/min on an Pentium 90MHz computer.

2 RESULTS AND DISCUSSION

The simulations confirmed that high flux densities can be achieved with focusing heliostats. Concentrations of about 8000 suns in the aperture of the reactor were obtained. 69.0-86.7% (location PSI) respectively 69.6-95.0% (location 20.0N) of the solar radiation enter the reactor. Independent of geographic location and time of the day only about 60% of this flux hits the reactor walls and thus contributes to the calcination process.

	PSI	20.0N
0800 UT	69.0 %	69.6 %
1000 UT	83.2 %	90.0 %
1030 UT (solar noon)	86.7 %	95.0 %

Tab. 1: Power entering the FPR (UT = lokale Sommerzeit abzüglich 1 h 33 m).

In Figure 2 the power distribution along the circumference of the reactor is reported. One notes a large variation along the circumference. The variation is strongest at low elevations of the sun but remains

strong during the day at location PSI. At 20.0N an almost complete levelling out is obtained around solar noon.

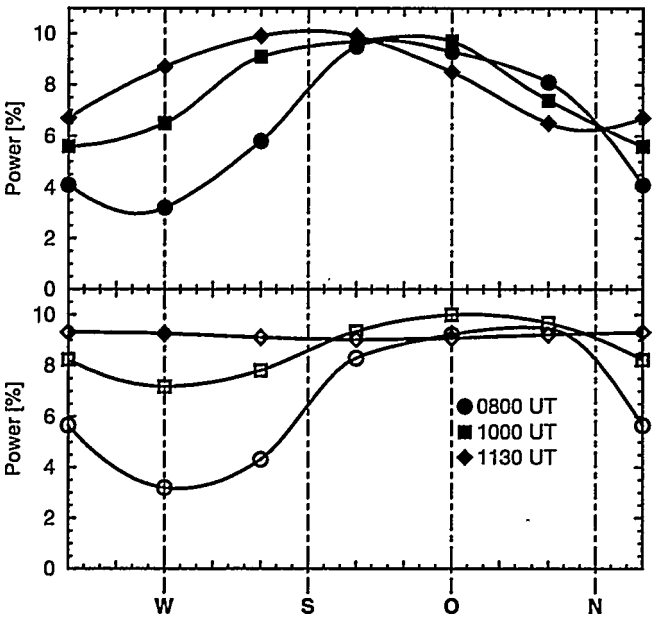

Fig. 2: Power distribution on the wall of the FPR.
Top: -8.23W/47.542N (PSI).
Bottom: -8.23W/20.0N.

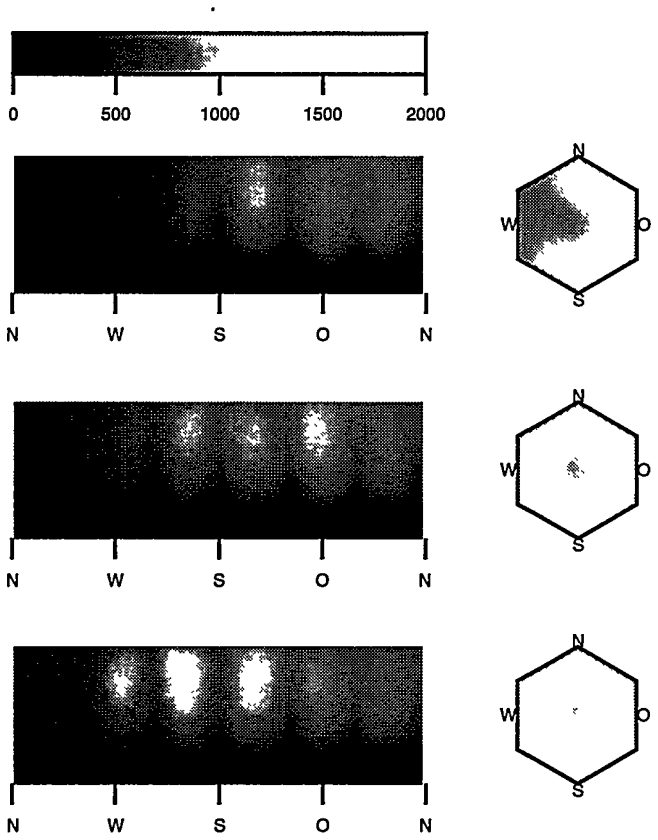

Fig. 3: Flux density distribution as concentration factors in the FPR at -8.23W/47.542N (location PSI) on May 30th.
Left: flux on the reactor wall, right on the reactor ceiling. Top: 0800 UT, middle: 1000 UT, bottom 1130 UT.

In Figure 3 the actual flux density distribution on the walls and on the reactor ceiling is exemplified for the geographic location 47.542N. Note that the wave-like distortions in Figure 3 are due to the approximation of the reactor by a hexagonal tube.

From Figure 3 and Table 1 one readily notes that the chosen geometry of the reactor is far from optimal. Due to the small aspect ratio (hight to diameter) the regions of high solar flux densities are found on the ceiling of the reactor. On the walls, maximum concentrations of about 800 suns are achieved, while maximum concentrations of almost 2000 suns are found in large regions of the ceiling. The flux density distribution on the ceiling of the reactor images the circular heliostat field. It exhibits a ring-like structure modulated by the cosine factor of the individual heliostats. It is most bright on the side facing the sun (south in Figure 3, 1130 UT). One notes the devastating influence of the tower shade. While small in absolute numbers (less than 4% worst case) the tower efficiently shades the heliostats that are facing the sun whose cosine losses are small and are responsible for the regions with a large flux density. In Figure 3, 1000 UT the dip in the flux density close to the south-east edge of the heaxagonal ceiling illustrates this fact.

3 CONCLUSION

The program RAY proved to be versatile in rating the quality of the design of a solar reactor. The FPR chosen in this study was identified to suffer from too small an aspect ratio (hight to diameter). This flaw can easily be corrected. Shading by the tower, a very general problem of central fields, could be identified. This leads to large inhomogeneities of the flux distribution inside a solar reactor. They will be partly smoothed, however, if one accounts for scattering of non-absorbed radiation inside the reactor.

4 ACKNOWLEDGEMENT

This work has been supported by the Swiss Federal Office of Energy (BFE).

5 REFERENCES

[1] D. Rose, S. Mainusch, Th.A. Lang, M. Gyurech, J. Kleinwächter, A. Hintermann, A. Reller, A. Wokaun, A. Imhof, *Industrielle Solarkalzinierung,* Dritter Workshop (1997).

[2] D.E. Knuth, *The Art of Computer Programming,* **2**, Seminumerical Algorithms, 3rd edition, Addison-Wesley (1997).
http://www-cs-faculty.stanford.edu/~knuth/programs.html.

[3] L.L. Vant-Hull, M.E. Izygon, A. Imhof, *Optimisation of central receiver fields to interface with applications requiring high flux density receivers*, 9th International Symposium on Solar Thermal Concentrating Technologies (1998).

SOURCES AND SPECIATION OF HEAVY METALS IN MUNICIPAL SOLID WASTE (MSW) AND ITS EFFECT ON THE SEPARATION TECHNIQUE

S. Biollaz, Ch. Ludwig, S. Stucki

A literature search was carried out to determine sources and speciation of heavy metals in MSW. A combination of thermal and mechanical separation techniques is necessary to achieve the required high degrees of metal separation. Metallic goods should be separated mechanically, chemically bound heavy metals by a thermal process.

1 INTRODUCTION

The goal of waste management in Switzerland is to produce either disposable residues or reusable products [1]. Disposable residues are regulated in the TVA [2]. Criteria for recycling mineral residues from waste are put down in the guideline for secondary raw materials in cement production [3].

With state-of-the-art MSW incineration technology the heavy metal concentrations in residues achieve neither the threshold values for landfill of inert material, nor the guideline values for secondary materials in cements (see Table 1).

Independent of which quality of residue is considered, there are two fundamental questions:

- How can the intended residue qualities be achieved, i.e. how can the heavy metals be separated from the mineral residues ?
- Within which range are the heavy metal concentrations in MSW and which degree of metal separation is therefore necessary for a given quality ?

Alternatively, thermal and mechanical separation techniques have been discussed for the heavy metal separation. The separating efficiency of these techniques depends considerably on the speciation (elemental or chemically bound) of the heavy metal, as well as their distribution (bulk, disperse).

2 HEAVY METAL CONCENTRATIONS

Element concentrations of different waste categories are represented in figure 1, as a function of typical element concentrations in MSW.

From Figure 1 it is recognisable that element concentrations in MSW can vary within one order of magnitude (see also Table 1).

For the estimation of sources and speciations of heavy metals in MSW, concentration data of different waste categories have been compiled. The waste components "paper & cardboard", "plastics", and "yard waste" approximately correspond to 75 weight-% of MSW [4].

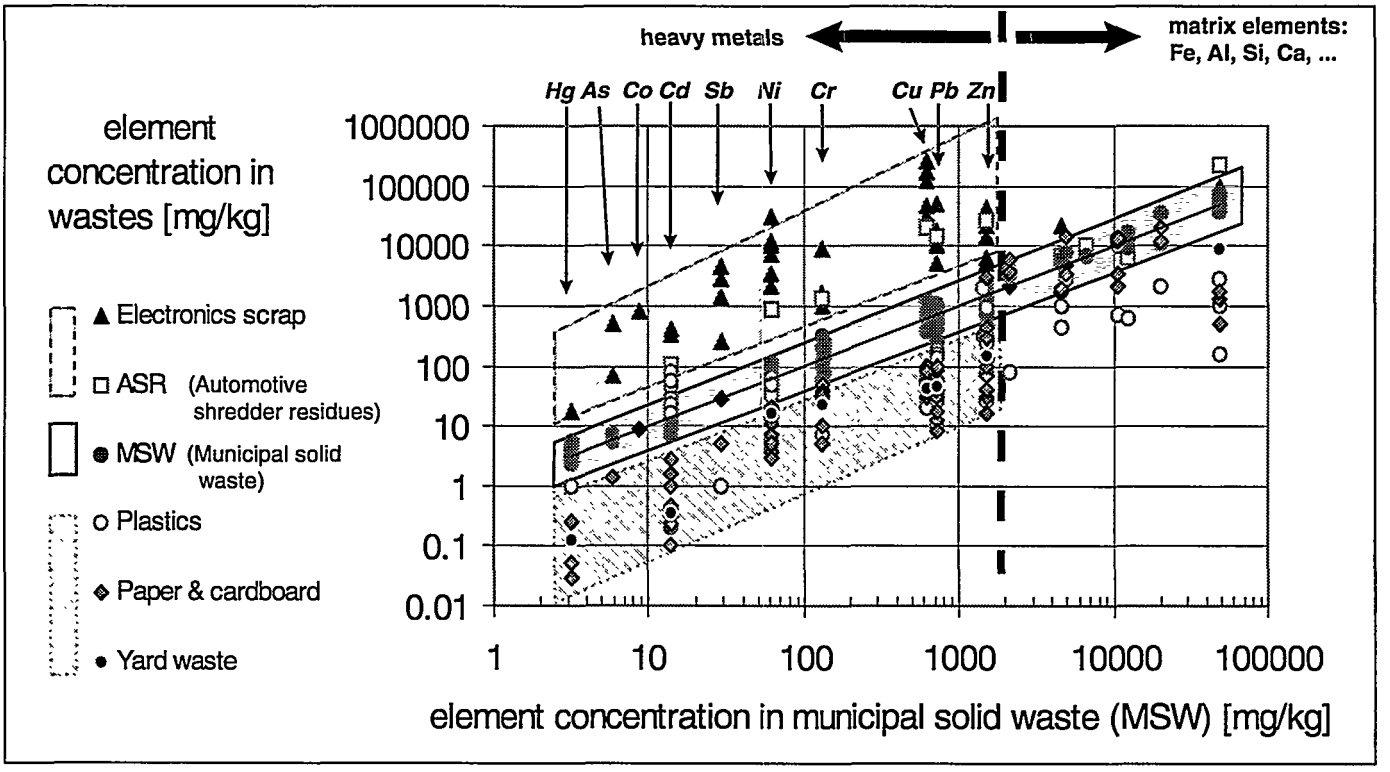

Fig. 1: Heavy metal concentrations in MSW, in MSW components, and in metallic waste components.

In Figure 1 literature data of heavy metal concentrations are shown for these wastes. It is recognisable that heavy metal concentrations are generally lower than in MSW. One exception is Cd in plastics with concentrations exceeds the values in MSW (Cd, and other heavy metals have been used as additives in plastics).

The heavy metal concentrations reported for MSW can not be explained by these waste components which account for the mass of MSW. According to reference [4], approximately 3 weight-% of MSW consists of metallic goods such as batteries, stainless steel, electronics scrap, etc. As examples for this type of goods, the heavy metal concentrations of electronics scrap and automotive shredder residues (ASR) from literature are represented in Figure 1. It is recognisable that these waste categories have concentrations substantially higher than in MSW.

From the above it is concluded that metal components can be identified as a main source of heavy metals. This can also explain the observed large concentration ranges in MSW. Waste components relevant for the bulk weight of MSW can in a first approximation be regarded as heavy metal-free.

Because of the dominating influence of the metallic goods on the concentration it is assumed that the predominant proportion of heavy metals in MSW is in elemental form. The heavy metals available in waste components such as paper, cardboard, plastics, and yard waste are present in chemically bound form.

3 HEAVY METAL SEPARATION

In Table 1 are listed the degrees to which heavy metals need to be separated in order to comply with standards for TVA inert materials and secondary materials in cement production. The degree of separation η_{sep} is calculated according to formula 1:

$$\eta_{sep} = 100 * \left(1 - \frac{t * c_{ash}}{MSW_{max}}\right) \qquad (1)$$

For the heavy metals regulated by the TVA it is recognisable in table 1 that for all elements a degree of separation of 90% must be achieved. An exception is nickel, whose small content in MSW leads to concentrations below the threshold value.

For the majority of the heavy metals which are regulated for secondary materials in cements the degree of separation is in the range of 95-98 %. For the elements V, Co, As, Se, and Tl no separation is yet required.

The elements Cu, Ni, and Cr are predominantly present in elemental form. Ni and Cr cannot be separated thermally from the mineral residues. Since these elements are mainly present in bulk form, a mechanical separation should be an efficient technique to achieve the required degrees of separation.

elements	*MSW* ash content (c_{ash}): 25 w.-%	*heavy metal separation*				
		NOMINAL				ACTUAL
		landfill of inert material [2]		secondary material in cement [3]		conventional MSWI [5]
		threshold	separation	guideline	separation	separation
	MWS_{min} MSW_{max} [mg/kg]	t [mg/kg]	η_{sep} [%]	t [mg/kg]	η_{sep} [%]	η_{sep} [%]
Hg	1 - 6	2	92	0.5	98	98
Cd	7 - 29	10	91	1	99	90
Pb	256 - 1095	500	89	75	98	50
Zn	725 - 2504	1000	90	400	96	50
Cu	333 - 1289	500	90	200	96	5
Ni	15 - 145	500	0	200	65	5
Cr	55 - 474	-	-	200	89	5
Sb	29 - 71	-	-	5	98	80
Sn	27 - 130	-	-	30	94	50
Ba	227 - 667	-	-	1000	63	10
Be	1	-	-	3	25	?
V	33 - 40	-	-	300	0	?
Co	4 - 9	-	-	100	0	10
As	4 - 7	-	-	30	0	30
Se	1	-	-	5	0	70 [6]
Tl	0.3	-	-	2	0	20 [6]

Table 1: Range of heavy metal concentration in MSW, actual and nominal degree of metal separation (η_{sep}) from mineral residues.

4 CONCLUSION

Given the sources and speciations of heavy metals outlined above a skilful combination of thermal and mechanical separation techniques is necessary to achieve the required high degrees of separation. Metallic goods should be separated mechanically, chemically bound heavy metals by a thermal process.

5 REFERENCES

[1] Swiss commission for waste management: *Guidelines to waste management in Switzerland.* Swiss Agency for the Environment, Forests and Landscape, Publication SRU-51E, Bern (1986).

[2] TVA, *Technical Ordinance on Waste Management*, Swiss Federal Government 814.015, VA 1.7.1994, Bern (1991).

[3] Richtlinie; *Entsorgung von Abfällen in Zementwerken,* BUWAL (hrsg.), Bern (1998).

[4] K. Stumpf, *Zusammensetzung der Siedlungsabfälle in der Schweiz 1992/93*, BUWAL (hrsg.), Schriftenreihe Umwelt Nr. 248, Bern (1995).

[5] H. Belevi, *Environmental Engineering of Municipal Solid Waste Incineration,* vdf, Hochschulverlag an der ETH Zürich (1998).

[6] F.J. Angenend, L. Trondt, *Schadstoffinput-Schadstoffoutput,* VGB Kraftwerkstechnik 70, Heft 1, 36-50, February (1990).

HEAVY METAL EVAPORATION KINETICS IN THERMAL WASTE TREATMENT PROCESSES

Ch. Ludwig, S. Stucki, A.J. Schuler

To investigate the evaporation kinetics of heavy metals, experiments were performed by conventional thermogravimetry and a new method using Inductively Coupled Plasma Optical Emission Spectroscopy (ICP-OES). The new method allows online measurements in time intervals that are typically below one minute. The evaporation of Cd, Cu, Pb, and Zn from synthetic mixtures and filter ashes (FA) from municipal solid waste incineration (MSWI) was of major interest.

1 INTRODUCTION

During the combustion of demolition wood, or incineration of municipal waste valuable energy can be recycled. These alternative sources of energy, however, are mostly contaminated by various heavy metals. In contrast to organic pollutants which can be thermally decomposed, heavy metals retain their toxicity potential. These alternative sources of energy can only be used if the processes can be optimised with respect to heavy metals. The knowledge about the partitioning of the heavy metals into the various residues is therefore essential for separating and concentrating the heavy metals.

On one hand the remaining residues should be cleaned of organics and heavy metals so that they can be reused as construction materials; on the other the heavy metals should remain in forms that can be easily recycled by the appropriate industry.

Emphasis has been put on the volatilisation which is controlled by a) the gas atmosphere, b) the mineral matrix composition, grain size, and surface area, c) the composition, structure, and oxidation state of the heavy metals and d) process engineering parameters.

During the thermal treatment the inorganic matrix reacts to form new solid phases. Simple model substances, such as SiO_2, CaO, Al_2O_3, and calcium-silicates, calcium-aluminates, and alumino-silicates are considered to play an important role, inhibiting the evaporation of heavy metals as new minerals form during the thermal treatment of waste and incineration residues.

2 MATERIALS AND METHODS

All chemicals were purchased in p.a. grade from Merck, Fluka, Sigma or Aldrich. For studying the volatilisation of Zn, $ZnCl_2$ was mixed with ZnO, SiO_2 (0.5-10µm, 0.007 µm), or grained $CaSiO_3$, Ca_2SiO_4, or $CaAl_2O_4$ synthesised in a Pt crucible from $CaCO_3$, SiO_2, and Al_2O_3 powder mixtures heated in air at 1580 °C. $CaAl_2O_4$ contained small impurities of $Ca_{12}Al_{14}O_{33}$. For investigating the influence and fate of contaminants during wood gasification 0.55 g of sawdust from debarked spruce (0.05-0.25 mm, Schwere AG) was loaded with a mixture of 0.24 g grained lava (0.05-0.5 mm, Lava-Union GmbH, Germany), 2 mg of Cu_2O, 2 mg of PbO, and 3 mg of ZnO. A detailed analysis of the lava and sawdust showed that the heavy metal content was small and can be neglected compared to the added amount of heavy metals. Certified MSWI fly ash (BCR #176) was obtained from Kupper & Co. (Switzerland).

The $ZnCl_2$ evaporation rates were measured with a thermogravimeter (TG, Netzsch, STA 409). The products after the TG experiments were analysed by X-ray spectroscopy. To study the evaporation of heavy metals from more complex mixtures a quartz-glass furnace tube was connected to an ICP-OES.

3 CONDENSATION INTERFACE

To solve the condensation problems in transferring heavy metal loaded carrier gas (Ar, Ar saturated with aqueous HCl solutions (0-37 %), or Ar enriched with O_2) into the ICP-OES, a special condensation interface (CI) was constructed and patented [1]. The interface reduces the amount of heavy metals in the gas phase producing an aerosol that can easily be transferred into a detector. The amount of heavy metal evaporated is proportional to the intensity measured, e.g. by ICP-OES.

4 RESULTS AND DISCUSSION

Volatilisation of Zn. The hydrolysis of $ZnCl_2$ in presence of H_2O does not influence the evaporation rates. Figure 1 shows the effect of various matrix compounds on the evaporation rates of $ZnCl_2$ in humidified Ar. ZnO as matrix showed no effect, SiO_2, $CaSiO_3$, Ca_2SiO_4 and $CaAl_2O_4$ lead to the formation of Zn_2SiO_4, $ZnCa_2Si_2O_7$, $ZnCa_8Si_4O_{16}Cl_2$, and $ZnAl_2O_4$, respectively. $ZnCa_8Si_4O_{16}Cl_2$ decomposed between 900 °C and 1300 °C. Zn remaining in the solid phase was identified as $ZnCa_2Si_2O_7$. The influence on the rates during the formation of new phases at different temperature ranges is shown in Figure 1. The surface area of the matrix seemed to be important as experiments with SiO_2 of high surface area showed a stronger inhibition on the $ZnCl_2$ evaporation due to the formation of Zn_2SiO_4 [2].

The interpretation of TG results with respect to heavy metal evaporation is difficult, as other reactions may also lead to a change in weight. The evaporation measured by CI-ICP-OES allows the simultaneous online detection of several elements. The method is

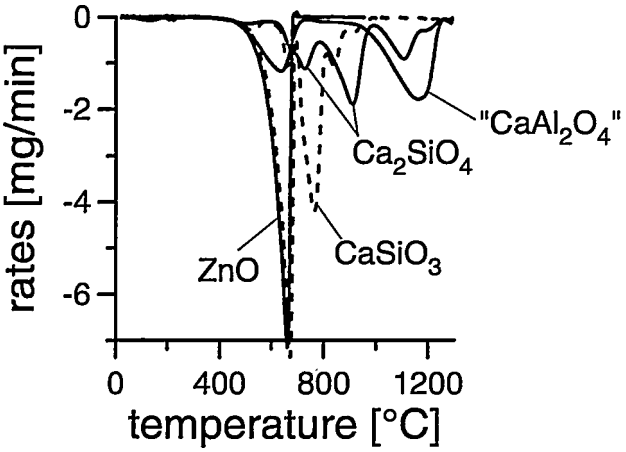

Fig. 1: $ZnCl_2$ evaporation in presence of different mineral phases and in absence of a matrix (dashed line identical with the evaporation in presence of ZnO). As carrier gas humidified Ar was used (50 ml/min) and the temperature was increased at a rate of 10K per minute.

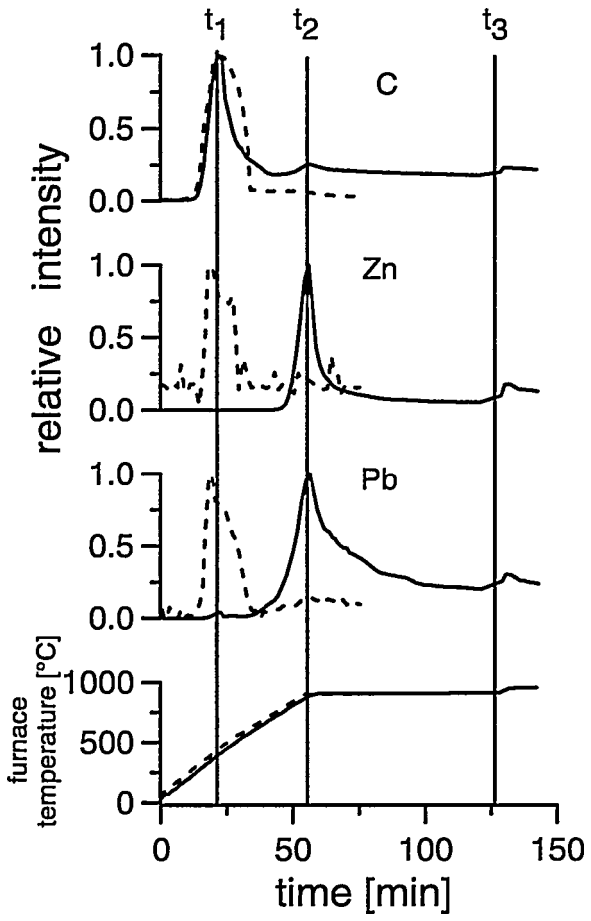

Fig. 2: Pyrolysis (solid line) and combustion (dashed line) of sawdust in presence of lava, Cu_2O, PbO, and ZnO was investigated by the CI-ICP-OES method. The intensities were standardised for the maximum intensity of each experiment. The maximum intensity in the combustion experiment reached only 75 % (C), 0.1 % (Zn) and 16 % (Pb) of the values measured during the pyrolysis experiment. A quantitative comparison of the two experiments, however, is not yet possible (see text).

still under development. It will be extended for analytical use determining trace elements in solid samples making use of the volatility of the heavy metals under reducing or corrosive conditions. E. g. heavy metals of filter ashes from municipal solid waste incinerators can be volatilised at 900 °C with HCl [3] and Cd, Cu, Pb, and Zn evaporation in Ar was successfully monitored using the CI-ICP-OES method [4].

Pyrolysis of contaminated wood samples. The volatilisation of heavy metals during the pyrolysis of sawdust in presence of Cu_2O, PbO, ZnO, and lava was monitored as shown in Figure 2 (solid line). The pyrolysis started at a lower temperature than the evaporation of Zn and Pb as indicated by t_1 and t_2 in Figure 2. Only very small amounts of Zn and Pb were simultaneously volatilised with C (t_1, Figure 2). The Cu measurements are not shown as no Cu could be detected. An extra increase in temperature (Figure 2) at the end of the experiment showed also an increase in volatilised C, Zn, and Pb. ICP-OES analysis of the dissolved residues showed that about 98% of Pb and 95% of Zn but no Cu evaporated.

The investigation of samples in an oxidising atmosphere is more difficult as the plasma of the ICP-OES in standard mode runs with Ar only and strong gassing can influence the ICP-OES signal. However, a qualitative signal can be obtained as shown in Figure 2 (dashed line). The small amount of Pb and Zn volatilised as observed by the CI-ICP-OES measurement were too small to be measured by conventional analysis of the residues, showing the high potential of the new method.

5 ACKNOWLEDGEMENTS

We thank A. Frei for his assistance in the laboratory and J. Wochele for helpful discussions. This work was financially supported by the Priority Program Environment of the Swiss National Science Foundation as part of the Module Waste (project B6).

6 REFERENCES

[1] Chr. Ludwig, A.J. Schuler, *Verfahren und Vorrichtung zum Überführen schwerflüchtiger Verbindungen in eine Detektionsapparatur*, patent application, Germany, August 24, (1998).

[2] S. Stucki, A. Jakob, *Thermal Treatment of Incinerator Fly Ash: Factors Influencing the Evaporation of $ZnCl_2$*, Waste Management **17,** 231-236 (1998).

[3] A. Jakob, R. Moergeli, B. Dettwiler, *Entgiftung und Wiederverwertung von Filterasche aus Müllverbrennungsanlagen*, Entsorgungs-Praxis, **7-8,** 29-32 (1998).

[4] Chr. Ludwig, A.J. Schuler, J. Wochele, S. Stucki, *Measuring the Evaporation Kinetics of Heavy Metals: A New Method*, 4th World Congress R'99, Proc., Eds. A. Barrage, X. Edelmann, Geneva, February (1999).

Materials Development and Methods of Characterization for Energy Research

CATALYST DEVELOPMENT AND SYSTEMS ANALYSIS OF METHANOL PARTIAL OXIDATION FOR THE FUEL PROCESSOR - FUEL CELL INTEGRATION

E. Newson, P. Mizsey, P. Hottinger, T.B. Truong, F. von Roth, Th. Schucan

Methanol partial oxidation (pox) to produce hydrogen for mobile fuel cell applications has proved initially more successful than hydrocarbon pox. Recent results of catalyst screening and kinetic studies with methanol show that hydrogen production rates have reached 7000 litres/hour/(litre reactor volume) for the „dry" pox route and 12,000 litres/hour/(litre reactor volume) for „wet" pox. These rates are equivalent to 21 and 35 kW_{th}/(litre reactor volume) respectively. The reaction engineering problems remain to be solved for dry pox due to the significant exotherm of the reaction (hot spots of 100-200 °C), but wet pox is essentially isothermal in operation.

Analyses of the integrated fuel processor - fuel cell systems show that two routes are available to satisfy the sensitivity of the fuel cell catalysts to carbon monoxide, i.e. a preferential oxidation reactor or a membrane separator. Targets for individual system components are evaluated for the „base" and „best" case systems for both routes to reach the combined 40 % efficiency required for the integrated fuel processor - fuel cell system.

1 INTRODUCTION

Due to the low emissions values, the integrated fuel processor - fuel cell system operating with methanol and coupled to an electric motor offers an environmentally friendly alternative to the internal combustion engine. To produce hydrogen for the fuel cell, methanol partial oxidation in a fixed bed reactor has been shown initially more successful than hydrocarbon (gasoline) pox [1]. However, the energy efficiency of the fuel processor - fuel cell system must reach 40 % so that the full fuel cycle efficiency is about 23 %, thus exceeding the comparable values of 18 % for the internal combustion engine [2].

This report describes results of catalyst screening and kinetic studies with methanol/water mixtures for the autothermal production of hydrogen. The results are used for systems analyses of fuel processor - fuel cell integration providing, for individual components, the target values necessary to reach the 40 % level.

2 EXPERIMENTAL

The experimental system consists of three major parts: feed, reactor, and analytical (Figure 1). The system is fully computer controlled for continuous operation and safety features. Flows, pressure, and temperature parameters are controlled (FC, PC, TC). The stoichiometric methanol / water mixture is vaporised and contacted in a static mixer with oxygen, nitrogen or hydrogen, according to requirements. This mixture enters the fuel processor for the autothermal „wet pox" reaction which is isothermal,

$$4\ CH_3OH + 3\ H_2O + ½\ O_2 \rightarrow 11\ H_2 + 4\ CO_2$$

In contrast, the „dry pox" exothermic reaction is

$$CH_3OH + ½\ O_2 \rightarrow CO_2 + 2\ H_2$$

with a heat of reaction of -193 kJ/mol.

The reactor has an internal diameter of 4 mm and a total length of 130 mm. The length of the catalyst bed is 14 mm, containing 100 mg of commercial catalyst. The product of the reactor is analysed by a GC (HP 6980) having 3 different columns and 2 different detectors (FID, TCD). The water content in the condenser is analysed by a 737KF Coulometer.

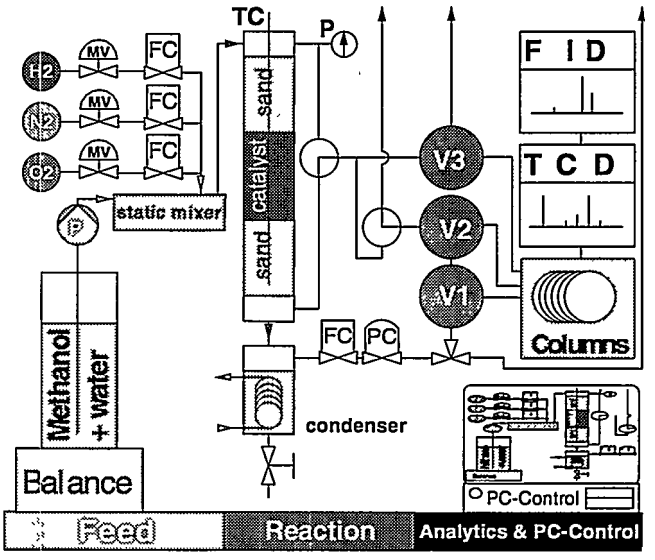

Fig. 1: Laboratory microreactor system for methanol partial oxidation.

3 RESULTS AND DISCUSSION

The major results for the „wet pox" reaction are summarised in Table 1. The temperature ranges between 275 and 330 °C, the weight hourly space velocities (WHSV) are 12 or 20 h^{-1}. The hydrogen produced based on the reactor volume is between 8300 and 17400 litres/hour/(litre reactor volume) [1]. The reactor proves to be almost isothermal because a hot spot of only 3 °C was measured. In the product gas there is a significant amount of CO (1.5 to 3.5 %), which is det-

rimental for the polymer electrolyte type fuel cell, so the product gas should be purified before further use.

Carbon balances are unsatisfactory at 80-90 %, but recent analytical improvements showing the presence of dimethylether will allow better closures of elemental balances.

Temperature [°C]	WHSV [1/h]	Conversion [%]	H_2 Yield [%]	$H_2/(h\ l_{re})$ [l/(h l_{re})]	C - balance [%]	CO %
275	12	59.9	54.8	8362	101.6	1.8
275	20	57.4	46.3	11444	95.95	1.5
300	12	93.5	73.3	10848	83.30	2.7
300	12	92.5	71. 6	10592	84.26	2.6
300	12	94.9	70.7	10458	81.04	3.5
300	20	85.9	68.2	16846	87.78	2.0
315	12	94.4	75.6	11193	87.65	3.1
315	20	92.2	70.5	17420	84.20	2.6
330	12	96.3	78.3	11595	87.96	3.5

Table 1: Results for autothermal methanol partial oxidation („wet pox").

4 SYSTEMS ANALYSIS

After the „wet pox" reaction the product gas, containing significant amounts of hydrogen, should be purified from the carbon monoxide (CO).

There are two routes for this purification: preferential oxidation (PROX), where the CO content is oxidised to CO_2, and membrane separation, where the hydrogen is permeated through a palladium - silver membrane. Both cases are studied. Figures 2,3 show these two alternatives, the numbers indicate the flows in mol/sec, other features are indicated. For the calculations, the lower heating values of the methanol and the hydrogen are considered (MeOH = 676.5 kJ/mol, H_2 = 241.8 kJ/mol). From the systems analyses it is shown that the heat content of a part of the fuel, about 10 %, has to be used to supply the necessary heat of vaporisation of the water and methanol. That means that the yield of the fuel processor should not exceed a limit of 90 %. The highest known efficiency of the fuel processor is 95 % and that of the PROX is 93 %. (These numbers are used for further systems analyses.) The overall efficiency of the fuel processor is the product of these two efficiencies, 88 % [3], which means that this efficiency is practically at the limit and the overall efficiency of the fuel processor - fuel cell system can only be further increased with the improvement of the fuel cell efficiency.

If a membrane is used, about 90 % of the hydrogen can be permeated [1] provided the CO adsorption, which inhibits permeation, can be reduced.

The efficiency of the fuel cell is about 50 %. If prox is used for the CO cleaning there will be some anode rejected gas of about 10 %, however, if a membrane is used, clean hydrogen can be produced which can be fully utilised with recycling.

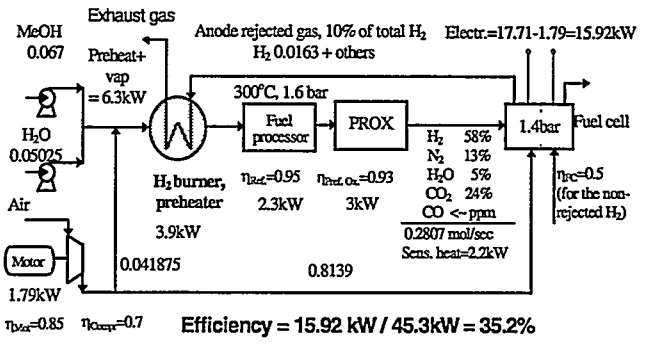

Fig. 2: Fuel processor - fuel cell system integration, CO cleaning with prox, units mol/s.

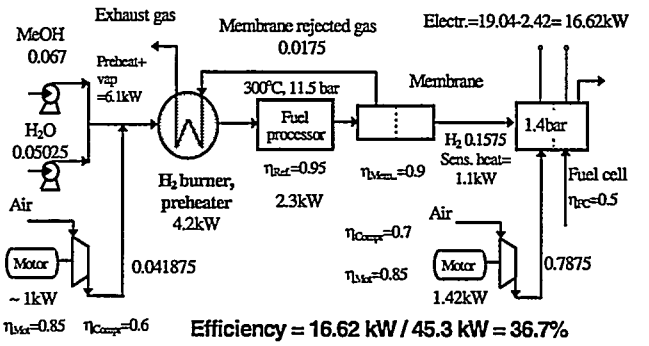

Fig. 3: Fuel processor - fuel cell system integration, CO cleaning with membrane, units mol/s.

According to the systems analyses the expected best overall efficiencies of the fuel processor- fuel cell system are similar for both cases, they are close to 40 %.

5 ACKNOWLEDGEMENT

Commercial catalysts were supplied by Johnson Matthey Ltd (UK) under secrecy agreement.

6 REFERENCES

[1] E. Newson et al., *Catalyst Screening for Hydrogen Production in Mobile Systems by the Partial Oxidation of Methanol or Hydrocarbons*, Proc. Hydrogen Energy Progress, XII, Eds. I.C. Bolcich, T.N. Veziroglu, **2**, 953 (1998).

[2] B. Höhlein, *Fuel cell systems for transportation*, 2nd IEA Advanced Fuel Cell Workshop, 43, Wislikofen, Switzerland (1997).

[3] N. Edwards et al., *ibidem*, 55.

LOW TEMPERATURE CATALYTIC COMBUSTION OF NATURAL GAS - HYDROGEN - AIR MIXTURES

E. Newson, F. von Roth, P. Hottinger, T.B. Truong

The low temperature catalytic combustion of natural gas - air mixtures would allow the development of no-NO_x burners for heating and power applications. Using commercially available catalysts, the room temperature ignition of methane-propane-air mixtures has been shown in laboratory reactors with combustion efficiencies over 95 % and maximum temperatures less than 700 °C. After a 500 hour stability test, severe deactivation of both methane and propane oxidation functions was observed. In cooperation with industrial partners, scaleup to 3 kW is being investigated together with startup dynamics and catalyst stability.

1 INTRODUCTION

Fossil fuel burners for heat and power are characterised by flame combustion which at temperatures over 2000 °C produces nitrogen oxides (NO_x) and other undesirable emissions in their exhaust gases. Catalytic combustion takes place generally below 1000 °C, thus excluding the formation of NO_x. When natural gas (primarily methane) is the fossil fuel, other emissions including carbon dioxide are also reduced. The difficulty with methane is its catalytic ignition temperature in air which is about 400 °C, in contrast to hydrogen which ignites at room temperature or below. A mixture of hydrogen with methane and other constituents of natural gas e.g. ethane, propane, butane, with lower ignition temperatures, is therefore a possibility for ignition at room temperature. Due to the exothermicity of the total oxidation reactions, an upper temperature limit exists which might deactivate the catalyst.

$$CH_4 + 2\,O_2 \Rightarrow CO_2 + 2\,H_2O \qquad \Delta T_{ad} = 245°C$$

$$C_3H_8 + 5\,O_2 \Rightarrow 3\,CO_2 + 4\,H_2O \qquad \Delta T_{ad} = 628°C$$

$$2\,H_2 + O_2 \Rightarrow 2\,H_2O \qquad \Delta T_{ad} = 82°C$$

In these equations ΔT_{ad} is the adiabatic temperature rise for combustion of each component in pure oxygen at atmospheric pressure.

Previous work in the literature from the Fraunhofer Institute and KFA Jülich shows that spark ignition is required to initiate the reaction [1, 2] with methane-hydrogen mixtures in the burner size range of 10 - 20 kW (thermal).

2 EXPERIMENTAL

In a project supported by „Gaz de France", the laboratory apparatus shown in Figure 1 has been built to investigate the low temperature combustion of natural gas. Synthetic mixtures containing methane (CH_4) and propane (C_3H_8) are passed with excess air and hydrogen over a commercial, noble metal, monolith catalyst in a reactor tube. For startup from room temperature, the oven was *not* in operation. Water is removed from the exhaust gases before online sampling by a gas chromatograph and an infrared analyser for carbon oxides (CO, CO_2). PC control of the apparatus allows unattended operation and continuous datalogging with safety controls.

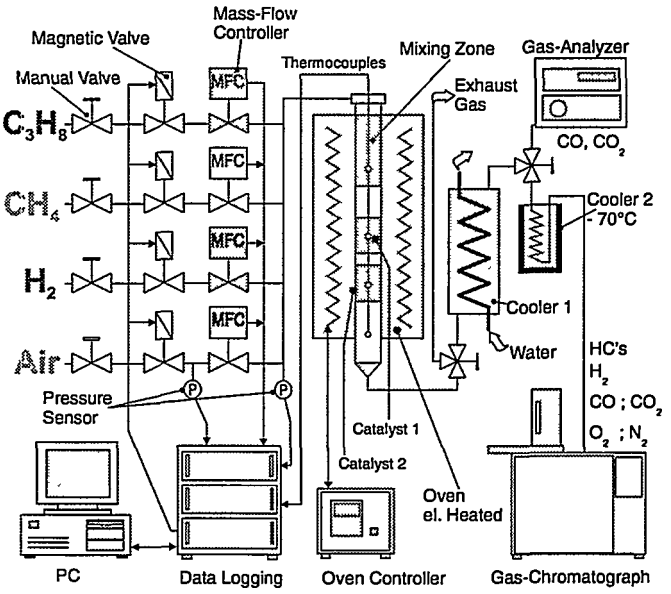

Fig. 1: Laboratory apparatus for Total Oxidation catalyst screening.

3 RESULTS AND DISCUSSION

A commercial, noble metal catayst on a metallic foam, previously successfully employed with a hydrogen catalytic burner [3], was inactive at room temperature for methane-propane-hydrogen-air mixtures. A change in the support and the noble metal composition provided the results shown in Figure 2. It is seen that the methane-propane-air mixture at first passes over the catalyst without reaction. On introducing hydrogen, ignition is immediate, the temperature rising approxi-

mately to the adiabatic temperature of the inlet mixture. Removal of propane and methane and finally hydrogen, results in inlet air temperatures being reached. The volume hourly space velocity (VHSV) was 47'000 h^{-1}. Further tests have shown that the presence of hydrogen is essential to maintain total oxidation suggesting that the hydrogen acts as a scavenger for oxygen adsorbed on the catalyst surface, thus allowing adsorption and reaction of the hydrocarbons.

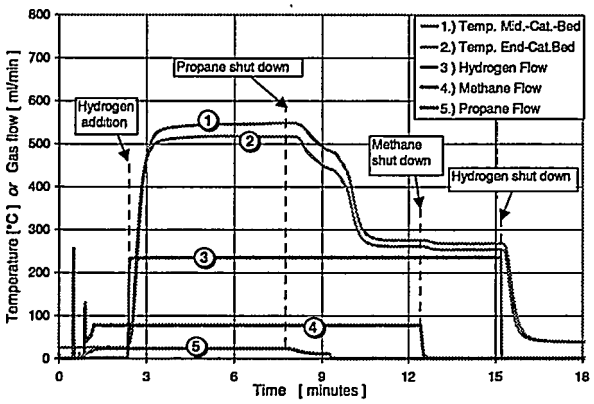

Fig. 2: Ignition from room temperature (22 °C) with methane-propane-hydrogen mixtures in air, flow: 7.7 l/min, VHSV: 47'000 h^{-1}.

The stability of the catalyst is shown in Figure 3 in a 500 hour continuous test without heating the catalyst and with 3 % hydrogen in the inlet. A hotspot temperature of 680 °C and conversions of 92 % for methane and 98 % for propane were initially observed with gradual deactivation of both the oxidation functions. Soon after 500 hours on stream, rapid deactivation was observed and the run was terminated. The used catalyst is being studied by surface characterisation techniques to determine the cause of deactivation. At the temperatures used, a sintering mechanism is certainly possible.

Cooperation with industrial partners is continuing to test new catalysts and develop a burner design for the 3 kW size.

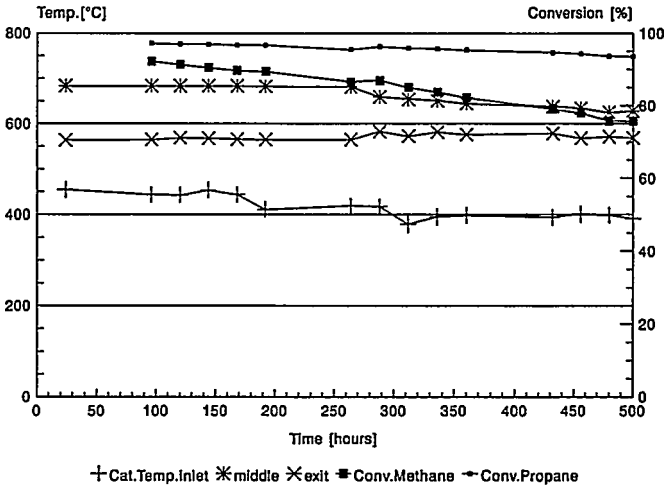

Fig. 3: Stability Test of a commercial, noble metal, Monolith, VHSV: 47'000 h^{-1}, dia.: 18 mm, l.: 40 mm.

4 CONCLUSION AND FUTURE WORK

The room temperature ignition of methane-propane-hydrogen-air mixtures has been shown in laboratory reactors with total oxidation efficiencies over 95 % and maximum temperatures less than 700 °C. A stability test was terminated after 500 hours due to severe deactivation of the catalyst.

Cooperation is continuing with industrial partners to find more stable catalysts and develop a 3 kW burner design.

5 ACKNOWLEDGEMENTS

Partial financial support was obtained from Gaz de France. UOP Ltd., (UK) supplied commercial catalysts under a confidentiality agreement.

6 REFERENCES

[1] A. Schuler, U. Maier, *Modellierung der katalytischen Verbrennung in Haushaltsbrennern,* 10.DVV/1.SVV Kolloquium, ETH Zürich, September 27 (1996).

[2] P. Bröckerhoff, B. Emonts, *Use of Hydrogen as an Additive to Natural Gas in a Catalytic Burner,* Proc.10th, World Hydrogen Energy Conf.,(Eds.) D.L. Block, T:N:Veziroglu **3**, 1581 (1994).

[3] P. Hottinger, F. von Roth, E. Newson, *Dauerbetrieb des Steuer- und Sicherheitssystems einer katalytischen Wasserstoffbrenner-Anlage (10-25 kW),* PSI Internal Report, TM-51-96-21.

USE OF PERIODIC VARIATIONS OF REACTANT CONCENTRATIONS IN TIME RESOLVED FTIR STUDIES OF CO OXIDATION ON Pd/ZrO_2 CATALYSTS

E. Ortelli, A. Wokaun

Sine wave modulation of feed concentrations was used to induce dynamic variations in the concentrations of products, intermediates and reactants, which were monitored in a diffuse reflectance FTIR (DRIFT) cell. The phase shift $\Delta\varphi$ between the external perturbation of the feed and the signals of products, intermediates and reactants was examined in dependence on the modulation frequency ω. Reaction constants of a simplified model mechanism were estimated for a $Pd_{25}Zr_{75}$ based catalyst for CO oxidation.

1 INTRODUCTION

CO oxidation is important in new energy conversion systems. Therefore we investigated this reaction using a concentration perturbation in feed. The time dependence of the concentrations of all the species was monitored to obtain information on the reaction pathways. In the chosen simplified model we assume that CO and O_2 have different adsorption sites on $Pd_{25}Zr_{75}$ [1], and that the concentration of adsorbed oxygen (*O) is constant due to excess of O_2. Furthermore the surface concentration of free sites (*) is proposed to be much greater than the one of *CO. The reaction pathway is:

$$CO \xrightarrow{k_1'} *CO \xrightarrow{k_2'} CO_2 \qquad (1)$$

Here k_1' and k_2' are effective first order rate constants (s^{-1}). The DRIFT cell was modelled as a continuous stirred tank reactor, with residence time τ.

2 EXPERIMENTAL

The set-up consists of a gas dosing system and a DRIFT reaction chamber. The activated catalyst was held under a constant overall mass flow, in which the feed concentration was sinusoidally varied [2]. The evolution of concentration of the different compounds (phase shift φ) was deduced by plotting the peak area as a function of time. The measurements were performed at 4 bar and 370 K with a feed composition of 5% CO/N_2, 0.03 ± 0.02 l_N min^{-1}; O_2, 0.04 l_N min^{-1}; and N_2, balance up to 0.175 l_N min^{-1}, using different modulation frequencies.

3 RESULTS AND DISCUSSION

The model can be described with a system of three differential equations, with the feed concentration CO_0 as external perturbation. Solving the system for the concentration CO, *CO and CO_2 we find that the frequency dependence of the phase shifts can be approximated by straight lines which are crossing the origin.

$$\tan\left[\varphi(CO_0)-\varphi(CO)\right]=\omega\frac{\tau}{1+\tau k_1'} \qquad (2)$$

$$\tan\left[\varphi(CO)-\varphi(*CO)\right]=\omega\frac{1}{k_2'} \qquad (3)$$

$$\tan\left[\varphi(*CO)-\varphi(CO_2)\right]=\omega\frac{\tau}{1} \qquad (4)$$

The phase shift between CO_2 and *CO (▲ in Figure 1) depends only on parameters of the modulation experiment ($\omega\cdot\tau$). The phase shift between CO and CO_0 (■ in Figure 1) is larger than between *CO and CO (▼ in Figure 1), indicating that under the employed conditions CO adsorption is the rate limiting step.

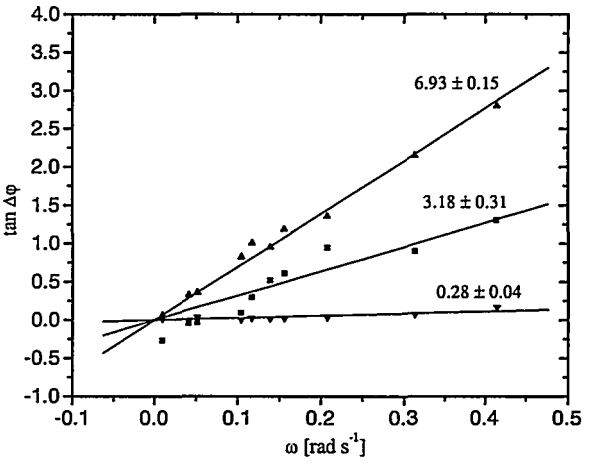

Fig. 1: Variation of phase shift of CO-CO_0 (■),*CO-CO (▼) and CO_2-*CO(▲) as function of ω.

The chosen model appears to conform with reality. Rate constants are derived from the slopes of fitted lines. We obtain:

$k_1' = 0.17\ s^{-1}$ $\quad$ $k_2' = 3.6\ s^{-1}$ $\quad$ $\tau = 6.95\ s$

The result appears to be in good agreement with previously published data [1,2].

4 CONCLUSION

The results demonstrate the validity of the modulation concept in heterogeneous catalysis. Additional information on the reaction pathways can be achieved by monitoring adsorbed species in a DRIFT cell.

5 REFERENCES

[1] P. Barnickel, A. Wokaun, A. Baiker, J. Chem. Soc. Faraday Trans., **87**, 333-336 (1991).

[2] J. Kritzenberger, A. Wokaun, J. Mol. Catal. A: Chem., **118**, 235-245 (1997).

XPS INVESTIGATIONS ON THE UV-LASER ABLATION MECHANISM OF POLY(ETHER IMIDE) [KAPTON®]

J. Wambach, T. Kunz, B. Schnyder, R. Kötz, A. Wokaun

UV-Laser ablated samples of poly(ether imide) [Kapton™] were studied with small-spot XPS. Applying fluences above the "threshold level" (0.167 J/cm²) resulted in the expected behaviour of a decline of both nitrogen and oxygen. Below the "threshold level" a hint for an altered ablation mechanism was found.

1 INTRODUCTION

Since the early 80ies UV-laser ablation is an established method for microstructuring of polymers [1]. The knowledge of the exact ablation mechanism for different polymers is still controversially discussed.

From a QMS study, R. Srinivasan [2] proposed a fragmentation for poly(ether imide) [Kapton™] [3] into

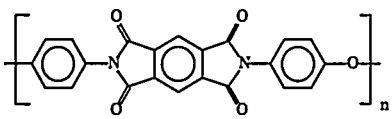

very small particles, namely CO, CN, C_2, and C_xH_y. Additional informations on the ablation mechanism, the re-deposition of debris, etc. are lacking so far.

To obtain these, we studied in a detailed small-spot XPS analysis (spot size 150 µm) the chemical changes introduced by a UV-laser (308 nm) ablation process. Samples with a single ablated crater (Ø 300 µm) were used to exclude the deposition of debris from an adjacent crater. Each crater was created by 5 pulses each, with fluences either above or below the "threshold level" (0.167 J/cm² [4]). For a description of the ablation procedure see [4]. In the XPS analysis the signals of C1s, O1s, and N1s, measured both inside and outside the ablated crater, were compared with an unmodified reference sample. The XPS apparatus is described in [5].

2 RESULTS AND DISCUSSION

Outside the ablated crater only a random deposition of debris from the plume was detected.

Inside the crater (Figure 1) the concentrations of both nitrogen and oxygen are lowered relative to an unablated polymer sample for fluences **above** the "threshold level". Most likely both, the nitrogen and oxygen containing chromophores are excited by the laser irradiation releasing e.g. gaseous CO or CN. Inside the crater the carbon concentration is enriched. From the spectroscopic data, we presume some newly formed graphitic species like C_x or even C_xO_y species, e.g. ketons, ethers, etc.

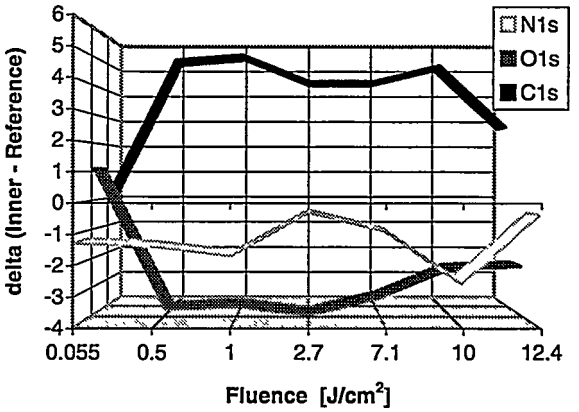

Fig. 1: Composition change *inside* the ablated crater with respect to the reference sample as a function of the applied fluence.

For fluences **below** the "threshold level", only the nitrogen signal is lowered. By contrast, the oxygen signal is increased. An explanation could be, that after the removal of the (>N-CO-) chromophore the residual fragments are oxidised. This observation might hint to a fluence dependent change in the ablation mechanism.

In ongoing investigations we want to proof these findings and to study the influence of the atmosphere during the ablation process. Furthermore, the study of different kinds of polymers is planned.

3 REFERENCES

[1] Y. Kawamura, K. Toyoda, S. Namba, Appl. Phys. Lett. **40**, 374 (1982);
R. Srinivasan, V. Mayne-Banton, Appl. Phys. Lett. **41**, 578 (1982).

[2] R. Srinivasan, Appl. Phys. A **56**, 417 (1993).

[3] High temperature thermoplastic material with good chemical resistance, used e.g in electronics.

[4] T. Kunz, Ph.D. thesis, ETH Zürich, 80 (1997).

[5] B. Schnyder, J. Wambach, T. Kunz, C. Hahn, A. Wokaun, PSI Annual Report 1997 / Annex V, 37.

IN-SITU RAMAN SPECTROSCOPY AS A CHARACTERIZATION TOOL FOR CARBON ELECTRODES

J.-C. Panitz, F.B. Joho, P. Novák

Lithium intercalation and de-intercalation into/from graphite electrodes in a nonaqueous electrolyte has been studied using in-situ Raman spectroscopy. Our experiments give information on the electrode-electrolyte interface with improved spatial resolution. The spectra taken from the electrode surface change with electrode potential. In this way, information on the nature of the chemical species present during charging and discharging half cycles is gained. For the first time, mapping techniques were applied to investigate if lithium intercalation proceeds homogeneously on the carbon electrode.

1 INTRODUCTION

Secondary lithium-ion batteries have been introduced into the market in the last years. In these batteries, lithiated metal oxides, for example Li_xCoO_2, are used as the positive electrode material, and carbon serves as the negative electrode material. For the electrolyte, lithium salts dissolved in non-aqueous solvents are employed. A recent review of the development in this field has been given by Winter *et al.* [1].

An open question is the change under continuous cycling in the microstructure of the carbon materials employed in the batteries. Raman spectroscopy is well suited for the analysis of the structural properties of carbon materials [2,3]. Besides an overview of the development that has taken place in our laboratory during 1998, we show here the first in-situ Raman spectra of carbon after several charge-discharge cycles.

2 IN-SITU RAMAN MICROSCOPY

In 1998, several successful experiments were carried out with a newly developed spectro-electrochemical in-situ cell [4]. We demonstrated that the degree of lithium intercalation varies on the electrode surface under potentiostatic conditions. In cycling experiments performed under galvanostatic conditions, we detected „blind spots" on the carbon electrodes that lag behind in the intercalation (charging) process.

Raman spectroscopy was performed on a LabRam I Raman microscope (Dilor - Instruments S.A.). The 530.901 nm emission from a krypton ion laser was used for excitation of the spectra. The laser was coupled into the in-situ cell through a sapphire window, using an Olympus 50x ULWD microscope objective. The carbon electrode was placed on a stainless steel current collector. A lithium foil was used as the counter electrode, and the electrolyte was lithium perchlorate, dissolved in a mixture of ethylene carbonate (EC) and dimethyl carbonate (DMC). The cycling performance of the in-situ cell is shown in Figure 1. Due to the large ratio of electrolyte:carbon, which is in the order of 10^4 (w/w), the initial charge losses are rather high. Nevertheless, the long-term performance of the cell is regarded as satisfactory.

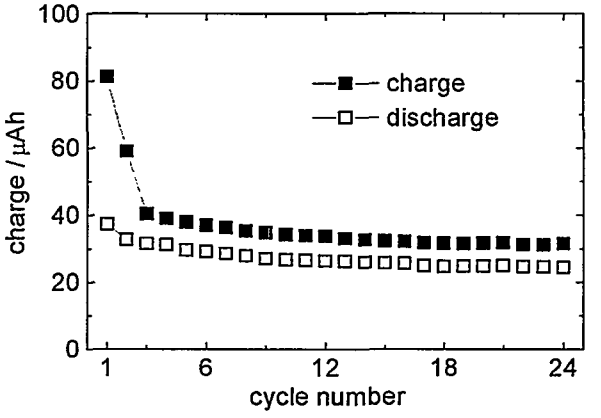

Fig. 1: Cycling performance of the in-situ Raman cell with SFG44 graphite. The cell was cycled at a C/8 rate.

In the following, we show the Raman spectrum of the SFG44 graphite (TIMCAL AG, Sins) used in the electrode prior to cycling (Figure 2), and two example spectra taken after lithium de-intercalation in the fourth cycle (Figure 3) at a potential of 1100 mV vs. Li/Li^+.

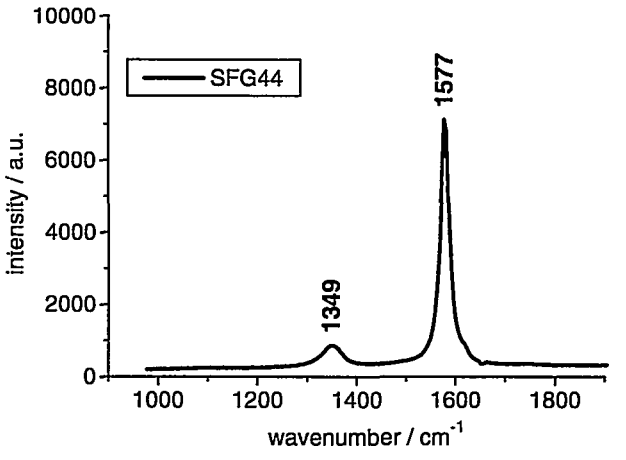

Fig. 2: Raman spectra recorded ex-situ from a SFG 44 synthetic graphite pellet.

The Raman spectrum of SFG 44 shows an intense signal of the G-band at 1577 cm^{-1} [FWHM (full width at half maximum) 21 cm^{-1}]. An additional feature, the D-band, is observed at 1349 cm^{-1} (FWHM 56 cm^{-1}). This band arises due to structural disorder in the material. The intensity ratio of the D-band and the G-band can

be used to calculate the correlation length L_a [2]. The correlation length L_a is defined as the average size of microcrystalline domains parallel to the graphene layers. L_a can be used as a measure of the order within the graphene layer of carbon materials. A value of 20 nm is obtained for L_a in this SFG 44 sample.

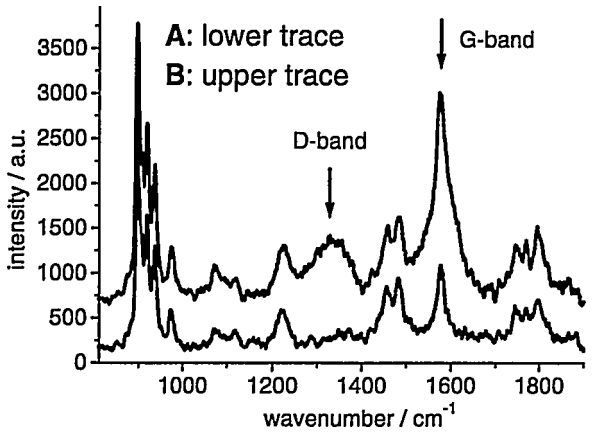

Fig. 3: Raman spectra recorded in-situ after four cycles on two arbitrarily selected sites (designated as A and B) on the SFG 44 graphite electrode. Data are displayed after background correction.

The spectra shown in Figure 3 were obtained in-situ at the electrode-electrolyte interface and show vibrational bands of both solvent mixture and electrode material. The G-band and the D-band positions are marked by arrows. In the upper trace, an intense signal of the D-band is observed, whereas this band is not detected in the lower trace. For traces A and B, the results of a non-linear least-squares calculation of band position, band area and linewidth are compiled in Table 1.

Spectrum	*band position*	*area (a.u.)*	*linewidth (FWHM)*
G-Band			
SFG44	1577	220500	20.7
A	1578	25450	21.3
B	1578	127050	48.2
D-Band			
SFG44	1349	51500	55.8
A		not observed	
B	1338	60100	68.7

Table 1: Parameters of D- and G-bands of SFG 44 graphite. Band positions and linewidths are given in cm^{-1}. The labels A and B correspond to the spectra shown in Figure 3.

Using the results from Table 1, we can calculate a correlation length L_a for trace B (Figure 3). A value of 9 nm is obtained. This suggests that, at this point on the carbon surface, the microstructure is more disordered than in the SFG 44 sample prior to cycling. Regarding trace A, where we were not able to evaluate a D-band area, we may infer from the linewidth that the long range order of graphite on a micrometer scale is still intact at this point.

3 CONCLUSION

Graphite electrodes suitable for secondary lithium-ion batteries have been characterised successfully with Raman microscopy techniques under in-situ conditions. A potential application of the developed method presented is the quality control of carbons used for batteries. A future target is to investigate the extent of restructuring phenomena taking place on carbon electrodes during repeated charge/discharge cycles.

4 ACKNOWLEDGEMENTS

Thanks are due to Christian Marmy for machining and assembling the in-situ cell. The financial support of TIMCAL AG, Sins, and the Federal Office of Energy, Bern, is gratefully acknowledged.

5 REFERENCES

[1] M. Winter, J.O. Besenhard, M.E. Spahr, P. Novák, Adv. Mater. **10**, 725 (1998).

[2] F. Tuinstra, J.L. Koenig, J. Chem. Phys. **53**, 1126 (1970).

[3] L. Nikiel, P.W. Jagodzinski, Carbon **31**, 1313 (1993).

[4] J.-C. Panitz, F.B. Joho, P. Novák, submitted for publication.

ATOMIC FORCE MICROSCOPY STUDY OF ANION INTERCALATION INTO HOPG

D. Alliata, P. Häring, O. Haas, R. Kötz, H. Siegenthaler (University of Bern)

In the context of ion transfer batteries, we studied highly oriented pyrolytic graphite (HOPG) in perchloric acid, as a model to elucidate the mechanism of electrochemical intercalation in graphite. Aim of the work is the local and time dependent investigation of dimensional changes of the host material during electrochemical intercalation processes on the nanometer scale. We used atomic force microscopy (AFM), combined with cyclic voltammetry, as in-situ tool of analysis during intercalation and expulsion of perchloric anions into the HOPG electrodes. According to the AFM measurements, the HOPG interlayer spacing increases by 32 % when perchloric anions intercalate, in agreement with the formation of stage IV of graphite intercalation compounds.

1 INTRODUCTION

In the context of battery applications, the knowledge of the dimensional changes occurring during electrochemical processes is fundamental for the understanding of the electrochemical intercalation / insertion mechanism and for the evaluation of potential applications [1].

In the present communication we examine the system of highly oriented pyrolytic graphite (HOPG) in perchloric acid, as a model in order to elucidate the mechanism of electrochemical anion intercalation in graphite [2]. The perchlorate anion has the advantage to be relatively big in diameter (4.6 Å) compare to the HOPG interlayer spacing. Furthermore, this particular anion intercalation process is free of secondary reactions like film formation. We used Atomic Force Microscopy (AFM), combined with Cyclic Voltammetry, as an in-situ analytical tool during intercalation and expulsion of perchlorate ions in HOPG [3].

2 EXPERIMENTAL

AFM investigations were performed with a Park Scientific Instruments Model AP-100 Autoprobe CP scanning probe microscope equipped with a home made electrochemical cell and an EG&G Versastat 270 potentiostat/galvanostat.

All potentials are quoted against a Platinum quasi reference electrode (Pt-QRef), which in turn was +700 mV vs. Saturated Calomel Electrode (SCE).

As a working electrode we used a HOPG crystal which was freshly cleaved with adhesive tape prior to each experiment. The electrolyte was a 2M $HClO_4$ solution.

The height of a HOPG step was obtained by calculating the difference between the mean values of the heights measured on the top and bottom layer of the step in a selected area.

3 RESULTS

Cyclic Voltammetry

Perchlorate ion intercalation into HOPG basal planes was induced under well controlled conditions in 2M $HClO_4$. As shown in Figure 1, different stages of graphite intercalation compounds (GIC) can easily be distinguished in cyclic voltammograms. Over a potential range of only about 200 mV four different stages of intercalation of anions and associated solvent or acid molecules into the graphite lattice are visible in the form of anodic peaks in the positive scan and reappear as cathodic peaks in the negative scan.

The main reaction involved is:

$$[C_x] + [A^-] + y(solv.) = [C_x{}^+A^-]y(solv.) + e^- \qquad (1)$$

Below a certain potential, reaction 1 is nearly reversible for $HClO_4$ concentrations greater than 2M. For lower concentration of the electrolyte or potentials too far on the anodic side, the reversibility of reaction 1 decreases and other reactions (graphite oxide formation, carbon dioxide formation, water electrolysis) can take place.

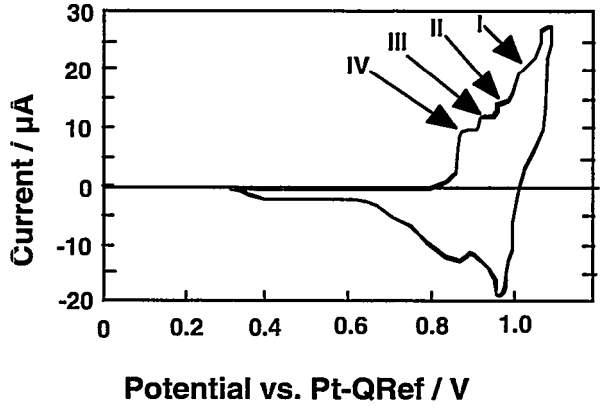

Fig. 1: Cyclic voltammetry curves (2nd cycle) on HOPG, 100 mV/s, in 2M $HClO_4$.

In-situ Electrochemical AFM

Figure 3 shows a sequence of images obtained by AFM for a multi step region on a HOPG electrode during the formation and dissolution of a stage IV GIC in 2M $HClO_4$.

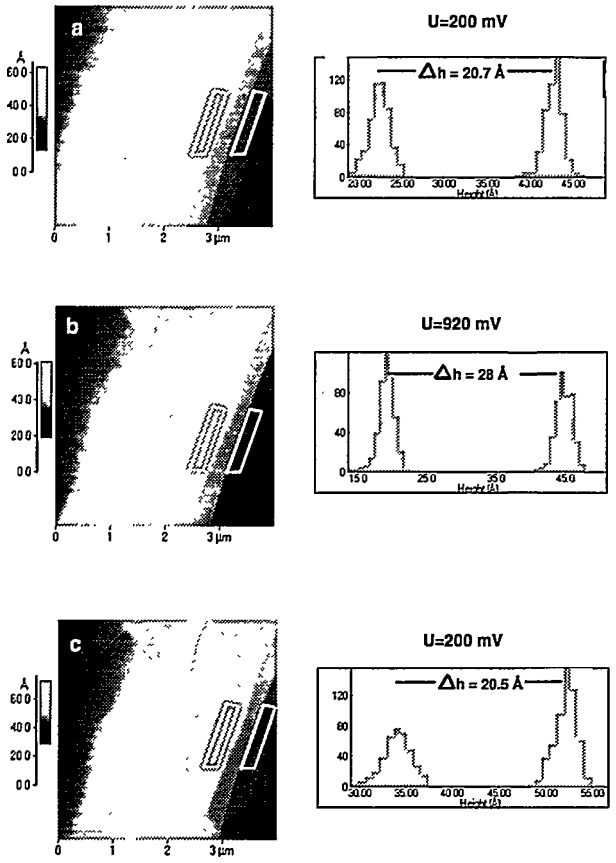

Fig. 2: AFM images of the same HOPG step in 2M $HClO_4$ at different potentials. The height of the double step is calculated by comparing the mean values of the distributions of heights within the two marked areas.

Since we are expecting to fill one gap every four and the step was composed of six layers, in principle we have the same probability to fill one gap or two gaps in the HOPG layer sequence. The corresponding expected expansion is 24.7 Å (one gap filled) and 29.3 Å (two gaps filled). Our experimental result was 28 ± 2 Å, therefore we think that two of the six available gaps were filled with anions.

By comparing Figures 2b and 2c, it is evident that the local kinetics of the two processes is different. In one direction (intercalation) the process is relatively isotropic (Figure 2b), i.e. changes in height appear to be similar at different locations parallel to the step. The reverse process (expulsion) is much more complicated as is evident from the existence of different kinetic regions for the diffusion of ClO_4^- anions in the HOPG structure. In the upper part of Figure 2c, the step is already completely restored, while in the lower part of the same image the step is still a bit higher than originally, therefore the expulsion process seems not to be finished.

The same experimental approach was repeated at steps with different heights, i.e. different number of graphite layers. As shown by the diagram plotted in Figure 3, the percentage of interlayer spacing change decreases with increasing step height.

This may be explained by the fact that the expansion energy increases with the number of adjacent graphene layers on both sides to a particular gap.

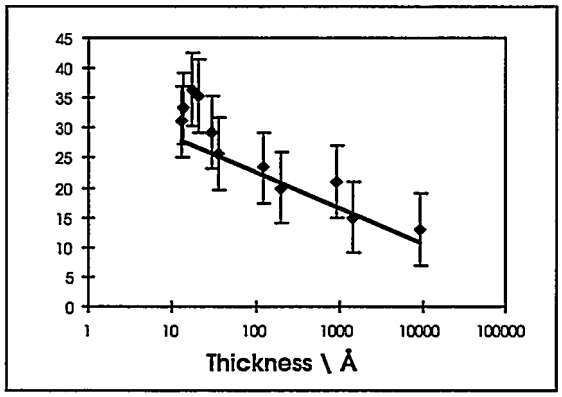

Fig. 3: Thickness change of HOPG interlayer spacing during stage IV formation and dissolution.

4 CONCLUSION

For the first time a reproducible, quantitative estimate of the interlayer spacing could be obtained by in-situ AFM measurement for a stage IV GIC formation of perchlorate ions in HOPG. The experimental value is in agreement with the theoretical expectation.

The AFM results clearly demonstrate the local aspect of the intercalation process into HOPG by revealing coexisting regions with different kinetics for the intercalation and expulsion process. The intercalation process appears to be faster than the reverse expulsion.

Finally, the expansion and the kinetics of the intercalation process depends on the number of graphite layers involved.

5 ACKNOWLEDGEMENT

Financial support by the Swiss National Science Foundation, Grant # 4036-044040, is gratefully acknowledged.

6 REFERENCES

[1] L.B. Ebert, *Intercalation compounds of graphite* Ann. Rev. Mat. Sci., **6**, 799 (1981).

[2] F. Beck, H. Junge, H. Krohn, Electrochemica Acta **26**, 799 (1981).

[3] D. Alliata, P. Häring, R. Kötz, O. Haas, H. Siegenthaler, Abstract NS.PTu.54, 5th International Conference on Nanometer-scale Science and Technology, Birmingham, UK, August 31 - September 4 (1998).

INVESTIGATION OF THE POROUS STRUCTURE OF GLASSY CARBON BY SAXS - AN APPLICATION OF SYNCHROTRON RADIATION

A. Braun, M. Bärtsch, B. Schnyder, R. Kötz, O. Haas

The porous structure of Electrochemical Double Layer Capacitor (EDC) Electrodes was investigated using Small Angle X-ray Scattering (SAXS), assuming logarithmically normal distributed micropores.

1 INTRODUCTION

Activated Glassy Carbon (GC) is a promising material for Electrochemical Double Layer Capacitors (EDC). GC can be prepared by vacuum pyrolysis of polymers at heat treatment temperatures (HTT) from 600 °C to 3000 °C. It is built up from graphit-like nanosized crystals, which enclose 1-5 nm sized pores (voids).

The pores have to be opened by an oxidation process to make them accessible for liquid electrolytes and thus attractive for EDC electrodes. The pore structure influences the electrochemical properties of the EDC. We therefore analysed the pore structure of our electrodes using SAXS [1].

2 EXPERIMENTAL

We studied commercial GC discs with a thickness of 60 µm and 1mm, which were manufactured from phenolic resins at various temperatures (800 °C, 1000 °C, 2200 °C). One sample was activated at its surface by 3 hours of oxidation. SAXS curves were obtained at HASYLAB synchrotron radiation source in Hamburg/Germany.

3 RESULTS

For a preliminary evaluation of the SAXS data, logarithmically normal distributed spherelike micropores were assumed with a structure factor S(Q,R) as indicated in Figure 1 and a distribution function P(R) as indicated in Figure 2. Using these assumptions, the scattering cross section of the whole irradiated sample with N spheres can be represented by the following expression:

$$\frac{d\Sigma}{d\Omega}(Q) = (n \cdot f)^2 \cdot N \int_0^\infty V^2(R)\, S(Q,R)\, P(R)\, dR \qquad (1)$$

Q being the scattering vector , f the atomic form factor of carbon and n the number density of carbon atoms in GC. V(R) is the volume of pores of radius R.

The scattering curves exhibit a bimodal distribution of large pores (small Q) with a radius of around 200 Å, which contribute to only less than 1 % to the total pore volume, and micropores (large Q) of about 10 Å. The micropore region of the curve ($0.05 < Q < 1$) was fitted for the large Q values using Equation 1, as shown in Figure 1. Pore radii distributions for the different samples are displayed in Figure 2. Differences in pore radii are due to different HTT. However, changes in micropore radii also occur upon oxidation, as can be seen from the 60 µm sample, oxidised for 3 hours.

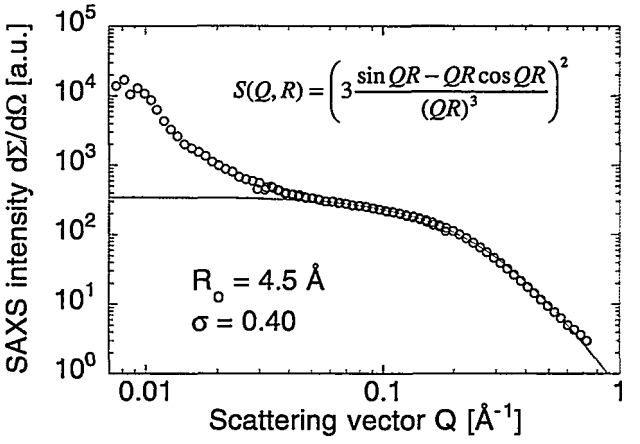

Fig. 1: SAXS curve of a 60 µm GC sample, produced at 1000 °C and oxidised 3 hours. The drawn line is the best fit function according to Equation 1.

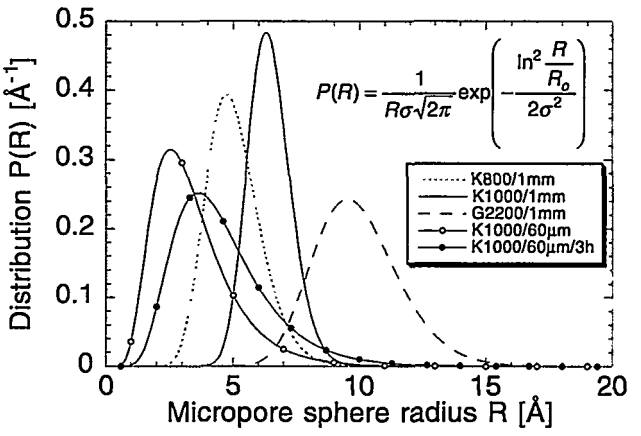

Fig. 2: Logarithmic normal distribution P(R) of micropores of GC with various thickness and HTT, using fit results (R_0, σ) from Equation 1.

4 ACKNOWLEDGEMENTS

Financial support by the Board of the Swiss Federal Institute of Technology is gratefully acknowledged. We are grateful to Prof. Fricke and Dipl.-Phys. R. Saliger (Universität Würzburg, Physikalisches Institut) and Dr. H.-G. Haubold and Dr. G. Görigk (Forschungszentrum Jülich (IFF) and HASYLAB Hamburg) for SAXS beamtime and suggestions in evaluating SAXS data.

5 REFERENCES

[1] O. Glatter, O. Kratky, *Small Angle X-ray Scattering*, Academic Press, London (1982).

ESR SPECTROSCOPIC INVESTIGATIONS OF THE RADIATION-GRAFTING OF FLUOROPOLYMERS

G. Hübner (University of Stuttgart), H.P. Brack, E. Roduner (University of Stuttgart), G.G. Scherer

ESR spectroscopic investigations have clarified the influence of several preparative parameters on the reaction rates and yields obtained in the radiation-grafting method used at PSI to prepare proton-conducting polymer membranes. At a given irradiation dose, a higher concentration of reactive radical sites was detected in ETFE films than in FEP films. This higher concentration explains the higher grafting levels and rates of the ETFE films found in our previous grafting experiments. Taken together, the in-situ ESR experiments and grafting experiments show that the rates of disappearance of radical species and grafting rates and final grafting levels depend strongly on the reaction temperature and the oxygen content of the system. Average grafted chain lengths were calculated to contain about 1,000 monomer units.

1 INTRODUCTION

Proton-conducting membranes for application as solid polymer electrolyte in fuel cells are prepared at PSI by the radiation-grafting method [1]. Electron irradiation of a base fluoropolymer film generates radical centres onto which styrene is grafted and thereafter sulfonated. How the sample irradiation is carried out influences the subsequent grafting reaction and many properties of the final membrane, e.g., mechanical properties [1], and the nature of the radical species and their concentration is expected to determine the grafting rates and final grafting levels. The initial radical species and their subsequent intermediates can be observed by means of ESR spectroscopy and identified based on their characteristic g-values and hyperfine splitting pattern.

The goal of the present investigation was to compare the two fluoropolymers, perfluorinated FEP, or poly(tetrafluoroethylene-*co*-hexafluoropropylene), and partially fluorinated ETFE, or poly(ethylene-*alt*-tetrafluoroethylene) regarding their response towards electron irradiation as well as the behaviour of the irradiated films during their grafting with styrene under different reaction conditions.

2 EXPERIMENTAL

Teflon-FEP (75 µm thick, DuPont, Circleville, OH, USA) and ETFE films (100 µm thick, Nowofol, Siegsdorf, D) were washed with ethanol, cut into small pieces and transferred into quartz ESR tubes. The tubes were evacuated, purged with argon, and sealed to keep the samples free from oxygen. Sample irradiation was performed with an electron beam at a dose between 1 and 100 kGy (Studer AG, Däniken, CH). During irradiation the empty half of the quartz tube was shielded by a steel block, and for the ESR measurements the polymer was transferred to the unirradiated part of the tube. The samples were kept at –80 °C until measurement to minimise reactions of the radical species.

ESR measurements were recorded on a Varian X-band spectrometer equipped with a variable temperature controller. Radical concentrations were determined by double integration of the spectra and comparison with a weak pitch standard sample. The spin concentrations were measured at –120 °C. The grafting process was investigated *in-situ* by exposing irradiated films to styrene under oxygen-free conditions in ESR tubes equipped with break seals.

3 RESULTS

3.1 Radical species

Depending on the irradiation dose, different radicals were identified on irradiated FEP. At lower doses (≤ 20 kGy) primary radicals resulting from chain scission reactions were found. They are still detected in small concentrations after irradiation at 40 kGy, but at a dose ≥ 40 kGy only the secondary and tertiary radicals originating from loss of atomic fluorine from the polymer chain are observed. The spectra of these radicals are known from previous investigations [2].

The ESR spectra of irradiated ETFE consist mainly of signals due to secondary radicals resulting primarily from the loss of atomic hydrogen [3] and possibly from the loss of atomic fluorine as well.

3.2 Determination of spin concentration

The spin densities of all the radical species observed in the two polymers are shown in Figure 1 as a function of the irradiation dose. The spin densities of irradiated ETFE are about twice those obtained at the same dose with FEP. This difference in the behaviour of the two fluoropolymers agrees with our expectation that ETFE, due to the comparatively weak C–H bonds which are absent in FEP, requires less energy for the generation of a given radical concentration [1].

The saturation behaviour observed with ETFE and FEP at higher irradiation doses is attributed to termination reactions of the radicals. At higher doses,

heating of the sample by the radiation increases the radical mobility and thus the rates of termination.

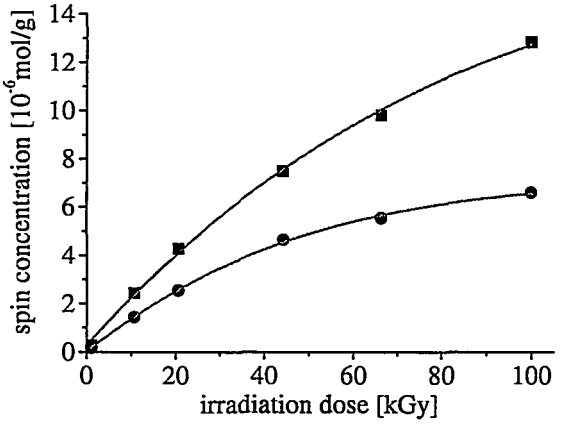

Fig. 1: Spin concentration as a function of irradiation dose: FEP (•), ETFE (▪).

When oxygen is present during the irradiation, peroxy radicals and their various reaction products are formed. In this case, spin concentration values at a dose of 40 kGy were lower by 45 % for ETFE and by 25 % for FEP. This decrease can be attributed to further reactions of the peroxy radicals to form hydroperoxides [1] in the case of ETFE or peroxides or various carbonyl species [1] in the cases of both ETFE and FEP.

3.3 *In-situ* grafting experiments

As in previous grafting experiments with styrene on fluoropolymers [4] the ESR spectra measured during the grafting of ETFE did not show any signals due to a polystyrene macroradical, probably because the steady-state concentration of this species is too low.

Figure 2 shows the relative radical decay curves observed during the grafting reactions on ETFE with styrene or during thermal decay in the absence of styrene. The reaction conditions have a considerable influence on the process. Thus, the radical decay during grafting at 60 °C (*) is much slower than at 80 °C (×). At a temperature of 80 °C the rate of radical decay decreases when styrene is diluted with benzene (+), or when peroxy radicals from an irradiation in air are reacted. For comparison, the thermal decay curves for radical termination at 80 °C in the absence of styrene are also included. The thermal decay is slower and less extensive in the samples with no oxygen present during irradiation and grafting (about 30 and 70 % in the case of the alkyl and peroxy radicals, respectively).

The final grafted film consists of a backbone with grafted chains of polystyrene at the former radical centres on the base polymer. Based on the spin contents (6.5×10^{-8} and 4.3×10^{-8} mol) and the amount of styrene grafted (8.11×10^{-5} and 3.44×10^{-5} mol), we estimate an average polystyrene chain length of about 800 and 1240 monomer units for the ETFE sample grafted at 80 °C and at 60 °C, respectively. This chain length estimation assumes that all of the radicals generated by the irradiation react with styrene, and thus the average chain lengths are likely to be underestimated.

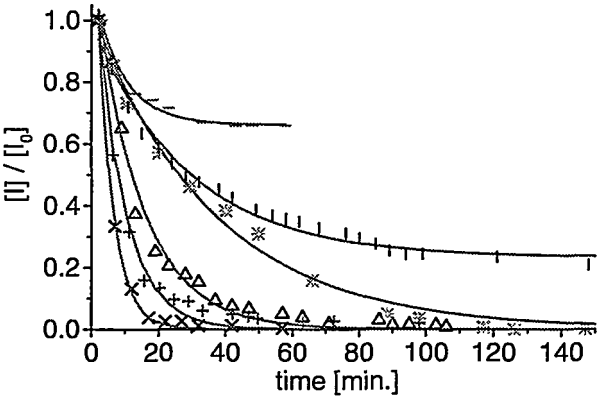

Fig. 2: Total radical intensity decay during grafting of styrene onto 20 kGy pre-irradiated ETFE: at 60 °C (*), at 80 °C (×), peroxy radical at 80 °C (Δ), 25 % styrene in benzene at 80 °C (+), thermal decay at 80 °C (—), thermal decay of peroxy radical at 80 °C (|).

4 CONCLUSION

The nature of the base fluoropolymer film, perfluorinated or partially fluorinated, affects the extent of radical formation and thus subsequent reactivity in the radiation-grafting method. The rate of radical disappearance and increase in graft level strongly correlate with one another, and they both depend greatly upon the reaction temperature and oxygen content of the system. Average chain lengths of the grafted side chains were determined to be on the order of about 1,000 monomer units long.

5 REFERENCES

[1] H.P. Brack, G. Scherer, Macromol. Symp., **126**, 25 (1997).

[2] M. Iwasaki, K.Toriyama, T. Sawaki, M. Inoue, J. Phys. Chem., **47**, 554 (1967).

[3] M. Kuzuya, J. Niwa, T. Noguchi, Polym. J., **27**, 251 (1995).

[4] I. Guilmeau, S. Esnouf, N. Betz, A. Le Moel, Nuclear Instruments and Methods in Physics Research B, **131**, 270 (1997).

PHOTOCELL MODELLING FOR THERMOPHOTOVOLTAIC APPLICATIONS

J.-C. Mayor, W. Durisch, B. Grob, J.-C. Panitz

Goal of the modelling described here is the extrapolation of the performance characteristics of solar photocells to TPV working conditions. The model accounts for higher flux of radiation and for the higher temperatures reached in TPV converters.

1 INTRODUCTION

The photocells utilised in TPV converters are subject to a radiation flux witch is substantially higher than in the case of solar photocells [1]. Flux as high as 5 times, or even more, of the sun intensity for photon energies greater than the bandgap energy of the cell (ε_G = 1.12 eV for Si-cell) are expected. At the same time, and in spite of cell cooling, the working temperature of the photocells is also expected to increase. In order to optimise the layout and design of this part of the TPV converter, a reliable extrapolation method of the cell characteristics measured under solar conditions is needed.

2 MODELLING

The classical *1-Diode-Model* has been extended in order to extrapolate and predict correctly the performance characteristics of solar photocells under TPV working conditions. The model accounts for the higher incident flux of radiation and for the higher temperature reached in a TPV converter. Figure 1 shows the equivalent electrical circuit used:

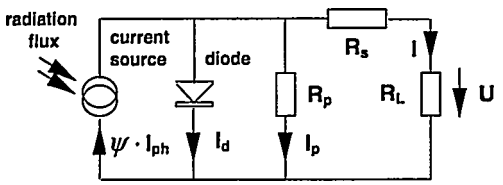

Fig. 1: Equivalent electrical circuit of the photocell.

Applying Kirchhoff's law (current balance) to this circuit leads to the characteristic equation of the *1-Diode-Model*:

$$I = \psi \cdot I_{ph} - I_d - I_p = \psi \cdot I_{ph} - I_s\left[\exp\left(\frac{U + R_s I}{n U_T}\right) - 1\right] - \frac{U + R_s I}{R_p} \qquad (1)$$

where n is the ideality factor, U_T the thermodynamic voltage ($U_{TT} = kT/e$), e the elementary charge and ψ the ratio of the photocurrents under the different radiation conditions ($\psi = I_{ph,TPV}/I_{ph,sun}$). The reverse saturation current of the diode (dark current) is a strong function of the temperature [2]:

$$\frac{I_s(T)}{I_s(T_0)} = \left(\frac{T}{T_0}\right)^3 \cdot \exp\left[-\frac{\varepsilon_{G,0}}{k \cdot \beta}\left(\frac{1}{T} - \frac{1}{T_0}\right)\right] \qquad (2)$$

where k is the Boltzmann's constant, β an adjustment parameter and $\varepsilon_{G,0}$ the extra-polated bandgap width of the cell for T = 0 K ($\varepsilon_{G,0}$ = 1.17 eV for a Si-cell). The linear temperature dependency of the series and parallel resistances has also to be taken into account:

$$R_k(T) = R_k(T_0) \cdot \left[1 + \alpha\left(T - T_0\right)\right] \qquad (3)$$

with $\alpha \cong 0.004$ [1/K].

3 RESULTS

In order to check the model, measurements of the same photocells have been performed for both cases: solar radiation and TPV radiation conditions.

A solar panel consisting of 8 cells connected in series (c-Si, ASE, Heilbronn, Germany, total area: 380 cm^2) was first measured under the following global radiation and temperature conditions: G_n = 909 W/m^2 and T = 37.3 °C.

A least square fit of the main parameters of equation (1) gave the following results (one cell, area = 47.5 cm^2, ψ = 1):

I_{ph} [A]	1.605
I_s [nA]	44.00
n [-]	1.403
R_s [m Ω]	5.65
R_p [Ω]	71.1

Table 1: Main parameters of the photocell.

These values are valid for one single cell at a reference temperature of T_{ref} = 25 °C. However they can

be used to calculate the characteristics of any panel consisting of p parallel rows, each with s identical cells connected in series. The following relationships exist between one single cell (small letters) and a panel consisting of $s \cdot p$ cells (capital letters):

$$I_{ph} = p \cdot i_{ph}; \quad I_s = p \cdot i_s; \quad N = s \cdot n;$$

$$R_s = \frac{s}{p} r_s; \qquad R_p = \frac{s}{p} r_p \qquad (4)$$

A second series of measurements were then performed under typical TPV conditions. In this case equation (1) was used with the parameters determined for the solar conditions (see Table 1) and only ψ and T were adapted to the new conditions (ψ = 3.1, T = 55 °C). Figures 2 and 3 show the comparison between the measured TPV-characteristics (broken line) and the extrapolated solar-characteristics (solid line): the validity of the model is excellent for the case presented.

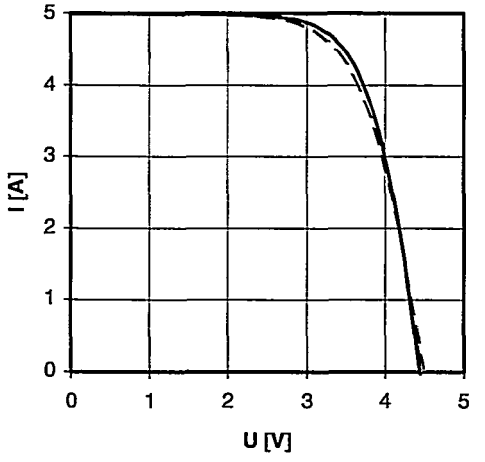

Fig. 2: Comparison of measured and extrapolated cell characteristics for a TPV application.

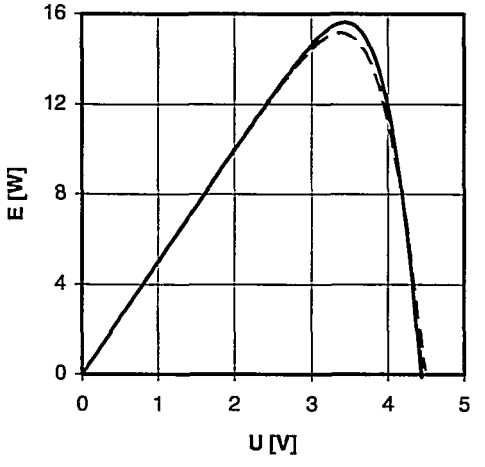

Fig. 3: Power characteristics of the photocells under TPV working conditions.

Figure 4 shows the influence of the cell temperature on the electrical power of the cell string.

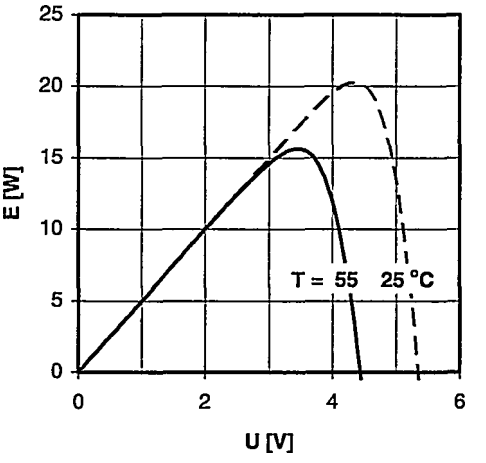

Fig. 4: Power characteristics of the photocells for different temperatures.

A temperature reduction of 30 K would increase the output power from 15.6 to 20.2 W, clearly demonstrating the importance of good cell cooling.

4 CONCLUSION AND OUTLOOK

The extension of the classical *1-Diode-Model* permits a reliable extrapolation of measured solar cell characteristics for TPV applications. First results show that the temperature has a strong influence on the efficiency of the photocells used under TPV conditions. This point should be carefully considered during the design of a TPV converter.

The next step will be the prediction of the ratio of the photocurrents, that means of the parameter ψ, directly as a function of the incoming TPV spectral radiation flux.

5 ACKNOWLEDGEMENT

Support by the Research Foundation of the Swiss Gas Industry (FOGA) is gratefully acknowledged.

6 REFERENCES

[1] J.-Ch. Panitz, J.-C. Mayor, A. Brunner, W. Durisch, M. Schubnell, *Development of Thermophotovoltaic Energy Converters,* PSI Annual Report, Annex V (1997).

[2] J.D. Chatelain, R. Dessoulavy, *Traité d'Electricité, Vol. VIII: Electronique,* Presses Polytechniques Romandes, Lausanne, 3ème édition (1989).

Electrochemical Energy Storage and Conversion

INFLUENCE OF WATER CONTAMINATION AND CONDUCTIVE ADDITIVES ON THE INTERCALATION OF LITHIUM INTO GRAPHITE

F. Joho, B. Rykart, P. Novák, M.E. Spahr (Timcal AG), A. Monnier (Timcal AG)

The irreversible charge loss in the first cycle of lithium intercalation into graphite electrodes for lithium-ion batteries is discussed as a function of water contamination of the electrolyte solution. Furthermore, the improvement of the electrode cycle life due to conductive additives to graphite is demonstrated.

1 INTRODUCTION

Commercial lithium-ion batteries with high energy density and good cycleability usually consist of a carbon based negative electrode, a positive lithium metal oxide electrode, and a separator soaked with organic electrolyte. Despite the high level of development of the batteries several unsolved problems remain. One of them is the rather high irreversible charge loss occurring during first charging of carbon electrodes. It is generally accepted that this charge loss is mainly due to reductive decomposition of the electrolyte on the negative electrode. The resulting protective film, called solid electrolyte interphase (SEI), allows the transfer of lithium ions but prevents the electron transfer. The SEI formation mechanism is rather complex and not yet completely understood.

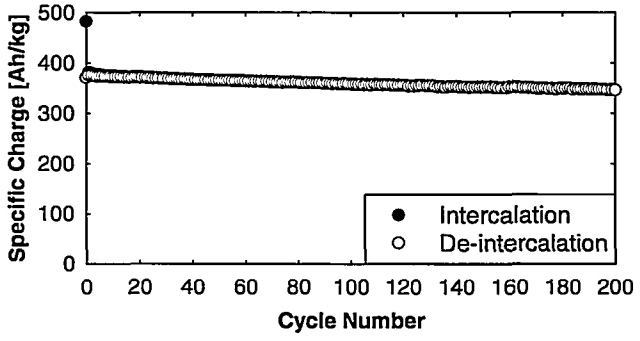

Fig. 1: Cycling performance of the graphite SFG 6 in the electrolyte 1M $LiClO_4$ + DMC/EC; Li counterelectrode.

SEI-related effects on lithium intercalation into graphite are more pronounced with samples having a high specific surface area and exhibiting therefore a high charge loss [1]. Our studies were performed with the graphites TIMREX SFG 6 (Timcal AG, Sins; specific surface area: 15 m^2/g) and SFG 44 (specific surface area: 4.3 m^2/g). The former graphite has been used mainly for the studies of the irreversible charge losses in the first cycle, the latter (exhibiting a lower charge loss in the first cycle of about 10 %) in electrodes intended for practical applications in lithium-ion batteries. The reversible specific charge of both graphites is close to the theoretical value of 372 Ah/kg (based on the graphite weight, Figure 1). The cycling behaviour of both graphites is practically identical.

2 INFLUENCE OF TRACE WATER IN THE ELECTROLYTE

One aim of this work was to investigate the influence of water as a common impurity in electrolyte solutions on the performance of graphite electrodes. In an effort to obtain comparable values, we attempted to assemble cells with a constant graphite-to-electrolyte ratio. Selecting slow cycling conditions for the first cycle most of the irreversible charge loss occurred during this cycle. In a dry electrolyte (≈8 ppm H_2O) the irreversible charge loss measured for the graphite SFG 6 as active electrode material was about 20 % during the first cycle. It increased progressively with increasing water content (Figure 2).

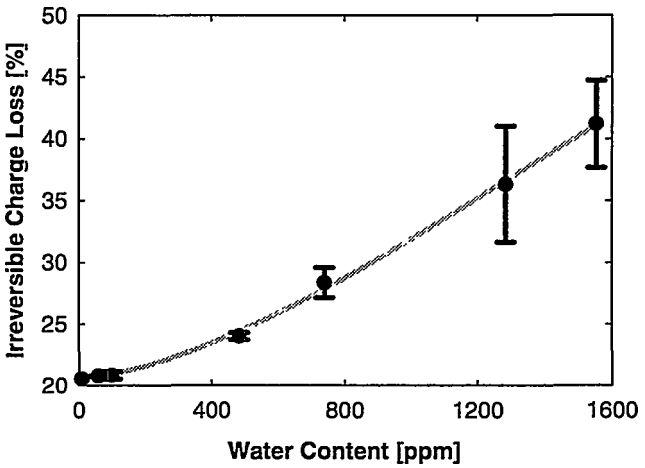

Fig. 2: Dependence of the irreversible charge loss of the graphite SFG 6 during the first cycle on the water content in the electrolyte.

3 INFLUENCE OF CARBON BLACK AND METAL PARTICLE ADDITIVES ON THE PERFORMANCE OF GRAPHITE ELECTRODES

It is known that the ohmic resistance of negative carbon electrodes increases during cycling [2]. This is a potential problem which can be possibly diminished by adding electronically well-conductive additives to the electrode mass. We tested this possibility performing cycling experiments on graphite electrodes with and without additives. As shown in Figure 3, the addition of carbon black improves the cycle life of the negative electrode significantly because of the diminished capacity fading. The curves usually overlap at the beginning of cycling but after several tens of cycles the difference is distinct.

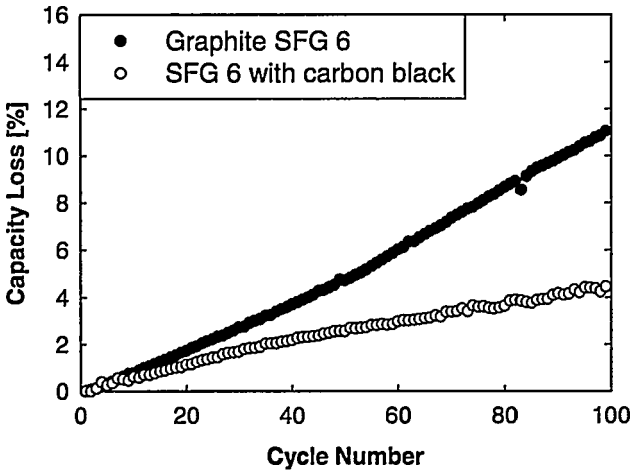

Fig. 3: Comparison of the capacity losses during galvanostatic cycling of graphite SFG 6 electrodes with and without carbon black additive.

We also investigated fine metal particles such as copper and nickel as additives for graphite electrodes. The results are shown in Figure 4. Electrodes containing nickel particles usually showed a better cycling stability than electrodes with copper particles. A possible explanation for this finding may be found in the surface oxides on these metals and especially in the different behaviour of these oxides upon reduction. The electrochemical copper oxide reduction is manifested by the appearance of two additional potential plateaus at about 1.6 V and 1.2 V vs. Li/Li^+ (Figure 5) during the

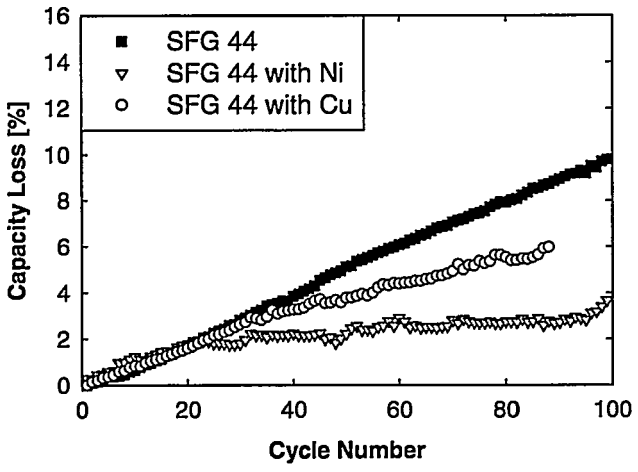

Fig. 4: Comparison of the capacity losses during galvanostatic cycling of graphite SFG 44 electrodes with and without the metal additives copper and nickel.

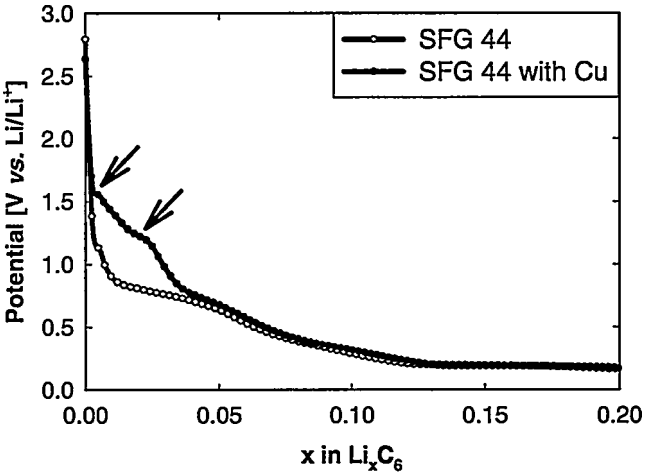

Fig. 5: Comparison of the first charge curves of graphite SFG 44 electrodes with and without the copper additive.

first galvanostatic charge [3]. On the other hand, no plateaus were observed for the reduction of surface oxides on nickel, although an additional irreversible charge loss was detected for both metals, 4 % and 6 % for the nickel and copper additive, respectively. However, in spite of these oxide impurities, both metal additives improved the cycleability of graphite electrodes to some extent.

4 CONCLUSION

(i) The presence of trace water in the electrolyte solution of lithium-ion batteries increases the irreversible charge loss in the first cycle due to water reduction. (ii) Conductivity-enhancing additives such as carbon black or metal particles improve the cycle life of a negative graphite electrode by reducing the increase of resistance of the electrode occurring during cycling.

5 ACKNOWLEDGEMENTS

We thank Dr. O. Haas, PSI, for helpful discussions and the Swiss Federal Office of Energy, Bern, for financial support.

6 REFERENCES

[1] M. Winter, P. Novák, A. Monnier, J. Electrochem. Soc. **145**, 428 (1998).

[2] K. Ozawa, Solid State Ionics **69**, 212 (1994).

[3] R. Bates, Y. Jumel, in Lithium Batteries (J. P. Gabano ed.) 73 (1983).

ELECTROCHEMICAL OXIDATION OF ORGANIC CARBONATE BASED ELECTROLYTE SOLUTIONS AT LITHIUM METAL OXIDE ELECTRODES

R. Imhof, P. Novák

The oxidative decomposition of carbonate based electrolyte solutions at practical lithium metal oxide composite electrodes was studied by differential electrochemical mass spectrometry. For propylene carbonate (PC), CO_2 evolution was detected at $LiNiO_2$, $LiCoO_2$, and $LiMn_2O_4$ composite electrodes. The starting point of gas evolution was 4.2 V vs. Li/Li+ at $LiNiO_2$, whereas at $LiCoO_2$ and $LiMn_2O_4$, CO_2 evolution was only observed above 4.8 V vs. Li/Li+. In addition, various other volatile electrolyte decomposition products of PC were detected when using $LiCoO_2$, $LiMn_2O_4$, and carbon black electrodes. In ethylene carbonate / dimethylcarbonate, CO_2 evolution was only detected at $LiNiO_2$ electrodes, again starting at about 4.2 V vs. Li/Li+.

1 INTRODUCTION

Li-ion batteries based on intercalation materials are among the most important recent achievements in battery technology. Carbon based negative electrodes are used in combination with lithium metal oxide positive electrodes to form batteries with high energy density and good cycling behavior.

Safety aspects of these batteries are widely discussed nowadays. However, the prediction and understanding of these safety related topics are still a major challenge. In order to improve our understanding about the behavior of these batteries upon overcharge we report on the results of our investigations of the oxidative decomposition of organic carbonate solvents at lithium metal oxide composite electrodes. We used differential electrochemical mass spectrometry (DEMS) to study these processes in some detail. The DEMS technique allows the in-situ detection and identification of gaseous and volatile products formed in an electrochemical reaction cell.

2 EXPERIMENTAL

For this study we used the three most common current positive electrode materials, namely $LiNiO_2$, $LiCoO_2$, and $LiMn_2O_4$, all from commercial sources. 45 w/w % graphitized carbon black XC72 was added to improve the conductivity, while 10 w/w % polyvinylidene fluoride (PVDF) was used as a binder because of its excellent chemical stability. These electrodes were investigated in two different electrolyte solutions, based on propylene carbonate (PC) and a 1:1 mixture of ethylene carbonate (EC) and dimethylcarbonate (DMC).

The DEMS setup and the preparation of the working electrodes were described in reference [1]. The measurements were carried out potentiodynamically by cycling the working electrode between the open circuit potential (about 3 V vs. Li/Li+) and 5.5 V vs. Li/Li+ with scan rates of 0.1, 0.2 or 0.4 mV/s, respectively (cyclic voltammetry, CV). In addition, the mass signals were recorded as functions of potential (mass spectrometry cyclic voltammogram, MSCV).

3 RESULTS AND DISCUSSION

It is known that the specific surface area of the electrode materials is one of the key factors influencing the extent of the electrochemical oxidation of the electrolyte solvent. Values in the range from 1 to 5 m^2/g were measured for all lithium metal oxides used in this study. In contrast, the specific surface area of the carbon black used is about 75 m^2/g. The surface of the composite electrode hence consists predominantly of carbon black. It is therefore necessary to first study the electrochemical behavior of this conductive filler. Figure 1 shows the cyclic voltammogram and MSCV's of a carbon black powder electrode with 10 % PVDF in PC / 1 M $LiN(SO_2CF_3)_2$.

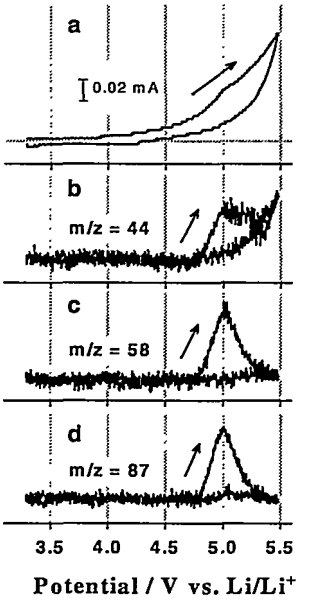

Fig. 1: CV (a) and MSCV's of masses m/z = 44 (b), 58 (c), and 87 (d), respectively, representing decomposition products of PC generated at carbon black in PC / 1 M $LiN(SO_2CF_3)_2$. Scan rate = 0.2 mV/s.

We detected mass signals m/z = 44, 58, and 87, all starting at about 4.8 V vs. Li/Li+. We interpret the three mass signals in terms of the formation of carbon dioxide, propanal, and 2-ethyl-4-methyl-dioxalane, $C_6H_{12}O_2$, respectively [2].

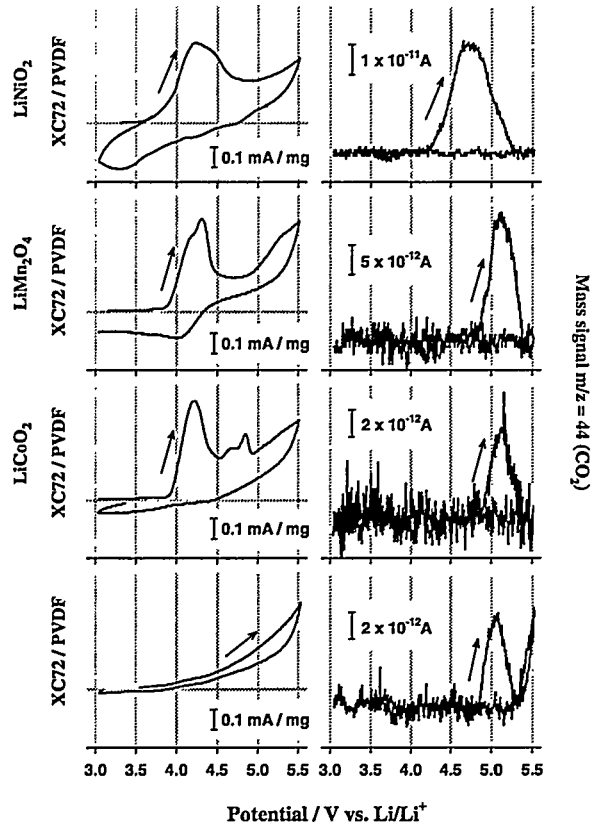

Fig. 2: CV's and MSCV's of mass m/z = 44 (CO_2) recorded at the three lithium metal oxide electrodes and a carbon black electrode in PC / 1 M $LiN(SO_2CF_3)_2$. Scan rate = 0.4 mV/s.

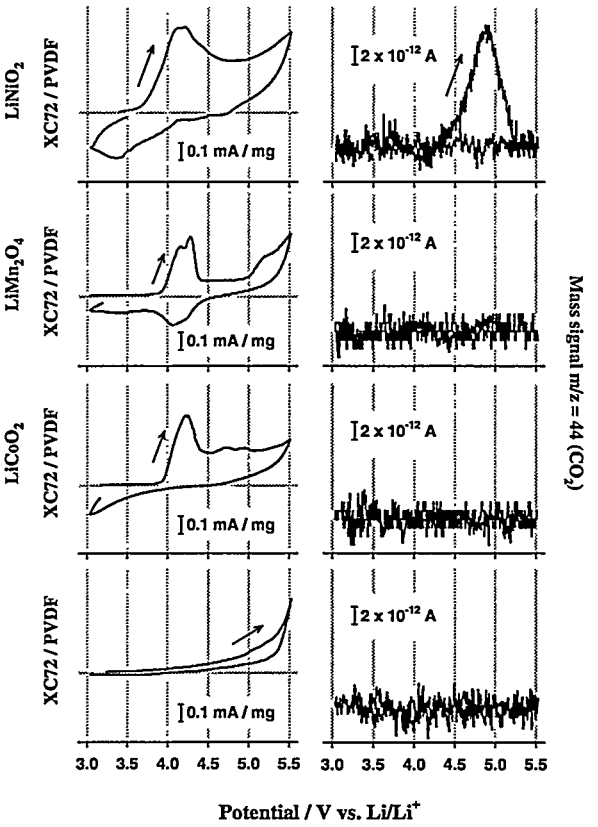

Fig. 3: CV's and MSCV's of mass m/z = 44 (CO_2) recorded at the three lithium metal oxide electrodes and a carbon black electrode in EC / DMC / 1 M $LiN(SO_2CF_3)_2$. Scan rate = 0.4 mV/s.

Figure 2 compares the DEMS measurements at carbon black in the PC based electrolyte solution with the results obtained at $LiMn_2O_4$, $LiCoO_2$, and $LiNiO_2$ composite electrodes in the same electrolyte solution. Obviously, all lithium metal oxide composite electrodes evolve CO_2 upon oxidation in the PC-based electrolyte. $LiNiO_2$ shows CO_2 evolution starting at about 4.2 V vs. Li/Li^+. In contrast, the electrochemical behavior of the $LiCoO_2$ and $LiMn_2O_4$ electrodes resembles the results found on the carbon black electrode (Figure 1). CO_2 evolution does not start before 4.8 V vs. Li/Li^+, and intensity changes in the mass signals m/z = 58 and 87 were detected too. However, it is not possible to decide conclusively whether the observed generation of volatile decomposition products occurs at the $LiCoO_2$ and $LiMn_2O_4$ or at the carbon black component of the composite electrodes.

The results of the DEMS measurements in the EC / DMC based electrolyte are summarized in Figure 3. Again, $LiNiO_2$ shows CO_2 evolution starting at about 4.2 V vs. Li/Li^+. In contrast, volatile oxidation products were detected neither at the other two lithium metal oxide materials nor at carbon black in this electrolyte solution.

4 CONCLUSION

No gas evolution was detected at $LiNiO_2$, $LiCoO_2$, and $LiMn_2O_4$ electrodes in organic carbonate based electrolyte solutions in the potential range where reversible cycling is usually performed. However, at $LiNiO_2$ composite electrodes, CO_2 was detected at potentials as low as 4.2 V vs. Li/Li^+. In contrast, both $LiCoO_2$ and $LiMn_2O_4$ composite electrodes show CO_2 only for potentials positive to 4.8 V vs. Li/Li^+. Thus, compared to $LiNiO_2$, both $LiCoO_2$ and $LiMn_2O_4$ reveal a securer behavior concerning gas evolution on overcharge.

5 ACKNOWLEDGEMENTS

Financial support by the Swiss Federal Office of Energy is gratefully acknowledged. We also thank Dr. C. Kormann, BASF, for the donation of the $LiMn_2O_4$ samples.

6 REFERENCES

[1] R. Imhof, P. Novák, J. Electrochem. Soc., **145**, 1081 (1998).

[2] R. Imhof, P. Novák, J. Electrochem. Soc., **146**, (1999).

ELECTRICALLY RECHARGEABLE ZINC/AIR BATTERY: A HIGH SPECIFIC ENERGY SYSTEM

F. Holzer, J.-C. Sauter, G. Masanz, S. Müller

This contribution describes our research and development efforts towards the demonstration of a light-weight, low-cost 12 V/20 Ah electrically rechargeable Zn/air battery. We successfully developed electrodes having active areas of up to 200 cm². Deep discharge cycles at different currents as well as current-voltage curves are reported for a 10 cell Zn/air battery (serial connection) with a rated capacity of 20 Ah. Based on the discharge cycle at a power of 19 W, and the weight of the battery, a specific energy of more than 90 Wh/kg could be evaluated for the whole system.

1 INTRODUCTION

It is the fundamental advantage of metal/air battery systems over other systems that only the metallic active material has to be stored in the battery, whereas the reactive component for the positive electrode (O_2) is absorbed from the ambient air. For this basic reason, metal/air systems have a high specific energy. The most promising results for electrically rechargeable metal/air systems have been achieved with Zn/air systems. Their high theoretical specific energy of 1085 Wh/kg, in combination with further advantages such as low price and environmental compatibility of all components make the zinc/air system a very attractive candidate for traction applications. Several different concepts were recently described for systems that are either mechanically [1] or electrically [2,3] rechargeable. Mechanically rechargeable systems, which are recharged by exchanging the zinc electrode, require additional infrastructure. Therefore electrically rechargeable Zn/air systems are preferred for consumer applications such as electric vehicles and portable devices.

2 EXPERIMENTAL

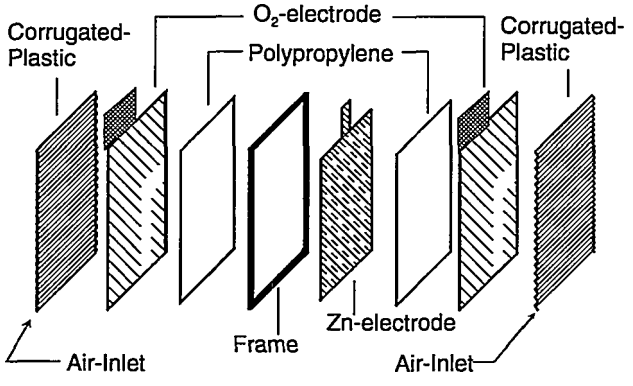

Fig. 1: Schematic view of a single Zn/air cell. The pasted Zn-electrode is held between two bifunctional O_2-electrodes.

Zinc electrodes were prepared by pasting zinc oxide with cellulose additive and PTFE binder onto a lead current collector [4]. The $La_{0.6}Ca_{0.4}CoO_3$-activated bifunctional oxygen-diffusion electrodes were prepared by a calendering rolling process [5]. Both electrodes were manufactured in sizes of up to 200 cm².

The electrodes were tested using a sandwich cell arrangement as depicted in Figure 1. The pasted zinc electrode, wrapped in Celgard separator, was held between two bifunctional oxygen electrodes, which are covered by a polypropylene wick. A corrugated plastic sheet was placed on the gas side of each oxygen electrode to achieve a homogeneous distribution of oxygen (or air) over the whole electrode area. The electrolyte used was a 30 % KOH solution saturated with ZnO and containing 1.5 M KF. Figure 2 shows a photograph of the battery package consisting of 10 cells connected in series. Finally the battery package was mounted into a light-weight polypropylene case.

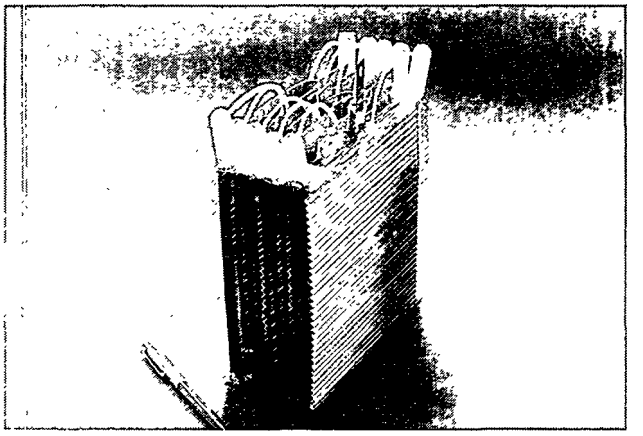

Fig. 2: 10-cell Zn/air-battery (12 V/20 Ah) without battery case.

Zinc was formed by charging 2/3 of the nominal capacity (30 Ah, nominal capacity) at a low current (~C/24, where C/n denotes complete discharge in a time of n hours). Afterwards the cell was discharged at the same current until the cell voltage dropped below 0.7 V. The formation process was repeated 2 - 3 times. The charged cells with a rated capacity of 20 Ah were then used for deep discharge cycles or for evaluation of peak power performance.

Deep discharge experiments were performed at different discharge rates. In each battery the cell voltages were monitored individually. The batteries were discharged at constant current until one of the cell voltages dropped below 0.7 V.

The peak power values were calculated from current-voltage curves measured for the system with either oxygen or air.

3 RESULTS AND DISCUSSION

Figure 3 shows the discharge capability of a 200 cm^2 Zn/air battery, with 10 cells connected in series and a rated capacity of 20 Ah, at different discharge rates. At discharge rates of C/8 (at 2.5 A) and of C/12 (at 1.67 A), more than 90 % of the charged capacity could be recovered from the battery. The discharge voltage of the battery is very stable over a long period of discharge, only at the end of the discharge process a drop in voltage was detected. The average power of the Zn/air battery was 27 W at C/8 and 19 W at C/12. The weights of the components are as follows:

component	number	mass /g	mass /%
O_2-electrode	20	320	14
Zn-electrode	10	721	30
electrolyte	10	560	24
frame/gas distributor	10/11	352.5	15
contacts	11	66	3
battery case	1	290	14
total		2309.5	100

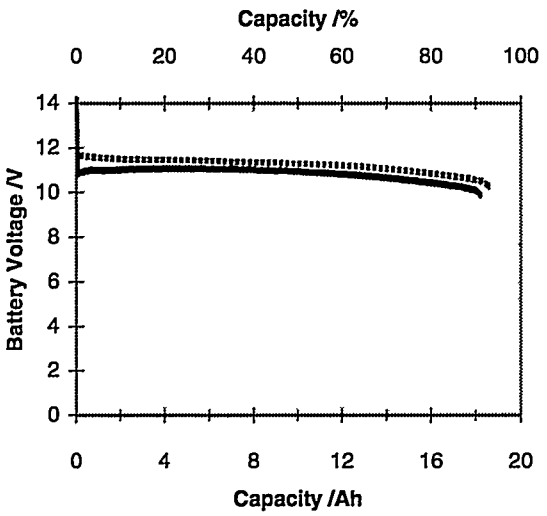

Fig. 3: Deep discharge performance of the 10 cell Zn/air battery. (—): C/8 (2.5 A); (- - -): C/12 (1.67 A).

The peak power performance of five- and ten-cell Zn/O_2 and Zn/air batteries is shown in Figure 4. The batteries were charged to 20 Ah. The Zn/O_2 battery with five cells connected in series shows a peak power of more than 130 W, while the corresponding Zn/air battery shows one of 110 W. Due to temperature increase inside the 10 cell module, the current was stopped at 12 A. Up to this current the power achieved is about doubled in the 10 cell module compared to the 5 cell module, so a peak power for the 10 cell module of ~260 W for Zn/O_2 and of ~220 W for Zn/air is expected.

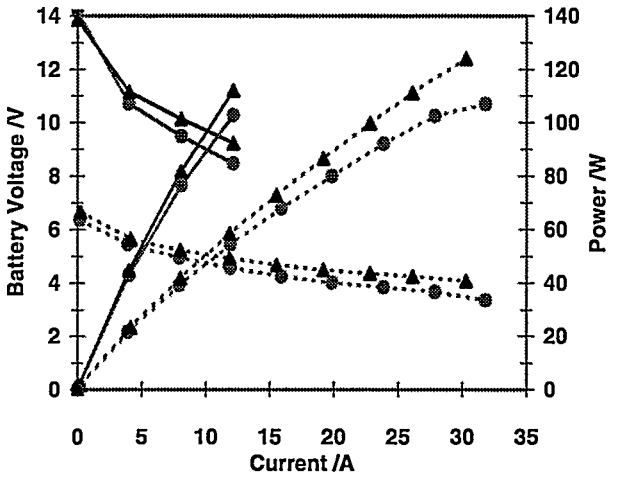

Fig. 4: Current-voltage curves: (—): 10 cell module, (- - -): 5 cell module, (▲) Zn/O_2 and (●) Zn/air battery.

4 CONCLUSION

Pasted zinc electrodes and bifunctional oxygen electrodes were successfully manufactured in active areas of 200 cm^2. The combination of $La_{0.6}Ca_{0.4}CoO_3$-activated bifunctional O_2-electrodes and pasted zinc electrodes was successfully demonstrated in sandwich-type batteries.

The deep discharge capability of the Zn/air battery was almost independent on the discharge rate. Based on the weight of the whole battery system a specific energy of 86 Wh/kg can be calculated for a C/8 discharge rate, and one of 91 Wh/kg for a C/12 discharge rate.

Peak powers of more than 115 W/kg for the Zn/O_2 battery and 95 W/kg for the Zn/air battery were reached (based on the weight of the whole system) for batteries with 5 cells connected in series.
For high power drain, beyond 100 W, the 10-cell battery requires a cooling system.

5 ACKNOWLEDGEMENTS

The financial support of the Swiss Federal Office of Energy and PSEL (Projekt- und Studienfonds der Elektrizitätswirtschaft) is gratefully acknowledged.

6 REFERENCES

[1] J.R. Goldstein, B. Koretz, Y. Harats, Proc. 31st Intersoc. Energy Conversion Engineering Conf., **3**, 1925 (1996).

[2] P.N. Ross Jr., US Patent No. 4 842 963.

[3] S. Müller, O. Haas, C. Schlatter, Ch. Comninellis, J. Appl. Electrochem. **28**, 305 (1998).

[4] F. Holzer, S. Müller, O. Haas, Proc. 38th Power Sources Conf., 354 (1998).

[5] S. Müller, K.A. Striebel, O. Haas, Electrochim. Acta **39**, 1661 (1994).

HIGH SURFACE AREA CARBON FOR BIFUNCTIONAL AIR ELECTRODES APPLIED IN ZINC-AIR BATTERIES

H. Arai (on leave from NTT Laboratories, Japan), S. Müller, O. Haas

Bifunctional air electrodes with high surface area carbon substrates showed low reduction overpotential, thus are promising for enhancing the energy efficiency and power capability of zinc-air batteries. The improved performance is attributed to lower overpotential due to diffusion of the reaction intermediate, namely the peroxide ion.

1 INTRODUCTION

Electrically rechargeable Zinc-air batteries show high specific energy and are interesting from an economical and ecological point of view. In order to improve the energy efficiency during the charge-discharge cycle the overpotential at the bifunctional air electrode has to be decreased. In preliminary experiments we found that carbon substrates greatly affect the overall electrode activity. In this study we examined the influence of the carbon surface area on the electrochemical activity and the life-time of bifunctional air electrodes.

2 EXPERIMENTAL

The air electrode consisted of two layers [1]: The hydrophobic gas diffusion layer, which was made from acetylene black and polytetrafluoroethylene (PTFE), and an active layer with high surface area carbon (Carbon A) and graphitized carbon (Carbon B) which were loaded with $La_{0.6}Ca_{0.4}CoO_3$ (15 m^2/g) and bound with PTFE. KOH was used as an electrolyte to test the air electrodes.

3 RESULTS AND DISCUSSION

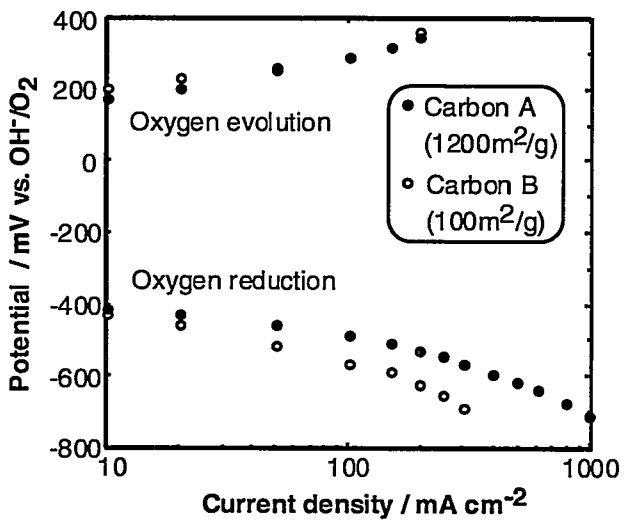

Fig. 1: Current-potential curve of air electrodes with carbons A and B as the substrate in the active layer. Electrode area: 0.5 cm^2.

Figure 1 shows the current-potential curve of the air electrodes. In the oxygen reduction step the electrode with high surface area carbon (Carbon A) showed lower overpotentials particularly at high current densities. For a fixed potential of -600 mV (vs. OH^-/O_2), the electrode with Carbon A showed a current density approximately 3 times higher than the electrode with Carbon B.

Using AC-impedance measurements we found that the main polarisation can be ascribed to two diffusion processes. One process is the oxygen diffusion in the active layer, and the other diffusion process was deduced to be the diffusion of the reaction intermediate, namely the peroxide ion from the electrocatalyst [2]. The high surface area Carbon, A showed a smaller diffusion polarisation than Carbon B in the peroxide diffusion process.

The short-term electrode stability test showed that the electrode was stable during the reduction step. However, during the oxygen evolution reaction the electrolyte became brown, suggesting that the carbon substrate was corroded. The life-time of the electrode can be improved considerably using higher catalyst loading.

4 CONCLUSION

With high surface area carbon materials the activity of the perovskite catalysed air electrode for oxygen reduction can be markedly improved. In order to protect the carbon material from corrosion the perovskite loading has to be increased.

5 ACKNOWLEDGEMENT

Financial support from Nippon Telegraph and Telephone (NTT) for this collaborative work is gratefully acknowledged.

6 REFERENCES

[1] S. Müller, K.A. Striebel, O. Haas, Electrochim. Acta **39**, 1661 (1994).

[2] D. Wabner, R. Holze, P. Schmittinger, Z. Naturforsch. **39B**, 157 (1984).

STUDIES OF ACTIVATED CARBON AND CARBON BLACK FOR SUPERCAPACITOR APPLICATIONS

R. Richner, S. Müller, R. Kötz, A. Wokaun

Carbon Black and activated carbon materials providing high surface areas and a distinct pore distribution are prime materials for supercapacitor applications at frequencies < 0.5 Hz. A number of these materials were tested for their specific capacitance, surface and pore size distribution. High capacitance electrodes were manufactured on the laboratory scale with attention to ease of processability.

1 INTRODUCTION

Electric double layer capacitors (EDLC) are of growing importance as devices with applications in areas intermediate between batteries and conventional capacitors. The EDLC market is expected to grow to US$ 1 billion by the year 2000 [1].

In EDLC the energy is stored in the electric field established at the electrode/electrolyte interface.

Typical EDLC are made of porous, high-surface-area carbonaceous materials and highly ion-conductive electrolytes.

2 EXPERIMENTAL

In the course of this program at PSI various carbonaceous materials such as activated carbon and carbon black were tested for their capacitance performance in electrodes. This paper reports results obtained with Black Pearls 2000, a carbon black provided by Cabot, USA.

In order to improve the conductivity of the electrode, Black Pearls 2000 was mixed with graphite in amounts of ca. 10 %. The influence of two different graphite materials (graphite A and B) on the specific capacitance of the electrode was investigated. The mixture of the two carbon materials was dispersed in deionized water, and a teflon particle suspension was stirred in. The resulting sludge was dried to a dough and rolled into a Nickel net to form an electrode of 0.2 mm thickness. The electrode was sintered at 320 °C under pressure. Impedance spectra were recorded using 1 M tetraethylammonium tetrafluoroborate ($TEABF_4$) in acetonitrile as an electrolyte.

3 RESULTS AND DISCUSSION

Figure 1 shows a typical plot of the specific capacity as a function of frequency measured for manually prepared electrodes using Black Pearls 2000 with a specific surface area of 1475 m^2/g in combination with graphite A and B. The best electrode showed a maximum specific capacity of 80 F/g in the frequency range useful for load levelling in traction applications. Apart from its high power drain capability, the specific energy of such a supercapacitor is much higher than for conventional capacitors. Using Black Pearls 2000 in combination with organic electrolyte (2.5 V system) a specific energy of about 17 Wh/kg for the EDLC can be calculated (based on the electrode weight).

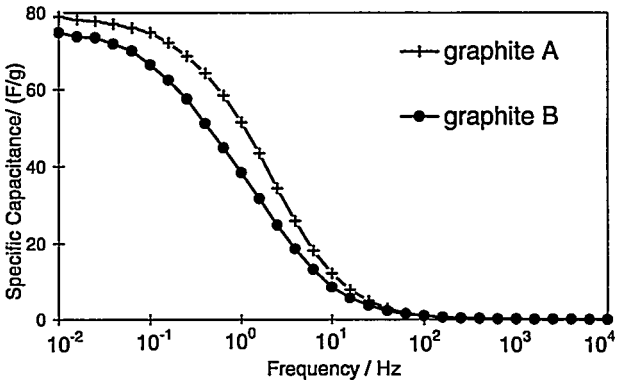

Fig. 1: Capacity behaviour of carbon-black-based electrodes. 80% Black Pearls 2000, 10% PTFE, 10% Graphite A and B, sintered at 320 °C and 4 kg/cm^2.

4 CONCLUSION

Electrodes made of high-surface-area carbon black Black Pearls 2000 in combination with highly conductive graphite achieved a specific capacitance of 80 F/g in organic electrolytes. Supercapacitors consisting of these materials will fulfil the requirements of electromotive applications.

5 ACKNOWLEDGEMENTS

Financial support by the Board of the Swiss Federal Institute of Technology is gratefully acknowledged. The authors thank Mrs. G. Masanz and Mrs. F. Geiger for excellent technical support.

6 REFERENCES

[1] A. Nishino, J. Pow. Sourc., **60**, 137-147 (1996).

OXYGEN EVOLUTION STUDIES ON PEROVSKITE FILMS IN ALKALINE MEDIA

V. Hermann (ETH Lausanne), Ch. Comninellis (ETH Lausanne), S. Müller

Thin films of $La_{0.6}Ca_{0.4}CoO_3$ perovskite were deposited on nickel plates by thermal decomposition of the metal nitrates. The electrochemical activity of the films for oxygen evolution in KOH solutions (0.1-1 M) was investigated. The reaction order with respect to OH^- ion was found to be around 0,7. The results correlate fairly well with a mechanism in which breaking of the intermediate metal-peroxide bond at the Co ion is the rate-determining step.

1 INTRODUCTION

Recently, a Zn/air battery containing perovskite-activated bifunctional air electrodes has been developed [1]. Zinc-air cells with $La_{0.6}Ca_{0.4}CoO_3$-activated bifunctional oxygen-diffusion electrodes showed a high service-life of ca. 3000 h in moderately alkaline electrolyte [2]. Parallel to this work we studied the electrocatalytical properties of the perovskite catalyst alone as a thin film deposited on a conductive substrate. This report presents some results for kinetic parameters of the O_2 evolution on thin film $La_{0.6}Ca_{0.4}CoO_3$ activated electrodes.

2 EXPERIMENTAL

Thin $La_{0.6}Ca_{0.4}CoO_3$ films were prepared on nickel substrate by thermal decomposition of the metal nitrates. The nickel foils had been pretreated with HCl. As a precursor solution a 1:1 mixture of isopropanol and aqueous metal nitrate was used. The precursor solution was deposited on the Ni substrate, dried at 120 °C for 15 min, and heated 10 min in air at 300 °C. The final annealing treatment to form the perovskite structure was performed at 700 °C for 2 h.

The oxygen evolution reaction was studied at $Ni/La_{0.6}Ca_{0.4}CoO_3$ electrodes in 0.1 - 1 M KOH by different electrochemical techniques. This report focuses on mechanistic aspects of the oxygen evolution reaction at different KOH concentrations.

3 RESULTS AND DISCUSSION

The morphological aspects of the $La_{0.6}Ca_{0.4}CoO_3$ film surface were investigated by SEM microphotographs as shown in Figure 1. The film is quite homogeneous and shows well defined crystallites. This was not the case without annealing the sample at 700 °C.

Figure 2 shows the X-ray diffraction spectrum of a thin film perovskite electrode. The formation of the expected perovskite phase is demonstrated, but some parasitic phases are present. First of all, because of the thinness of the film, the Ni substrate is visible despite the low angle (2°) used for the analysis. It seems that an oxide of the substrate (NiO) is formed during the high temperature treatment of the electrode. The non-indexed peaks are attributed to a parasitic cubic phase of cobalt oxide.

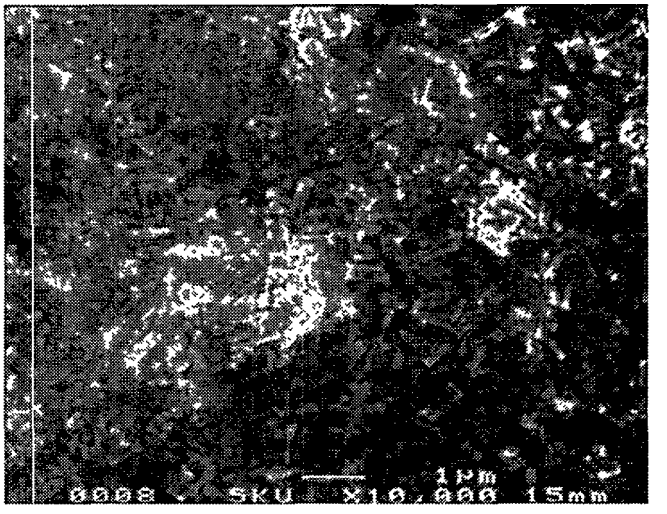

Fig. 1: SEM microphotography of $La_{0.6}Ca_{0.4}CoO_3$ film obtained at 700 °C, 2 hours.

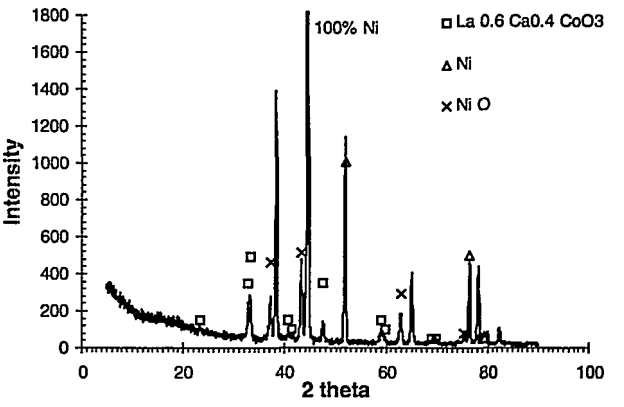

Fig. 2: Low angle X-ray diffractogram of the $La_{0.6}Ca_{0.4}CoO_3$ film on the Ni substrate.

Anodic polarisation curves were recorded in order to study the kinetic parameters of O_2 evolution on the $Ni/La_{0.6}Ca_{0.4}CoO_3$ electrodes. Figure 3 illustrates the potential versus log(i) plots for different OH^- concentrations. It shows two different Tafel slopes, around 40 mV/decade at lower and from 90 to 130 mV/decade at higher overpotentials, decreasing with increasing KOH concentration.

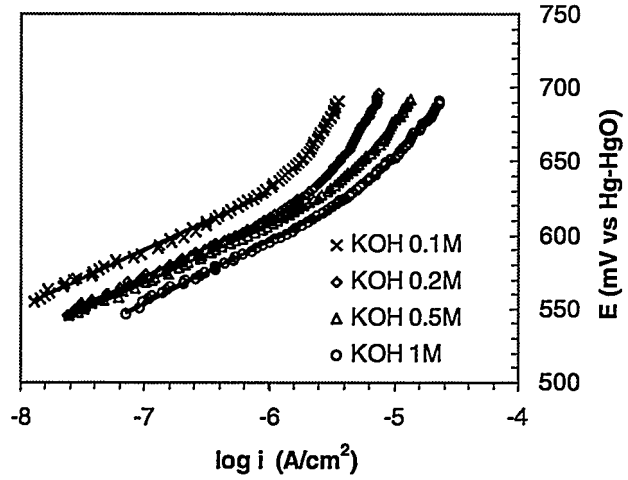

Fig. 3: Potential vs. log i curves of a Ni/ $La_{0.6}Ca_{0.4}CoO_3$ electrode for O_2 evolution using different KOH concentrations. Scan rate = 0.2 mV/s.

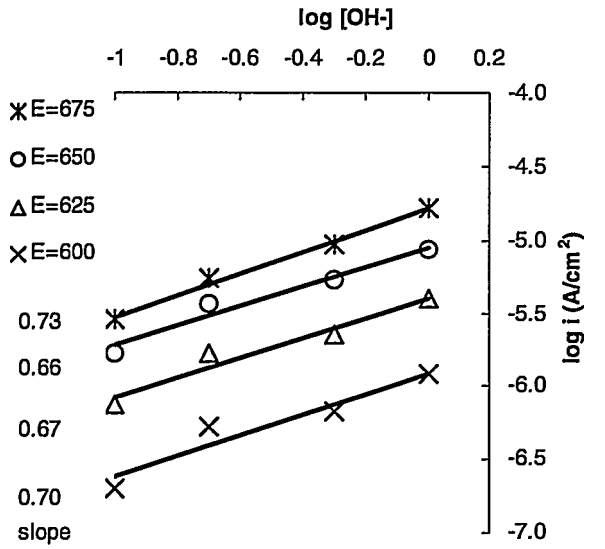

Fig. 4: Log(i) vs. log(OH^-) for O_2 evolution on Ni/$La_{0.6}Ca_{0.4}CoO_3$ electrodes at different potentials.

The reaction order of oxygen evolution with respect to the concentration of OH^- is given by the slope of the plot of log(i) vs log(OH^-) at each particular potential, as shown in Figure 4. The average value of the slopes was about 0.70, which is close to the value reported by Bockris et al. [3] for other types of cobaltate. From the measured Tafel slopes we may conclude in analogy to Bockris's work [3,4] that the rate determining step is the Co-peroxide cleavage at the $La_{0.6}Ca_{0.4}CoO_3$ catalyst.

4 CONCLUSION

XRD analyses revealed that $La_{0.6}Ca_{0.4}CoO_3$ can be deposited on Ni foils by thermal oxidation of the metal nitrates. SEM photographs confirmed the formation of a homogenous film with well defined crystallites. The electrodes showed a good activity for oxygen evolution in alkaline medium. The kinetic studies showed two different Tafel slopes depending on the potential applied and a reaction order with respect to the OH^- concentration close to unity. These results support a mechanism proposed by Bockris et al. where the rate determining step for oxygen evolution on perovskites is the desorption of the peroxide formed at the transition metal ion. Further investigations will focus on alternative perovskites with lower peroxide-bonding energy showing faster kinetics for the oxygen evolution reaction.

5 ACKNOWLEDGEMENTS

We thank Mr P. Moeckli and Mr B. Senior of EPFL for the film characterisations.

6 REFERENCES

[1] S. Müller, F. Holzer, O. Haas, C. Schlatter, C. Comninellis, Chimia **49**, 27 (1995); cf. this report.

[2] S. Müller, F. Holzer, O. Haas, Electrochem. Soc. Proc. **97-18**, 859 (1997).

[3] J. O'M. Bockris, T. Ottagawa, J. Electrochem. Soc. **131**, 290 (1984).

[4] J. O'M. Bockris, T. Ottagawa, J. Phys. Chem. **87**, 2960 (1983).

GLASSY CARBON SUPERCAPACITOR: 100,000 CYCLES DEMONSTRATED

M. Bärtsch, A. Braun, B. Schnyder, R. Kötz

A 5 V glassy carbon capacitor stack was built consisting of four bipolar and two end-plate electrodes. More than 100,000 charging/discharging cycles were applied to test the stability of the double-layer capacitor. Low and high frequency resistances were measured as a function of the number of cycles.

1 INTRODUCTION

Electrochemical double-layer capacitors (EDLC) - also called supercapacitors - represent, concerning energy storage, a very promising alternative to batteries, especially in peak power applications [1]. Their advantages over batteries are:

- Specific powers of several kW/kg;
- Excellent high-power charging;
- Outstanding cycle life stability.

The full charging/discharging of a glassy carbon (GC) supercapacitor for more than 100,000 cycles is demonstrated.

2 EXPERIMENTAL

We have built a 5 V bipolar EDLC consisting of 5 cells using glassy carbon (GC) electrodes. The electrodes were thermally activated and had an effective active area of 14 cm^2. 3 M sulphuric acid was used as electrolyte. The high (1 kHz) and low frequency (1 Hz) resistance of the GC stack was measured by electrochemical impedance spectroscopy (EIS) at 0 V DC potential. The capacitance values are the real part of the complex capacitance and are calculated from impedance data at 0.1 Hz. The GC stack was charged and discharged between 0 and 5 V applying a constant current of 0.5 A. The potential was kept at 0 and 5 V respectively for 12 s.

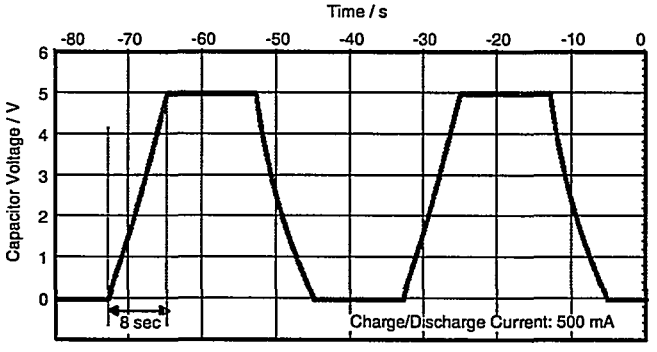

Fig. 1: Cycle numbers 59954 and 59955 of the 5 V GC stack cycled at constant current.

3 RESULTS AND DISCUSSION

More than 100,000 complete charging/discharging cycles were recorded within about 1½ months. Figure 1 shows two successive cycles out of the 100,000. It took 8 s to charge or discharge the capacitor stack. According to equation (1),

$$C = I \cdot t / U, \qquad (1)$$

in which C is the capacitance, I the current, t the time and U the voltage, the capacitance of the 5 V stack yields 0.8 F. Batteries have much lower charging rates and work only some hundreds of cycles. The slightly curved charging or discharging line indicates that the capacitance is weakly potential dependent.

Figure 2 shows the dependence of the resistance at 1 kHz and 1 Hz on the number of cycles (left scale). The high frequency resistance at 1 kHz (contact, electrolyte and electronic active layer resistance) increases quite linearly and is only 7 mΩ higher after 100,000 cycles whereas the resistance at 1 Hz (the above resistances, plus diffusion resistance of the active layer) increases more irregularly by about 20 mΩ. The right scale in Figure 2 shows the capacitance as a function of the cycle number. The capacitance decreases steadily. At about 70,000 cycles the polarity of the capacitor was reversed what improved the capacitance somewhat. Despite the first encouraging results further efforts are needed to obtain even more stable resistance and capacitance values.

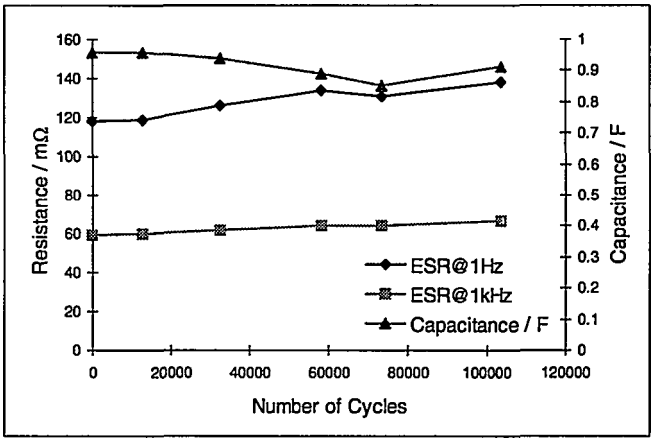

Fig. 2: Capacitance, low and high frequency resistance as a function of the number of charging/discharging cycles.

4 ACKNOWLEDGEMENT

Financial support by the Board of the Swiss Federal Institutes of Technology BSIT [Swiss Priority Program on Materials Research] is gratefully acknowledged.

5 REFERENCES

[1] M. Bärtsch, A. Braun, R. Kötz, O. Haas. Proceedings of the 38th Power Sources Conference, 8-11 June, 17-20, Cherry Hill, NJ (1998).

LONG TERM TESTING OF PSI-MEMBRANES

J. Huslage, H.P. Brack, F. Geiger, F.N. Büchi, A. Tsukada, G.G. Scherer

Long term tests of PSI membranes based on radiation-grafted FEP and ETFE films were carried out and FEP-based membranes were evaluated by monitoring the in-situ membrane area resistance measured by a current pulse method. By modifying our irradiation procedure and using the double crosslinking concept we obtain reproducible membrane cell lifetimes (in term of in-situ membrane resistance) of greater than 5000 hours at 60-65 °C. Preliminary tests at 80-85 °C with lifetimes of greater than 2500 demonstrate the potential long term stability of PSI proton exchange membranes based on FEP over the whole operating temperature range of low-temperature polymer electrolyte fuel cells. Radiation grafted PSI membranes based on ETFE have better mechanical properties than those of the FEP membranes. Mechanical properties are particularly important in large area cells and fuel cell stacks. ETFE membranes have been tested successfully for approximately 1,000 h in a 2-cell stack (100 cm² active area each cell).

1 INTRODUCTION

Radiation-grafting can be used to combine the desirable properties of two dissimilar polymers in a graft copolymer structure. For example, the chemical and thermal stability of commodity fluoropolymers can be combined with the proton-conducting properties of partially para-sulfonated polystyrene to yield materials useful for electrochemical devices, e.g., fuel and electrolysis cells, batteries, and sensors.

In the past PSI has developed radiation-grafted membranes with high performance current-voltage properties when used as solid electrolytes in low-temperature polymer electrolyte fuel cells. In addition to the current-voltage properties membrane lifetimes greater than 3000 hours are necessary, especially for mobile applications. Therefore, in the present work long term tests of optimised PSI membranes, based on 75 µm FEP (poly(tetrafluoroethylene-co-hexafluoropropylene)) and 50 µm ETFE (poly(ethylene-*alt*-tetrafluoroethy-lene)) films have been carried out to demonstrate that PSI membranes could be an interesting and potentially inexpensive PEFC membrane.

2 EXPERIMENTAL

The proton conducting membranes, based on FEP and ETFE films, were manufactured by using the method [1] shown in Figure 1 for the case of FEP.

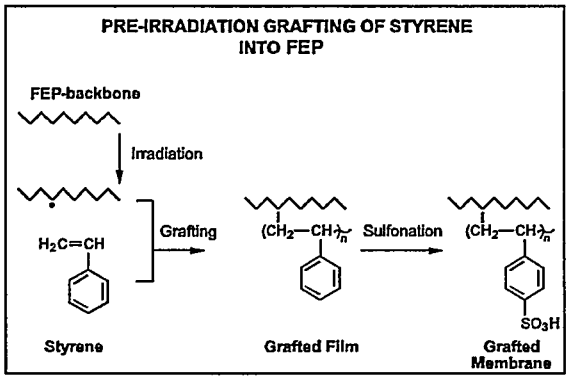

Fig. 1: Schematic illustration of the radiation-grafting method of membrane preparation.

As we reported earlier based on *in-situ* membrane resistance and cell polarisation measurements during long-term PEFC testing, the *in-situ* stability of our membranes prepared using the double crosslinking concept (DVB and TAC) is much better than that of uncrosslinked radiation-grafted membranes [1]. In contrast to earlier results, electron beam irradiation is now used instead of γ-beam irradiation. In order to determine the membrane lifetime the membranes were tested in 30 cm² active area stainless steel fuel cells and two graphite cell (100 cm² active area each) stacks with E-TEK electrodes (loading of 0.8 mg/cm² Pt) and hydrogen and oxygen gases. The *in-situ* membrane resistance was determined by a current pulse method [2].

3 RESULTS AND DISCUSSION

We have recently obtained reproducible membrane cell lifetimes (in terms of *in-situ* membrane resistance) of greater than 5000 hours at 65 °C with our radiation-grafted PSI membranes [3] as shown in Figure 2.

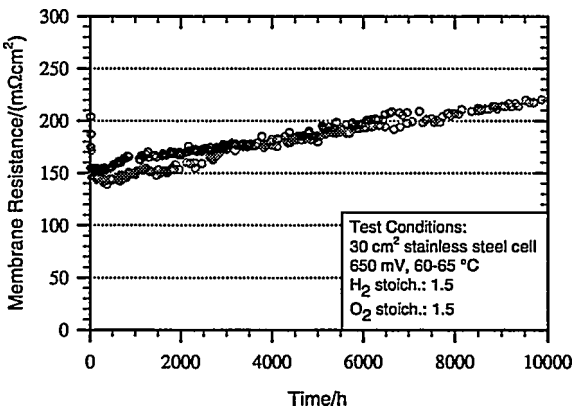

Fig. 2: *In-situ* membrane resistances of double crosslinked PSI-membranes (based on FEP 75 µm) at 60-65 °C as a function of time.

In this test the PEFC was restricted to operating at voltages greater than about 650 mV and thus in the cell operating region characterised by useful electrical efficiencies and low heat generation. Over this period of time the membrane resistance increased only by

about 0.5 %/100 h, qualitatively indicating that the loss of proton-conducting groups has not been too extensive.

More recently, we have begun tests under similar operating conditions at higher temperatures. An example of a long-term test currently in progress at 80 °C is shown in Figure 3. The membrane resistance does not exhibit any large-scale changes indicating that the membrane remains fairly stable during the first 2500 hours of this experiment. First tests of PSI ETFE-based membranes in a two graphite cell stack (100 cm^2 active area each cell) indicate that the cell currents and voltages do not exhibit any large-scale changes either over a testing period of about 1,000 h. This relatively stable behaviour indicates that significant membrane degradation leading to loss of the proton-conducting graft component has not occurred in this test.

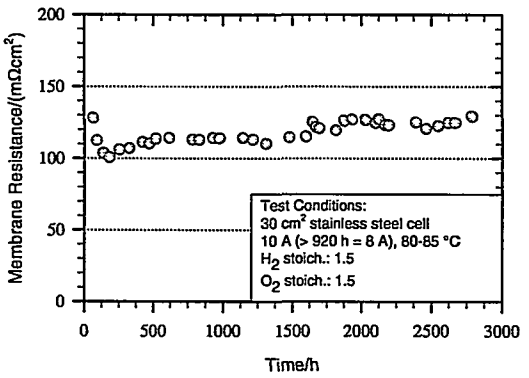

Fig. 3: *In-situ* membrane resistances of double crosslinked PSI-membranes (based on FEP 75 µm) at 80-85 °C as a function of time.

Post-mortem membrane analysis by means of FTIR or FT-Raman spectroscopy indicates that membrane degradation is limited to the sulfonated polystyrene-based graft component in both FEP-based [4] or ETFE-based membranes (Figure 4). The bands that are assigned to the sulfonated polystyrene graft component (Figure 4c) diminish in intensity in the case of uncrosslinked membranes over long periods of testing in fuel cells (Figure 4d). The membrane lifetime is limited to an increasing membrane resistance due to a loss of the sulfonated polystyrene-based graft component. It is important to note that in some of our present cell and stack designs, mechanical breakage of the membrane during cell operation can be a problem with either thinner Nafion membranes or the thinner PSI *crosslinked* radiation-grafted membranes. In these cases, mechanical failure, probably due to swelling stresses near the active area (swollen membrane) /gasket (non-swollen) border in the PEFC often seem to be solely responsible for the membrane failure. Future research efforts will be devoted to improving the mechanical properties and chemical stability of our membranes even further.

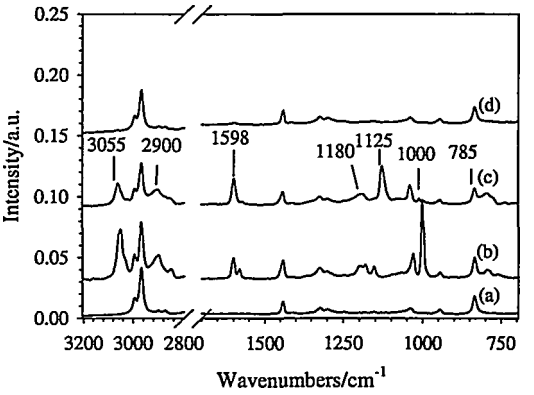

Fig. 4: FT-Raman Spectra: (a) 100 µm ETFE film, (b) uncrosslinked grafted film, (c) untested uncrosslinked membrane, and (d) tested active area of uncrosslinked membrane.

4 CONCLUSION

Operating lifetimes of several thousands of hours time at different operating temperatures were demonstrated in single 30 cm^2 active area stainless steel fuel cells and for one thousand hours in a graphite two cell stack (100 cm^2 active area each cell). These results demonstrate that PSI radiation-grafted proton-conducting membranes could be a viable alternative membrane for mobile PEFC applications. We are currently examining ways to further improve the mechanical properties of our crosslinked membranes and our cell and stack designs.

5 ACKNOWLEDGEMENTS

Financial support for this work by the Swiss Federal Office of Energy (BFE) and electron beam irradiation by Mr. C. Günthard of Studer AG, CH-4658 Däniken are gratefully acknowledged.

6 REFERENCES

[1] F.N. Büchi, B. Gupta, O. Haas, G.G. Scherer, *Performance of Differently Cross-Linked, Partially Fluorinated Proton Exchange Membranes in Polymer Electrolyte Fuel Cells*, J. Electrochem. Soc. **142**, 3044-3048 (1995).

[2] F.N. Büchi, A. Marek, G.G. Scherer, *In-situ Membrane Resistance Measurements in PEFC by fast Auxiliary Current Pulses,* J. Electrochem. Soc. **142**, 1895-1901 (1995).

[3] H.P. Brack, F.N. Büchi, J. Huslage, G.G. Scherer, *Recent progress in the Development of the Radiation-Grafted PSI Membrane*, Proc. books, 194th ECS Fall Meeting 1998, MA USA..

[4] F.N. Büchi, B. Gupta, O. Haas, G.G. Scherer, *Study of Radiation-Grafted FEP-g-Polystyrene Membranes as Polymer Electrolytes in Fuel*, Electrochim. Acta **40(3)**, 345-353 (1995).

TOUGHNESS OF MEMBRANES APPLIED IN POLYMER ELECTROLYTE FUEL CELLS

J. Kiefer, H.P. Brack, G.G. Scherer

Since several years we apply the radiation-grafting technique to prepare polymeric membranes for application in polymer electrolyte fuel cells (PEFCs). Our investigations presented here focus on changes in toughness of these materials after the various synthesis steps and the importance of membrane toughness for their application in PEFCs.

1 MOTIVATION

The strategy of the radiation-grafting technique consists of first irradiating a base polymer film to generate active radicals. In a subsequent step grafting with a radically polymerizable monomer such as styrene is carried out while optionally performing crosslinking reactions *in-situ*. This yields grafted films which are subsequently sulfonated by reaction with chlorosulfonic acid to achieve a proton conducting membrane [1-3].

Besides important factors such as design of flow field, water management, catalyst loading, membrane-electrode assembly and others, the functional properties of the membrane such as proton conductivity, chemical stability and low gas permeability are predominant to yield a high power density of one single cell. Very recently we have successfully demonstrated that our crosslinked PSI-membranes which satisfy the electrochemical requirements display a life time up to 10.000 h at constant operating conditions in a cell with an active area of 30 cm^2 [4]. To enter industrial applications, the size of the active area has to be increased and dozens or even hundreds of cells must be connected in series to give stacks capable of delivering electrical power in the multi kW-range. In such a scenario the mechanical properties of the membrane become important, because mechanical failure of one single membrane will require to shut down the entire stack. Therefore it is of utmost importance to guarantee for the reliability of the membrane in the application.

The toughness describes qualitatively the ability of the material to absorb energy upon deformation and is most likely suitable as a selection criterion for the mechanical properties of grafted films and membranes. A high toughness of grafted films and membranes is highly desirable (i) to allow for their handling during and after the various preparation steps and (ii) to withstand stresses encountered during the application of membranes in PEFC stacks. A high toughness is of particular importance in fuel cells, where stresses are generated owing to the swelling of the membrane in water. The water swelling ability of the membrane is necessary to achieve a desired level of proton conductivity. On the other hand swelling leads to volume changes which in turn create internal stresses. Owing to the cell design a water concentration gradient exists at the boundary between the active area where the membrane remains hydrated, and the gasket where external humidification cannot be carried out. It is at this boundary where we observe in some of our cell and stack designs mechanical failure particularly if membranes less than around 100 µm in thickness are used.

It was therefore our objective to measure the toughness of grafted films and membranes and explore a method for toughness enhancement to prevent premature failure.

2 EXPERIMENTAL

The toughness of grafted films and membranes has been determined by tensile testing measurements. A Mecmesin E100 universal testing machine equipped with a load cell of 10N or alternatively 500N (depending on sample thickness and strength) was used. The deformation rate was controlled by the crosshead speed set at 6 mm/min. Dumbbell-type specimens ($b = 3$ mm, $l_0 = 5$ mm) were prepared using a punching tool with appropriate dimensions. The toughness is then taken as the area under the load-displacement curve until the start of unstable crack propagation.

3 TOUGHNESS OF UNCROSSLINKED GRAFTED FILMS AND MEMBRANES

Besides the evaluation of absolute values for toughness, it is interesting to note the change in the deformation behaviour, which takes place after the various preparation steps starting from the base polymer film to the grafted film and finally yielding the proton conducting membrane (Figure 1).

The deformation behaviour of the base polymer film (line a in Figure 1) and the uncrosslinked grafted film (line b in Figure 1) are both typical for semicrystalline polymers below their glass transition temperature. It is clearly seen that the incorporation of stiff polystyrene side chains leads to a decrease in elongation at break and toughness. However the yield strength, where extensive plastic deformation starts is higher in the grafted film. At the yield point, the grafted film shows a typical necking which involves strain softening followed by strain hardening prior to the fracture of the grafted film.

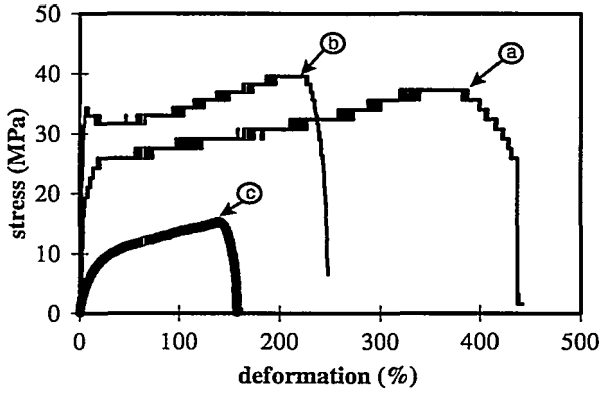

Fig. 1: Typical stress-deformation curves of a) base polymer film, b) uncrosslinked grafted film and c) uncrosslinked membrane of identical degree of grafting prepared via the radiation-grafting technique.

A completely different deformation behaviour is observed for membranes (line c in Figure 1), which are tested in the wet state after equilibrating in water at room temperature. Uncrosslinked membranes do obey a non-linear deformation behaviour, which is typical for viscoelastic materials such as amorphous or plasticized polymers. Upon deformation, membranes become softer and can be deformed very easily. This is due to the presence of a plasticizer, in our case water. The water interacts with the sulfonated groups attached to the styrene units in the grafted side chains. This renders the previously brittle and stiff side chains highly flexible and allows for large deformation at low stress levels. Such a behaviour is highly desirable for application in fuel cells.

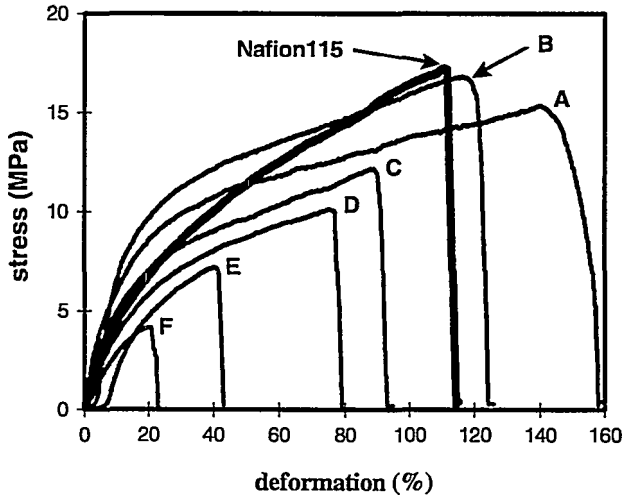

Fig. 2: Deformation behaviour of uncrosslinked membranes prepared via the radiation-grafting technique with various graft levels (increasing from A to F) in comparison to commercial Nafion®115.

Our studies also demonstrated how the mechanical properties of grafted films and membranes depend on the degree of grafting. Careful adjustment of reaction parameters allows us to vary the degree of grafting and hence to mimic the deformation behaviour of commercial Nafion®, which is widely used in the fuel cell technology and known to exhibit sufficient toughness for the application (Figure 2).

4 TOUGHNESS OF CROSSLINKED MEBRANES

We have found previously [2,3], that crosslinking is necessary to improve the life time of the membranes. However tensile testing measurements demonstrated that crosslinking is also to the expense of toughness and a brittle deformation behaviour is typically observed. Such a deformation behaviour is very undesirable for any application where reliability is an absolute necessity, because such brittle materials, like glass, ceramics or other highly crosslinked polymers, suffer from a considerable experimental error and it becomes difficult to predict their failure. Ongoing investigations are dedicated to explore ways to prepare crosslinked membranes with enhanced toughness in order to prevent premature failure. Such toughness enhancement must be performed without altering the other desired functional properties of the membranes. Preliminary experiments attempting to modify the grafting process in order to reduce the build-up of internal stresses without requiring any modifications in chemical reagents gave promising results. As a consequence we have designed new reaction vessels aiming for a batchwise production of crosslinked membranes with larger sizes and enhanced toughness thus enabling for their application in fuel cell stacks.

5 CONCLUSION

The application of membranes in PEFC stacks requires a high membrane toughness to ensure for a reliable operation. Tensile testing were used to determine mechanical properties as a function of graft level. Our research will now focus on improvements in the membrane preparation technique with the objective to allow for the batchwise preparation of crosslinked membranes with enhanced toughness.

6 REFERENCES

[1] H.P. Brack, G.G. Scherer, Macromol. Symp. **126**, 25 (1997).

[2] F.N. Büchi, B. Gupta, G.G. Scherer, European Patent 0 667 983.

[3] F.N. Büchi, B. Gupta, O. Haas, G.G. Scherer, Electrochem. Soc. **142**, 3044 (1995).

[4] J. Huslage, H.P. Brack, F.N. Büchi, G.G. Scherer, Article in this volume.

CONDUCTIVITY STUDIES ON COMMERCIALLY AVAILABLE PROTON-CONDUCTING MEMBRANES WITH DIFFERENT EQUIVALENT WEIGHT

J. Huslage, F.N. Büchi, G.G. Scherer

Two perfluorosulfonic acid membranes, Nafion® 105 and Nafion® 115 with the same thickness but different equivalent weights (EW = 1000 g/eq. resp. 1100 g/eq.) were characterised by conductivity measurements at different water vapour activities in the temperature range of 25-70 °C. The results demonstrate that a lower membrane equivalent weight opens the possibility to obtain the needed proton conductivity at lower water vapour activity. This is especially important for those fuel cell applications, in which the cell is operated without external humidification of the fuel gases.

1 INTRODUCTION

Proton-conducting membranes are used as electrolyte in low-temperature polymer electrolyte fuel cells (PEFC). For this application the most important requirements of the membranes are: (1) high proton conductivity, (2) low gas permeation of the reactant gases, (3) long term chemical, thermal, and mechanical stability (≥ 3000 hours), (4) low cost, and (5) environmentally benign production and disposal.

Fuel cell performance strongly depends on the conductivity of the membrane, which is strongly dependent on its water content [1,2] and the cell temperature. For an optimisation of fuel cell performance, the hydration properties of the membranes have to be understood. This is especially important, if the cell is operated without external humidification of the reactant gases.

Due to their chemical stability perfluorinated sulfonic acid membranes are the most common type of PEFC membranes. One well known example is the Nafion® membrane series from DuPont, whose formula is shown in Figure 1 [3]. This series differ with respect to thickness and/or equivalent weight. In the present work, the conductivity of the Nafion® 105 and 115 membranes, having the same thickness (150 µm, dry) but different equivalent weight (EW = 1000 and 1100 g/eq., respectively), were investigated in dependence of the water vapour activity in the adjacent gas phase.

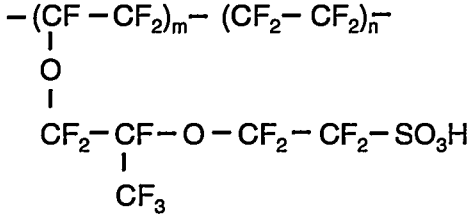

Fig. 1: Structure of Nafion®.

2 EXPERIMENTAL

The membranes were first pre-treated for 1 h in a 30-35 %w solution of 65 % nitric acid at 90 °C followed by swelling in boiling water for 1 h. Next the membranes were equilibrated for ten days at different water vapour activities (equilibration temperature 20 °C). The temperature dependence of the membrane conductivity was determined by impedance measurements (Zahner IM6). The cell design allowed to control the mechanical force used to compress stacks of variable number of membranes. The cell was sealed so that the water content did not change during the heating and cooling cycle. Platinum discs were used to contact the membrane stack. The resulting dc-resistance was corrected for the contact resistance [4].

3 RESULTS AND DISCUSSION

The dependence of the membrane hydration level (H_2O/SO_3H, determined by titration and gravimetric measurements) on the water vapour activity, used for equilibration at 20 °C, is shown in Figure 2. The hydration level of the Nafion® 105 membrane is higher than that of the Nafion® 115 membrane over the whole range of water vapour activity investigated.

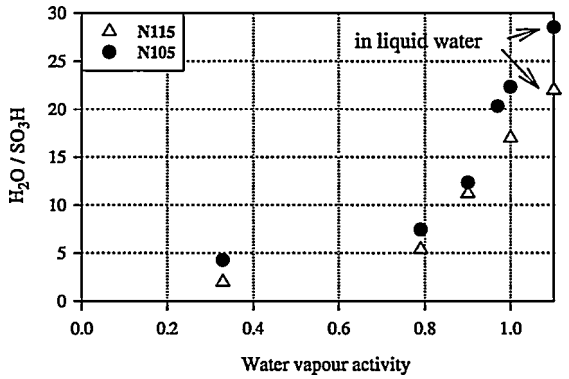

Fig. 2: Water content of Nafion® 105 and Nafion® 115 membranes as a function of water vapour activity at 20 °C.

As a result the Nafion® 105 membrane shows up to 50 % higher specific conductivity values (Figure 3) as compared to the Nafion® 115 membrane under the same humidification conditions. This higher conductivity is due to the higher water uptake of the Nafion® 105 membrane and hence higher proton mobility which results from its lower equivalent weight [4]. The specific conductivity of both membranes decreases strongly if the water vapour activity is lowered from

1.00 to 0.78. This result clearly demonstrates the strong influence of the humidification atmosphere on the membrane conductivity and, therefore, on the expected fuel cell performance.

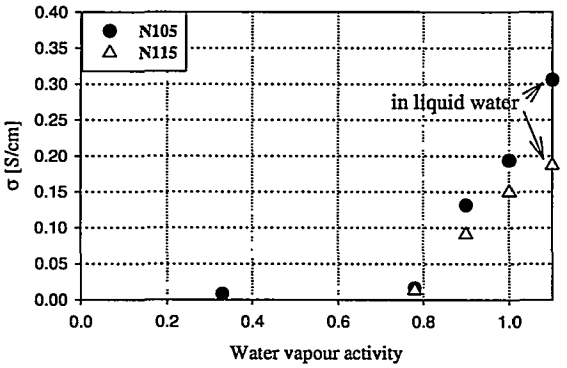

Fig. 3: Specific conductivity of Nafion® 105 and Nafion® 115 membranes at 70 °C as a function of water vapour activity (20 °C).

The specific conductivities of Nafion® 105 and Nafion® 115 membranes at temperatures of 25, 50, and 70 °C are plotted vs. the hydration level (equilibrated at different water vapour activities at 20 °C) in Figure 4 and 5.

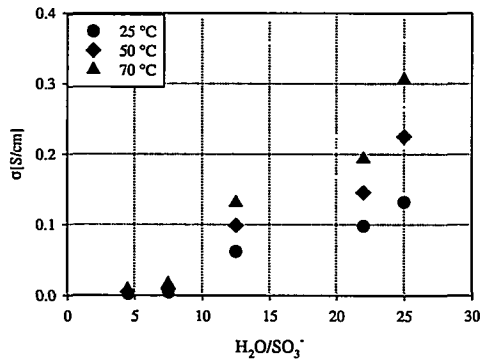

Fig. 4: Specific conductivity of Nafion® 105 as a function of water content.

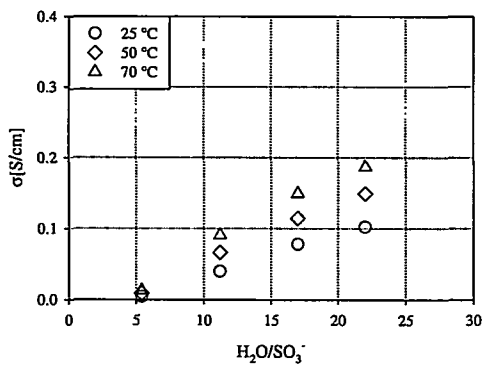

Fig. 5: Specific conductivity of Nafion® 115 as a function of water content.

At hydration levels above 5 H_2O/SO_3H the conductivity increases strongly with increasing water content. The conductivity of the Nafion® 115 membrane increases approximately linearly up to a water content of 22 H_2O/SO_3H. The same is observed for the Nafion® 105 membrane, but up to 25 H_2O/SO_3H. Below hydration levels of about 5 H_2O/SO_3H there is no significant proton conductivity for both types of membranes. It is interesting to note that at the *same* hydration level the specific conductivity of both membranes is comparable.

4 CONCLUSION

Our measurements show that for Nafion® 105 and Nafion® 115 a hydration level ≥12 H_2O/SO_3H is necessary to obtain a proton-conductivity (>0.1 S/cm at 70 °C) high enough for acceptable fuel cell performance. Consequently, these membranes have to be in contact with a gaseous atmosphere of high water vapour activity (>0.8) or even better partially with liquid water. A lower membrane EW opens the possibility to obtain higher hydration levels and, as a consequence, higher proton conductivity at a comparable water vapour activity in the adjacent gas phase. The obtained results are useful as a fundamental set of data for *in-situ* membrane humidification studies [5].

5 ACKNOWLEDGEMENTS

Financial support from the Swiss Federal Office of Education and Science (BBW) for this work as part of the program *„2nd Generation SPFC"* of the EU-research program *„Joule III"* is gratefully acknowledged.

6 REFERENCES

[1] T.A. Zawodzinski Jr., C. Derouin, S. Radzinski, R.J. Sherman, V.T. Smith, T.E. Springer, S. Gottesfeld, *Water Uptake by and Transport Through Nafion® 117 Membranes,* J. Electrochem. Soc. **140**, 1041-1047 (1993).

[2] K.D. Kreuer, *On the Development of Proton Conducting Materials for Technological Applications,* Solid State Ionics **97**, 1-15 (1997).

[3] W.G. Grot, *Perfluorinated Ion Exchange Polymers and their Use in Research and Industry,* Macromol. Symp. **82**, 161-172 (1994).

[4] J. Halim, F.N. Büchi, O. Haas, M. Stamm, G.G. Scherer, *Characterisation of Perfluorosulfonic Acid Membranes by Conductivity Measurements and Small-Angle X-Ray Scattering,* Electrochimica Acta **39**, 1303-1307 (1994).

[5] F.N. Büchi, G.G. Scherer, *In-Plane Resolved In-Situ Measurements of the Membrane Resistance in PEFCs,* PSI Annual Report, Annex V (1998).

IN-PLANE RESOLVED *IN-SITU* MEASUREMENTS OF THE MEMBRANE RESISTANCE IN PEFCs

F.N. Büchi, G.G. Scherer

The conductivity of the membrane is a limiting factor for the efficiency and power density of PEFCs. Because this conductivity is strongly dependent on the membrane hydration, water management is an important aspect of PEFC optimisation. Single cell model experiments were made in order to determine the in-plane hydration of a Nafion® membrane under fuel cell conditions as function of the gas humidities.

1 INTRODUCTION

In Polymer Electrolyte Fuel Cells (PEFCs) a low resistance of the electrolyte is one of the key parameters for attaining high power density and efficiency. The conductivity of the Nafion® membranes, the most commonly used membrane material, is a strong and monotonous function of the membrane water content. Therefore, the water management, aiming at retaining a maximum water content in the membrane during operation, is one of the key parameters in the optimisation of PEFCs.

A number of modelling approaches for the water management with respect to the hydration of the membrane during fuel cell operation are available in the literature [1], however only little experimental data is accessible. We have previously studied the hydration of Nafion® membranes in 1-dimensional cells by using membranes composed from several thin sheets with interlaying thin gold wires as potential probes [2]. This technique allowed for determination of the water profile across the membrane thickness. We have now employed the same technique to measure the differences of membrane hydration with respect to the *in-plane* location in the fuel cell.

2 EXPERIMENTAL

H_2/O_2 fuel cells with a graphite cell body and a channel type flow field with 28 cm^2 active area were employed. For the membrane electrode assembly E-Tek electrodes (0.6 mg/cm^2 Pt) and two Nafion® 117 membranes were used. Between the membranes two 25 µm gold wires were inserted at the position of the gas inlets and outlets of the flow field, as shown in Figure 1. Two more gold wires were inserted between cathode and membrane in the same location. This set-up allows for measuring the resistance of both membranes at the two locations with the auxiliary current pulse technique [3]. By comparison of the resistance with values determined *ex-situ*, the membrane hydration may be calculated. All experiments were conducted at 1 bar_a gas pressures and the gases were fed in the counter flow mode.

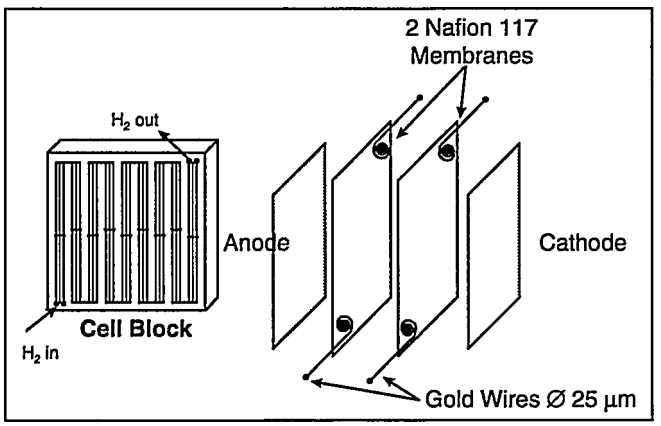

Fig. 1: Experimental set-up of the measurement for the in-plane resolved membrane resistance.

3 RESULTS

In cells with a gas flow field, in which the gases flow in a channel along the surface of the electrode backing, volume flow, temperature and humidity of the gases vary along the flow path. Therefore differences in membrane hydration also occur with respect to the *in-plane* location of the MEA. With respect to the width of the channel the parameters in the MEA are assumed to be homogeneous, therefore the cell is quasi 2-D (dimensions parallel to flow and across membrane) and may be represented by a single channel as shown in the top of Figure 2.

When both gases, hydrogen and oxygen, are humidified to a dew-point which is at least as high as the cell temperature, the MEA is in a well humidified condition. As shown in the lower part of Figure 2, the hydration states of the anode and cathode side membranes are similar at both ends of the channel when no current is drawn form the cell. A constant membrane hydration of λ = 12-14 H_2O/SO_3H is calculated from the resistance measurements. When a current of 0.5 A/cm^2 is drawn from the cell, then the anode side membrane is drying and an average water content of this membrane of 7-8 H_2O/SO_3H is observed. At the cathode side of the membrane no changes in hydration with current density are detected. No significant differences of the membrane hydration between the gas-inlets and gas-outlets are observed, indicating that the membrane hydration is uniform over the entire active area under these well humidified conditions.

When dry hydrogen is supplied at a volumetric flow rate corresponding to a 6 fold excess (matching an air stoichiometry of 2), then a similar behaviour of the membrane hydration is observed as in the fully humidified case: the membrane hydration is almost identical at both ends of the channel, however when current is drawn from the cell, then the anode side mem-

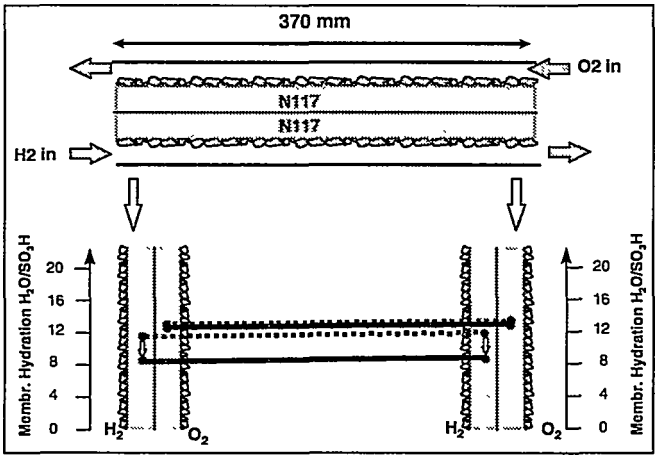

Fig. 2: Top: Schematic drawing of the measured membrane hydration at two different in-plane locations. Bottom: Profile of hydration of the anode (H2) and cathode (O2) side membranes along the channel (dotted line at 0 A/cm^2; solid line at 0.5 A/cm^2) at T_{cell} = 60 °C, hydrogen and oxygen humidified at 80 °C. H_2: 6x stoichiometric flow; O_2 10x stoichiometric flow.

brane is drying more severely than in the fully humidified case as shown in Figure 3. At a current density of 0.5 A/cm^2 the hydration drops to λ = 4-5 instead of 7-8 H_2O/SO_3H in the fully humidified case and the hydration at the H_2 inlet is slightly less than at the H_2 outlet with $\Delta\lambda \approx$ 1-2.

When oxygen is fed dry at a volumetric flow rate (10 x stoichiometric) which is representative for operation with air and hydrogen is humidified, then a more complex membrane hydration behaviour is observed as shown in Figure 4. At the ending of the channel, where oxygen is entering dry, the membrane at the cathode side is dry ($\lambda \approx$ 6). The anode side membrane in this location however is well humidified ($\lambda \approx$ 20). Probably because of the strong water gradient across the membrane, water is diffusing readily into the anode side membrane from the hydrogen gas phase. At the other end of the channel humidified hydrogen is entering

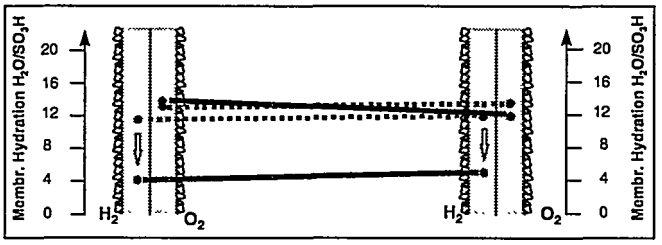

Fig. 3: Profile of membrane hydration at the same conditions as in Figure 2, except : hydrogen dry and oxygen humidified at 80 °C.

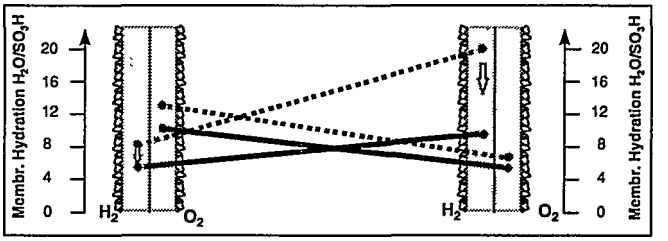

Fig. 4: Profile of membrane hydration at the same conditions as in Figure 2, except hydrogen humidified at 80 °C and oxygen dry.

and the oxygen has become humid due to the product water. Therefore at this end of the channel the difference in membrane water content is smaller. Again when current is drawn from the cell, the major change is observed in the anode side membrane, which becomes dryer as observed in earlier work [1] and in Figure 2. When the cell is operated with dry oxygen, then gradients of membrane hydration across the active area evolve.

The present results show, that the membrane hydration in our model system is more sensitive to the humidity of the cathode gas than to the humidity of hydrogen. This work provides a qualitative understanding of the hydration of the membrane under fuel cell conditions when the gases are not fully humidified. The quantitative understanding of this observation will need more work of locally resolved resistance measurements within the active area of the cell.

4 ACKNOWLEDGEMENT

Financial support from the Swiss Federal Office of Education and Science (BBW) for this work, carried out under the program "2nd Generation SPFC" of the EU-research program "Joule III", is gratefully acknowledged.

5 REFERENCES

[1] T.E. Springer, T.A. Zawodzinzki, S. Gottesfeld, *Polymer Electrolyte Fuel Cell Model,* J. Eletrochem. Soc., **138**, 2234-2342 (1991); T.F. Fuller, J. Newman, *Water and Thermal Management in Solid-Polymer-Electrolyte Fuel Cells*, J. Electrochem. Soc., **140**, 1218-1225 (1993).

[2] F.N. Büchi, G.G. Scherer, *Determination of In-situ Water Profiles in Polymer Electrolyte Fuel Cell Membranes*, PSI Annual Report 1997, Annex V, 48-49 (1997).

[3] F.N. Büchi, A. Marek, G.G. Scherer, *In-situ Membrane Resistance Measurements in PEFC by fast Auxilliary Current Pulses,* J. Electrochem. Soc., **142**, 1895-1901 (1995).

CO TOLERANCE OF POLYMER ELECTROLYTE FUEL CELLS

L. Gubler, G.G. Scherer, A. Wokaun

Reformed methanol can be used as a fuel for polymer electrolyte fuel cells instead of pure hydrogen. The reformate gas contains mainly H_2, CO_2 in the order of 20 % and low levels of CO in the order of 100 ppm. CO causes severe voltage losses due to poisoning of the anode catalyst. The effect of CO on cell performance was investigated at different CO levels up to 100 ppm. Various options to improve the CO tolerance of the fuel cell were assessed thereafter, of which the injection of a few percents of oxygen into the fuel feed stream proved to be most effective. By mixing 1 % of oxygen with hydrogen containing 100 ppm CO, complete recovery of the cell performance could be attained.

1 INTRODUCTION

Polymer electrolyte fuel cells (PEFC) are considered as potential power sources for electric vehicles of the future due to their high power density (~1 kW/L) and low operation temperature (60-80 °C), which enables a rapid start-up. Conventionally, PEFCs are operated with pure hydrogen as a fuel. The storage of *on-board* hydrogen is, however, unsuitable because of the low volumetric energy density of compressed H_2-gas. Therefore, methanol as a liquid fuel is preferred. It can be stored *on-board* like gasoline in a tank.

The methanol is converted to a H_2-rich fuel gas for the PEFC in a catalytic fuel processor at around 300 °C. The obtained reformate gas contains CO in the order of 1 to 3 %. With this reformate fuel the performance of the PEFC would suffer severe degradation due to reversible poisoning of the Pt electrocatalyst by adsorption of CO, impeding thereby H_2-electrooxidation.

One approach to tackle this problem consists in additional CO clean-up systems between the reformer and the fuel cell, yielding CO-levels between 0 and 100 ppm. In addition, the CO tolerance of the PEFC is critical and needs to be improved. A PEFC running on reformate should be able to tolerate 10 ppm continuously and 100 ppm in transient operation. In this work, different methods for an improved CO tolerance were identified and assessed.

2 EFFECT OF CO

The effect of CO on fuel cell operation has been extensively investigated by various groups (e.g. [1]). In all cases, a severe drop in cell performance was observed at CO contents in the order of only 100 ppm. In a first series of measurments, these results were reproduced in a 1-dimensional fuel cell already described previously [2], which yields an uniform current distribution. The electrodes comprised pure Pt as electrocatalyst with a loading of 0.6 mg/cm^2. Reactant gases were dry hydrogen, with CO concentration ranging from 0 to 100 ppm, and dry oxygen. The cell was operated at a constant current of 100 mA/cm^2 until stable operation was attained before polarization data was recorded (Figure 1). The operation voltage of a fuel cell should be between 0.6 to 0.8 V to assure a high conversion efficiency. A significant increase in CO tolerance is therefore required in this region.

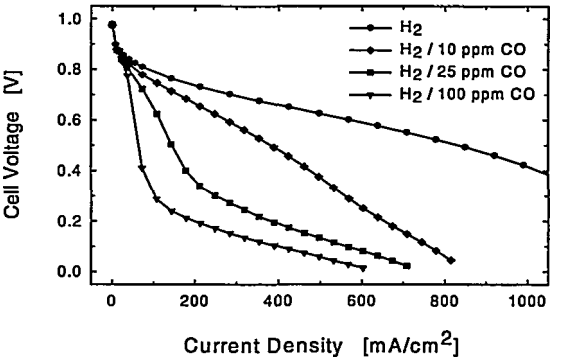

Fig. 1: Dependence of the cell performance on CO content at 60 °C and 1 bar$_a$. Membrane: Nafion® 115, Electrodes: E-TEK 0.6 mg/cm^2 Pt.

3 METHODS TO IMPROVE THE CO TOLERANCE

To improve the CO tolerance of the PEFC, different options were identified from individual methods documented in the literature:

a) increase of cell temperature

b) use of electrocatalysts with a higher CO tolerance

c) *in-situ* CO oxidation

d) adequate cell design

The specific novelty of the approach presented here is that these methods are all investigated in parallel under the same conditions. Therefore, direct comparison can be made and the methods assessed quantitatively.

a) First, the influence of a higher cell temperature was investigated. To prevent drying out of the membrane, the operating pressure was raised to 3 bar$_a$. As a measure for CO tolerance, the ratio q of the current density obtained with CO present in the fuel stream and the current density measured with pure H_2 at a cell voltage of 650 mV was calculated using the measured polarization curves (Table 1).

Temp. / °C	60	60	70	80
Press. /bar_a	1	3	3	3
CO tolerance q	0.12	0.19	0.32	0.40

Table 1: CO tolerance q for H_2 / 100 ppm CO as a function of operation temperature and pressure.

Evidently, the CO tolerance at higher temperature is substantially enhanced.

b) In the second approach investigated, the intrinsically more CO tolerant electrocatalyst PtRu was used at the anode (loading: 0.6 mg/cm^2) instead of pure Pt. The CO tolerance q was again calculated and compared to the values obtained with pure Pt (Table 2).

ppm CO	10	25	50	100
q with Pt	0.50	0.23	0.16	0.12
q with PtRu	**0.41-1.00**	0.30	0.25	0.21

Table 2: CO tolerance q as a function of CO content and anode electrocatalyst at T = 60 °C and 1 bar_a.

At CO levels of 25 ppm and more the PtRu catalyst shows only a slightly enhanced performance. Repeated measurements with 100 ppm CO showed a good reproducibility of the results. Various measurments with 10 ppm CO and PtRu showed that the performance fluctuated strongly, depending on the operation history of the electrode. Sometimes, complete tolerance was observed (q = 1.00).

c) It was shown already a decade ago by Gottesfeld and Pafford that the addition of small amounts of oxygen to the fuel stream prior to the inlet of the fuel cell is an effective means to recover the cell from poisoning by CO [1]. We investigated this method using both Pt and PtRu with equal loading as anode electrocatalysts. The current density at a cell voltage of 650 mV was measured for H_2 / 100 ppm CO and pure hydrogen as a funtion of O_2-content of the fuel (Figure 2). One result is that the oxygen obviously does not affect the fuel cell performance if pure hydrogen is used as fuel. However, with H_2 / 100 ppm CO one observes a sharp drop in current density if the amount of O_2 in the fuel is decreased below a certain level. An important result is the fact that with PtRu only half the oxygen is required to fully restore the performance to the value obtained with pure H_2. Continuous operation over 180 h on H_2 / 100 ppm CO and 1 % O_2 with a PtRu-anode showed

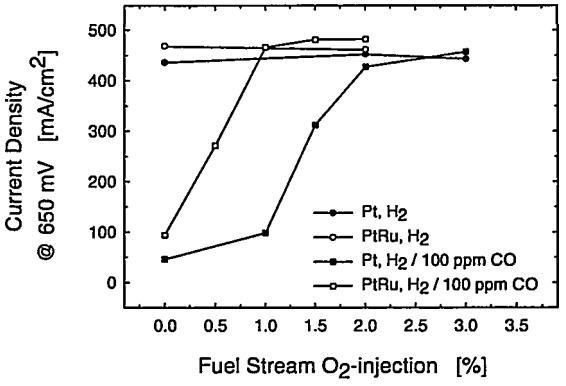

Fig. 2: Injecting low levels of O_2 into the fuel stream.

stable performance at 94 % of the current density of pure H_2.

d) The structure of the electrode and design of the fuel cell or fuel cell stack is of great importance for the CO tolerance. In the forthcoming period, this aspect will be investigated in detail. For example, an anode comprising a deliberate gas phase catalyst layer is expected to be even more susceptible for the O_2-injection technique [3].

In addition, the effect of CO_2, which makes up about 20 % of the volume of the reformate gas, and the humidification of the CO contaminated fuel gas will be studied.

4 CONCLUSION

Of the different methods explored, the injection of O_2 into the fuel stream was found most effective, especially when combined with the use of a PtRu-anode. 100 ppm CO in H_2 could be tolerated in long term operation. Without O_2, 10 ppm CO could be tolerated, but not permanently. The performance depended strongly on the operation history of the fuel cell.

5 ACKNOWLEDGEMENT

Funding by the Alliance for Global Sustainability (AGS) is gratefully acknowledged.

6 REFERENCES

[1] S. Gottesfeld, J. Pafford, J. Electrochem. Soc. **135**, 10, 2651-2652 (1988).

[2] F.N. Büchi, J. Huslage, G.G. Scherer, PSI Annual Report 1997 / Annex V, 48-49 (1997).

[3] D.P. Wilkinson, D. Thompsett, Proc. Second International Symposium on New Materials for Fuel Cell and Modern Battery Systems, Montreal, 266-285 (1997).

MINIATURIZED POLYMER ELECTROLYTE FUEL CELL (PEFC) STACK USING MICROSTRUCTURED BIPOLAR PLATE

Z. Veziridis, G.G. Scherer, Ch. Marmy, F. Glaus

In Polymer Electrolyte Fuel Cell (PEFC) technology the reducing of volume and mass of the fuel cell stack and the improvement of catalyst utilization are of great interest. These parameters affect applicability and system cost. In this work we present an alternative way for reducing the stack volume by combining gas distribution and catalytic active area in one plate. Micromachined glassy carbon electrodes serve as support material for the platinum catalyst, as well as gas distributer at the same time. A comparison of these electrodes with conventional platinum-black gas diffusion electrodes under fuel cell conditions shows that the new system is a promising electrode type for enhanced power density and catalyst utilization.

1 INTRODUCTION

One of the most promising technologies to be used in the future as power converters for transport and stationary applications is the polymer electrolyte fuel cell (PEFC) technology. Over the past few years considerable progress has been made in lowering the system cost necessary to compete with internal combustion engine technology [1]. The specific power and the power density targets for fuel cell stacks are 1 kW/kg and 1 kW/L, respectively, at a long range cost target of less than 50 DM/kW for the automotive application [2]. The stack cost mainly depends on the three key components: (i) the membrane electrolyte, (ii) the electrodes and (iii) the flow field plate. Progress in improving electrode performance and catalyst utilization, for example, has been achieved by localising the Pt-catalyst within a thin layer on top of the gas diffusion structure [3]. A brief review of improvements in electrode, membrane and flow field plate development is given by T. Ralph [4]. However, for successful commercialisation all aspects of fuel cell development have to be further investigated.

In cells of standard design three regimes of porosity are located on both sides of the membrane electrolyte. These are the electroactive layer, the gas diffusion layer and the gas-distribution channels within the bipolar plate. The aim of this work is to evaluate a new method to increase the specific power and power density on one side and catalyst utilization on the other side at the same time. The idea is to achieve this progress by integration of electrode and bipolar plate into one component, hence, locate the electroactive layer, e.g., platinum, on top of microstructured bipolar plates and contact these directly to the polymer electrolyte surfaces, thus avoiding the gas diffusion structure.

The prototype of this new fuel cell stack arrangement consists of microstructured glassy carbon electrodes. A micromachining process, described earlier [5], creates a comb-like structure on top of glassy carbon plates. This structure has a well defined geometric surface area with a high aspect ratio close to ten. Preliminary fuel cell results using these platinized microstructured electrodes will be reported and compared to results based on the use of conventional Pt-black gas diffusion electrodes in the same cell. Catalyst utilization and application limits of these new components will be discussed.

2 EXPERIMENTAL

Glassy carbon (GC) plates (1x1 cm^2, HTW, D-86672 Thierhaupten) were microstructured by a rotating wafer blade microsaw (Disco Corp., Japan), to obtain a "comb-like" surface structure. Typical dimensions for the channels and ridges are a depth of 150 µm and a width of 20 µm, respectively, thus yielding a total surface area of 8.5 cm^2 per cm^2 geometric area. In order to create a "bipolar plate" the surfaces on both sides of the plate were structured (Figure 1). Other surface topographies, e.g., "column patterns" are possible. Platinum deposition onto the top of these structures was carried out by plating from a 0.05 M Hexachloroplatinic acid solution at room temperature, applying a current of 10 mA.

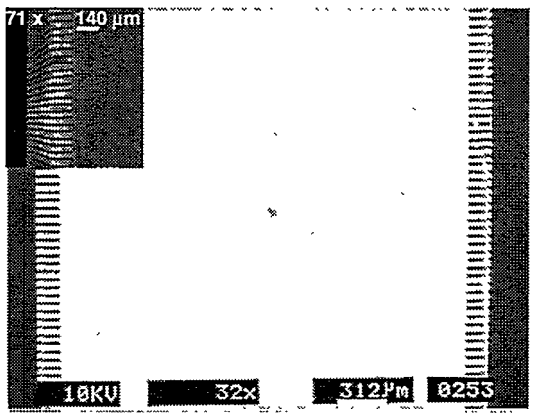

Fig. 1: SEM-image of a cross section through the microstructured bipolar plate with close up view.

Pt-black gas diffusion electrodes (E-TEK corp., USA) with a platinum loading of 1.8 mg/cm^2 were used as the standard to be compared with platinum covered glassy carbon electrodes. The active platinum surface area of the microstructured and the gas diffusion electrode in the fuel cell arrangement, as determined by cyclic voltammetry, was 120 cm^2 and 250 cm^2, respectively. A Nafion®-117-membrane was used as the

polymer electrolyte. Fuel cell experiments were carried out in a stainless steel housing (316-L-steel) with an active area of 1 cm^2 (Figure 2). The operation parameters were as follows:

Cell temperature, pressure:	25 °C; ambient pressure
Gas flow:	H_2/O_2; 10 ml/min
Humidification:	H_2 at 60 °C

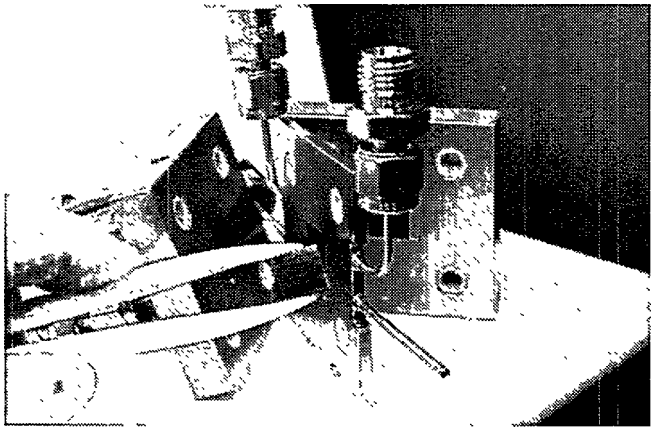

Fig. 2: Two-cell stack housing containing microstructured electrodes and bipolar plate.

3 RESULTS AND DISCUSSION

The first result of a two cell "microstructure" stack with an active area of 1 cm^2 is displayed in Figure 3. The current-voltage curve of this stack is compared with the one of a two cell stack comprising conventional E-TEK electrodes. At a stack voltage of 1 V current densities of 200 and 600 µA/cm^2 active platinum area are determined, respectively. The latter value is based on the active area of 250 cm^2 per cm^2 geometric area determined by cyclic voltammetry. If one takes into account the "true" active area of these platinum black electrodes (500 cm^2/cm^2), as specified by the supplier, the respective current density is 300 µA per cm^2 of active Pt-area. This platinum utilization factor would only be 1.5 times higher than the one obtained with microstructured electrodes. In this context one has to discuss the platinum deposition on top of the microstructured surface. It is assumed that platinum is mainly deposited on top of the ridges due to the current distribution under the used deposition conditions. It is very likely that most of the platinum that can be determined by cyclic voltammetry is covered by polymer, which causes a diffusion barrier for the reacting gases. This indicates that a more even platinum deposition over the total microstructured surface would increase the platinum utilization considerably. Further experiments are needed to evaluate the upper limit of platinum utilization with these electrodes. Due to the fact that the microsawing technique does not allow an unstructured surrounding for gas inlet and collector channels at this size of electrode, the electrodes must be integrated in a support cell. With laser ablation or micro-embossing of the glassy carbon precursor, one could achieve more compact cells.

Although this first two cell stack is far from being representative for a stack of technical relevance, one might speculate about the achievable specific power. It must be realised, however, that these preliminary experiments were carried out without optimising stack compaction pressure, gas pressure drop, and water management. Furthermore, the low cell temperature and the short operation time are the main causes for the low power density. For example, assuming a current density of 600 mA/cm^2 at 0.5 V per cell, obtained with platinum black electrodes in standard cells under optimised operating conditions, one could achieve in this configuration a specific power of 1100 W/kg with 2 mm GC-plates (0.26 g/cm^2) or even 3.7 kW/kg with 0.6 mm GC-plates (0.08 g/cm^2). However, end-plates and membranes as well as gas manifolds and a cooling system, which are needed for stacks, were not included in this calculation.

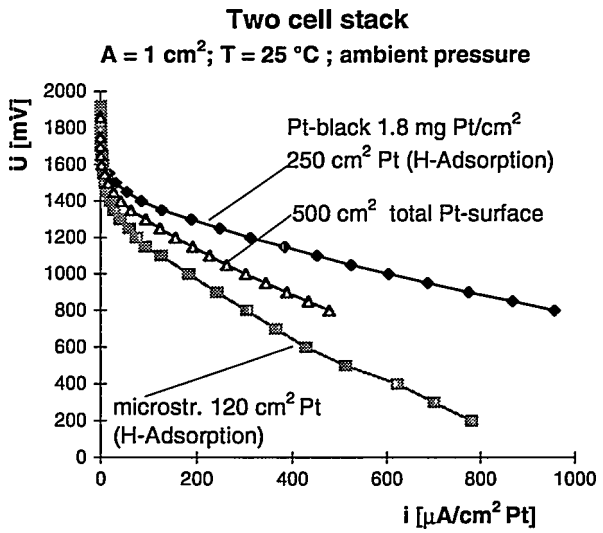

Fig. 3: Polarisation curves of conventional gas-diffusion electrodes vs microstructured electrodes.

4 ACKNOWLEDGEMENT

The financial support of Elektrowatt Ingenieure AG, Zürich is gratefully acknowledged.

5 REFERENCES

[1] R. Pow, M. Reindl, W. Tillmetz, Fuel Cell Seminar, Florida, 276 (1996).

[2] T.R. Ralph, G. Hards, J. Keating, S.A. Campbell, D. Wilkinson, M. Davis, J. St-Pierre, M.C. Johnson, J. Electrochem. Soc. **144**, 3845 (1997).

[3] S. Hirano, J. Kim, S. Srinivasan, Electrochim. Acta **42**, 1587 (1997).

[4] T.R. Ralph, Platinum Metals Rev. **41**, 102 (1997).

[5] G.G. Scherer, Z. Veziridis, M. Staub, H. Freimuth, PSI Annual Report, Annex V, 55 (1996).

EXPERIMENTAL 1 kW 20 CELL PEFC STACK

F.N. Büchi, C.A. Marmy, M. Ruge (ETH Zürich), G.G. Scherer

A 20-cell PEFC stack was designed and built. Resin impregnated graphite was used as bipolar plate material. The air cooling of the stack was optimized by introducing high surface structures into the open space of the cooling plates. At $\eta(H_2$ LHV) = 0.5 a power of 880 W was obtained under conditions of low gas-pressures of 1.15 bar_a. The auxiliary power for process air supply and cooling at 880 W power is less than 7 % of the power output, indicating that the described system may be operated at a high efficiency.

1 MOTIVATION

For a high efficiency fuel cell system, minimum energy should be used for auxiliary loads such as process air supply, cooling and system control. Previously we optimized the air flow field for a PEFC stack, with respect to low air operating pressure and moderate air stoichiometry [1]. This flow field minimizes the auxiliary load for air supply in the fuel cell system. Before we had tested this flow field in a 10-cell stack with a power of approx. 500 W (at 0.6 V/cell) [2]. Here we present results from a 20-cell experimental stack based on this flow-field design.

2 CONSTRUCTION

Resin impregnated graphite (from Sigri Great Lakes, Meitingen, D) was chosen as construction material for the bipolar plates. This graphite has an excellent chemical stability, good thermal and electrical conductivity and a low density (1.9 g/cm^3). In the 20-cell stack (see Figure 1) every third cell was a cooling cell with an open structure to allow for air cooling. The stack therefore was composed from 20 electrochemical cells and 9 cooling cells. The active part of the stack (graphite plates and electrochemical components) had a weight of 7.1 kg, the total stack weight was 11.7 kg. The bipolar and cooling plates were machined from plates with a thickness of 4.5 mm. In order to enhance air cooling efficiency and to maintain a homogeneous distribution of clamping pressure over the entire area of the plates the open space in the cooling plates was filled with high strength, high surface structures. Two elements containing 52 aluminium tubes, sandwiched between carbon fibre sheets and bonded with epoxy were inserted in each cooling plate (see Figure 2). The MEA's with an active area of 190 cm^2 were made by hotpressing E-Tek ELAT electrodes (anode 0.6 mg/cm^2 Pt, cathode 2.0 mg/cm^2 Pt) onto Nafion® 1135 membranes.

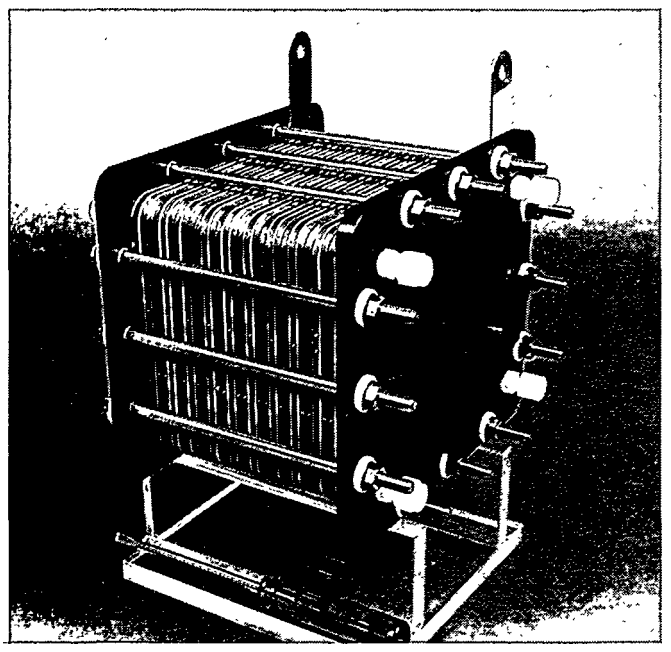

Fig. 1: 20 cell, air cooled PEFC stack. The outer dimensions are 23 x 22 x 19 cm (L x W x H).

3 RESULTS

Start-up : The stack can be started from room temperature and it reaches 50 % of the rated power at 12.8 V after 120 sec of operation, and 90 % after 5 min, respectively. This indicates that, due to the low heat capacity in the absence of liquid water in the system, the air cooled system can be started rapidly. A typical start-up in terms of temperature and power is shown in Figure 3.

Performance : A stack polarization curve of the 20-cell stack is shown in Figure 4. At an efficiency (referred to the LHV of H2) of η = 50% (U = 12.4 V) a power of

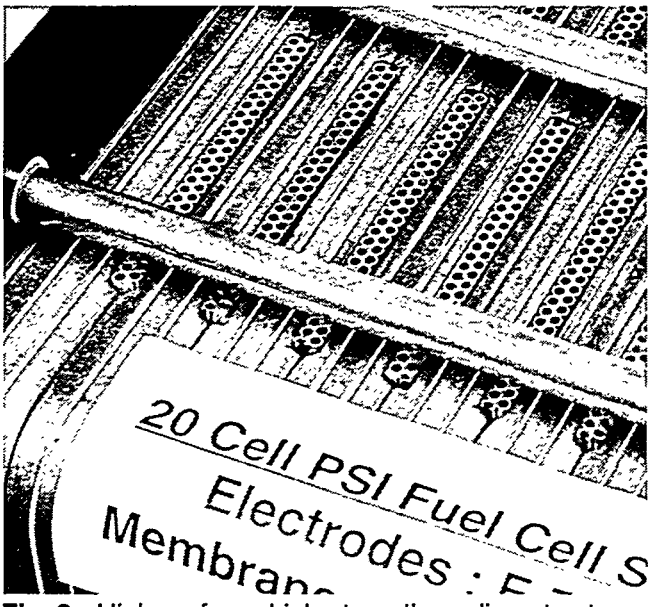

Fig. 2: High surface, high strength cooling structures in the cooling plates of the stack.

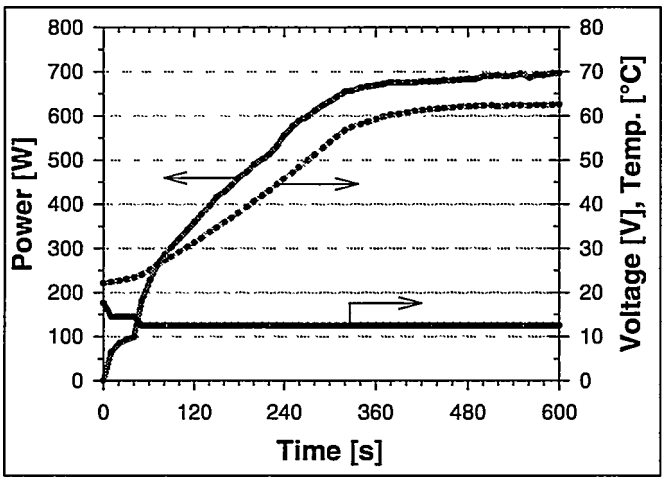

Fig. 3: Start-up of 20-cell stack from room temperature in constant voltage mode operation. 0-40 sec at 14.5 V, 41-600 sec at 12.8 V.

approx. 880 W was obtained at the conditions specified in the Figure caption (1.15 bar_a gas pressures). For the active part of the stack a specific power of 122 W/kg is calculated for the operating point at $\eta_{LHV} = 50$ %. This is an improvement of 30 % as compared to the previous stack generation [2]. Based on the total weight of the stack a specific power of 77 W/kg is obtained.

The stack performance was tested as function of the air dew point while hydrogen was fed dry. Figure 5 shows the dependence of the stack current at a constant stack voltage of 13 V on the air dew point for a cell temperature of 60 °C. When the relative air humidity is lowered from 100 % to about 40 % the current decreases by only 15 %. However below 35 % relative air humidity the decrease of current density and power output with decreasing air humidity is rapid, as indicated by instable operation.

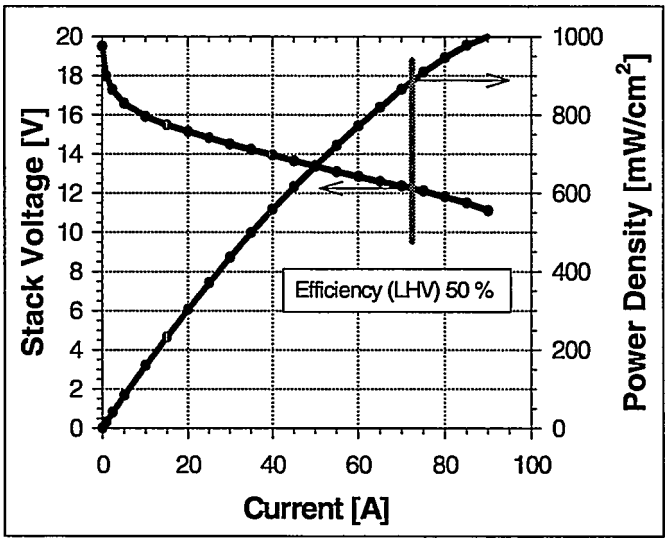

Fig. 4: Performance of 20-cell stack with gas pressures of 1.15 bar_a, $\lambda_{air} = 2.5$, rel. air humidity 61 %, hydrogen dry, $\lambda_{H2} = 1.5$, stack temperature 60 °C.

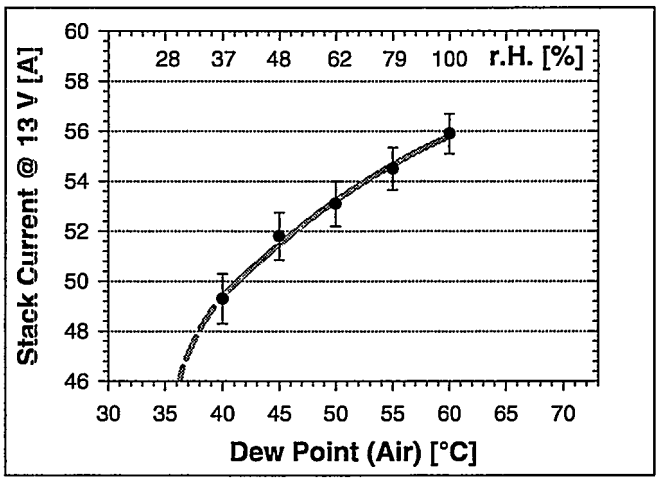

Fig. 5: Steady state currents at a stack voltage of 13 V as function of air dew point. Gas pressures 1.15 bar_a, $\lambda_{air} = 2.5$, hydrogen dry, $\lambda_{H2} = 1.5$, stack temperature 60 °C.

Efficiency: The electrochemical performance at low gas pressures of < 1.2 bar_a and moderate air humidity shows that the system can be operated with a minimum of auxiliary power. The main requirements for the auxiliary power are process air supply and stack cooling. Based on an efficiency for the air supply of 0.56 (blower $\eta = 0.7$ and electric motor $\eta = 0.8$) an auxiliary power of 28 W for the air supply is calculated at 1.15 bar_a at the rated point of 880 W. The experimentally determined power for the (non-optimized) cooling fan is 30 W at 60 °C stack temperature. Therefore, at the rated point of 880 W power, the auxiliary power need for process air supply and cooling is only 6.6 % of the power output of the stack. The system efficiency (ηLHV) accounting for cooling and air supply is 46.7 % at the rated point of operation. This value does not take into account possible parasitic power for the air humidification.

4 ACKNOWLEDGEMENTS

Design of the end-plates by D. Kuster (PSI), milling of the end and bipolar plates in the PSI machine shop and financial support for this project from the Swiss Federal Office of Energy (BFE) are gratefully acknowledged.

5 REFERENCES

[1] F.N. Büchi, A. Tsukada, O. Haas, G.G. Scherer, *Polymer Electrolyte Fuel Cells : Flow Field for Efficient Air Operation*, PSI Annual Report 1996, Annex V, 57-58 (1996).

[2] F.N. Büchi, C.A. Marmy, G.G. Scherer, *Progress towards a PSI kW-Polymer Electrolyte Fuel Cell Stack*, PSI Annual Report 1997, Annex V, 50-51 (1997).

300 W POLYMER ELECTROLYTE FUEL CELL GENERATORS FOR EDUCATIONAL PURPOSES

A. Tsukada, I. Popelis (Fachhochschule Solothurn Nordwestschweiz), F.N. Büchi, G.G. Scherer, O. Haas

A 300 W fuel cell power pack has been developed for educational purposes in close collaboration with the Fachhochschule Solothurn Nordwestschweiz. The project was initiated and financed by the Swiss Federal Office of Energy. The outlay and the performance of the power pack are described.

1 INTRODUCTION

Last year, a series of 10 fuel cell power packs using H_2/O_2 and producing 100 W of continuous power were delivered to technical colleges (FHSs) and universities. These generators and the fuel cell technology in general have aroused a great interest among the professors and students. Encouraged by this success, the Swiss Federal Office of Energy decided to finance a second generation of fuel cells with a continuous power output of about 300 W as part of a joint project between the Electrochemistry Section of the Paul Scherrer Institut and the Electrical Engineering Department of the technical college Fachhochschule Solothurn Nordwestschweiz.

2 POWER PACK OUTLAY

To reduce the weight and the volume of the power pack, a simple external membrane humidification system was adopted. The product water was distributed with a water pump (3.4 W) to injectors which were fixed at the air entrance of the bipolar plates. As long as the current is higher than 15 A, the external humidification is not needed thanks to sufficient back diffusion of the product water in the membranes.

The 20-cell stack (see Figure 1) weighs 7.5 kg including the cooling system. The stack is cooled by natural and forced convection of air around 19 aluminium fins, which are fixed in the grooves of the bipolar plates. As long as the power is less than 300 W, the stack temperature does not exceed 80 °C. The use of two small axial fans (ca. 3 W each) is necessary at higher power. A small DC/DC converter was installed in the power pack to supply an adjustable constant voltage of 24-48 V to the power consumer. The unit has been installed in a frame (total weight: ca. 12 kg; dim.: 25 x 25 x 45 cm), which includes the DC/DC converter, an air compressor (15 W), a 12 V starter battery, a water injection pump and a H_2 control valve (see Figure 2).

3 RESULTS

Figure 2 shows the 20-cell stack with two cooling fans which start automatically at 60 °C. At a gas pressure (H_2 /air) of 1.1/1.3 bar_a, the 20-cell stack delivers 300 W at about 14 V with a hydrogen stoichiometry of $\lambda_{H_2} = 1.1$ and an air stoichiometry of $\lambda_{air} = 2.5$ at 67 °C. The polarisation and power/current curve of the 20-cell stack is shown in Figure 3.

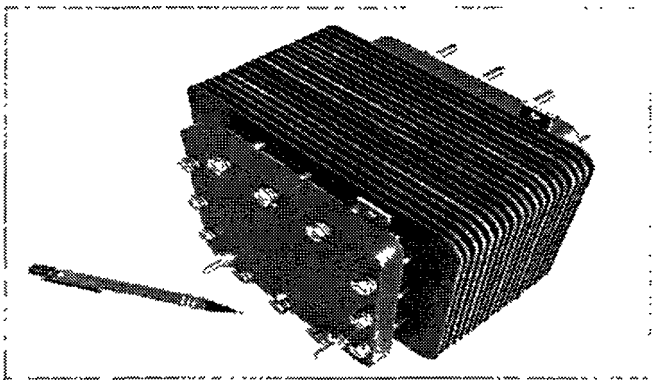

Fig. 1: 20-cell stack with 19 fins.

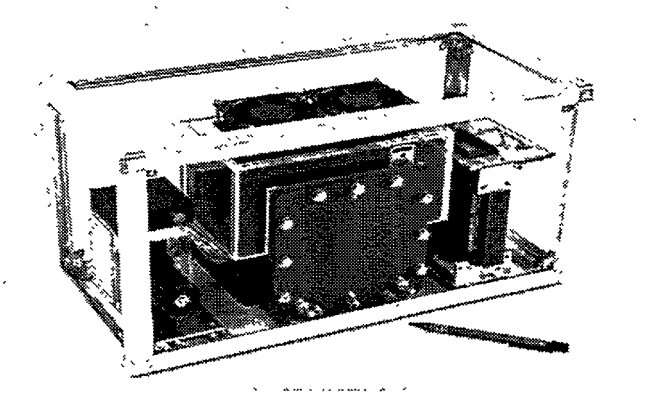

Fig. 2: Power pack containing a fuel cell stack, an air compressor, 2 cooling fans and a 12 V DC/DC converter.

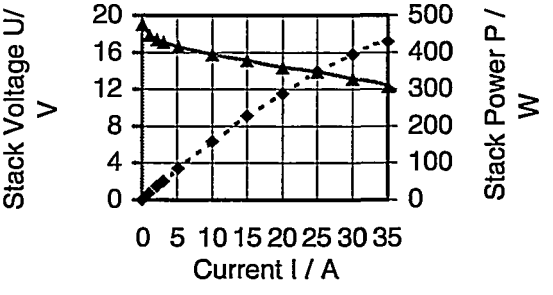

Fig. 3: Polarisation curve and power/current curve of the 20-cell stack. Active electrode area: 100 cm^2.

4 ACKNOWLEDGEMENT

The financial support of the Swiss Federal Office of Energy is gratefully acknowledged.

Combustion Research

NO_x FORMATION IN LEAN PREMIXED COMBUSTION OF METHANE AT HIGH PRESSURES

K.U.M. Bengtsson, P. Griebel, R. Schären

High pressure experiments in a jet-stirred reactor have been performed to study the NO_x formation in lean premixed combustion of methane/air mixtures. The experimental results are compared with numerical predictions using four well known reaction mechanisms and a model which consists of a series of two perfectly stirred reactors and a plug flow reactor.

1 INTRODUCTION

Lean premixed combustion is a well established technology for achieving low NO_x emissions by burning gaseous fuels (natural gas, methane). For a further NO_x reduction in future gas turbines with higher turbine inlet temperatures and pressures, an improved knowledge of the NO_x kinetics is needed. Currently there is a deficiency of experimental kinetic data for gas turbine conditions and, in particular, the pressure dependence of the NO_x formation is not well understood. Therefore, experiments in a jet-stirred reactor (JSR) were performed to study the NO_x formation at realistic gas turbine conditions (flame temperatures in the range of 1450-1600 °C, equivalence ratio of 0.55, and pressures up to 20 bars). In addition, numerical studies using four well known reaction mechanisms were performed.

2 EXPERIMENTAL SET-UP

A test rig that can be operated at pressures up to 30 bars was built with a maximum thermal power of 100 kW. Compressed air, that can be resistively preheated to temperatures up to 550 °C, is premixed with gaseous fuel in a static mixer. The test rig can be used for various high-pressure combustion projects.

For the investigation of the NO_x formation, a JSR coupled with a tubular reactor that fitted into the pressure vessel of the rig was constructed. Efforts have been made in the JSR-design to attain as close as possible perfectly stirred reactor (PSR) operating conditions. Although the final JSR-design did not have an ideal PSR-behaviour, the experimental results could be still simulated with reasonable accuracy.

The JSR had a volume of 19 ml and was made of castable ceramics embedded in an insulating material. The premixed air/fuel mixture was fed into the reactor through 20 small nozzles with a diameter of 0.6 mm. At residence times smaller than 2.4 ms in the JSR, the velocity of the jets at the inlet was sonic, the turbulence intensity was high, and hence fast mixing in the reactor was achieved. All studies have been performed with methane/air mixtures.

The temperatures were measured with coated Pt/Pt-Rh-thermocouples (S-type). The exhaust gas was sampled continuously through a water-cooled gas probe and the composition was determined with conventional gas analysers. N_2O was measured discontinuously with a gas chromatograph.

3 EXPERIMENTAL RESULTS

Whereas measurements were performed at different test conditions (temperatures, residence times, etc.), representative results are presented for an exit temperature of 1555 °C, a residence time of 1.5 ms, and an equivalence ratio of 0.55. Additional results are given in [1,2].

Figure 1 shows the pressure dependence of the measured NO_x concentration at the exit of the JSR. As the pressure increases the NO_x clearly decreases due to the decrease of the radical pool concentration. The radical pool concentration, especially the O radical, has a large influence on the NO_x formation.

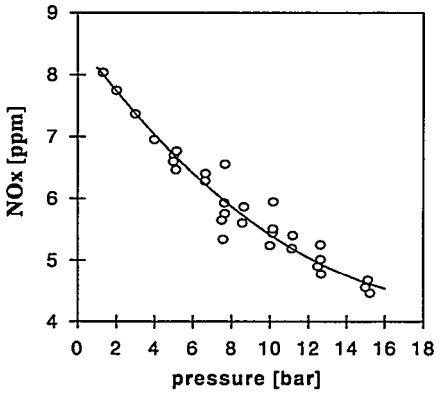

Fig. 1: Measured NO_x concentration at several pressures (exit temperature 1555 °C, residence time 1.5 ms, equivalence ratio 0.55).

4 NUMERICAL ANALYSIS

Turbulent premixed combustion can be modelled using a series of a perfectly stirred reactor (PSR), representing the flame zone, followed by a plug flow reactor (PFR), representing the burn out zone. In such simple ideal model reactors (PSR, PFR) the chemistry is decoupled from the flow field and hence numerical studies with detailed chemistry are easy to perform.

The predictions of the simple PSR-PFR model did not correspond very well with the experimental results [1,2]. For a better description of the JSR-behaviour a model of two PSRs and one PFR was used. The volume partition among the reactors was determined by

matching the measured and predicted CO concentrations for all test conditions and the extinction limits at different pressures (1, 5, 10 bars). The resulting reactor volume fractions were: 30 % (PSR1), 60 % (PSR2) and 10 % (PFR). The numerical calculations were performed with the chemical kinetics package CHEMKIN-II [3]. The following four different reaction mechanisms of the C/H/O/N-system have been used to predict the NO_x concentration for combustion of methane/air: Miller-Bowman [4], GRI [5], Bockhorn [6], Leeds [7] + NO-reactions from [6]. In addition, reaction path analysis and sensitivity analysis have been performed to gain information about the most important reactions.

At atmospheric pressure NO is mainly formed through the Zeldovich- (O super-equilibrium) and the N_2O-submechanisms. At high pressures the N_2O-submechanism is dominant. Reaction path analysis has shown that the most important route is $N_2 \rightarrow N_2O \rightarrow NO$ [1,2]. N_2O is mainly formed via the third body reaction $N_2+O+M \rightarrow N_2O+M$, and NO is mainly formed via the reaction $NO_2+O \rightarrow 2NO$.

Figure 2 shows the predicted NO_x concentrations at several pressures for all four reaction mechanisms (marked with „undoped"). For comparison purposes the measured concentrations are also shown. The test conditions are the same as in Figure 1.

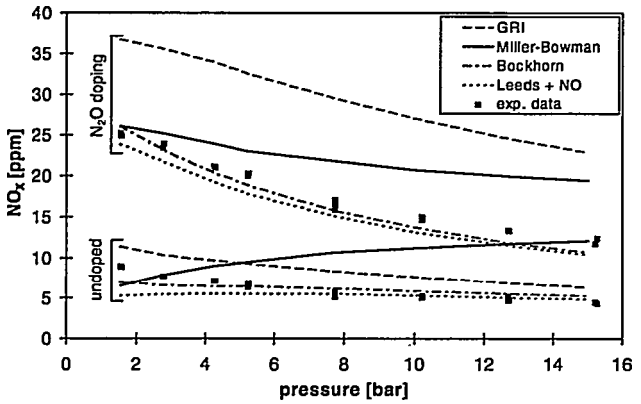

Fig. 2: Measured and predicted NO_x concentration at several pressures with and without N_2O doping (exit temperature 1555 °C, residence time 1.5 ms, equivalence ratio 0.55).

The agreement between the measurements and the predictions using the Leeds+NO or the Bockhorn mechanism is quite good. The predictions using the GRI mechanism give the right pressure trend but the absolute concentrations are slightly higher than the measured values. The discrepancy between the measured NO_x and the predicted ones using the Miller-Bowman mechanism is due to the overestimation of the radical pool concentration. This leads to a different pressure trend and to higher NO_x concentrations, as the NO_x formation is very sensitive to the radical pool. To test the 2PSR-PFR model, results of N_2O doping experiments were compared with predictions. The incoming air/fuel mixture was doped with 100 ppm N_2O. The results are also shown in Figure 2 (marked with „N_2O doping"). The measured pressure dependence of the NO_x concentration is confirmed by the doping experiments. The agreement between measurements and predictions for both the doped and the undoped case is nearly the same. This strengthens the confidence on the 2PSR-PFR model. The comparison between the experimental results and the predictions indicates that the Miller-Bowman mechanism is not suited to predict the NO_x concentrations at the present conditions.

5 ACKNOWLEDGEMENTS

The authors would like to thank the Swiss National Energy Research Foundation (NEFF) as well as ABB Ltd for their financial support.

6 REFERENCES

[1] K.U.M. Bengtsson, P. Benz, R. Schären, C.E. Frouzakis, *N_yO_x Formation in Lean Premixed Combustion of Methane in a High-Pressure Jet-Stirred Reactor,* 27 th International Symposium of Combustion, Boulder, August 2-7 (1998).

[2] K.U.M. Bengtsson, *Numerical and Experimental Study of NO_x formation in High-Pressure Lean Premixed Combustion of Methane,* Ph.D. Thesis ETH Zürich, Nr. 12877 (1998).

[3] R.J. Kee, F.M. Rupley, J.A. Miller, *Chemkin-II: A Fortran Chemical Kinetics Package for the Analysis of Gas-Phase Chemical Kinetics,* Sandia Report SAND89-8009B-UC-706 (1996).

[4] J.A. Miller, C.T. Bowman, *Mechanism and Modelling of Nitrogen Chemistry in Combustion,* Prog. Energy Combust. Sci., **15**, 287-338 (1989).

[5] G.P. Smith, D.R. Crosley, D.M. Golden, M. Frenklach, W.C. Gardiner, R.K. Hanson, C.T. Bowman, *GRI-Mech 2.11,* Annual Report SRI International (1996).

[6] A. Schlegel, *Experimentelle und numerische Untersuchung der NO_x-Bildung bei der katalytisch stabilisierten und der nicht-katalysierten, mageren Vormischverbrennung,* Dissertation ETH Zürich, Nr. 10887 (1994).

[7] M.J. Pilling, T. Turanyi, K.J. Hughes, A.R. Clague, *The Leeds Methane Oxidation Mechanism,* Version 2.1, School of Chemistry at Leeds University (1996).

AN INVESTIGATION OF TURBULENT CATALYTICALLY STABILIZED CHANNEL FLOW COMBUSTION OF LEAN HYDROGEN - AIR MIXTURES

I. Mantzaras, P. Benz, R. Schaeren, R. Bombach

The catalytically stabilised thermal combustion (CST) of lean hydrogen-air mixtures was investigated numerically in a turbulent channel flow configuration using a two-dimensional elliptic model with detailed heterogeneous and homogeneous chemical reactions. Comparison between turbulent and laminar cases having the same incoming mean properties shows that turbulence inhibits homogeneous ignition due to increased heat transport away from the near-wall layer. The peak root-mean-square temperature and species fluctuations are always located outside the extent of the homogeneous reaction zone indicating that thermochemical fluctuations have no significant influence on gaseous combustion.

1 INTRODUCTION

We have recently investigated numerically and experimentally [1-3] the catalytically stabilised thermal combustion (CST) of lean methane-air mixtures in laminar channel flow configurations. The key surface reactions influencing homogeneous ignition were identified to be the adsorption and desorption of the OH radical [1]. Numerically predicted homogeneous ignition distances were then successfully compared to measured ones [2], thus strengthening the confidence on the applicability to CST of newly developed [4] surface reaction schemes. We extend our previous work to turbulent channel CST flows, relevant to many practical applications. Surface and gaseous reactions interact with turbulence and with each other. Turbulence enhances the heat and mass transport coefficients towards or away from the catalyst surface and can be strongly coupled to gaseous combustion due to the increased transport and the induced thermochemical fluctuations.

The main objective is to examine the influence of fluid mechanical turbulence on CST of lean hydrogen-air mixtures. Comparisons are made with corresponding laminar cases to assess fundamental differences between the turbulent and laminar flow modes. Preliminary experiments in a newly built turbulent catalytic combustor are also presented.

2 NUMERICAL PREDICTIONS

A 2-D elliptic description is employed for a statistically steady turbulent flow. A moment closure approach is adopted by constructing Favre-averaged modelled transport equations for all gas-phase variables. Turbulence closure is achieved by a two-layer k-ε model. The thermochemistry modelling includes transport equations for the Favre-averaged mean values, variances, and covariances of the total enthalpy and the species mass fractions. To evaluate mean gaseous reaction rates a presumed Gaussian joint probability density function (pdf) was used as a coupling submodel. The surface species coverage equations are solved along with the gas-phase interfacial boundary conditions using a modified Newton's method. For gaseous chemistry the H/O mechanism from [5] is used (8 species, 38 reactions). For surface chemistry the H_2 oxidation scheme over Pt from [4] is employed (6 gaseous and 4 surface species, 23 reactions).

Simulations are performed in a channel formed by two infinitely-wide parallel plates which are 150 mm long and are separated by a distance of 10 mm (H). The inlet conditions are: U_{IN}=15 m/s, T_{IN}=400 K, turbulent kinetic energy $k_{IN} = 0.007U^2_{IN}$, and dissipation rate of k_{IN} equal to $\varepsilon_{IN} = k^{3/2}_{IN}/b$ with b=0.1H. The pressure is 1 bar and the equivalence ratio is 0.24. The channel wall temperature is 1220 K and the catalyst site density is 2.7×10^{-9} moles/cm^2 simulating polycrystalline platinum. Streamwise profiles of catalytic (C) and homogeneous (G) fuel conversion rates are given in Figure 1; homogeneous ignition is seen to take place at x≈26 mm.

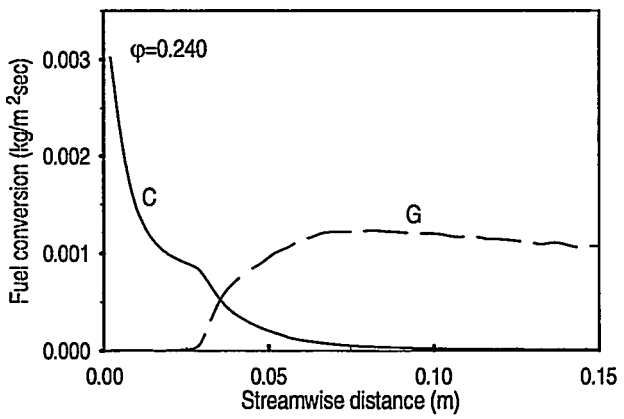

Fig. 1: Streamwise profiles of catalytic (C) and gaseous (G) fuel conversion rates. The G rate has been integrated over the channel half-width.

The effect of thermochemical fluctuations on gaseous combustion is discussed with the aid of Figure 2; transverse profiles of Favre-averaged root mean square (rms) temperature fluctuations are plotted at four selected streamwise distances. The vertical bars in Figure 2 define the transverse extent of the gaseous reaction zone for the three x-locations downstream

homogeneous ignition; 95% of gaseous combustion has been completed in the zones defined by the vertical bars and the wall. The peak rms temperatures are always located outside the reaction zone. Temperature fluctuations still persist in the reaction zone but their levels are low enough to have any significant influence on gaseous combustion.

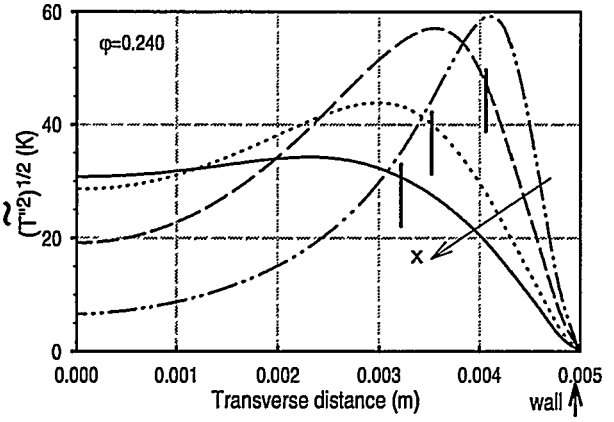

Fig 2: Transverse profiles of Favre-averaged rms temperature fluctuations at x = 26, 61, 98 and 150 mm. The vertical bars indicate the extent of the gaseous reaction zone from the catalytic wall.

Computations at different equivalence ratios indicate that turbulent kinetic energy is considerably suppressed by gaseous combustion so that leaner mixtures have higher turbulent transport coefficients. The higher transport coefficients and the slower reaction rates of the leaner cases push the reaction zone closer to the wall leading to incomplete gaseous combustion; fuel leaks through the gaseous reaction zone towards the catalytic surface. Both catalytic and gaseous fuel conversion modes can then be present downstream the homogeneous ignition point.

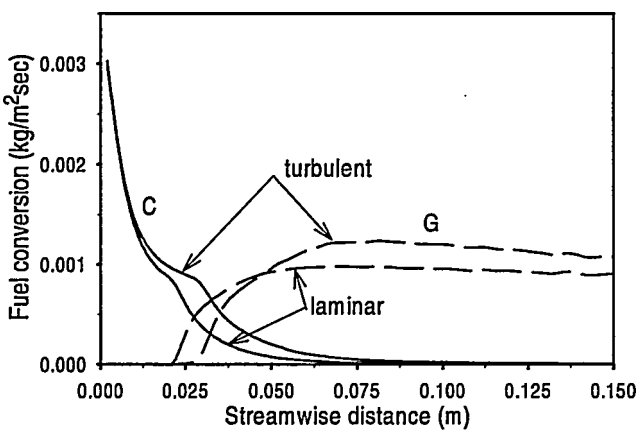

Fig 3: Comparison between laminar and turbulent catalytic (C) and gaseous (G) conversion rates.

Of particular interest in CST is the assessment of performance differences between the laminar and turbulent flow modes. In Figure 3 the C and G fuel conversions are plotted for the turbulent and a corresponding laminar case having the same mean inlet properties. Homogeneous ignition takes place about 5 mm earlier in the laminar case, hence turbulence inhibits homogeneous ignition. This is due to increased heat losses in the turbulent case from the near-wall zone towards the channel core, a result of the increased effective turbulent Lewis number. The turbulent CST performance indicated in Figure 3 could be desirable in practical applications where increased heterogeneous conversion is sought with late homogeneous ignition (or no homogeneous ignition at all if a post-catalyst staged gaseous combustor is provided for this purpose [6]).

3 EXPERIMENTAL

Preliminary experiments were carried out in a newly built turbulent catalytic channel combustor. The geometry of the burner is similar to our previous laminar burner [3]. The channel combustor consists of two ceramic Pt-coated plates 300 mm long and 100 mm wide that are placed 7 mm apart. The other two channel surfaces are formed by two 3-mm thick quartz windows spring pressed against the ceramic plates. A long entry section provides a fully developed turbulent inlet velocity profile. Planar laser induced fluorescence (PLIF) images of the OH radical along the streamwise plane of symmetry are presented in Figure 4 for a case with an inlet velocity of 15m/s and an equivalence ratio of 0.24.

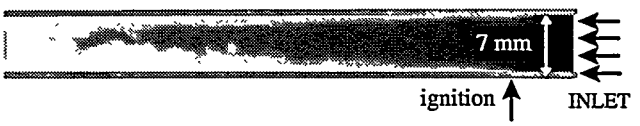

Fig 4: PLIF image of the OH radical in the catalytic channel burner. White colour indicates high OH levels.

4 REFERENCES

[1] U. Dogwiler, P. Benz, J. Mantzaras, Combustion and Flame **116,** 243-258 (1999).

[2] U. Dogwiler, Ph.D. Thesis, ETH-Zürich, Thesis No. 12648 (1998).

[3] U. Dogwiler, J. Mantzaras, P. Benz, B. Kaeppeli, R. Bombach, A. Arnold, Paper presented at the 27th Symp. (Int.) on Combustion, August (1998).

[4] O. Deutchmann, R. Schmidt, F. Behrendt, J. Warnatz, 26th Symposium (Int.) on Combustion, 1747-1754 (1996).

[5] J. Warnatz, U. Maas, Technische Verbrennung, Springer-Verlag (1993).

[6] I. Stambler, Gas Turbine World 23,3 (1993).

LASER-INDUCED INCANDESCENCE: TOWARDS QUANTITATIVE SOOT VOLUME FRACTION MEASUREMENTS

A.P. Tzannis, F. Wienbeucker, P. Beaud, H.-M. Frey, T. Gerber, B. Mischler, P.P. Radi

Laser-Induced Incandescence has recently emerged as a versatile tool for measuring soot volume fraction in a wide range of combustion systems. In this work we investigate the essential features of the method. LII is based on the acquisition of the incandescence of soot when heated through a high power laser pulse. Initial experiments have been performed on a model laboratory flame. The behaviour of the LII signal is studied experimentally. By applying numerical calculations we investigate the possibility to obtain two-dimensional soot volume fraction distributions. For this purpose a combination of LII with other techniques is required. This part is discussed in some extent and the future work is outlined.

1 INTRODUCTION

The High Temperature, High Pressure Cell (HTDZ) provides a facility, with optical access, to study spray combustion in a broad range of parameters relevant for Diesel engines. Laser diagnostic techniques are required that can record important parameters of the combustion process.

Soot is a major pollutant emerging from Diesel engines. Increased attention has to be paid to the understanding of soot formation and oxidation and to actual possibilities to reduce soot emission without increasing NOx emissions. Improvements in this field require diagnostic tools allowing to collect data with high temporal and spatial resolution and minimised interference from concurrent effects. Moreover multidimensional data acquisition is required to assess instantaneous combustion patterns in turbulent flows. Most optical studies in recent years have concentrated on characterising the soot particle field in terms of the soot volume fraction, particle size, and number density [1].

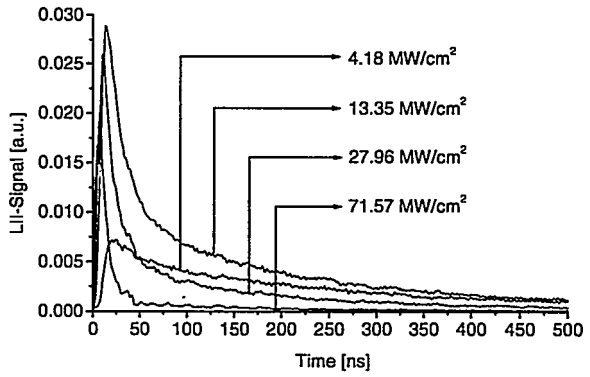

Fig. 1: Experimental results: Single point, time resolved detection of the LII-Signals in a test burner for various input laser irradiances [MW/cm²]; λdet=444 nm; 2 cm height above burner (HAB), 200 averages.

In this context the implementation of Laser-Induced Incandescence (LII) is of importance, since the obtained signals are in essence proportional to the soot volume fraction in the flame. LII involves the rapid heating of soot particles to temperatures at which their resultant incandescence can be distinguished, by temporal gating and wavelength filtering, against the natural luminosity arising of the flame and against laser induced fluorescence (LIF) from PAHs. For a practical implementation the soot particles are typically heated up with a laser pulse to their vaporisation temperature (~3915 K for graphite), or even up to ≈ 5000 K. At these temperatures the LII spectrum exhibits a maximum emission at visible wavelengths and extends from the near IR region to the near UV.

2 EXPERIMENTAL

Before applying the technique on the HDTZ, we conducted experiments on a simple laboratory flame i.e., an acetylene diffusion flame stabilised on a Wolfhard-Parker slot burner. This diffusion flame provides two equivalent flame fronts and a large variety of soot volume fractions with different number densities, aggregate sizes, morphologies and temperature-time histories. All these parameters have an influence on the LII signals. In our tests acetylene was chosen as a high sooting fuel to ease detection issues.

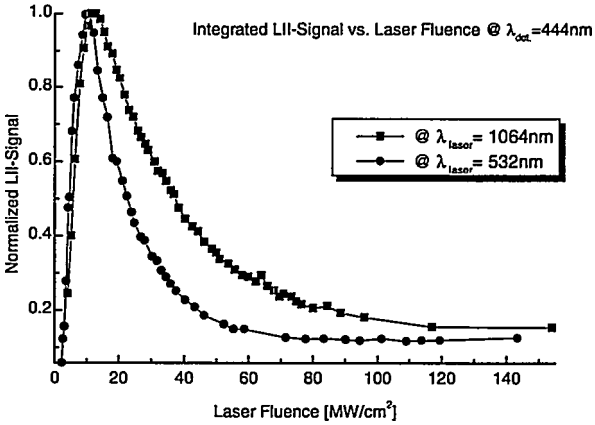

Fig. 2: Experimental results: Intensity measurements. The total detected LII signal plotted as a function of the input laser irradiance [MW/cm²] for two different input laser wavelengths; 2 cm HAB.

Temporally resolved LII signals are frequency selected with a monochromator, λdet =444±2 nm, and saved on a digital oscilloscope, see Figure 1. In order to successfully apply LII for quantitative soot volume fraction measurements it is important to find the laser irradiances [MW/cm²] that will deliver a constant LII-signal, thus eliminating shot-to-shot LII intensity fluctuations

and intensity variations over the laser probe-sheet. In Figure 2 the total emitted incandescence is plotted as a function of the input laser irradiance [MW/cm^2] indicating an optimal irradiance of ~14 MW/cm^2 for both applied probe lasers.

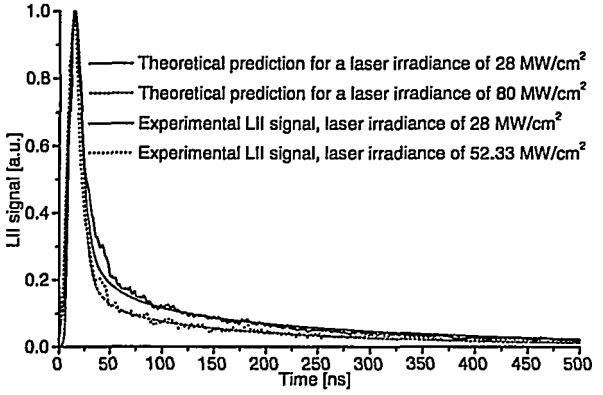

Fig. 3: Comparison between numerical simulations and experimental data with an assumed flame temperature of T=1500 K and an assumed mean soot particle diameter of 40 nm.

Furthermore, a model [2] describing the heating of a soot particle by the laser pulse, its incandescence and its cooling rate was successfully applied and compared with the experiments, see Figure 3. For the model we use a flame temperature of 1500 K and an average particle size of 40 nm. Though the model predicts accurately the recorded signal for low laser irradiances, it deviates for higher input irradiances. This is attributed to the onset of other processes such as the physical destruction of the soot particles by high energies, an effect not accounted for in the model.

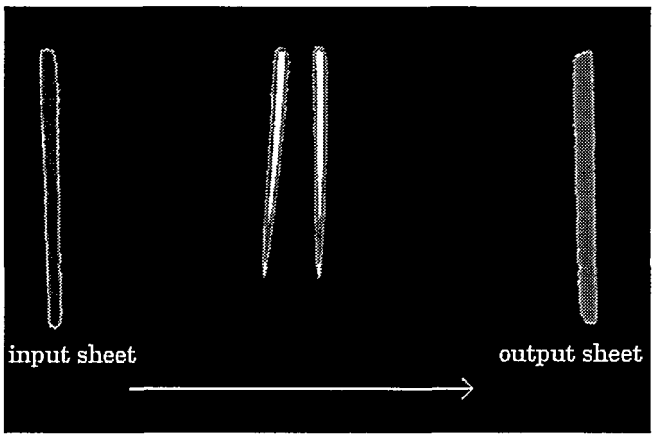

Fig. 4: LII-Signal arriving from the two flame fronts (middle), input-(left) and output-laser sheets (right) @ 13.88 MW/cm^2; λ_{laser} =532 nm, prompt detection [0 ns-1000 ns] (arrow indicates laser beam propagation).

Two-dimensional images of the soot distribution in the flame are recorded. The incoming laser probe beam of λ= 532 nm is formed to a laser sheet with dimensions of 3.5 cm x 0.1 cm that crosses the flame. Two beam splitters image the laser beam on a camera before and after traversing the flame. A 700±15 nm bandpass-filter is placed in front of the camera (in order to reduce scattered laser light and fluorescence from PAHs and the C_2 Swan band. The laser sheet profiles are transformed into detectable signals by placing two cuvettes filled with pyridine which flourescences at ~700 nm. With this setup we can detect the LII signal and simultaneously the extinction of the input laser sheet through the flame, i.e. the amount of light absorbed by the soot particles, see Figure 4. By assuming a temperature-field, a size distribution of the soot particles and a mean diameter, one can transform the two-dimensional LII images to soot volume fraction distributions in the flame.

3 CONCLUSION

- Initial LII experiments were successfully performed in a model flame.
- The method has the potential to yield soot volume fractions in a complicated combustion environment.
- The numerical modelling of the technique reproduces the experiment satisfactorily.
- The experimental set-up records 2D LII images with a good signal to noise ratio, and simultaneously performs extinction measurements.

4 OUTLOOK

- The model will be utilised together with recorded simultaneous extinction and 2D LII images to obtain first soot volume distributions in the flame, under the assumption of a log-normal soot size distribution.
- The measuring technique will be applied in a complex environment i.e. the HDTZ.
- Effects due to particle shapes other than spherical and the real flame temperature distribution will be accommodated in the model.
- Simultaneous measurement of Laser-Induced Incandescence (LII), Rayleigh scattering and extinction will be implemented in order to avoid assumptions on size distribution [3].

5 ACKNOWLEDGEMENT

The financial support of Federal Office of Energy (BFE) is gratefully acknowledged.

6 REFERENCES

[1] R.L. Vander Wal, K.J. Weiland, *Laser-induced incandescence; Development and characterization towards a measurement of soot-volume fraction*, Appl. Phys. B **59**, 445-452 (1994).

[2] D.L. Hofeldt, *Real-Time Soot Concentration Measurement Technique for Engine Exhaust Streams*, SAE paper 930079.

[3] H. Geitlinger, TH. Streibel, R. Stuntz, H. Bockhorn, *Two-dimensional imaging of soot volume fractions, particle number dinsities and particle radii in laminar and turbulent diffusion flames*, 26th Symposium (Int.) on Combustion, Boulder, August (1998).

DISSOCIATION DYNAMICS OF METHYLAL

P. Beaud, H.-M. Frey, T. Gerber, B. Mischler, P.P. Radi, A.-P. Tzannis

The dissociation of methylal is investigated using mass spectrometry, combined with a pyrolytic radical source and femtosecond pump probe experiments. Based on preliminary results two reaction paths of methylal dissociation are proposed and discussed.

1 INTRODUCTION

Addition of methylal (DMM: di-methoxy-methane, $CH_3OCH_2OCH_3$) to Diesel fuel has shown to reduce emission of particulates and NO_x without affecting the efficiency of the combustion [1]. We started a program with the goal to evaluate the reaction pathways - and if possible reaction rates - of DMM in combustion chemistry. Initial experiments have been performed using the following experimental techniques available in our laboratory: (i) molecular beam mass spectrometry; (ii) a pyrolytic radical source; (iii) femtosecond two colour pump and probe measurements.

2 FEMTOSECOND IONIZATION OF DMM

Recently it was shown for a number of polyatomic molecules that they do hardly fragment when ionised with ultrashort (<100 fs) intense (10^{14}-10^{15} W/cm^2) near infrared pulses [2]. In contrast to this result the DMM cation is found to be unstable. The DMM mass spectra obtained with femtosecond ionisation for three different wavelengths at intensities of approximately 10^{14} W/cm^2 are shown in Figure 1. An increased fragmentation with increasing frequency is observed.

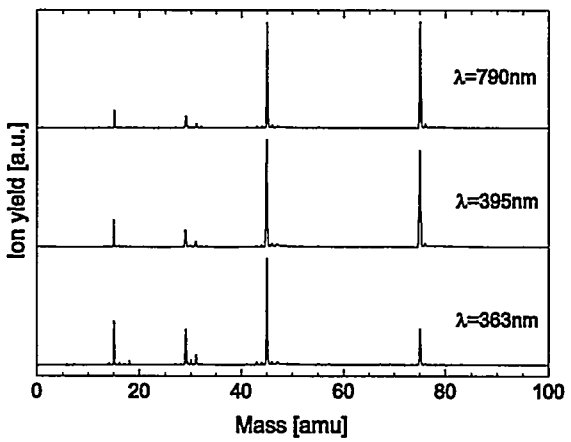

Fig. 1: Mass spectra obtained from DMM in a supersonic molecular beam by femtosecond ionisation.

The parent ion (76 amu) does not occur. The main fragments in Figure 1 are $CH_3OCHOCH_3$ and/or $CH_3OCH_2OCH_2$ (75 amu), CH_3 (15 amu), HCO (29 amu), and CH_3OCH_2 (45 amu). The radical OCHO (amu 45) can be excluded as a dissociation product since the isotopic ratio between mass 45 and 46 indicates that the complex measured at 45 amu contains two C atoms.

The ion yield of the two major fragments versus pump energy is shown in Figure 2. The maximum irradiance for all three wavelength is estimated in the range of 10^{14}-10^{15} W/cm^2. The measured exponents are not integers which is typical for high field ionisation.

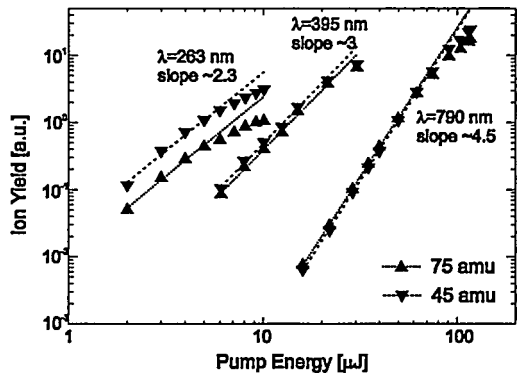

Fig. 2: Power dependence of the two major fragment cations of DMM.

3 THERMAL DECOMPOSITION OF DMM

In this experiment the gas pulse is expanded through a silicon carbide tube that can resistively be heated to temperatures up to 2000 K. The residence time in the hot zone is on the order of a few microseconds which permits one or several unimolecular decomposition events. After the reaction zone the molecules expand into high vacuum. No recombination is possible in the collision free environment of the molecular beam. The mass spectra are shown in Figure 3.

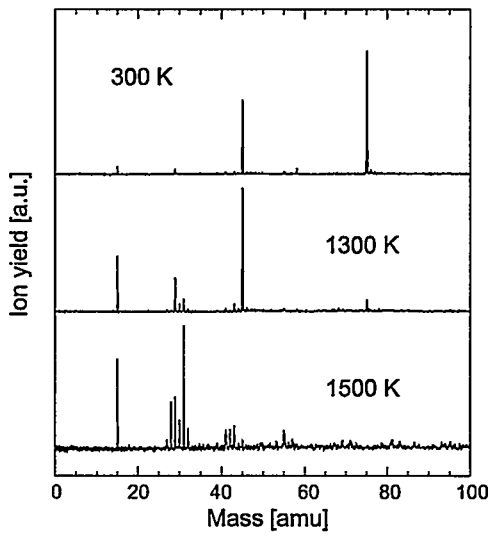

Fig. 3: Mass spectra of DMM for increasing nozzle temperature.

At 1300K the mass 75 fragment nearly vanishes indicating that almost all DMM decomposes at this temperature. The main fragments at 1300 K are CH_3, HCO, and CH_3OCH_2. The signal for methoxy (CH_3O, 31 amu) is discernible but relatively weak at 1300 K.

At 1500 K also the mass 45 cation is decomposed and the methoxy ion becomes the major fragment in the mass spectrum.

4 UNIMOLECULAR DISSOCIATION OF DMM

In recent years it has been shown that the femtosecond pump-probe technique is a useful tool to evaluate dissociation dynamics of a molecule. In a pump-probe experiment the molecule is excited by an ultrashort pump pulse. A second ultrashort pulse then probes the excited molecule or its fragments at a variable delay. In this experiment we detect the ion yield versus the delay of the probe pulse. As probe we use the 100 fs pulses from our Ti:sapphire laser system at 790 nm. The pump pulses at wavelengths of 264, 298 and 395 nm were generated using third and second harmonic generation, and white light amplification, respectively. The result obtained for 264 nm is shown in Figure 4. At all pump wavelengths the measured transients are slightly broader than the cross - correlation between pump- and probe pulse and slightly asymmetric. The derived lifetimes of the mass 75 and 45 species are in the order of 100 fs. The peak of the mass 45 signal is consistently delayed by 20-30 fs compared to the peak of the mass 75 signal.

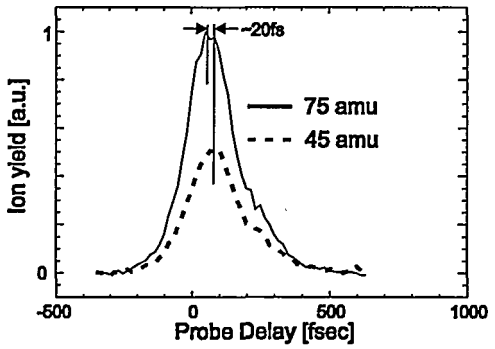

Fig. 4: Ion yield versus probe pulse delay following excitation of DMM by 100 fs pulses at 264 nm.

5 DISCUSSION

There is some evidence that DMM decomposes as:

$$CH_3OCH_2OCH_3 \rightarrow CH_3OCH_2^{\bullet} + CH_3O^{\bullet} \quad (1)$$
$$CH_3OCH_2^{\bullet} \rightarrow CH_3^{\bullet} + CH_2O \quad (2).$$

According to this path DMM pyrolysis can be compared to the initiating process in the case of dimethyl ether DME combustion [3]:

$$CH_3OCH_3 \rightarrow CH_3O^{\bullet} + CH_3^{\bullet} \quad (3).$$

However, a distinct reaction path may show up for DMM. The photo dissociation experiment indicates the immediate formation of the $CH_3OCH^{\bullet}OCH_3$ radical cation. In our experiment we can unfortunately not determine whether dissociation precedes ionisation. Part of the fragments could emanate from dissociating ions. MOPAC calculations predict that the $CH_3OCH^{\bullet}OCH_3$ fragment is the most stable fragment of the DMM ion. The ionisation potential for both complexes are comparable and it may be concluded that also neutral $CH_3OCH^{\bullet}OCH_3$ is a rather stable fragment of DMM following photo dissociation:

$$CH_3OCH_2OCH_3 \rightarrow CH_3OCH^{\bullet}OCH_3 + H \quad (4).$$

Dissociation of $CH_3OCH^{\bullet}OCH_3$ will result in a radical pool different than that found in DME combustion:

$$CH_3OCH^{\bullet}OCH_3 \rightarrow CH_3OCH + CH_3O^{\bullet} \quad (5),$$
$$CH_3OCH^{\bullet}OCH_3 \rightarrow CH_3OCHO + CH_3^{\bullet} \quad (6).$$

These complexes could prove to be of some importance at high temperatures, as further pyrolysis leads to $CH_3^{\bullet}$, $CH_3O^{\bullet}$ and $CHO^{\bullet}$ simultaneously:

$$CH_3OCH \rightarrow CH_3^{\bullet} + CHO^{\bullet} \quad (7),$$
$$CH_3OCHO \rightarrow CH_3O^{\bullet} + CHO^{\bullet} \quad (8).$$

The pyrolysis results of DMM show on the one hand some evidence for both reaction paths (1-3) and (4-8), but are on the other hand contradictory. The product CH_3OCH_2 formed by reaction (1) can be readily observed at 1300 K, but not at 1500 K. On the other hand the methoxy radical also associated with (1) becomes an important fragment only at 1500 K. The high methoxy yield at 1500 K can not simply be explained by further decomposition of CH_3OCH_2 since the associated fragment CH_2 is not observed. In all cases HCO is observed which can only be generated by reaction path (4-8). However, important intermediates in (4-8) CH_3OCH (44 amu) and CH_3OCHO (60 amu) are never observed and may be unstable. Femtosecond pump-probe experiments have the potential to clarify the time-ordering of dissociation events. Unfortunately, the fast decay times and ambiguities due to the fragmentation of DMM inhibit unequivocal interpretation of the femtosecond transients.

Possibly more information about the dissociation of DMM can be obtained by studying derivatives, such as fluorinated species. Moreover, implementing longer side chains will slow down the dissociation process. Another way is to combine the femtosecond pump-probe technique with other detection schemes such as LIF or FWM. Ab initio calculations are currently performed which may help to evaluate the reaction path of DMM dissociation. Finally, further reaction schemes in addition to those proposed here must be considered.

6 ACKNOWLEDGEMENT

We thank the Swiss Federal Energy Office (BFE) for financial support.

7 REFERENCES

[1] D. Näggeli, Report No. SWRI 03-130, Southwest Research Institute, San Antonio, Texas (1992).

[2] K.W.D. Ledingham et al., J. Phys. Chem. **A 102**, 3002 (1998).

[3] H.J. Currane et al., Int. J. Chem. Kinetics **30**, 229 (1998).

REACTION PATHWAYS OF THE DISSOCIATION OF METHYLAL: A DFT STUDY

H.-M. Frey, P. Beaud, T. Gerber, B. Mischler, P.P. Radi, A.-P. Tzannis

*Schemata for modelling combustion processes do not yet include reaction rates for oxygenated fuels like methylal (DMM) which is considered as an additive or replacement for diesel due to its low sooting propensity. Density functional theory (DFT) studies of the possible reaction pathways for different dissociation steps of methylal are presented. Cleavage of a hydrogen bond to the methoxy group or the central carbon atom were simulated at the BLYP/6-311++G** level of theory. The results are compared to the experiment when dissociating and/or ionising DMM with femtosecond pulses.*

1 INTRODUCTION

Similar to the anomeric effect in sugars, acetals like DMM show an effect in conformation, where one methoxy group prefers the eclipsed position with regard to the other. As a result, the global minimum structure of methylal is not the sterically least hindered shown in Figure 1(a), but the gauche conformation (b) shown with its resonance structure (c).

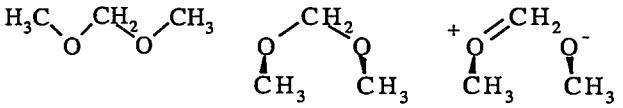

a) b) c)

Fig. 1: Different Conformations of DMM.

Upon ionisation of DMM with intense fs laser pulses and subsequent mass spectrometric detection, the parent ion (M^+) can not be observed but (M^+-1) is the most abundant peak. This fragment can either emerge from dissociation of a terminal hydrogen at the methoxy group or from the acetal hydrogen. However the absence of methoxy in the mass spectra does not fit to the presence of mass 45 which is $CH_3OCH_2^+$. The goal of our calculations was to obtain hints regarding the hydrogen expulsion and possible succeeding dissociation steps in both the neutral and the charged molecule.

2 METHOD

The structures of the neutral and positively charged DMM and its fragments were calculated using Gaussian 94 [1]. Becke's three parameter hybrid method using the Lee, Young and Parr functional (BLYP) was used. Frequency analysis yielded the enthalpy of the molecules at room temperature.

3 RESULTS

Unlike in sugars with a real anomeric effect, in DMM both oxygen atoms are stereochemically equivalent. The bond length of any oxygen to the central carbon atom is shorter than the C-O distance in the methoxy group. The dihedral angle from methoxy to methoxy is 135°. The enthalpies at room temperature for fragment pairs relative to the DMM parent molecule are listed in Table1.

	ΔH^{298} [kcal/mol]
DMM	0
$CH_3OCHOCH_3^{\bullet} + H^{\bullet}$	90.7
$CH_3OCH_2OCH_2^{\bullet} + H^{\bullet}$	147.2
$CH_3OCH_2O^{\bullet} + CH_3^{\bullet}$	69.0
$CH_3OCH_2^{\bullet} + OCH_3^{\bullet}$	81.5

Table 1: Relative Enthalpies of DMM and Fragments.

Table 1 confirms that DMM (in its gauche conformation) is the most stable configuration at room temperature compared to the sum of the energies of the possible fragment combinations. The fragmentation with methyl formation lies 69.0 kcal/mol above the energy of DMM. The methoxy fragmentation channel requires an additional 12.5 kcal/mol. This can be explained by the resonance effect which stabilises $CH_3OCH_2O^{\bullet}$. From a thermodynamic point of view the methyl fragmentation channel and not the methoxy abstraction should be preferred. This is in contrast to our experimental findings where $CH_3OCH_2O^{\bullet}$ is missing. Calculations on the fragment ion however have shown that $CH_3OCH_2O^+$ is not stable and therefore possibly can not be detected by mass spectrometry. The dissociation of the acetal hydrogen is by 56 kcal/mol more favourable than the loss of the terminal hydrogen. From the absence of DMM^+ in the mass spectra, and from the fact that the DMM radical is stable, we conclude that in our experiment DMM fragments in its ionic state, indicating a ladder climbing type ionisation. We will proceed on the theoretical side with pinning down transition states of the different fragmentation channels and subsequent reaction coordinate analysis. Experiments will concentrate in finding appropriate excitation and detection means for transient fragments and their spectroscopy.

4 ACKNOWLEDGEMENT

Support of this work by the Swiss Federal Office of Energy (BFE) is gratefully acknowledged.

5 REFERENCES

[1] M.J. Frisch et al, *Gaussian 94, Revision C3*, Gaussian Inc. Philadelphia (1994).

LASER INDUCED FLUORESCENCE MEASUREMENTS OF THE MIXING OF FUEL OIL WITH AIR

A. Arnold, R. Bombach, W. Hubschmid, B. Käppeli

We report on measurements of the mixing of fuel oil with air at atmospheric pressure in an industrial premixed gas turbine burner. The concentration of the vaporized fuel oil was measured with laser induced fluorescence. We reason that the fuel oil concentration can be considered with good accuracy as proportional to the fluorescence intensity.

1 INTRODUCTION

A better knowledge of the process of combustion is required in order to reduce the output of nitric oxides and other air pollutants. Numerical modeling of the combustion process and experimental diagnostics are the tools for that objective. Quantitative diagnostics is necessary to validate the calculations from the theoretical models.

For premixed combustion of liquid fuels in gas turbines the process of the evaporation of the liquid fuel and the subsequent mixing with air is of special interest. Experiments with commercially used liquid fuel (i.e. fuel oil light, below abbreviated as "fuel oil") represent better the given technical conditions than experiments with model fuels which are composed of one or very few well defined components.

We are providing quantitative results on the mixing and evaporation process of fuel oil in a gas turbine burner for power generation by applying the technique of 2-dimensional laser-induced fluorescence (LIF). The fuel oil was excited with light from an excimer laser. We report first on measurements of the absorption of the excimer laser light by the fuel (Sec. 3).

We investigate then the fluorescence of the fuel oil. The strength of the fluorescence signal S_F depends on a number of experimental parameters. Generally, an unsaturated signal is given by (single pulse or averaged over a group of pulses):

$$S_F(x,\lambda,\alpha,z) = \sum_{Species} S_{F,m}(x,\lambda,\alpha,z), \qquad (1)$$

where

$$S_{F,m}(x,\lambda,\alpha,z) \propto I_L(x) n_m(\alpha,x,z) \cdot \sum_j \frac{\exp(-E_{m,j}/kT) g_{m,j}}{Z_m} \frac{B_{m,j}(\lambda) A_{m,j}(\lambda)}{A_{m,j}(\lambda) + Q_{m,j}(\lambda,T,n,n_{air})}. \qquad (2)$$

The unspecified proportionality factor in (2) contains the influence of the unspecified detection geometry and the efficiency of the detector. The following symbols are used in (1) and (2): $S_{F,m}$ is the fluorescence signal from the fuel species m, x is the position within the light sheet, λ is the excitation wavelength, α indicates the sort of fuel oil under investigation, and the variable z designates the set of the parameters T_{in} (temperature of the preheated air which mixes with the fuel), the air mass flow $\dot{m}_{air}$ and the fuel mass flow $\dot{m}_{fuel}$. Furthermore, $I_L(x)$ is the laser intensity, n (n_m) and n_{air} are the local molar concentrations of the various fuel species and of the air, respectively, T is the local gas temperature, the index j designates the various upwards transitions of a given species m. $B_{m,j}$, $A_{m,j}$ and $Q_{m,j}$ are the Einstein coefficients for absorption and spontaneous emission of the fuel species and the electronic quenching rates, respectively, of the transition (m,j), Z_m is the partition function of species m, and $E_{m,j}$ and $g_{m,j}$ are the energy level and the degeneracy of the initial state for the given fluorescence transition. The equations (1) and (2) indicate various effects which can give rise to deviations from a proportionality between fuel concentration and fluorescence signal. Test experiments are discussed in Sec. 4 of this paper.

A number of works by other groups reported on aspects of LIF measurements in gas turbines or Diesel engines. These works considered, however, either model fuel or gave measurements of a semiquantitative nature. We refer here especially to a paper by Bazile and Stepowski [1], to investigations performed at DLR Köln [2], and to a recent paper from Cranfield University [3]. The present paper is a preliminary report on our measurements of fuel oil concentrations with the method of laser induced fluorescence. A more complete article will be published elsewhere.

2 THE EXPERIMENTAL SETUP

The physical properties, the chemical composition, and more specifically the fluorescence behaviour of fuel oil used in gas turbine burners, change with origin and processing. We performed therefore measurement series with three different oils (here called A, B, and C) and assume that this procedure allows us to make statements of some generality about the fluorescence of an arbitrary fuel oil.

The fuel oil is injected by a nozzle into the burner. An oil spray is formed and caught by a flow of preheated and swirled air under atmospheric pressure. The air equivalence ratio λ_{air} was in the range 2...4 (λ_{air} = 1 corresponds to stoichiometric conditions) and the air temperature had values between 400 and 500°C. The fuel air mixture passes a tube of quartz glass which is transparent for the laser beams and for the fluores-

cence light. During the first measurements the mixing tube was out of standard quartz glass; for later measurements, a tube of Suprasil 2 quartz was mounted. In the glass tube the process of the evaporation of the fuel oil and the mixture of the oil with the air can be analyzed with optical methods.

Various types of nozzles were mounted in the course of the experiments. Some of them lead to a quick blackening of the glass tube. The measurements with oil A reported on here were then carried out with one definite nozzle with one hole, the measurements with oils B and C with a different one-hole-nozzle.

For the excitation of the fuel oil fluorescence we used an excimer laser system (Lambda Physik Compex 150) with two tubes which can be filled with two different gas mixtures. The experiments described in Sec. 4.5 were performed with KrF in one tube and with XeF in the other. This corresponds to excitation wavelengths of 248 nm and 351nm, respectively. The two tubes can be fired with an arbitrary time delay so that LIF pictures with two different excitation wavelengths can be generated under otherwise stationary conditions.

Because of the higher fluorescence signals, most of the measurements were performed with the 248 nm light of the KrF laser. As described in Sec. 3, the absorption of the laser light at this wavelength is, however, rather strong so that for future measurements at higher gas pressures longer wavelengths have probably to be used.

The general layout of the experiment is depicted in Figure 1. The light beam from the laser has a rectangular cross section (8x24 mm). A 24 mm wide and 1 mm thick light sheet is formed by a diaphragm. The light sheet passes a cylindrical lens so that it diverges and irradiates the whole cross section of the mixing tube. The tube itself behaves like a cylindrical lens with a large negative focal length. This effect adds to the divergence of the light sheet. The energy of the pulse is 10 mJ after diaphragm and cylindrical lens.

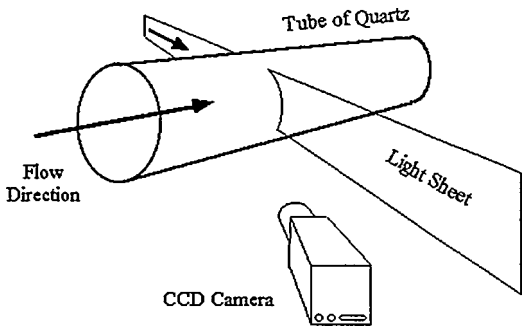

Fig. 1: General layout of the experiment.

The scheme for the detection of the fuel fluorescence is depicted in Figure 2. The signals are observed at an angle of 37° or less with respect to the light sheet plane, depending on the chosen distance of the observed tube cross section from the nozzle (see Figure 1). This leads to a distortion to elliptic form of the observed circular tube cross section.

A beamsplitter separates the LIF signal from a Mie scattering signal, which could be generated by oil droplets or by other particles. An intensified CCD camera registers the light which passes through the beam splitter. The Mie signal, which is reflected at the beamsplitter, is observed with a second intensified CCD camera.

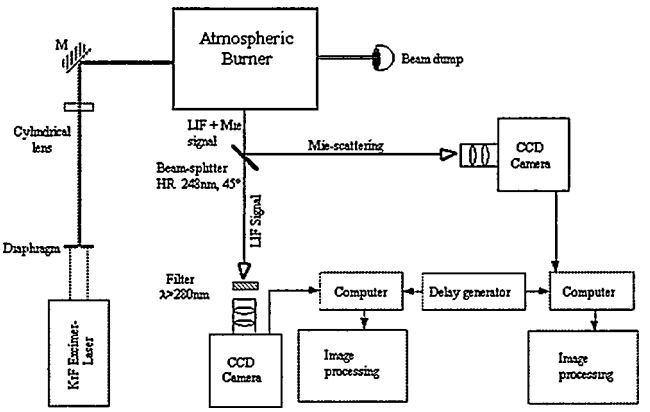

Fig. 2: Setup of the experiment.

3 LIGHT ABSORPTION BY FUEL OIL

During the experiments with the vaporized fuel in the glass tube, the laser light is absorbed by the oil in the fuel air mixture and by oil and oil products deposited at the tube. This total absorption reached values up to 90 % and more for low temperatures of the gas mixture (400°C or less). We explain this effect by the growing thickness of the oil film at the tube at low temperatures.

The absorption from the oil in the mixture with air alone can be approximately determined by the average reduction of the fluorescence intensity at the light sheet exit of the mixing tube compared with the fluorescence at the light sheet entrance assuming an axial symmetry of the burner construction and of the air flow. The assumed burner symmetry was partly tested by rotating the nozzle by an angle of 180°. No change in the induced average fluorescence could be observed as consequence of this operation.

For the 248 nm light, the absorption within the tube was determined to be about 70...80 % for oil A and B at λ_{air}-values of about 2. This means that for the wavelength 248 nm the light absorption is a critical parameter, and that the application of the KrF laser light will be rendered difficult for the same geometry at desired technical pressures of 15 bar and λ_{air}-values in the range of 2. We saw also an approximate proportionality between light absorption and ϕ ($\equiv\lambda_{air}^{-1}$) in the range $0.25 \le \phi \le 0.5$ for the light with the wavelength λ = 248 nm. At λ = 351 nm however, the light absorption was small («10%) for all considered conditions.

Figure 3 shows the average LIF intensity in the cross section of the light sheet with the 248 nm excitation. Because of the camera observation angle, the cross section appears in the form of an ellipse. Additionally, the ellipse is cut on two sides by the shadow from a metal construction around the tube.

We attribute the asymmetry in intensity between entrance and exit of the sheet mainly to laser light absorption. For an analysis of LIF data which aims at a quantitative measurement of the fuel concentration, this effect of the absorption of the laser light along the propagation in the tube has to be taken into account.

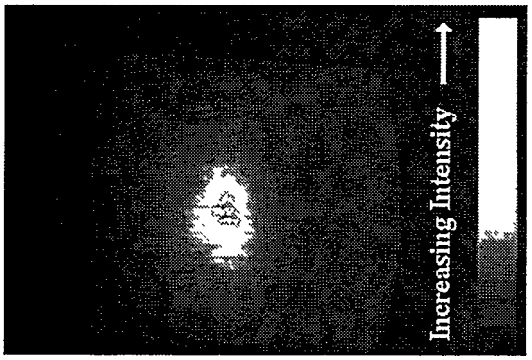

Fig. 3: Fluorescence intensity at the exit of the mixing tube averaged over 48 pulses.

4 FLUORESCENCE OF THE FUEL OIL

4.1 Temperature dependence of the fuel oil fluorescence

The dependence of the fuel oil fluorescence with temperature was measured by preheating the air to temperatures between 450 and 500°C and determining the spatial and temporal (for 300 pulses) average of the fluorescence intensity in the cross section of the laser sheet with the mixing tube of the burner. Experiments at still lower temperatures caused a blackening of the quartz tube. The result of this experiment shows that the fluorescence depends only weakly, compared with the statistical errors, on the temperature. It is also compatible with a T^{-1} dependence (from density) of the fluorescence intensity.

4.2 Dependence of the fuel oil fluorescence on the fuel oil concentration

We measured the LIF intensity averaged over a rectangle at the entrance of the light sheet and averaged over 300 pulses for various mass flows of fuel oil. They corresponded to values of the inverse air equivalence ratio λ_{air}^{-1} in the range between 0.25 and 0.5. Figure 4 shows the measured LIF signal intensity for an air temperature of 450°C. The background has been subtracted. The measurements show an approximately linear rise of the signal intensity with increasing values of $\phi = \lambda_{air}^{-1}$.

Measurements with variation of the air mass flow (which will change the flow pattern in the mixing tube) at constant fuel mass flow showed also (within statistical errors) a linear rise of the LIF signal with the average fuel concentration.

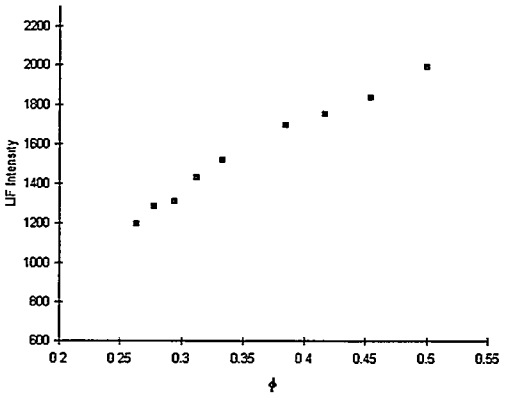

Fig. 4: Integrated fluorescence intensity vs. total fuel flow.

We conclude therefore that the influence of the quenching of excited fuel oil molecules by collisions with other fuel molecules is negligible for the considered fuel oil concentrations. Our results, however, do not allow to make a statement on the situation at technical pressures of 15 bar with correspondingly higher average fuel concentrations. This will be an objective of forthcoming experiments at a test site allowing pressures up to 30 bar.

4.3 Dependence of the fuel oil fluorescence on the residence time of the fuel in the burner

At temperatures of about 400°C, chemical reactions can change the species content of the fuel. Depending on the residence time of the fuel, the fluorescence intensity of the oil may therefore change. As a test experiment, the integrated fluorescence intensity (over the beam cross section and over 50 pulses) was measured at four different distances of the light sheet from the nozzle with a total spatial variation of 3.4 cm. This corresponds to different average residence times of the fuel in the tube. We didn't see any change in the integrated intensity of the fluorescence in this range of spatial variation and conclude therefore that chemical reactions in the vaporized oil have a small effect on the induced fluorescence under our experimental conditions.

4.4 Variation of the excitation wavelength

The oil in the burner was excited with 248 nm light and 100 ns later with 351 nm light. The time delay of 100 ns corresponds to a practically unchanged distribution of the oil in the burner. Figure 5 shows pictures of the induced single pulse fluorescence for oil A at the tube exit with light of the two different wavelengths. The intensity of the image with the 351 nm excitation was scaled up. We see a very similar distribution of the fluorescence intensity.

4.5 Variation of the oil

The study of the mixing process with different oil brands (i.e., in general, of different chemical composition) is both a specification of the general formula for

the fluorescence signal (Eq. 2) and a test on the variability of the behaviour of different oil brands. Indeed, from different physical properties (viscosity, surface tension) of various oils, we have in general to expect a different distribution of the fluorescence intensity.

For the check described in this subsection, we restricted ourselves to an experiment with two oils. Recordings of the fluorescence were made at the entrance of the mixing glass tube with oils B and C under otherwise unchanged conditions.In their physical prop-

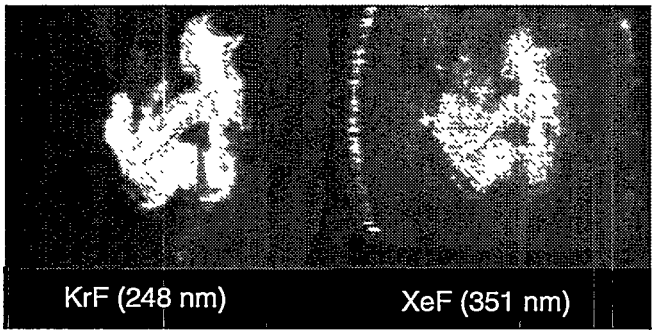

Fig. 5: Recordings of the fuel distribution. Left: excitation with light of 248 nm. Right: excitation with light of 351 nm, with a time delay of 100 ns.

erties, e.g. the viscosity, oils B and C differed strongly. The camera showed for these recordings, contrary to the scheme of Figure 1, into the direction of the laser beam.

Figure 6 shows the result for averages over 100 pulses for oil B and C, respectively. For the comparison, the fluorescence intensity from oil B was multiplied in the reproduced picture by the factor 1.09. Then, we see a very similar distribution of the fluorescence intensity.

5 CONCLUDING REMARKS

Our experiments showed that the irradiation of fuel oil by excimer laser light is suitable to induce fluorescence in the oil. The excitation with short wavelengths (from KrF laser light, 248 nm) can however cause problems due to too strong light absorption. We showed that the fluorescence intensity depends approximately linearly on the average fuel oil concentration (within an assumed error of the measurement) and that it does not depend sensitively on variations of the local temperature.

In order to have a clue whether the fluorescence induced in the oil vapor depends sensitively on the oil composition, we have compared measurements with two different excitation wavelengths for a given oil and with two different oils at a given wavelength. Furthermore, we made measurements at various distances from the nozzle to look for a possible influence of the

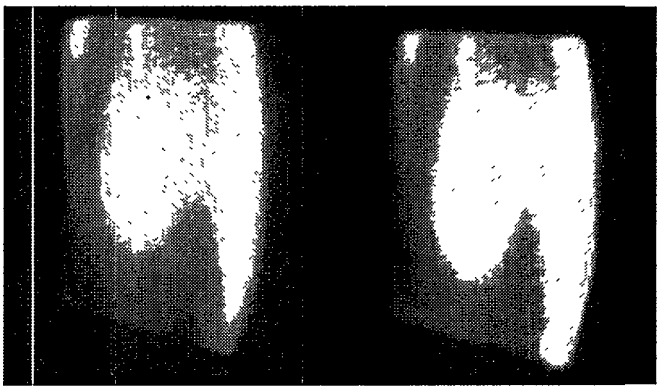

Fig. 6: Comparison of averaged fluorescence signals for oil B (left) and oil C (right) at otherwise same conditions.

average residence time of the fuel in the burner and we performed an additonal Mie scattering experiment to detect nonvaporized oil droplets. At the exit of the mixing tube, where most of the LIF measurements were performed, no Mie scattering signal was observed. From all these tests we conclude that the fluorescence intensity is approximatey proportional to the fuel oil concentration and that laser induced fluorescence is therefore a reliable instrument to investigate the mixing of technical fuel (fuel oil) with air in premixed gas turbine burners.

6 ACKNOWLEDGEMENTS

We thank the team of K. Döbbeling, J. Lloyd, D. Winkler, and W. Weisenstein of ABB Corporate Research for the possibilty to use the test site of ABB, for the construction of the optical access of the burner, and for active help during the experiments.

For financial support we acknowledge ABB Corporate Research in Baden-Dättwil, Switzerland and the Swiss Federal Office of Energy (BFE) in Bern.

7 REFERENCES

[1] R. Bazile, D. Stepowski, *Measurements of the vaporization dynamics in the development zone of a burning spray by planar laser induced fluorescence and Raman scattering*, Exp. in Fluids **16**, 171-180 (1994).

[2] M. Rachner, M. Brandt, H. Eickhoff, C. Hassa, *A numerical and experimental study of fuel evaporation and mixing for lean premixed combustion at high pressure*, 26th Symp. (International) on Combustion, The Combustion Institute, 2741-2748 (1996).

[3] S.C. Harding, D.A. Greenhalgh, *Fuel-air mixing and combustion in an optical lean, premixed, prevaporised gas turbine combustor,* paper presented at the International Gas Turbine & Aeroengine Congress, Stockholm, June 2-5 (1998).

MEASUREMENT OF GAS FLOW VELOCITIES BY LASER-INDUCED GRATINGS

B. Hemmerling, D.N. Kozlov (General Physics Institute, Moscow), A. Stampanoni-Panariello

Time resolved light scattering from laser-induced electrostrictive gratings was used for the determination of flow velocities in air at room temperature. By measuring the velocity profile across the width of a slit nozzle we demonstrated the high spatial resolution (about 200 μm) of this novel technique.

To characterise a reacting gas flow, as represented by, for example, a flame, one has to measure temperature, density, and velocity. Coherent anti-Stokes Raman scattering (CARS) is the method of choice for the non-intrusive determination of temperatures and densities. However, although CARS is a fairly mature method, it is still a demanding measurement to make, and it is not yet available as an off-the-shelf technique. Modern systems for the measurement of flow velocity have attained a high level of technological development, and techniques as Laser Doppler Velocimetry (LDV) and Particle Imaging Velocimetry (PIV) became commercially available during recent years. However, these methods rely on seeding of the flow with particles, which narrows the field of possible applications. Doppler shift of atomic or molecular absorption or Raman frequencies has been employed in a number of applications to measure the flow velocity. Flow tagging is based on marking the flow components with one laser and monitoring the temporal evolution of the mark with another laser. Laser-induced electrostrictive gratings have a potential for the simultaneous determination of temperature and flow velocity. While the measurement of temperatures has already been demonstrated [1], we report in this contribution on the possibility to determine flow velocities by laser-induced electrostrictive gratings.

Laser-induced electrostrictive gratings are generated in a medium by the sinusoidal spatial intensity distribution formed by the interference of two pulsed laser beams. The electric field of the interference pattern polarises the medium and the spatial inhomogeneity of the field exerts a force acting on the medium. Sound waves are generated, with the wavelength defined by the fringe spacing of the interference pattern. They propagate in two opposite directions, normal to the planes of the fringes. The counter-propagating sound waves form a standing acoustic wave and thereby a spatially periodic density grating that oscillates in time. Satisfying the Bragg condition, this grating can be read out by the beam of another laser.

The experimental set-up is explained in detail in Ref. 1 and only the most salient features will be repeated here. Two pump beams, provided by a pulsed Nd:YAG laser at a wavelength of 1064 nm, are focused by the same lens (f = 1000 mm) and intersect in the measurement region at an angle of about 0.6°.

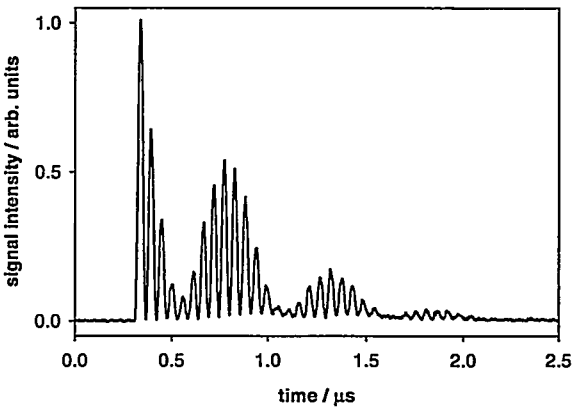

Fig. 1: Temporal evolution of the signal intensity in a flow in ambient air. The grating was formed at the exit of a slit nozzle (see text), and the flow rate through the nozzle was 100 l/min.

The read-out beam is furnished by a cw Ar^+ laser. It enters the interaction volume opposite to the direction of the pump beams, is focused by a second lens (f = 1000 mm), and is aligned to satisfy the Bragg condition. The signal beam is collimated and is directed over a distance of 5 m onto the aperture of a photomultiplier tube. By using a pulsed laser for the grating formation and a cw laser for the read-out process one can follow the temporal evolution of the grating. The time resolved acquisition of the signal is performed by a digitizer with a full bandwidth of 500 MHz and a 2 GHz sampling rate.

All measurements were carried out at room temperature in air flows. Consider the flow propagating parallel to the z axis and the exit plane of the nozzle lying in the x-y plane. The nozzle was manufactured from a copper tube by squeezing one of its ends so that a channel with a square-shaped cross section was formed. This channel had a length of about 20 mm (z direction). The short side of the slit nozzle, the width, measured 1.5 mm in x direction and the long side measured 18 mm in y direction.

Figure 1 depicts the temporal evolution of the signal intensity, averaged over 100 laser shots, which is obtained from a grating formed in the y-z plane at the exit of the nozzle. The line bisecting the intersection angle of the two pump beams is parallel to the y axis. About 100 l/min of air at room temperature were put through the nozzle. The fast oscillation of the signal intensity is due to the standing acoustic wave, which is formed by the two pump beams. From the measured oscillation period and the known intersection angle of the two pump beams one can deduce the sound velocity in the medium and thereby the temperature [1]. The overlaying slower oscillation of the signal intensity is caused by the flow. We assume that this additional modulation of the signal is due to the Doppler shift experienced by the two pump beams in the system of the flow. An increase of the flow velocity leads to a shorter oscillation period.

We verified the proportionality between the frequency of the overlaying oscillation of the signal intensity and the air flow rate in the range 10 l/min-200 l/min (see Figure 2).

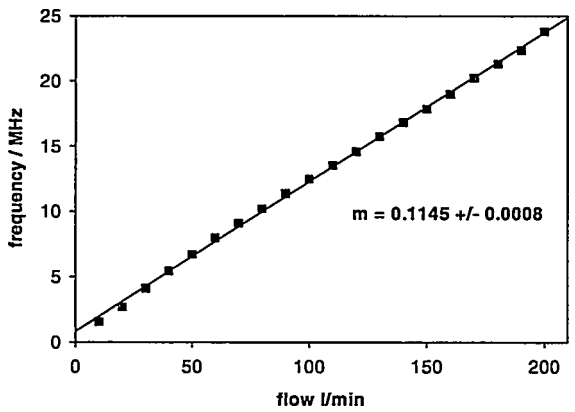

Fig. 2: Frequency of the overlaying oscillation structure versus the air flow rate through the nozzle.

Due to the high spatial resolution of the grating technique in x direction (about 200 µm), we were able to measure the velocity profile across the width (x direction) of the nozzle at a distance of 1 mm from its edge (see Figure 3). The throughput of air was 52 l/min.

At a large downstream distance from the inlet the velocity distribution is assumed to be uniform and parabolic across the height of the nozzle. However, the measured velocity profile rather resembles a plug flow, indicating that the channel, following the inlet section of the nozzle, is too short. From the cross section of the nozzle and flow rate we calculated an averaged flow velocity of 34 m/s. This agrees well with the velocity measurement by the laser-induced grating method.

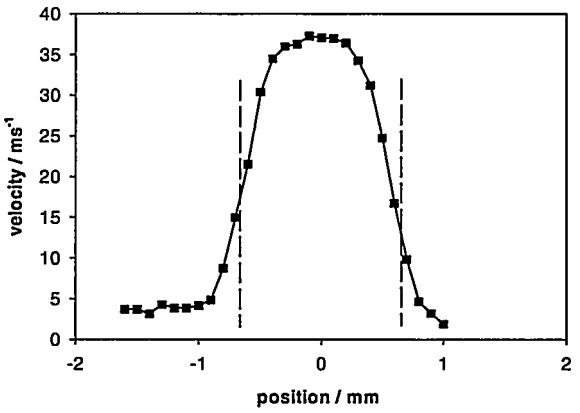

Fig. 3: Velocity profile across a nozzle with a slit width of 1.5 mm and an air throughput of 52 l/min. The dashed lines mark the positions of the nozzle walls.

Further work is directed towards a comparison of the laser-induced grating method with already established velocity measuring techniques. From a theoretical point of view we have to verify that the Doppler shift of the two pump beams is the origin for the additional modulation of the grating signal.

ACKNOWLEDGEMENT

We thank the Swiss Federal Office of Energy (BFE) for financial support.

REFERENCES

[1] A. Stampanoni-Panariello, B. Hemmerling, W. Hubschmid, *Temperature measurements in gases using laser-induced electrostrictive gratings*, Appl. Phys. **67**, 125-130 (1998).

INVESTIGATION OF SOOT BY TWO-COLOR FOUR-WAVE MIXING

B. Hemmerling, A. Stampanoni-Panariello

A novel, non-intrusive technique has been used for the temporally resolved investigation of the interaction of laser radiation and soot in a flame. While there is a fairly good agreement between measurement and simulation remaining discrepancies indicate some shortcomings of the model employed.

During recent years, concerns about the health impact of particulate emissions of fossil combustion processes have fostered the development of sophisticated diagnostic methods for in-situ soot measurements. From a more applied point of view, to properly design the walls of combustion chambers one has to know the energy flux by electromagnetic radiation from a technical flame. Because the band radiation of the gas molecules is strongly affected by the local soot concentration there is a demand for non-intrusive diagnostics of soot. Besides light scattering and extinction measurements, laser-induced fluorescence of C_2 from laser-vaporised soot, and laser-induced incandescence have been used to characterise soot in flames in terms of number density, particle diameter, and soot volume fraction. Laser-induced gratings have been proposed for temperature measurements in sooty flames. However, little is known about the interaction of soot particles and laser radiation. To gain some insight into this process we employed the technique of two-colour four-wave mixing (TCFWM).

In the process of TCFWM, the non-linearity of the investigated medium couples two pump beams of one wavelength and a probe beam of another wavelength to a signal beam having the same wavelength as the probe beam. In our experiment the two pump beams, with a wavelength of 1064 nm, are provided by a pulsed Nd:YAG laser (Continuum, NY81-20), and the probe beam is furnished by a cw Ar^+ laser (Spectra Physics 587 Z-LOK). The pulse length of the pump laser is about 8 ns. The experimental set-up is similar to the one used for laser-induced gratings and is explained in detail in Reference 1. However, in the present set-up all beams propagate within the same plane.

To avoid contributions to the signal that originate from thermal gratings [1] we used perpendicularly polarised pump beams. The pump beams are focused by the same lens (f = 1000 mm) and intersect in the measurement region at an angle of 0.6°. In opposite direction the probe beam passes a polariser, is focused by a second lens (f = 1000 mm), and is aligned to satisfy the Bragg condition. The signal beam is collimated, passes an analyser, and is directed over a distance of 5 m onto the aperture of a photomultiplier tube (Philips

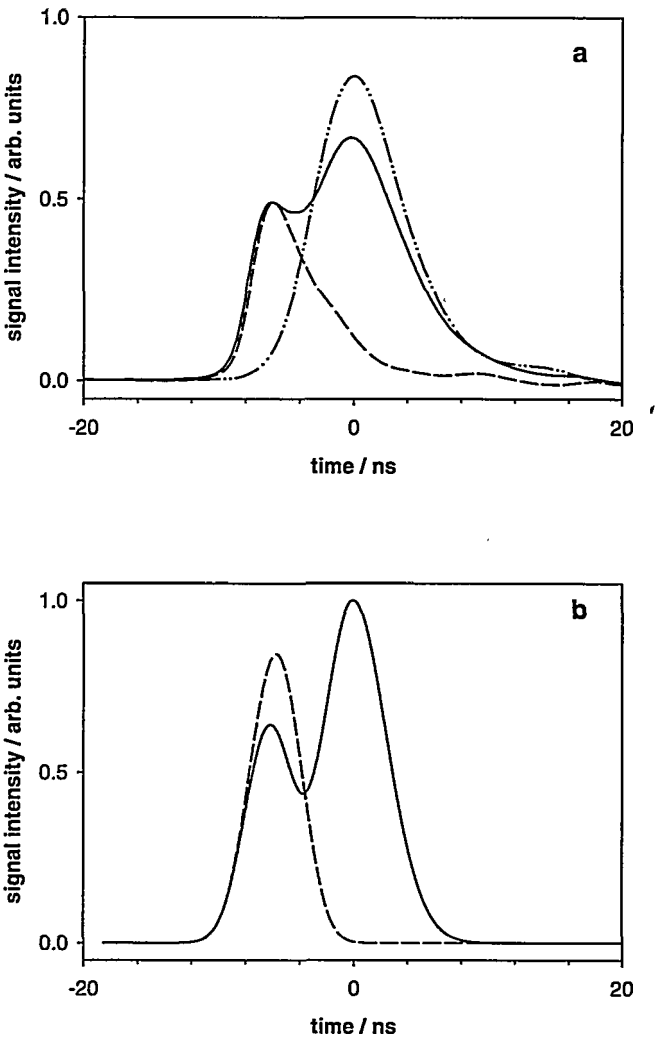

Fig. 1: **a** Measured temporal behaviour of the resonant signal (solid line) and the non-resonant signal (dashed line). Represented by the dashed-dotted line is the temporal signature of the pump pulse. **b** Calculated temporal behaviour of the resonant signal (solid line) and the non-resonant signal (dashed line).

XP2020). The analyser in the signal path is set to an angle of 90° with respect to the polarisation of the probe beam. The time resolved acquisition of the signal is performed by a digitizer (Tektronics, RTD 720) with a full bandwidth of 500 MHz and a 2 GHz sampling rate.

Figure 1a depicts the temporal evolution of two TCFWM signals acquired in the vicinity of the flame front of a acetylene/air diffusion flame. The signal, displayed by the dashed line, was obtained employing the 488 nm emission line of the Ar^+-laser as probe beam. With exception of the emission line at 514 nm, other emission lines of the Ar^+-laser (496 nm, 476 nm, 458 nm) caused a similar temporal behaviour of the signal. Throughout the text this signal will be referred to as the non-resonant one. The temporal signature of the TCFWM signal changes and exhibits a double-peak structure if radiation of the Ar^+-laser at 514 nm was used as probe beam (solid line in Figure 1a). We will refer to this signal as the resonant one. Also displayed in Figure 1a is the temporal signature of the exciting Nd:YAG laser pulse (dashed-dotted line). The measured pulse width of 8.3 ns (FWHM) is comprised of 7.5 ns actual pulse width, measured by a fast photo diode, and of 3.5 ns temporal response of the detection system (digitizer, photo-multiplier). All signals, which are displayed in Figure 1a, were averaged over 100 single shot measurements. As origin of the time scale we selected the middle of the excitation pulse.

Soot particles in the flame absorb the incident laser light and heat to temperatures far above ambient. On the leading wing of the laser pulse the temperature of the soot particles rises with time. Below 3300 K, heat transfer to the medium is the dominant energy loss mechanism. Above 3700 K, energy loss due to vaporisation becomes the governing process. The vapour, streaming away from the particle surface, consists primarily of C_3, but also contains some C_2 and C species as well. The large heat of vaporisation of carbon prevents the particle from reaching temperatures far above the boiling point rendering heat loss by radiation unimportant. Therefore, at high temperatures the absorbed laser energy is solely compensated by vaporisation that causes shrinking of the soot particle. In deriving the coupled differential equations for the time dependence of temperature and radius of a laser-heated particle, we followed closely the treatment by Melton [2]. The energy balance of the particle is made, respectively, by the absorbed laser energy, the energy expended for vaporisation, the energy transfer to the surrounding medium by heat conduction, internal energy rise, and radiation. For the pump laser intensities, employed in our experiment, the simulation indicates complete evaporation of the soot particle already on the leading wing of the laser pulse. We interpret the non-resonant signal as a TCFWM signal that is solely caused by the solid particle. In this way, the temporal evolution of the non-resonant TCFWM signal mirrors the evaporation process. Due to an accidental coincidence of the wavelengths of the Ar^+-emission line at 514 nm and a transition in C_2, the resonant signal is comprised of the signal generated by the solid particle

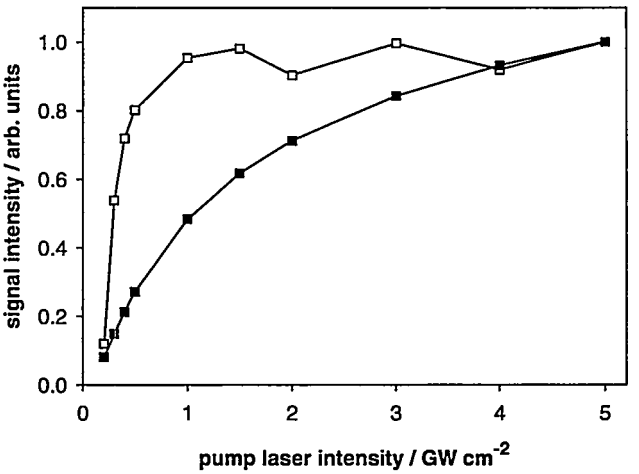

Fig. 2: Dependence of the non-resonant signal intensity upon the pump laser intensity (*solid square*: calculation; *open square*: measurement).

and a signal formed in the vapour zone. In this way, the resonant signal additionally depicts the formation of C_2 by evaporation. Figure 1b shows the result of the simulation. There is a good qualitative agreement with the measurements. However, some discrepancies remain. A plot of the non-resonant signal intensity versus the pump laser intensity is depicted in Figure 2. While the simulation predicts an continuous increase of the signal intensity with increasing pump laser intensity (filled squares), the measurement shows a rapid increase of the signal at low levels of the pump laser intensity and a levelling off of the signal at higher intensities (open squares). Because a threshold behaviour is less probable for a non-resonant TCFWM-process, the measured intensity dependence of the non-resonant signal indicates some short-comings of the employed evaporation model. A double logarithmic plot of the resonant signal intensity versus the pump laser intensity shows for the measurement a linear relationship with a slope of 5.4 ± 0.3. This is considerable larger than the expected quadratic dependence on the pump laser intensity and suggests a more complicated generation process of the resonant signal.

ACKNOWLEDGEMENT

We thank the Swiss Federal Office of Energy (BFE) for financial support.

REFERENCES

[1] A. Stampanoni-Panariello, B. Hemmerling, W. Hubschmid, *Temperature measurements in gases using laser-induced electrostrictive gratings*, Appl. Phys. **67**, 125-130 (1998).

[2] L.A. Melton, *Soot diagnostics based on laser heating*, Appl. Opt. **23**, 2201-2208 (1984).

HYDROLYSIS OF ISOCYANIC ACID ON SCR CATALYSTS

M. Elsener, M. Kleemann, M. Koebel

Standard SCR catalysts possess high activity for the hydrolysis of HNCO and thus explain the suitability of urea as a selective reducing agent for NO_x. At high space velocities HNCO-slip can get perceptible over the entire temperature range. This can be attributed to the fact that the temperature dependence is strong for the SCR reaction, but weak for the hydrolysis reaction.

1 INTRODUCTION

Urea-SCR, the selective catalytic reduction using urea as reducing agent, is presently the most promising way to diminish NO_x emissions originating from heavy duty vehicles, especially trucks [1, 2]. Urea is considered a solid storage compound for ammonia and is usually used as an aqueous solution (30-40%). When this solution is atomised into the hot exhaust gas stream the droplets first lose water by evaporation. The next step is the thermal decomposition of urea into ammonia and isocyanic acid:

$$NH_2\text{-}CO\text{-}NH_2 \rightarrow NH_3 + HNCO \quad (1)$$

The ammonia formed may directly participate in the SCR reaction. Isocyanic acid is stable at these temperatures (150-500°C) in the humid gas phase, but rapidly hydrolyses over various solid oxides:

$$HNCO + H_2O \rightarrow NH_3 + CO_2 \quad (2)$$

It has therefore been proposed to use an additional „hydrolysis catalyst" upstream of the SCR catalyst [3]. On the other hand our experiments on a diesel test stand have shown that at moderate space velocities (GHSV) the performance of the SCR catalyst does not depend on the type of reducing agent used (urea or ammonia). However, if the catalyst is operated at higher space velocities, the effluent gas stream shows a definite slip of HNCO in addition to NH_3-slip. This is not expected at high temperatures considering the thermodynamic equilibrium of equation (2).

In the following we compare the rate of HNCO hydrolysis with the rate of the SCR reaction. First order rate laws are assumed with respect to HNCO and NO, respectively.

2 EXPERIMENTAL

A gas stream of 250 l_N/h containing 5% H_2O, 10 % O_2, ≈1000 ppm HNCO, ≈100 ppm NH_3, 1000 ppm NO, balance N_2 was used in the tests. The gas stream was fed to a microreactor containing the crushed catalyst samples (≈0.12 g). An FTIR spectrometer (Nicolet Magna 560) was used to analyse the gas composition before and after the reactor.

The HNCO gas stream was obtained by passing a stream of dry nitrogen (≈15 l_N/h) over a bed of cyanuric acid contained in a steel reactor. The bed was kept at a constant temperature of 300-330°C and was followed by a second heating zone at 480°C to obtain complete depolymerisation of cyanuric acid. In this way a constant flux of HNCO was obtained which, however, contained about 10 % of NH_3 as an impurity due to hydrolysis.

Two commercial catalysts based on TiO_2-WO_3-V_2O_5, crushed and sieved to a particle fraction of 0.16-0.20 mm, were tested. They bear the PSI-internal designation D21 and D35 and contain ≈1 and ≈3 % V_2O_5. Further details on these catalysts and the determination of their respective SCR rate-constants using ammonia have been given previously [4].

3 RESULTS AND DISCUSSION

The measured conversions of HNCO and NO were used to calculate the first order rate constants of the HNCO hydrolysis and of the SCR reaction. No corrections for external and internal mass transfer were applied in these calculations. The rate constants thus obtained could only be used for a relative comparison. We emphasise that very high space velocities (≈10^6 h^{-1}) were necessary for the determination of the high rates of HNCO hydrolysis. This leads to low conversions of NO that could therefore be measured only with very limited precision.

Figure 1 shows typical results for catalyst D21 (≈1 % V_2O_5) and Figure 2 for catalyst D35 (≈3 % V_2O_5). Earlier determinations of the SCR reaction kinetics obtained with ammonia as reducing agent and corrected for mass transfer [4] are also included for comparison (dashed lines).

Both figures show the same basic behaviour: at low temperatures the rate constant for the hydrolysis of HNCO is several orders of magnitude higher than the respective rate constant for the SCR-reaction with NO. This difference is definitely more pronounced with D21 containing less V_2O_5. Due to the fast hydrolysis of HNCO the catalyst still uses NH_3 as the effective reductant, even if the dosed reductant is urea. This is true at least at low-to-medium temperatures.

This fact therefore explains our previous observations in diesel test stand experiments, where we found similar values of NO_x-reduction for both urea and ammonia. The fact that the rates of hydrolysis and of SCR converge at higher temperatures is also in agreement with the observed increase of HNCO efflux with rising catalyst temperature in test stand experiments using urea.

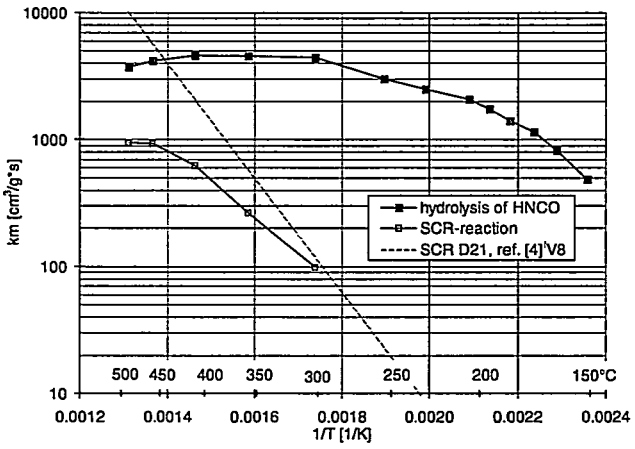

Fig. 1: Uncorrected reaction rate constants for hydrolysis of HNCO and SCR for catalyst D21.

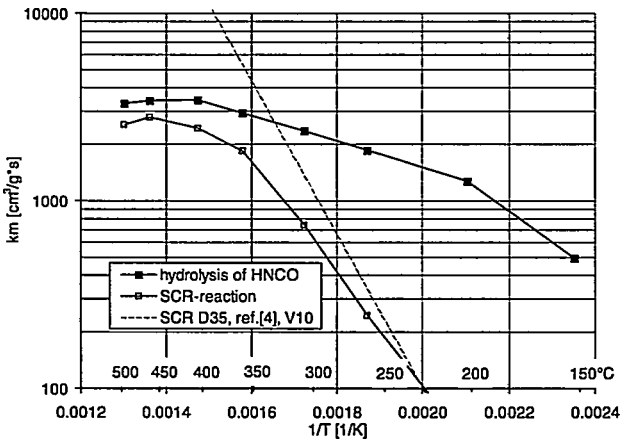

Fig. 2: Uncorrected reaction rate constants for hydrolysis of HNCO and SCR for catalyst D35.

Focusing on the hydrolysis of HNCO we stated above that the calculation of truly intrinsic kinetic parameters for the first order rate constants is not useful due to the very high reaction rates that are falsified by internal and external mass transport limitations. The Arrhenius plots show a decreasing slope at higher temperatures. This is expected when mass transfer limitations begin to prevail. However, at the highest temperatures examined (>400°C), the rate constant (or HNCO conversion) actually decreases. This can be no longer attributed to mass transfer limitations alone, but to a real decrease of the reaction rate. This is probably due to a decrease of one of the reactive intermediates adsorbed on the catalyst:

a) Assuming an *Eley-Rideal* mechanism where adsorbed water reacts with HNCO from the gas phase: The decreasing water adsorption with rising temperature will reduce the reaction rate of HNCO hydrolysis. The importance of adsorbed water is further supported by the experimental observation from Figure 3 that NH_3 has a negative effect on the rate of hydrolysis: NH_3 and H_2O probably compete for the same adsorption sites.

b) Assuming a *Langmuir-Hinshelwood* mechanism where both H_2O and HNCO react from an adsorbed state: in this case the decreasing adsorption of HNCO with rising temperature would be mainly responsible for the decreasing rate.

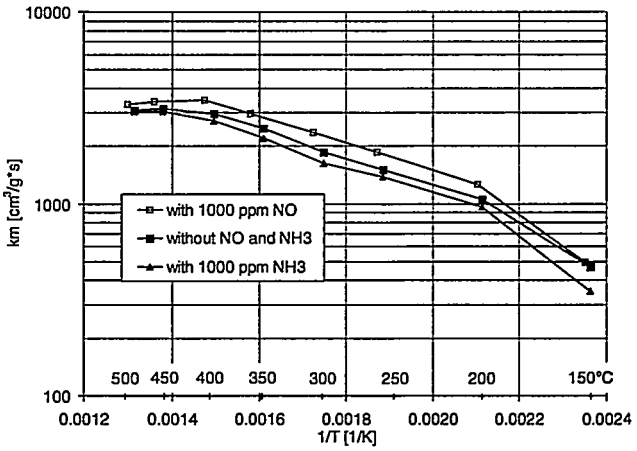

Fig. 3: Influence of ammonia and NO on the uncorrected reaction rate constants for hydrolysis of HNCO.

In conclusion we may say that the hydrolytic decomposition of isocyanic acid is a very fast reaction on standard SCR catalysts. This rate can exceed the SCR reaction rate by several orders of magnitude at lower temperatures, but approaches the SCR rate at higher temperatures. Using urea as selective reductant the problem of HNCO efflux may not only arise at very low temperatures, but also at high temperatures (above 400°C) due to incomplete conversion. However, in the practical application of urea-SCR to diesel engines urea solution is usually atomised directly into the exhaust gas stream. The formation of gaseous HNCO is then preceded by the additional steps of water evaporation from the droplet and the thermal decomposition of urea, which further complicate the exact understanding of urea-SCR.

4 REFERENCES

[1] M. Koebel, M. Elsener, T. Marti, *NO_x-Reduction in Diesel Exhaust Gas with Urea and Selective Catalytic Reduction*, Combust. Sci. and Tech. **121,** 85-102 (1996).

[2] G. Fränkle et al., *SINOx The Exhaust Gas Purification System for Trucks*, 18th Int. Wiener Motorensymposium, April 24-25 (1996).

[3] EP Application 0487886A1, MAN Technologie AG, Munich (1991).

[4] M. Koebel, M. Elsener, *Selective catalytic reduction of NO over commercial DeNOx-catalysts: experimental determination of kinetic and thermodynamic parameters.* Chem. Eng. Sci. **53,** 657-669 (1998).

[5] M. Koebel, M. Elsener, *Selective catalytic reduction of NO over commercial DeNOx-catalysts: Comparison of the measured and calculated performance,* Ind. Eng. Chem. Res. **37,** 327-335 (1998).

Consequences of Energy Use for Atmosphere and Climate

INCREASING ALPINE TRANSIT TRAFFIC THROUGH SWITZERLAND WILL CONSIDERABLY ENHANCE HIGH ALTITUDE ALPINE POLLUTANT LEVELS

A.S.H. Prévôt, J. Dommen, M. Furger, W.K. Graber

Within the EU-Project VOTALP (Vertical Ozone Transports in the ALPs), we have shown that deep alpine valleys like the Mesolcina Valley very efficiently transport air out of the polluted valley up to altitudes between 2000 and near 4000 m asl (above sea level). Pollutants emitted in these valleys are very efficiently transported up to high altitudes.

1 INTRODUCTION

In the Mesolcina Valley, we performed an intensive field campaign to study vertical exchange mechanisms of atmospheric constituents between the boundary layer and the free troposphere. Scintillometers, aircraft and ground based instruments were used to measure winds.

2 AIR VOLUME BUDGET

The concept mainly consists of the measurement of the up-valley flow at two cross-sections in a valley. The resulting flow difference is the net vertical air volume flux. The cross-sections in the Mesolcina valley were separated by about 20 kilometers (Figure 2). The budget volume was confined to the up-valley wind regime typically reaching altitudes up to around 2000 m asl.

The air volume flux calculations on 5 field experiment days yielded 300 to 600 km^3/day for the lower cross-section and 30 to 150 km^3/day volume flux for the upper cross-section during the up-valley wind periods, typically lasting from 10 h to 18 h (Table 1). The resulting net vertical flux of this valley section with a volume of 100 km^3 varied from 270 to 580 km^3, about 3 to 5 times larger than the valley volume [1].

	Santa Maria Castaneda (km^3/day)	Pradiron Sei (km^3/day)	Vertical flux (km^3/day)
July 19	650	70	580
July 22	600	150	450
August 16	300	30	270
August 17	500	100	400
August 18	600	140	460

Table 1: Air volume fluxes through the southern (Santa Maria-Castaneda) and northern cross-section (Pradiron-Sei) during the up-valley wind periods of each of the five days.

3 DISCUSSION

The deep valleys near the Alpine crest are most efficient in transporting air from the polluted boundary layer up to the pristine high Alpine areas. On the main transit routes, the traffic, including heavy trucks, is emitting a manifold of what is expected from emission measurements on level roads. The past increase and the expected future increase of traffic through the Alps has led and will lead to large enhancements of pollutants in the high Alpine area and generally in the lower free troposphere of Central Europe (Figure 1). The high altitude concentration increases are a possible threat to fragile Alpine ecosystems. Vertical transport of aerosols, also emitted by traffic, will lead to a further reduction of visibility in the Alps.

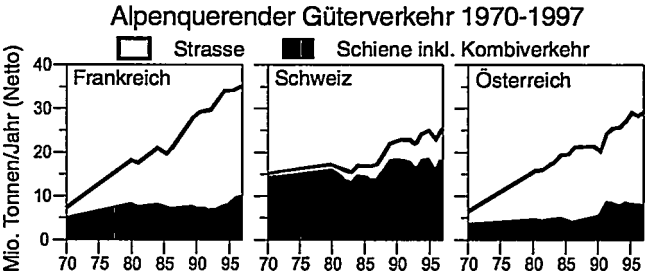

Fig. 1: Increase of goods traffic on the most important Alpine transit roads in Switzerland, Austria and France between 1970-1997 [2].

4 REFERENCES

[1] A.S.H. Prévôt, M. Furger, B. Neininger, L. Poggio, J. Dommen, W.K. Graber, *Mesolcina Valley = Highly Efficient Air Pump For Vertical Transport,* Eighth Conference on Mountain Meteorology, Flagstaff, Arizona, August 3-7, American Meteorological Society, 401-403 (1998).

[2] GVF, Alpenquerender Güterverkehr auf Strasse und Schiene 1987, 1991, 1996 und 1997, GVF-News, 48/1, Alpinfo Güterverkehr, Dienst für Gesamtverkehrsfragen, Bern.

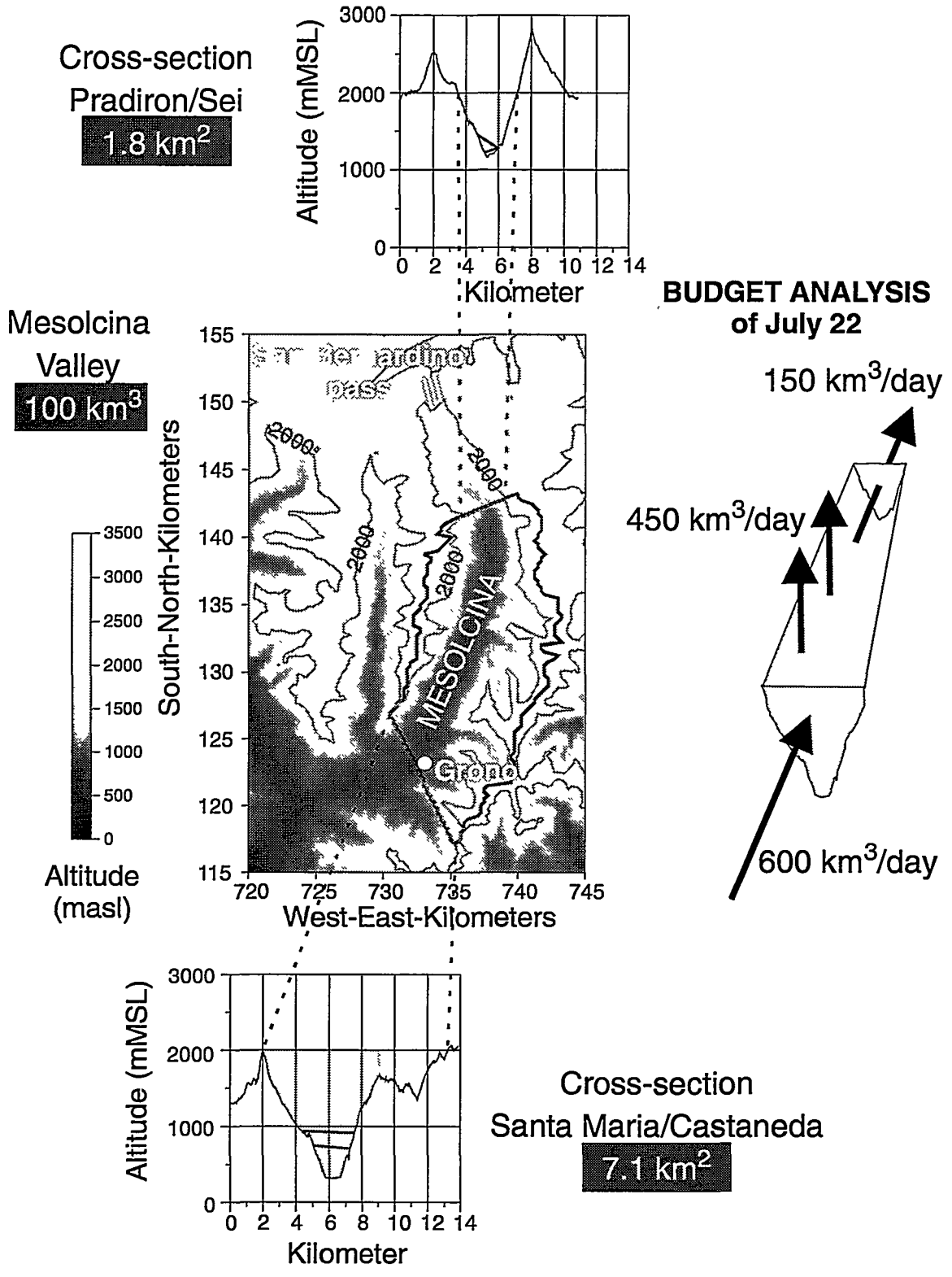

Fig. 2: Section of the Mesolcina valley used for the budget analysis. The cross-sections include the scintillometer beam paths. Air flux calculation results of July, 22 are shown.

HOW REPRESENTATIVE WAS THE 1996 VOTALP MESOLCINA VALLEY CAMPAIGN?

M. Furger

Each meteorological measurement reflects the conditions under which it was obtained, e.g. site, weather, and instrumentation. It is shown how the VOTALP Intensive Observation Periods (IOPs) [1] were embedded in the climatic context of the summer months of 1996.

1 METHODS

Episodic atmospheric measurements must be carefully evaluated before any generalisation of the observations can be made. In contrast to laboratory work, field work can never be repeated under identical weather conditions. The methods of synoptic climatology provide a tool for the evaluation of weather situations. We used the synoptic weather situations of the Alpine Weather Statistics ('Alpenwetterstatistik', AWS, [2]) for July and August 1987-96. This 10-year period is considered more typical for the nineties than the whole 50-year period. In AWS one of 40 weather situations is assigned to each day, according to a set of parameters obtained from measurements and synoptic weather charts. These 40 weather situations are grouped into 8 synoptic groups for more convenience, each group representing characteristic synoptic situations in the central Alps. Frequencies of occurrence of the synoptic groups in July and August 1996 were compared to the frequencies of the 10-year period. In addition, time series of ozone and meteorological parameters were analysed with conventional statistical methods.

2 RESULTS

It becomes evident from Figure 1 that in 1996 a strong predominance of indifferent (I) weather situations occurred, and that anticyclonic (A) situations were remarkably underrepresented. While the synoptic group I occurred in 35 % of all cases during the 10-year period, its frequency in 1996 was 47 %. Group A at the same time comprised only 8 % instead of 34 %. Persistence was not high for the southern valleys, because the Alps were under the influence of a succession of fronts such that no weather situation lasted for more than 4 days. The IOP days belonged to the groups I (22 July, 17 August), N (19 July, 16 and 18 August) and W (23 July). The AWS data reveal that convective activity was high, and that cloudiness often reduced the amount of sunshine received within the valleys and hence the local formation of ozone. Furthermore days with northerly advection (group N) were about twice as frequent in 1996 than in the 10-year period. Weak northerly flow leads to reduced cloudiness south of the Alpine crest and thus favours the generation of thermal circulations which transport polluted air into the valleys. Strong northerly flow may delay or completely suppress the formation of the up-valley winds.

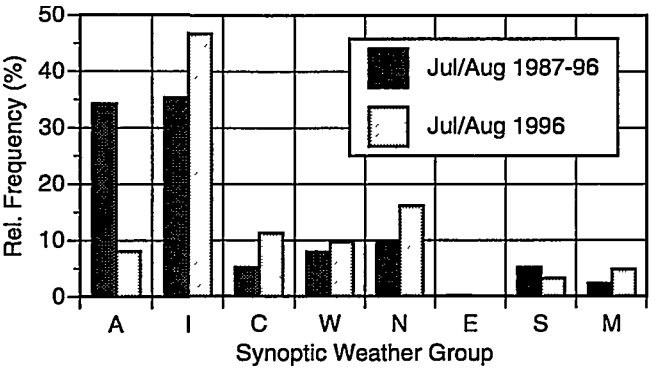

Fig. 1: Relative frequencies of occurrence of the synoptic situations from the Alpine Weather Statistics, for July and August of the periods 1987-96 and for 1996.

Ozone concentrations did not reach extreme levels in 1996, but both IOPs exhibited ozone levels that were above average.

3 CONCLUSION

The summer of 1996 was remarkable with respect to a rather low persistence of anticyclonic conditions. The Azores high never really stretched into the continent, and the general weather development was characterised by a succession of cold fronts moving over central Europe. This strong variability also limited the build-up of very high ozone concentrations. Hence, the VOTALP Mesolcina valley measurements may be regarded as representative for normal, non-extreme summer ozone situations.

4 ACKNOWLEDGEMENT

This study was supported by the Swiss Federal Office for Education and Science grant 95.0386-2.

5 REFERENCES

[1] M. Furger, J. Dommen, W.K. Graber, L. Poggio, A. Prévôt, B. Neininger, *The VOTALP valley campaign 1996 - results and climatological evaluation*, 25th International Conference on Alpine Meteorology (ICAM'98), Turin, Italy (1998).

[2] H. Wanner, E. Salvisberg, R. Rickli, M. Schüepp, *50 years of Alpine Weather Statistics (AWS)*, Meteorologische Zeitschrift, **N.F. 7**, 99-111 (1998).

PLUME SPREAD AND ATMOSPHERIC STABILITY

R.O. Weber

The horizontal spread of a plume in atmospheric dispersion can be described by the standard deviation of horizontal direction. The widely used Pasquill-Gifford classes of atmospheric stability have assigned typical values of the standard deviation of horizontal wind direction and of the lapse rate. A measured lapse rate can thus be used to estimate the standard deviation of wind direction. It is examined by means of a large dataset of fast wind measurements how good these estimates are.

The transport and dispersion of air pollutants depend on the mean wind field and on turbulent properties of the atmosphere. The horizontal spread of a plume in atmospheric dispersion can be described by the standard deviation of horizontal wind direction, which is one of the fundamental parameters describing turbulent dispersion, but is difficult to measure directly. Another way of describing the turbulent state of the atmosphere is the definition of atmospheric stability classes as done by Pasquill and Gifford. Each of the so-called Pasquill-Gifford classes has assigned typical values of the standard deviation of horizontal wind direction and typical values of the lapse rate, which is defined as the negative vertical temperature gradient. A measured lapse rate can thus be used to estimate the standard deviation of wind direction.

On a building of the Paul Scherrer Institute a small mast (14 m high) was mounted bearing an ultrasonic anemometer on top. A total of 1431 hours of wind data measured every 0.048 seconds is available. From these data, the standard deviation of wind direction is calculated with a fast multipass method [1]. On the PSI area, the air temperatures at 2 m and at 70 m are routinely measured by the Swiss Meteorological Institute. From these temperature measurements the lapse rate is calculated.

In Figure 1a, the standard deviation of wind direction is shown as a function of the vertical temperature gradient. The two quantities seem to be unrelated. Large values of the standard deviation are observed for all temperature gradients and, therefore, for all stability classes. To see a possible effect of the wind speed condition on the standard deviation, the data are stratified into low and high wind speed conditions. Figure 1b shows the data for high wind speeds. The observed data are fairly well represented by the parameterization as taken from [2], although in many cases the observed standard deviation is larger than the one estimated from the lapse rate. The few outliers may be due to sudden changes of wind direction during the sampling period. Figure 1c shows the data for low wind speeds. Under these light wind conditions large standard deviations are observed. Thus, the lapse rate gives often, mainly in low wind speed conditions, a poor description of dispersion in the atmosphere.

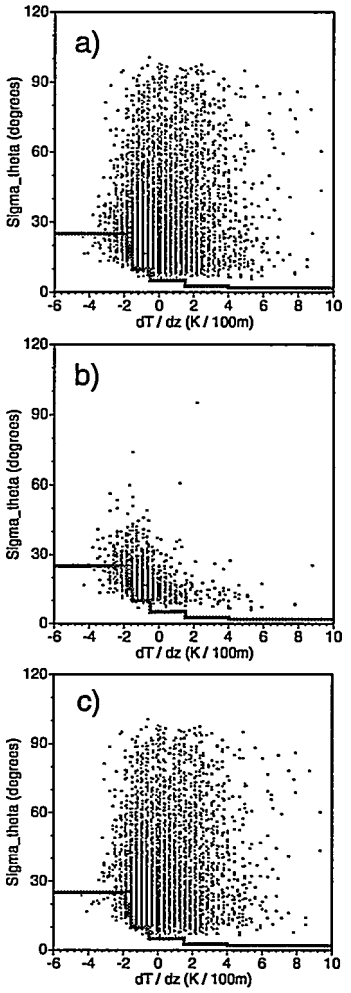

Fig. 1: Standard deviation σ_θ of horizontal wind direction as a function of vertical temperature gradient: a) for all 8588 10-min averages, b) for v>2.5 m/s, c) for v<2.5 m/s. The solid line represents the parameterization taken from [2].

ACKNOWLEDGEMENTS

The author thanks M. Furger and G. Stefanicki from PSI for their help with the wind measurements and the Swiss Meteorological Institute for kindly providing the temperature measurements.

REFERENCES

[1] R.O. Weber, *Estimators for the standard deviation of horizontal wind direction*, J. Appl. Meteor. **36**, 1341-1353 (1997).

[2] U.S. Nuclear Regulatory Commission (NRC), *On-site meteorological programs, regulatory guide 1.23*, U.S. NRC, Washington (1972).

TWO-SCALE ANALYSIS OF INTERMITTENCY IN FULLY DEVELOPED TURBULENCE

R. Badii, P. Talkner

A self-affinity test for turbulent time series is applied to experimental data for the estimation of intermittency exponents. The method employs exact relations satisfied by joint expectations of observables computed across two different length scales. One of these constitutes a verification tool for the existence and the extent of the inertial range.

1 INTRODUCTION

The fundamental theory of turbulence focuses on the scaling properties of velocity differences measured at different spatio-temporal points in fluids [1]. The velocity field in a regime of fully developed turbulence exhibits approximate self-affine properties upon a suitable rescaling of time, space, and velocity [1,2]. In fact, longitudinal velocity differences d computed across nested intervals are, on average, proportional to each other, provided that the interval lengths belong to the so-called inertial range. This is delimited by Kolmogorov's length, below which dissipation prevails, and by the outer length, at which external forces input energy into the system.

As a consequence, the moments of order p of the distribution of d present a remarkable power-law behaviour in the intervals' lengths with universal exponents ζ_p which, however, do not depend linearly on p. Not only the nonlinearity of ζ_p is in contrast with Kolmogorov's first prediction [1] but the existence itself of an inertial range is often questionable, especially for large p [3].

The deviations from self-affinity are quite large and cannot be treated perturbatively. Moreover, the behaviour for large p is hardly accessible from the data because of a lack of resolution and of statistical convergence. A typical problem encountered in the theory is the occurrence of distributions without finite higher-order moments [4].

Refinements of the original theory have been presented [5,6] as well as models for the energy cascade [4,7-10], most of them based on fluctuations of the locally averaged energy dissipation ε. In order to test these models and to aid further theoretical progress, it is necessary to devise techniques which permit overcoming the intrinsic difficulties of the analysis of experimental data. An alternative path which is worth being pursued consists of finding new observables which can be shown to satisfy scaling laws with measurable exponents and are better amenable to numerical analysis.

2 TWO-SCALE APPROACH

In Ref. [11], we have investigated the statistical self-affinity of turbulent time series by introducing a noisy map to model the scale transformation of the signal. Its form, a linear contraction with an arbitrary nonlinear noise term, allowed us to estimate the average ratio γ between velocity differences computed across intervals staying in the ratio $r \in [0,1]$ with one another.

The comparison of observables referring to different scales has led to improved quality of the scaling laws and, thus, to more accurate estimate of the exponents. This result is, however, limited to a few values of p, since the transformations we have introduced are exact only in those cases.

This approach has also shown that different observables than powers of d or ε can be profitably studied and that their scaling behaviour, although not of a power-law type, can be analytically inferred. Among the applications of this two-scale method, there is a test for the existence and extension of the inertial range: the condition is expressed as a third-order correlation function with a specific form related to the one-dimensional nature of the measured time-series and to the geometry of the time intervals involved in the scale splitting we have adopted.

Finally, by choosing the nonlinear noise amplitude as proportional to $\varepsilon^{-1/2}$, and the observable as ε itself, it is possible to show that the "average breakdown coefficient" [8,12] $\langle \varepsilon(rL)/\varepsilon(L) \rangle$ is neither independent of r nor logarithmically dependent on it, as assumed in [8,12,13], but satisfies the law

$$\langle \varepsilon(rL) / \varepsilon(L) \rangle \approx 2 - \frac{1 + r^{\zeta_6} - (1-r)^{\zeta_6}}{2r}$$

where $\zeta_6 \cong 1.832$ is the sixth-order velocity scaling exponent. We have analysed three data sets, each containing 10^7 scalar velocity values. The first two were recorded in the atmosphere, with a sampling frequency of 3 and 30 kHz, at a height of 25 m above

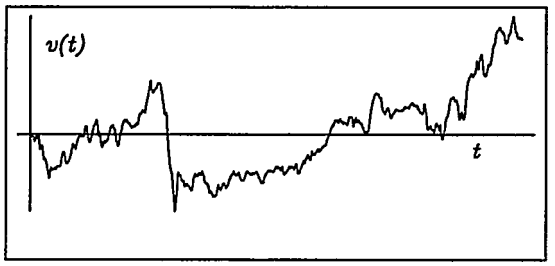

Fig. 1: Short sample of wind velocity as a function of time measured in the atmosphere on the OVGA building.

ground, using a hot-film anemometer with a spatial resolution of 2 mm (M. Furger and R. Weber, PSI). The average and rms velocities were 3.7 and 1.6 m/s, the integral length 100 m, the Kolmogorov length 0.45 mm, and the Taylor-Reynolds number 10000. The third one was recorded in an axisymmetric free jet (dry air in air) at 8 kHz with a hot-wire anemometer (resolution 1 mm), placed at a distance of 125 nozzle diameters from the source, along the axis of the jet (Ch. Renner, J. Peinke, University of Bayreuth, Germany). The Reynolds number at the nozzle was 27000. At the probe, the mean velocity was 2.25 m/s, the integral length 67 mm, the Kolmogorov length 0.25 mm and the Taylor-Reynolds number 200.

In Figure 1 a typical sample of a velocity time series is shown. In Figure 2, estimates of the longitudinal velocity difference correlation function $\gamma(r)$, defined as, $\gamma(r) \equiv \langle d(L)d(rL)\rangle / \langle d(L)^2\rangle$, are shown together with the theoretical curve

$$\gamma(r) = \frac{1 + r^{\zeta_2} - (1-r)^{\zeta_2}}{2}$$

for the scale-to-scale contraction coefficient. The symmetry of the curve, its difference from a power law, and the agreement between theory and experiment are evident: the estimated value for ζ_2 was 0.7 ± 0.015. This accuracy is much higher than the one yielded by the direct method. These results refer uniquely to the deterministic, average part of the stochastic self-affinity relation postulated for the turbulent cascade. The next step in the investigation must address the nature of the fluctuations which exhibit broad distributions, in analogy with those measured for the velocity differences d and the (logarithm of the) locally averaged energy dissipation ε. The freedom given by the nonlinear term in our stochastic map could provide a clue for the understanding of the underlying mechanisms. Work is in progress on the scaling exponents of the energy dissipation, the behaviour of negative-index moments, cascade models, breakdown coefficients, and conditional statistics.

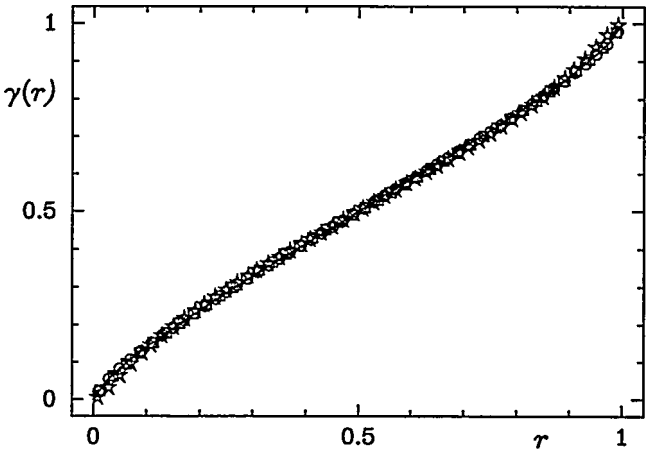

Fig. 2: Curve $\gamma(r)$ estimated from 3 experimental time series and theoretical prediction (solid line, see text).

3 ACKNOWLEDGEMENT

The authors acknowledge receipt of data by J. Peinke (Bayreuth).

4 REFERENCES

[1] A.N. Kolmogorov, Dokl. Akad. Nauk SSSR **30**, 301 (1941).

[2] B.B. Mandelbrot, J. Fluid. Mech. **62**, 331 (1974).

[3] A. Arneodo et al., Europhys. Lett. **34**, 411 (1996).

[4] U. Frisch, *Turbulence: the legacy of A.N. Kolmogorov*, Cambridge University Press, Cambridge (1995).

[5] A.M. Obukhov, J. Fluid. Mech. **13**, 77 (1962).

[6] A.N. Kolmogorov, J. Fluid. Mech. **13**, 82 (1962).

[7] C. Meneveau and K.R. Sreenivasan, J. Fluid Mech. **224**, 429 (1991).

[8] E.A. Novikov, Appl. Math. Mech. **35**, 231 (1971).

[9] Z.S. She and E. Lévêque, Phys. Rev. Lett. **72**, 336 (1994).

[10] S. Chen, K.R. Sreenivasan, and M. Nelkin, Phys. Rev. Lett. **79**, 1253 (1997).

[11] R. Badii and P. Talkner, Europhys. Lett. **43**, 284 (1998).

[12] E.A. Novikov, Sov. Phys. Dokl. **14**, 104 (1969).

[13] G. Pedrizzetti, E.A. Novikov and A.A. Praskovsky, Phys. Rev. E **53**, 475 (1996).

SEMIADIABATIC THEORY OF SEASONAL MARKOV PROCESSES

P. Talkner

The dynamics of many natural and technical systems are essentially influenced by a periodic forcing. Analytic solutions of the equations of motion for periodically driven systems are generally not known. Simulations, numerical solutions or in some limiting cases approximate analytic solutions represent the known approaches to study the dynamics of such systems. Besides the regime of weak periodic forces where linear response theory works, the limit of a slow driving force can often be treated analytically using an adiabatic approximation. For this approximation to hold all intrinsic *processes must be fast on the time-scale of a period of the external driving force. We developed a perturbation theory for periodically driven Markovian systems that covers the adiabatic regime but also works if the system has a single slow mode that may even be slower than the driving force. We call it the* semiadiabatic *approximation. Some results of this approximation for a system exhibiting stochastic resonance which usually takes place within the semi-adiabatic regime are indicated.*

1 INTRODUCTION

Various phenomena of physics, chemistry, and other natural and engineering sciences can be properly modelled by stochastic processes that are driven by an external periodic forcing. As long as the periodic driving force is weak, linear response theory describes the output of such systems and provides a wealth of information about the dynamics of the undriven system [1,2]. Countless experimental techniques are based on this mechanism. Dielectric relaxation, resonance absorption, nuclear magnetic resonance and dynamic light scattering are just a few examples. In the past two decades, however, nonlinear effects have attracted much interest. The interaction of irregular perturbations as given by thermal noise with a periodic forcing mediated by a nonlinear dynamical system can produce surprising effects. The amplification of a weak periodic signal by means of noise, known as stochastic resonance [3,4] was originally suggested as the essential mechanism how the small secular variations of the earth's orbital parameters may lead to the recurrent ice ages. In the past two decades many other realisations of stochastic resonance have been found [5].

In a spatially periodic system which lacks symmetry within a unit cell an external periodic field may produce a direct current. Such rectifying devices are particular examples of so-called ratchets [6] which have been proposed as models for transport in living cells.

Coming back to stochastic resonance one can understand it as a synchronisation of the random transitions between two metastable states of a system with an external periodic driving force. As a rule of thumb, the matching of these antagonistic processes is best if in the absence of the periodic driving the two metastable states are symmetric and their common mean waiting time is just half the period of the driving force. According to this simple picture, at the most favourable moment when the barrier as seen from the initial state is lowest, the system hops from the initial state to the other one, and half a period later back again. Typically, the waiting time of the metastable state is of Arrhenius type and therefore much longer than all other intrinsic time-scales of the system [7], except the period of the external forcing. Hence, the dynamics of the driven system is governed by two distinct slow processes while all other time-scales of the system are much faster. In a naive adiabatic approach one would assume that at each instant of time the system is in its equilibrium state at the instantaneous value of the external forcing. In the interesting regime of stochastic resonance this approximation does not hold since the populations of the metastable states cannot follow the external forcing fast enough and hence are not in equilibrium.

2 SEMIADIABATIC APPROXIMATION

For the details of the semiadiabatic theory we refer to Ref. [8]. This theory can be applied to Markovian processes with a spectrum of typical relaxation times all of which but one are short compared to the period of the frequency of the external driving. The fast relaxation processes can be treated in an adiabatic way i.e. their time dependence can algebraically be expressed in terms of the slowly moving modes of the system. It turns out that in simple cases there are only two of these slow modes the dynamics of which can exactly be determined. In this way it is possible to determine the conditional probability of the system which together with an initial probability distribution of the system completely determines the investigated process. There is a systematic way to improve the semiadiabatic theory. The smallness parameter of the ensuing perturbation theory is the ratio between the frequency of the periodic driving force and a typical fast relaxation rate of the system. The theory is not restricted to small driving fields and in particular also works for weak noise, or low temperatures, for which linear response theory fails even for rather small external fields.

3 SPECTRAL AMPLIFICATION FOR STOCHASTIC RESONANCE

The performance of a device showing stochastic resonance can be characterised by the spectral amplification η. This is the ratio between the output power

of the device at the driving frequency and the power of the driving force. Figure 1 shows η as a function of the noise strength $1/\beta$ for different frequencies Ω of the driving force. The frequency Ω is given in units of a characteristic internal frequency of the considered device. For details see Ref. [8]. The amplitude of the driving force is the same for all cases shown here. For a slow driving force the transition rates between the states of the considered device are fast and the system as a whole behaves adiabatically, i.e. it quickly adapts to the equilibrium distribution at the instantaneous value of the external force. With decreasing noise the spectral amplification follows the limiting adiabatic curve as long as the equilibration is fast. Since, however, the transition rates depend exponentially on β [7] the equilibration eventually becomes slow and with further decreasing noise strength the spectral amplification suddenly drops to very small values. This results in a maximum of the spectral amplification which defines the point of stochastic resonance at the considered driving frequency.

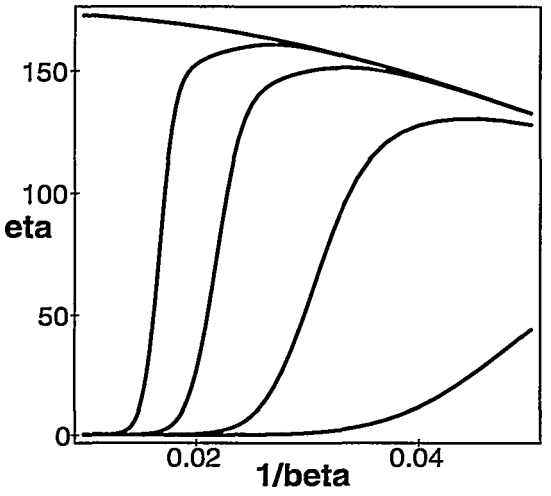

Fig. 3: Spectral amplification η as a function of the noise strength $1/\beta$ for a constant amplitude A=0.1 and different values of the driving frequency $\Omega=10^{-n}$. The uppermost curve represents the adiabatic limit corresponding to $n=\infty$. The following curves correspond to n=5, n=4, n=3, and n=2 from top to bottom.

Within the semiadiabatic theory, a complete description of the behaviour of a stochastic resonance device can be given [8]. Quantitative agreement is found with the known results in the fully adiabatic limit and in the regime of linear response theory [8].

The semiadiabatic theory provides a versatile tool to investigate various different natural and technical processes that are forced by an external periodic driving with relatively slow frequency.

4 REFERENCES

[1] R. Kubo, Rep. Prog. Phys. **29**, 255 (1966).

[2] P. Hänggi, and H. Thomas, Phys. Rep. **88**, 207 (1982).

[3] R. Benzi, A. Sutera, G. Parisi, and A. Vulpiani, J. Phys. A **14**, L453 (1981).

[4] C. Nicolis, and G. Nicolis, Tellus **33**, 225 (1981).

[5] for a recent comprehensive report see L. Gammaitoni, P. Hänggi, P. Jung, and F. Marchesoni, Rev. Mod. Phys. **70**, 223 (1998).

[6] for recent reviews see R.D. Astumian, Science **276**, 917 (1997); F. Jülicher, A. Ajdari, J. Prost, Rev. Mod. Phys. **69**, 1269 (1997).

[7] P. Hänggi, P. Talkner, M. Borkovec, Rev. Mod. Phys. **62**, 252 (1990).

[8] P. Talkner, *Stochastic resonance in the semiadiabatic limit*, submitted.

SHORT-TERM IMPACTS OF AIR POLLUTANTS IN SWITZERLAND: PRELIMINARY SCENARIO CALCULATIONS FOR SELECTED SWISS ENERGY SYSTEMS

S. Andreani-Aksoyoglu, J. Keller

In the frame of the comprehensive assessment of Swiss energy systems, air quality simulations were performed by using a 3-dimensional photo-chemical dispersion model. The objective is to investigate the impacts of pollutants in Switzerland for future options of Swiss energy systems. Four scenarios were investigated: Base Case: simulations with the projected emissions for the year 2030, Scenario 1) all nuclear power plants were replaced by oil-driven combined cycle plants (CCP), Scenarios 2 to 4) traffic emissions were reduced in whole Switzerland as well as in the cities and on the highways separately. Changes in the pollutant concentrations and depositions, and the possible short-term impacts are discussed on the basis of exceedences of critical levels for plants and limits given to protect the public health

1 INTRODUCTION

Two important issues addressed in the PSI project "Comprehensive Assessment of Energy Systems" (Project GaBE, [1]) are the environmental impacts and the health risks of air pollutants in Switzerland. The photo-chemical dispersion model UAM (Urban Airshed Model) is used to simulate concentrations and deposition rates of the most important species (in particular NO_2, O_3, VOC, CO and SO_2) in a 3-dimensional grid of 5 km x 5 km horizontal resolution. Impacts on ecosystems (e.g. crop loss) and public health (e.g. respiratory diseases) are supposed to occur if the levels or loads exceed specified thresholds. The short term performance of UAM has been tested using summer smog data of the field experiment POLLUMET [2,3]. To estimate the seasonal impacts, calculations for all typical meteorological conditions encountered over the whole year are in progress [4].

In this study, we investigated the impact of four energy scenarios on the short-term air quality in summer 2030. The base case was defined as a summer smog situation with low westerly wind, the anthropogenic emissions being projected according the long-term trend of the Swiss annual totals [5]. The scenarios were defined as follows:

Scenario 1): According to the prospect of the Swiss electricity demand and supply [6], there will be a deficit of 4 GWe in summer 2030. This is mainly due to the decommissioning of the Swiss nuclear power plants and the expiration of electricity import contracts. In this scenario, this deficit is assumed to be covered by 4 CCP [6,7] placed at the sites given in Figure 2. These plants are usually driven by natural gas. In the case of shortage they can also be fuelled with oil, The expected annual shares are approximately 25 % oil and 75 % gas. In this scenario, however, we assume a short term use of 100 % oil which is an extreme case.

Scenario 2): 30 % reduction of all traffic emissions.

Scenario 3): 30 % reduction of traffic emissions only in the cities.

Scenario 4): 30 % reduction of traffic emissions only on the highways.

The simulation results are compared with the short-term critical levels for plants and with limits given to protect the public health. Details are given in [3]

2 RESULTS AND DISCUSSION

Base case: The short term concentrations of CO, PAN, SO_2, NO_2, and O_3, predicted for 2030 were compared with the critical levels for short-term impacts on plants and with the limits given to protect the public health. The predicted CO levels (~400 ppb/d) are far below the limits for health effects. The PAN concentrations which can cause acute damages on plants (10-20 ppb/2h) are not reached, the maximum concentrations being 4.4 ppb/2h. Similarly, SO_2 levels are too low to cause any damage to plants or public. The maximum concentrations of NO_2 are close to the limits. O_3 concentrations on the other hand, exceed both limits (Figure 1).

We reduced VOC and NO_x emissions separately by 35 % and simulated the change of peak ozone for each case. The VOC-sensitive areas where the decrease of ozone is predominantly due to the reduction of the VOC were found in the plume of the cities. These areas are larger for low wind conditions than for moderate ones. In most of the model region, however, O_3 formation was predicted to be sensitive to emissions of NO_x only or of both species.

Scenario 1: This simulation shows local effects in the areas where the power plants are placed. Compared to the base case, NO_2 levels increase substantially and approach the limits. There is no significant change in CO concentrations. However, SO_2 concentrations increase dramatically and exceed the critical levels for plants and approach the limits given to protect the human health. On the one hand, ozone concentrations increased by up to 10 % in the north-east of power plants (Figure 2). On the other hand, they decreased by the same amount in the east of the sources. Since O_3 formation is not linearly correlated to the emissions, these results are not surprising. SO_2 and NO_2 depositions responsible for acidification increased locally 15 and 8 times respectively and deposition of HNO_3 was about 30 % higher.

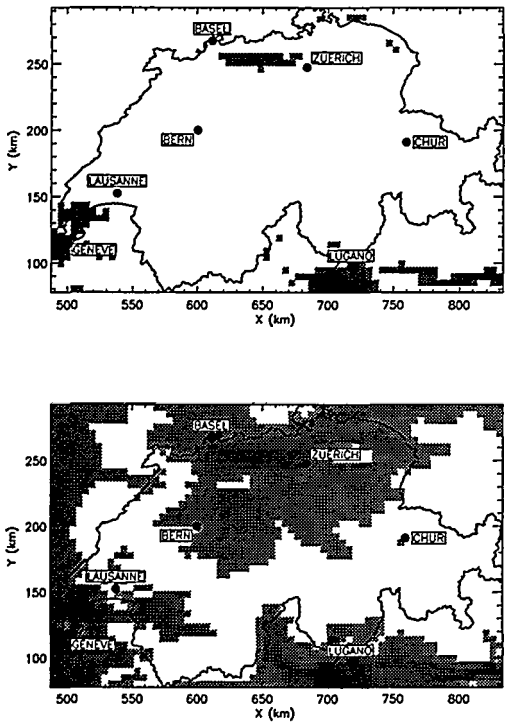

Fig. 1: Locations of peak ozone concentrations (dark areas) exceeding the critical levels of 75 ppb for plants (top) and the limits of 60 ppb for protecting the public health (bottom), respectively.

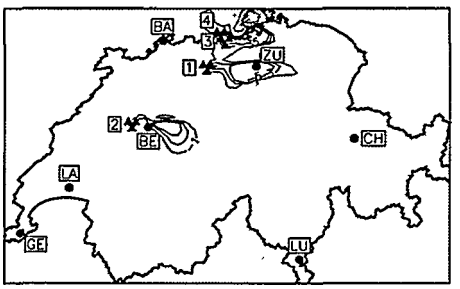

Fig. 2: Changes (%) in peak O_3 concentrations in scenario 1 with respect to the base case. 1: Goesgen, 2: Muehleberg, 3: Beznau, 4: Leibstadt. Contour lines: -5,-3,-1, 5,10,15. Darker areas: increased concentrations, lighter areas: decreased concentrations.

Scenario 2: A reduction of all the traffic emissions by 30 % decreases daily average concentrations of NO_2 and CO by a few percent. SO_2 concentrations were practically not affected because SO_2 emissions from the traffic in Switzerland are quite low compared to other sources. O_3 levels decreased in the countryside by 1 to 5 %. However, they increased by 10 to 15 % around the towns. It is well known that reduction of NO_x emissions may lead to an increase if O_3 formation is VOC limited. Depositions of SO_2, HNO_3 and NO_2 decreased by 7, 20, and 40 %, respectively.

Scenario 3: If traffic emissions were reduced by 30 % only in the cities, CO levels decreased by about 12 %. This scenario predicted almost no decrease in O_3 levels, the concentrations even increased around the big cities. The effects on deposition are found only around the cities. HNO_3 and SO_2 depositions decreased by 6 %, and about 23 % decrease was predicted for NO_2 depositions. On the other hand, ozone deposition increased by ~ 10 % in big cities such as Geneva and Zurich.

Scenario 4: The decrease of the highway traffic emissions only causes changes in O_3 levels similar to those in scenario 2. However, the effect is less than that when all traffic emissions are reduced. The results on the deposition of species are similar to those in Scenario 2. SO_2, HNO_3 and NO_2 depositions decreased by 6, 19, and 37 %. There was about 8 % increase in ozone depositions at some locations.

3 ACKNOWLEDGEMENT

This study was supported by the "Kommission für Technologie und Innovation (KTI)".

4 REFERENCES

[1] S. Hirschberg, *Integral assessment of energy systems. Environment and Nuclear Energy*, (ed. B.N. Kursonoglu), Plenum Publishing Corporation, New York, in press (1998).

[2] POLLUMET Report, *Luftverschmutzung und Meteorologie in der Schweiz*, **No. 63**, BUWAL, Bern (1996).

[3] S. Andreani-Aksoyoglu, J. Keller, *Short-term impacts of air pollutants in Switzerland: Model evaluation and preliminary scenario calculations for selected Swiss energy systems*, in C.A. Brebbia, C.F. Ratto, and H. Power (Eds.), Air Pollution VI, Computational Mechanics Publications, 799-808 (1998).

[4] J. Keller, D. Bürki, S. Andreani-Aksoyoglu, *An approach for the estimation of seasonal impacts of air pollutants in Switzerland on the basis of an air quality classification*, Proc. Eurotrac-2 Symp. Garmisch-Partenkirchen, in press, March 23-27 (1998).

[5] BUWAL Report, *Vom Menschen verursachte Luftschadstoff-Emissionen in der Schweiz von 1900 bis 2010*, **No. 256**, Bern (1995).

[6] VSE Report, *Vorschau 1995 auf die Elektrizitätsversorgung der Schweiz bis zum Jahr 2030*, VSE (1995).

[7] R. Dones, U. Gantner, S. Hirschberg., G. Doka, I. Knoepfel, *Environmental Inventories for future electricity supply systems for Switzerland*, PSI Report No. 96-07, Villigen (1996).

COMPARISON OF ECOSYSTEM WATER FLUX MEASURED WITH THE EDDY COVARIANCE- AND THE DIRECT XYLEM SAP FLUX METHOD IN A MOUNTAINOUS FOREST

G. Stefanicki, P. Geissbühler, R. Siegwolf

The Eddy covariance technique allows to measure different components of turbulent air fluxes, including the flow of water vapour. Sap flux measurements determine directly the water flow in tree stems. We compared the water flux just above the crowns of trees in a forest by the technique of eddy covariance and the water flux by the xylem sap flux method. These two completely different approaches showed a good qualitative correspondence. The correlation coefficient is 0.8. With an estimation of the crown diameter of the measured tree we also find a very good quantitative agreement.

1 INTRODUCTION

Within the ECOMONT project [1] we measured the water flux from a mountainous forest to the atmosphere, using two completely different and independent approaches: the eddy covariance method for direct measurements of turbulent exchange of water vapour in the atmosphere and the xylem sap flux method on a tree stem, measuring the water flow inside a tree.

2 INSTRUMENTAL ARRANGEMENT

The eddy covariance method allows to measure fluxes of different components in the vegetation boundary layer by means of a sonic anemometer and an IRGA (Infrared Gas Analyser). The sonic anemometer measures the three wind components and the speed of sound from which the course of turbulent flux of water vapour can be determined [2]. Water vapour and carbondioxide concentration are measured with a closed path IRGA (LICOR 6262). Air is pumped through a teflon tube from the anemometer. A sample of this air is led to the IRGA and analysed [3].

The device we used to measure the xylem sap flux includes a power supply, a control unit and a data logger. A set of heating electrodes and thermocouple wire cascades was connected, allowing the registration of sap flow simultaneously in six differently chosen trees. The sap flux was determined according to the heat balance method, measuring the heat flux in the vessels of the xylem. A wood segment between 5 electrodes was heated by a current of constant power [4,5]. Thermocouples were inserted between the heating electrodes. These sensors were connected to another set of thermocouples, inserted in the tree 15 cm below the heated segment. The temperature difference between the heated and unheated segments was monitored. An increasing water flux in the xylem reduces the temperature difference between the heated and the cold segments. Knowing the heating power and the temperature difference the water flux or xylem sap flow can be calculated.

The measurements have been done on Monte Bondone, Italy, at 1520 m above mean sea level in a Fagus stand. For the eddy covariance measurements the anemometer's position was above the canopy (at 16 m above ground level). The anemometer was installed perpendicular to the slope, taking into account the influence of the advective air component [2]. The canopy was a homogenous fagus sylvatica stand, whereas the terrain was rather complex.

The xylem sap flow devices were fixed in a height of 1.3 m above ground. The data considered in this report have been collected in the period from August 2 1998, 0:00 to August 4 1998, 24:00 - three full days. Since the xylem sap flow data were registered every 15 minute the sonic anemometer data have been transformed into 15 minutes average data.

3 RESULTS

Figures 1 and 2 show the time series of fluxes of the two mentioned methods.

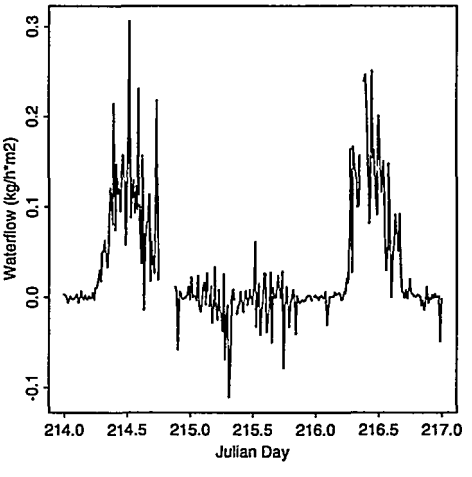

Fig. 1: Water vapour flux measurements in a fagus stand on Monte Bondone with the eddy covariance method. The sonic sensor was placed 8 m above the canopy crown. The data represent 3 full days. Day 2 was cloudy and rainy.

The eddy covariance plot shows the diurnal water flux, the increase starting at 7:00 in the morning to a maximum around midday and decrease in the afternoon

until 16:30 h on day 1 and 3. Day 2 was cloudy and rainy. Thus there was no net water vapour transport from the crown into the atmosphere.

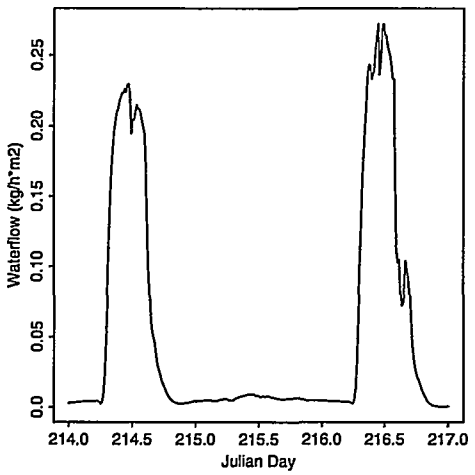

Fig. 2: Xylem sap flux of a Fagus on Monte Bondone, showing the same period as in Figure 1. Day 2 (rainy and cloudy) had practically no flux (no transpiration of the tree). The xylem sap flux values have been divided by the estimated projected crown area of 14 m^2.

The plot of xylem sap flow (Figure 2) shows the same qualitative behaviour as in Figure 1, but the start of the increase and the maximum are shifted by half an hour. The time delay for the xylem sap flux measurements in comparison to the eddy covariance measurements is a result of the time lag of the xylem sap flux in the tree trunk, in which water is stored.

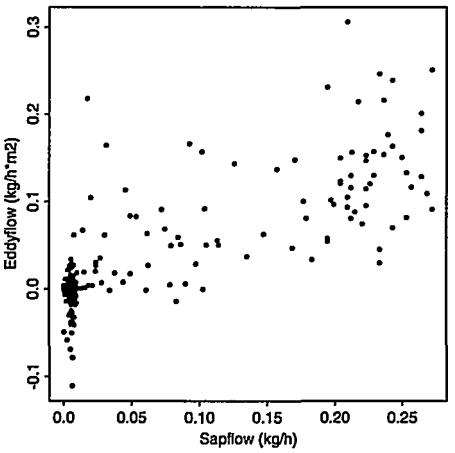

Fig. 3: Correlation between sap flux and eddy flux. The values of sap flux have been divided by the estimated projected crown area. The correlation coefficient is 0.82.

4 DISCUSSION AND QUESTIONS

The discussed two different measurement methods show a good qualitative correspondence (see Figure 3). For a quantitative comparison the fluxes of the xylem measurements must be divided by the projected crown area which is estimated to 14 m^2. Then we find a good quantitative agreement. Calculating Pearson's correlation coefficient between the water flux measured by the method of sap flow and the water flux determined by eddy covariance gives values between 0.78 and 0.82.

The results shown are from a Fagus stand on a mountain slope with a quite homogenous canopy. The water flux could be determined either by xylem sap flux or by eddy covariance method. Thus depending on the demands and difficulties of the terrain, there is a choice of the measurement method for water flux.

An interesting question to be addressed is the influence of a non-homogenous canopy and of another species of trees and a possible difference between coniferous and deciduous trees.

5 ACKNOWLEDGEMENTS

This study was supported by the ECOMONT project (Swiss Federal Office for Education and Science under Contract 95.0386-2). We also thank R. Erne and R. Richter for their technical support.

6 REFERENCES

[1] W. Portmann et al., *PSI Contribution to the EU Project ECOMONT*, Annex V, 80-81 (1996).

[2] H.A. Panofsky, J.A. Dutton, *Atmospheric Turbulence*, John Wiley&Sons, New York, 397 (1984).

[3] A. Grelle, A. Lindroth, *Eddy-Correlation system for long-term monitoring of fluxes of heat, water vapour and CO_2*, Global Change Biology, **2**, 297-307 (1996).

[4] J. Cermak, M. Deml, J. Kucera, V. Zidek, *Xylem water flow in a crack willow tree (Salix fragilis L.) in relation to diurnal changes of the environment*, Oecologia, **64**,145-151 (1984).

[5] B.M. Köstner, E.D. Schulze, F.M. Kelliher, D.Y. Hollinger, J.N. Byers, J.E. Hunt, T.M. Mcseveny, R. Meserth, P.L. Weir, *Transpiration and Canopy Conductance in a Pristine Broad-Leaved Forest of Nothofagus: An Analysis of Xylem Sap Flow and Eddy Correlation Measurements*, Oecologia, **91**, 350-359 (1992).

THE ADAPTATION RATE OF TERRESTRIAL ECOSYSTEMS AS A CRITICAL FACTOR IN GLOBAL CLIMATE DYNAMICS

J.S. Füssler, F. Gassmann

A conceptual climate model describing regional two-way atmosphere-vegetation interaction has been extended by a simple qualitative scheme of ecosystem adaptation to drought stress. The results of this explorative study indicate that the role of terrestrial vegetation under different forcing scenarios depends crucially on the rate of the ecosystems adaptation to drought stress. The faster the adaptation of important ecosystems such as forests the better global climate is protected from abrupt climate changes.

1 INTRODUCTION

Atmosphere and terrestrial vegetation constitute an important interacting pair of climate subsystems: on the one hand, the climate shapes vegetation. The large impact of climate changes (e.g. at the end of the last ice age) on ecosystem communities and individual plants is documented in pollen records and, on a shorter time-scale, in tree ring studies. On the other hand, terrestrial vegetation actively controls fluxes of energy, mass and momentum between land surfaces and the atmosphere and may therefore exert a large influence on climate. Evidence for this impact comes largely from global circulation models (GCMs) showing for instance that changes of soil moisture availability or surface albedo may result in significant changes of precipitation and temperature.

However, there have been only few attempts to close the loop of climate-vegetation interaction and to combine GCMs, models of vegetation structure and soil-vegetation-atmosphere transfer schemes in their dynamical mutual interdependence because of different serious problems, such as the lack of available data, of process knowledge and of computing power. To circumvent some of these difficulties, the preliminary study presented here is carried out in the framework of a simple conceptual model of atmosphere-vegetation interaction [1,2].

2 MODEL OF ECOSYSTEM ADAPTATION

In our conceptual model, no explicit distinction between biomes is made, but vegetation abundance is characterised by a biomass density M. To find a representation for the adaptation of vegetation cover in spite of this simplification, an *adaptation index* γ is introduced. This highly integrated, dimensionless index represents a continuous vegetation classification, which describes the grade of adaptation to drought stress of a particular terrestrial ecosystem. $\gamma = 0$ specifies the equilibrium characteristics of an ecosystem, such as species composition, plant physiology and rooting depth, that is established under „basic" climate conditions, where drought stress is absent ($\varepsilon = 0$). $\gamma = 1$, in turn, specifies the equilibrium ecosystems characteristics, that is reached under a continuous severe drought stress, represented by a drought parameter of $\varepsilon = \varepsilon_{ca}$. The dynamics of γ is described by the following equation, where C_a describes the rate of adaptation:

$$\frac{d\gamma}{dt} = C_a\left(\frac{\varepsilon}{\varepsilon_{ca}} - \gamma\right) \qquad (1)$$

Drought stress affects not only aboveground shoot growth, but also root development. Several studies indicate reduced root growth under soil moisture deficits. Because of the plasticity of the allocation processes in many plants in response to drought stress, root growth is generally less reduced than shoot growth. Adaptation to drought stress on the individual level is extended by adaptation on the level of the plant community by the successional replacement of existing species by better adapted species. In general, this adaptation on the community level is slower but more thorough [3].

In contrast to most soil-vegetation-atmosphere transfer schemes, our conceptual model has no explicit representation of rooting depth. However, the parameter describing the critical limit of evapotranspiration, E_c, depends on the amount of water available to the plants for transpiration, and is therefore influenced by root system modifications. So, biomass and adaptation index serve as indicators for climate induced changes in the root systems, which in turn influence plant water availability. However, water availability is the key factor influencing actual evapotranspiration and therefore the surface energy balance, as well as the amount of drought stress that the plants are exposed to [3].

The occurrence of drought stress increases also tree mortality because stressed trees dispose of reduced photosynthate reserves to ward off disease or pests and to repair damage to tree structure, and also lack vigour. In our model, the adaptation of individual plants as well as the species composition to drought stress gradually reduces their vulnerability to drought stress. The increase of the mortality rate in response to drought is therefore mitigated with increasing adaptation index γ [3].

3 SIMULATION EXPERIMENTS, RESULTS

Figure 1 shows the dynamic response of surface temperature deviation ΔT, normalised biomass M and the adaptation index γ to an increasing forcing for two adaptation rates. With slow adaptation, vegetation

cover cannot keep pace with the increasing forcing, leading to a transition to a dry and hot climatic state*. This transition begins rather slowly and only after the forcing has reached its plateau. The late but considerable adaptation of the vegetation cover (year 600: $\gamma = 0.95$) leads only to an insignificant increase of biomass and is unable to re-establish previous vegetation density. With faster adaptation, however, the immediate modification of vegetation in response to increasing drought stress reduces drought induced mortality and improves water accessibility early enough to prevent the abrupt transition. In addition, only a partial adaptation of vegetation is required (year 600: $\gamma = 0.22$). For a given rate of forcing increase, our simulations indicate the existence of a critical threshold value for the adaptation rate dividing the response of the atmosphere-vegetation system between stability and transition.

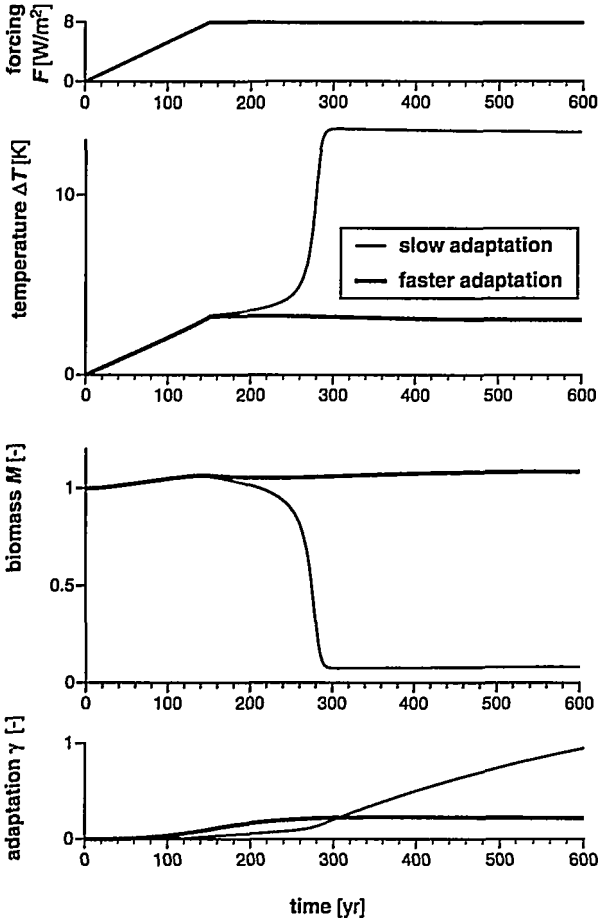

Fig. 1: Response of surface temperature deviation ΔT, normalised biomass M and adaptation index γ to an increasing radiative forcing F for slow (thin lines) and fast (thick lines) adaptation rate: if the adaptation is too slow, the system undergoes a transition to the dry and hot state.

* A doubling of atmospheric CO_2 relative to the pre-industrial value corresponds to a forcing $\Delta F = 4.4$ W/m². The intent of the simulation is to show the effect of different adaptation rates resulting in a small and a four times larger temperature change, whereas no emphasis should be placed on the absolute values of ΔT.

In a second simulation experiment, the impact of a single forcing pulse of 10 W/m² during 10 years on the system within its bistable range [1,2] is investigated. Without adaptation, the perturbation is sufficient to trigger a transition to the dry and hot state. However, when adaptation to the drought conditions is fast enough, a transition is prevented. For an intermediate rate of adaptation, the system initially flips to the dry and hot state, but is able to recover after 2-3 centuries and to return to the state with abundant vegetation due to a transient adaptation.

In a third simulation, the response of the system to periodically recurring but weaker perturbations of different frequencies was investigated. For a low perturbation frequency (100 yr intervals), vegetation is able to recover even without adaptation. However, if the frequency is doubled (50 yr intervals), their cumulative effect leads to a step-wise decline of biomass and finally, the atmosphere-vegetation system makes a transition to the dry and hot state. The „memory-effect" [1] makes the system sensitive to the frequency of the perturbations. With slow adaptation, the transition cannot be prevented in the 50 yr-perturbation experiment, but a higher adaptation rate leads to a stabilisation of the climate even in the presence of this higher rate of perturbations.

4 CONCLUSION

Our investigations indicate that the rate and the extent of the adaptation of terrestrial ecosystems to changing climate conditions are crucial factors in the assessment of possible future changes in the climate-vegetation system. They indicate the possibility for the existence of critical thresholds for the adaptation rate of land vegetation systems to climate changes. If terrestrial vegetation in mid-latitudes adapts fast enough to the increasing climate forcing or to changes in the perturbation regime, turns out to be an important question to be addressed in future research.

5 ACKNOWLEDGEMENTS

We thank F. Klötzli, A. Wokaun and A. Kleidon for their valuable suggestions and comments.

6 REFERENCES

[1] J.S. Füssler, *On the interaction between atmosphere and vegetation under increasing radiative forcing: a model analysis*, Ph.D. thesis No. 12802, ETHZ (1998).

[2] J.S. Füssler, F. Gassmann, *On the role of dynamical atmosphere-vegetation interactions under increasing radiative forcing: a conceptual model*, submitted for publication (1998).

[3] J.S. Füssler, F. Gassmann, *The adaptation rate of terrestrial ecosystems as a critical factor in global climate dynamics*, submitted for publication (1998).

SIMULATION OF PLANT COMMUNITIES WITH A CELLULAR AUTOMATON

F. Gassmann

With a modelling approach based on cellular automata, five observed types of plant development can be simulated. In addition, the proposed model shows a strong tendency towards the formation of patches and a high degree of dynamical and structural instability leading to limits of predictability for the asymptotic solution chosen by the system among several possible metastable patterns (multistability). Further, external fluctuations can be shown to have advantages for certain plant types. The presented model unifies the fundamental dichotomy in vegetation dynamics between determinism (understood as predictability) and disorder (chance effects) by showing the outcome of both classical theories as special cases.

1 INTRODUCTION

During the last two decades, Cellular Automata (CA) have been established as a very successful methodology for spatiotemporal modelling in many scientific disciplines. For ecological investigations, they have been applied for a wide range of phenomena [1]. Especially to describe local competition among plants and the resulting patterns, CAs proved to be useful, because they conserve the possibility for chance effects undoubtedly observed in vegetation dynamics, being not adequately described by Markov chain succession models leading to a unique climax-state.

We investigated observed plant behaviour [2] in the context of global climate change as described in a second article published in this report [3].

2 MODEL DESCRIPTION

A two-dimensional CA is used to describe the time evolution of a plant community on a given test area of several square meters to several hectares [4]. The dynamics describing the modification of a given pattern within one year is defined by interactions involving the eight nearest neighbours of each cell, the considered cell itself and one or several environmental parameters. The nearest neighbour interactions are described by a preference matrix $P_{i,k}$. By convenience, the values attributed to different $P_{i,k}$ are integers between -5 and +5. This range of total 11 points showed to be adequate for a translation of the qualitative experience of botanists into hard numbers. The diagonal elements $P_{i,i}$ of the matrix describe the intraspecific preference, i.e. the degree of favour of a specific plant towards its own type. All the other matrix elements describe the degree of interspecific preferences. It has to be pointed out that the matrix, in general, will not be symmetric, i.e. $P_{i,k} \neq P_{k,i}$. Such an asymmetry describes the well known fact that a plant type i can prefer to have type k as a neighbour but type k shows no preference for type i. $P_{i,k} = P_{k,i} = 0$ means that types i and k are neutral towards each other. As an example, we have chosen the following matrix for 5 plant types (types 1 to 5 were chosen to describe respectively Molinia caerulea, Narthecium ossifragum, Sphagnum recurvum ssp. apiculatum M, Chiloscyphus pallescens M and Erica tetralix):

$$P_{i,k} = \begin{bmatrix} 3 & -3 & 0 & 1 & -3 \\ -2 & 5 & 0 & 2 & -2 \\ 0 & -1 & 3 & 1 & -2 \\ 0 & 0 & 0 & -5 & 0 \\ -1 & 0 & 0 & 0 & 3 \end{bmatrix}$$ preference matrix

The first row $P_{1,k}$ describes the preference of plant type 1 for type k, whereas the first column $P_{i,1}$ shows how type 1 is promoted by the others. To describe the advantage of a perennial plant to occupy a certain pixel also in the following year, a site preference and advantage-vector has been introduced. Its elements S_i quantify this effect for every plant type i. Perennial plants are characterised by positive numbers, annual plants by 0, whereas negative values would tend to prevent the same plant type to be at the same place in the following year. In our example, the vector reads:

S_i = [4 1 3 2 1] site preference/advantage

In addition, two environmental sensitivity vectors are considered describing effects by average temperature and humidity on the different plant types:

T_i = [0 -1 -1 -1 -1] temperature sensitivity

H_i = [0 +1 0 +1 +1] humidity sensitivity

The integration of the above described vector- and matrix-elements into the decision which plant type will live next year on a certain pixel p (i.e. the state $Z_{p,t+1}$ of this pixel), if the states $Z_{p,t}$ of all N^2 pixels p are known for this year, can be best understood in terms of voting. For every pixel, 5 votes are performed, one for each plant type L_p; the winner is the type with the maximum number of points. The point evaluating scheme consists of the following 4 terms:

$$Q_{L_p} = \left(\sum_{k=0}^{8} P_{L_k, L_p} \right) + \sigma_T G_N T_{L_p} + \sigma_H G_N H_{L_p} + S_{L_p} \delta_{L_p, L_0} \quad (1)$$

Q is the number of points for a hypothetical plant type L_p on pixel p. The first term is the sum over all points that type gets from all 8 neighbours with types L_k (k=1...8) of the considered pixel p and also from the plant type L_0 sitting actually on p (k=0). The next two terms describe the environmental enhancement or stress for the considered plant type. In these terms, G_N is a random number distributed according to a nor-

malised Gaussian distribution function with zero mean and unit variance and σ_T, σ_H are the standard deviations of the respective environmental variables. The last term describes the site preference and advantage and is different from zero only if the vote is made for the plant type actually populating the considered pixel p (i.e. if $L_p = L_0$, $\delta_{i,k}$ is the Kronecker-delta). After determination of the Q-value for each type L_p , the type assigned to pixel p for next year (t+1) is the one with the highest Q-value:

$$Q_{L\max_p} = \max\left\{Q_{L_p},\ L_p = 1..5\right\}$$
$$Z_{p,t+1} = L\max_p \qquad (2)$$

It is important to realise that we calculate a new array $Z_{p,t+1}$ with $Z_{p,t}$ unchanged according to the usual procedure when dealing with CAs. Only after finishing the calculation for all N^2 pixels we overwrite the old Z-array for time t with the new one for time t+1.

3 RESULTS

Figure 1 shows an example for the dynamics emerging from the interplay of the 5 plant types.

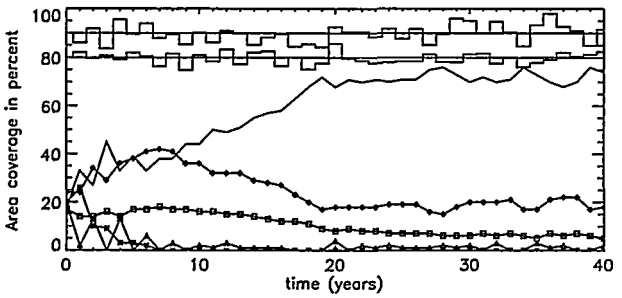

Fig. 1: Typical example for the development of the 5 plant types over 40 years. Area coverage is given for type 1 (line), type 2 (squares), type 3 (diamonds), type 4 (triangles) and type 5 (asterisks). The two environmental variables are displayed in arbitrary units at the top of the figure. Note the occurrence of the five different types of development termed constant (type 1,3 after year 20), fluctuating (type 3 years 0-20), growing (type 1 years 0-20), decaying (types 2,5) and intermittent (type 4).

To demonstrate weak causality or dynamical instability with our model, we repeat a history calculated with the same environmental fluctuations but one minor difference in the initial conditions only: we exchange the plant type on one of the 400 pixels. Figure 2 shows the two histories for type 3 exhibiting a strikingly different development over 120 years. It has to be mentioned that roughly 90 % of all the 1600 possible 1-pixel-changes lead to no effects that would be of practical relevance within 40 years. Only 3 % of the considered changes in the initial conditions caused clearly observable effects after 40 years. These results indicate a certain stability of the development of the simulated plant population in respect to small disturbances in the initial conditions but at the same time underline the importance of details that can have long range effects. Further, it is clear that similar instabilities have to be expected arising from small changes in the record of the environmental variables.

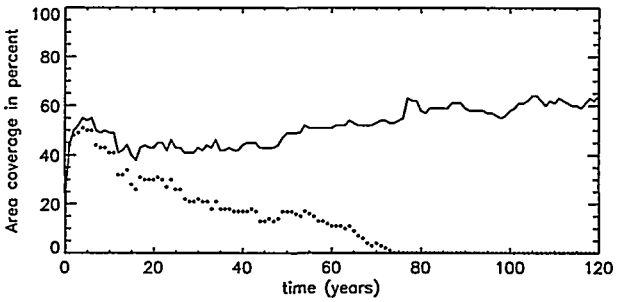

Fig. 2: Demonstration of dynamical instability („butterfly effect"). A first run covering 120 years was performed with random initial conditions. This calculation was repeated with the only difference that in the initial conditions, plant type 2 on field (5,7) has been exchanged by type 4. The difference between the first run for type 3 (line) and the second run (points) is clearly visible. After year 75 the whole field is populated by type 1 in the second run. Realise that the calculation has been repeated with the same environmental history.

4 CONCLUSION

We show that basic aspects of vegetation dynamics resulting from long-term observations can be understood on the basis of a CA. Our approach centred on a preference matrix and sensitivity vectors as interfaces to expert knowledge revealed to be simple enough from a practical point of view and at the same time realistic enough to reflect basic observed traits. Our model simulations clearly show a realistic possibility for the combination of stability and instability in the development of a plant community and help to reconcile the old fundamental dichotomy in vegetation dynamics between the two classical theories based on determinism (understood as long-term predictability) and disorder (chance effects). This insight can help to give more confidence in the interpretation of observed unexpected fluctuations in nature.

5 REFERENCES

[1] H. Balzter et al., *Cellular automata models for vegetation dynamics*, Ecol. Modelling **107**(2-3), 113-125 (1998).

[2] F. Klötzli, *Projected and chaotic changes in forest and grassland plant communities*, Ann. Botanica **53**, 225-231 (1995).

[3] F. Gassmann, J. Füssler, *Adaptation rate of the biosphere as a critical parameter in global climate dynamics*, this report.

[4] F. Gassmann, F. Klötzli, G.-R. Walther, *Simulation of observed types of development of plants and plant communities: chaos, patterns and fluctuations*, submitted to J. Veg. Sci.

AUTOMOBILE TECHNOLOGY IN A CO_2-CONSTRAINED WORLD

A. Schafer (MIT, Cambridge), S. Kypreos, L. Barreto Gomez, H.D. Jacoby (MIT, Cambridge)
Ph. Dietrich (ETH Zürich and PSI)

This study identifies the environmental conditions under which less CO_2-emitting and more expensive automobile technology might enter the North American transportation sector. For that purpose, different exogenous CO_2-reduction targets are imposed and the resulting market shares of hypothetical future automobile technologies calculated. The criteria for the selection of different types of automobiles/fuels is the minimisation of discounted, cumulative transport sector costs over the scenario time horizon.

1 INTRODUCTION

The objective of the study refers to the evolution of future demand for transportation services, the transportation sector's contribution to meeting an energy sector CO_2 target and the contribution of the different modes of transport in reducing emissions. The study addresses also questions related to the technologies required, and their time of introduction in the market.

The implications of greenhouse warming policies on the demand for automobile transportation are assessed in this study. The analysis is conducted by two linked models. A passenger Transport Demand Model (TDM) formulates a consistent set of long-term world-regional demand scenarios. Then, a greenhouse gas reduction target for the transportation sector, related to the Kyoto protocol and its potential extensions, serves as a constraint for the supply model MARKAL which identifies the time-dependent market share of least-cost technology to reduce transport sector greenhouse gas emissions, while satisfying the projected transportation demand.

2 FUTURE TRAVEL DEMAND

On highly aggregate (e.g. world-regional) levels, travel demand follows well-defined patterns and can be described by only a few variables, mainly the "Zahavi-budgets" [5]. Based on empirical analysis, Zahavi concluded that – on average – humans dedicate a fixed share of their income to travel (the travel money budget). In addition, they spend an average of 1.1 hours on their travel per day (the travel time budget). The two budgets alone describe the evolution of passenger transport in all regions of the world taking into account the economic development path and the increased per capita income. The fixed travel money budget translates rising income into rising mobility, whereas the constant travel time budget pushes people towards faster modes of transport as their demand for mobility grows. In addition, the modal share is determined by land-use characteristics and path-dependence of infrastructures. These are the core relationships of the TD-model. The MARKAL-MEDI model is used to determine the detailed cost-minimum supply structure of the transportation sector (composed of technologies, time of their market introduction and withdrawal, etc.) subject to the CO_2 constraint. The market penetration of new and the withdrawal of existing technologies is constrained with logistic equations. The MEDI model, employed at the Paul Scherrer Institute, solves for partial equilibrium between demand and supply by maximising a linearised form of consumer's and producer's surpluses [2].

3 TRANSPORTATION SUPPLY OPTIONS

Low greenhouse-gas emission automobile technology data are derived from authoritative studies of the U.S. National Research Council [3] and the former U.S. Office of Technology Assessment [4]. Both projections are based on a number of premises including U.S. federal emission standards, occupant safety standards, and similar quality-of-service characteristics as the corresponding baseline car. The reference point, zero reduction in fuel consumption at zero incremental investment costs, reflects the baseline vehicle, i.e. the sales-weighted gasoline driven car in the U.S. in 1995. We include estimates for corresponding CNG- and alcohol-fuelled vehicles with specifically designed engines, assuming that engine efficiency is 15 % higher compared to their gasoline fuelled counterpart. The resulting cost and fuel consumption characteristics are shown in Table 1 for all 12 derived automobiles and the existing vehicle fleet in 1995. The fuel consumption of the sales-weighted 1995 -automobile in the U.S. was 9.5 litre per 100 km and the retail price US$ 15,735.

The evolutionary vehicle may incorporate a direct injection gasoline engine and a standard auto body, whereas the vehicle with moderate changes may represent a 4-valve low-friction port-injected engine integrated in a first-generation aluminium space frame body. The vehicle representing radical technological change may be based on a hybrid electric drive train with a bipolar lead-acid battery and the revolutionary concept on a PEM fuel cell hybrid drive train with a Nickel-Metal Hydride battery and a fuel reformer.

	Y.o.I.	Gasoline	CNG	Alcohols
Existing Fleet	1987	15.4/3.7	-/-	-/-
Evolutionary	2005	16.4/2.6	17.7/2.4	16.4/2.3
Moderate	2010	17.4/2.2	18.5/2.0	17.4/1.9
Radical	2010	20.3/1.4	20.9/1.2	20.3/1.2
Revolutionary	2015	22.5/1.1	22.9/0.9	22.4/0.9

Table 1: Retail price (1000 US$(90)) / final energy use (MJ/km) characteristics of all automobiles considered in this paper. Y.o.I.: year of introduction.

For simplicity of this analysis, fuel consumption levels of all vehicles are assumed to remain at their initial level. Operating and maintenance costs were assumed to be 5.1 % (fixed) and 2.2 % (variable) of the vehicle retail price per year.

4 RESULTS

In the *reference* scenario, CO_2 emissions follow the increase and subsequent the decline in automobile traffic volume (as estimated in the TD model due to an increasing share of faster mobility modes), as no vehicle fuel efficiency improvements are assumed and no cost-effective, more fuel efficient vehicle technologies exist. The *stabilisation* scenario already imposes a significant constraint on CO_2 emissions, culminating at a 45 % emissions reduction in 2030. The cost-minimum way to meet this target essentially consists of using evolutionary gasoline cars, accounting for a 87 % market share in 2050, and evolutionary alcohol-fuelled vehicles, ultimately fuelled with bio-ethanol (repre-senting the remaining 13 %). In addition, CNG- and methanol- fuelled (from natural gas) vehicles are needed as intermediate technologies to guarantee the strong and early transition towards the 2010 emission target.

The *zero emissions* case by 2050 demands drastic alterations in automobile and fuel technology. Automobiles fuelled with bio-ethanol, the only zero-carbon fuel considered in this paper, necessarily account for the entire market share in 2050. As with the stabilisation scenario, CNG- and methanol-fuelled (from natural gas) automobiles enable the achievement of the 2010 emission target. However, even in this stringent reduction scenario, the more fuel efficient and expensive hybrid or fuel cell vehicles essentially are not required. The reason is the assumed land-availability, which in turn determines the fuel costs. Based on a heating value of 20 GJ per ton of biomass and a (conservative) yield of 11 tons of biomass per hectare, land requirements for the production of 10.5 EJ of ethanol in 2050 result in nearly 80 million hectare or one-third of the North American cropland. To a large extent, the energy plantations could be located on idled cropland, which today accounts for one-fifth of total U.S. cropland alone and is increasing. However, more stringent cropland constraints would - in the absence of fuel imports - require the introduction of more fuel-efficient and thus more expensive vehicle technology. The use of low CO_2 emission technology causes undiscounted annual travel costs to rise by up to 13 % above the baseline scenario.

5 OUTLOOK

These results build on preliminary data of automobile and fuel production and processing technology. The next steps of the project include the calibration of the general equilibrium model EPPA [6] to be used as driving force of demand, its full integration with the other models and the use of final transportation data for different world regions [1].

6 ACKNOWLEDGEMENT

Research underlying this paper was partially funded by the Alliance for Global Sustainability (AGS).

7 REFERENCES

[1] P. Dietrich, A. Amstutz, A. Schafer, *Low Greenhouse Gas Emission Automobiles, Technology and Costs*, MIT, The Cooperative Mobility Program, Discussion Paper 98–6–1 (1998).

[2] S. Kypreos, A. Schafer, H.D. Jacoby, *Mobility in a CO_2-constrained World—Description of the Model System*, paper in preparation (1998).

[3] National Research Council (NRC), *Automotive Fuel Economy – How Far Should We Go?* National Academy Press, Washington DC (1992).

[4] Office of Technology Assessment (OTA), *Advanced Automotive Technology, Visions of a super-efficient Family Car*, OTA–ETI–638, Congress of the United States, Washington, DC (1995).

[5] A. Schafer, D.G. Victor, *The Past and Future of Global Mobility*, Scientific American **277(4)**, 58–61, October (1997).

[6] H.D. Jacoby, R.S. Eckhaus, A.D. Ellerman, R.G. Prinn, D.M. Reiner, Z. Yang, CO_2 *Emission Limits: Economic Adjustments and the Distribution of Burdens*, The Energy Journal **18(3)**, 31–58 (1997).

GHG-EMISSIONS FOR CARS WITH DIFFERENT POWER TRAINS OVER THE WHOLE LIFE CYCLE

A. Röder

The method of life-cycle assessment (LCA) has been applied to cars with different power trains. As an example, the results for greenhouse gas (GHG) emissions are presented. They show possibilities and limits for the reduction of these emissions in the transportation sector by means of advanced technology.

1 INTRODUCTION

The transportation sector is the source of a significant share of total global greenhouse gas (GHG) emissions. Technical solutions to reduce these emissions can be mainly divided into the following three categories:

- reduction of driving resistance (weight, aerodynamic drag, rolling resistance coefficient).
- improvement of power train efficiency (subsystem efficiencies, hybrid systems, introduction of electric motors with either battery storage or fuel cell systems).
- switch to less CO_2-intensive fuels (methanol, hydrogen, biodiesel).

This study focuses on the latter two points in order to determine which combinations of fuel and power train technology offer large potential for reduction.

2 THE CONCEPT OF LIFE-CYCLE ASSESSMENT (LCA)

In LCA one tries to determine the total ecological impact that is related to the use of a good. For the example of a car this includes direct emissions from the utilization phase as well as contributions from the production, maintenance and disposal of the car or the production of the fuel.

Not considered in this study are the production, maintenance and disposal of infrastructure such as roads, bridges or tunnels.

3 TECHNOLOGIES CONSIDERED

The analysis has been restricted to the following technologies:

Power Trains:

- Spark Ignition Internal Combustion Engine (ICE) with manual gearbox
- Electric Motor with Fuel Cell system (FC) and supercapacitor as storage device to provide peak power for acceleration

Fuels:

- (Unleaded) Gasoline
- Compressed Natural Gas (CNG)
- Methanol (MeOH) from Natural Gas
- Compressed Hydrogen (CH_2) from Natural Gas
- CH_2 via electrolysis from decentralised, roof-integrated PV-systems in Switzerland
- CH_2 via electrolysis from a hypothetical GHG-free (over the whole life cycle) electricity source

The reference case is a car with ICE running on gasoline.

All the fuels can be used both in ICEs and fuel cell systems. In the latter case, gasoline, CNG and MeOH must first be reformed to a hydrogen-rich gas. For lack of data only on-board reforming of MeOH has been considered so far. For the average efficiency of this reformer two cases have been analysed: a rather pessimistic estimate of 65 % and a more optimistic one of 75 %.

CH_2 from a hypothetical GHG-free electricity source has been included to give a rough estimate of the maximum reduction possible by switching to a CO_2-free primary energy carrier.

In order to make the different cars comparable to one another, the different power trains have been installed in the same car body. The weight (and material) calculations take into account that a heavier power train also leads to structural reinforcement. The basis for the models is a further optimised Twingo SmILE [1] with a consumption of 2.7 l/100 km in the FTP-cycle (without cold start).

On-board technologies considered represent the expected state-of-the-art in 2005, other technologies (e.g. basic materials, fuel production and distribution) refer to the mid-nineties.

4 DATA

Many of the data sets needed for the study (especially for basic materials, fossil energy carriers, electricity) had already been elaborated at PSI and ETH [2]. The power train subsystems and the production and distribution of unconventional fuels have been analysed using literature data and expertise from both PSI and industry.

The consumption of fuel has been calculated with a toolbox that was provided by ETH [3]. Direct CO_2-emissions have been calculated from the carbon balance, emissions of other GHGs (mainly N_2O) were estimated considering data from literature. The figures used in the present paper are for the FTP-cycle without cold start.

For proper allocation of emissions from production and disposal, the total distance driven during the lifetime of the car was assumed to be 120'000 km.

5 RESULTS AND DISCUSSION

The following two figures show the results of first calculations of GHG-emissions over the whole life cycle of cars with ICE and FC system, respectively. The different GHGs have been weighted with their Global Warming Potentials over 100 years (GWP_{100}) according to [4]. The numbers indicate the fuels assumed:

1: Gasoline

2: MeOH from NG; 2a stands for an average reformer efficiency of 65 %, 2b for an efficiency of 75 %

3: CNG

4: CH_2 from NG

5: CH_2 from Swiss PV

6: CH_2 from GHG-free electricity

The analysis must be restricted to GHGs at this stage because only for these emissions available data was sufficient for a reliable calculation. Future updates that will be carried out are not likely to change the general picture.

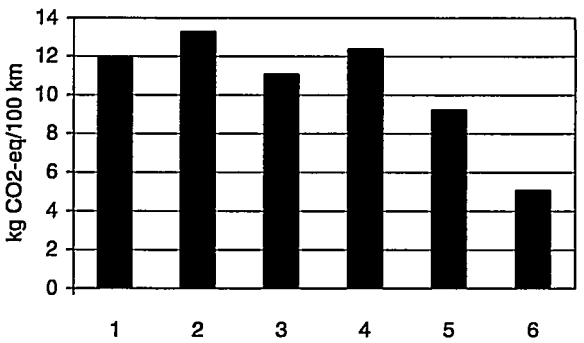

Fig. 4: GHG-emissions over the whole life cycle for cars with internal combustion engine and different fuels. 1 kg CO_2-eq/100 km is equivalent to 0.31 l gasoline/100 km (lifetime emissions).

For the case of the conventional power train (Figure 1) fossil-based fuels offer only a small potential for reduction compared to the reference case, with the most promising fuel being CNG (nearly 8 % less GHG-emissions than gasoline). With CH_2 from PV reductions of more than 20 % have been calculated. Moreover, the production of solar PV cells still has large potential for improvement, whereas the fossil fuel technologies have to be considered mature. Thus, the gap between fossil and PV-derived fuels will further increase in the future.

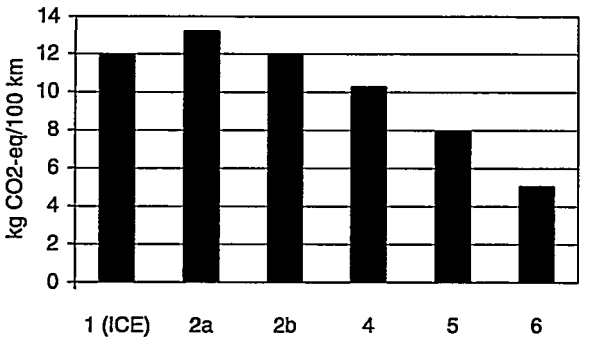

Fig. 5: GHG-emissions over the whole life cycle for cars with supercap-assisted fuel cell system and different fuels; the value for the gasoline-fuelled ICE-car on the left is given for comparison.

Fuel cells could reduce GHG-emissions (compared to ICE cars running on the same fuel) by 0 % (for the case of MeOH under pessimistic assumptions for reformer efficiency as well as for CH_2 from GHG-free electricity) to 17 % (CH_2 from NG). Nonetheless the figures for the hypothetical GHG-free electricity source show that reductions of more than 60 %, compared to the reference case, are hardly achievable. Thus the question remains whether long-term reduction targets for total GHG-emissions can be achieved without actions to mitigate the predicted increase of traffic volume.

Further activities will broaden the scope of the study: on the one hand, other technologies will be analysed (e.g. gasoline reformer, hybrid cars, biomass-derived fuels), on the other hand more ecological as well as economic aspects will be included.

6 REFERENCES

[1] Greenpeace, *Das SmILE-Konzept. Die Technik.* Greenpeace Germany, Hamburg (1996).

[2] R. Frischknecht, U. Bollens, S. Bosshart, M. Ciot, L. Ciseri, G. Doka, R. Hischier, A. Martin, R. Dones, U. Gantner, *Ökoinventare von Energiesystemen*, 3rd ed., BEW, Bern (1996).

[3] L. Guzzella, A. Amstutz, *QSS-Toolbox, Benutzeranleitung*, Laboratorium für Energiesysteme, ETH Zürich (1997).

[4] Intergovernmental Panel on Climate Change (IPCC), *Climate Change 1995 - The Science of Climate Change*, Cambridge (1996).

LEARNING CURVES IN ENERGY PLANNING MODELS

L. Barreto, S. Kypreos

This study describes the endogenous representation of investment cost learning curves into the MARKAL energy planning model. A piece-wise representation of the learning curves is implemented using Mixed Integer Programming. The approach is briefly described and some results are presented.

1 INTRODUCTION

Technological change is one of the most important driving forces of productivity growth and economic development. Its dynamics is a strong conditioning factor on the achievement of sustainable goals, both at local and global levels, for energy systems.

The successful introduction of environmentally sound energy technologies into the marketplace will depend, among other factors, of the cost-competitiveness relative to the existing ones. Technological paths heading to the long term de-carbonisation of the global energy system will only occur if supported by previous R&D but, not less important, by early investments and diffusion of innovative technologies into the marketplace, which allow for cumulative learning processes to take place [1].

Technological change dynamics should be endogenised in energy planning models. For the TEEM project, PSI has incorporated learning curves for the investment cost of technologies into the MARKAL model. The resulting effects on the structure of the energy systems are analysed.

2 LEARNING CURVES

A learning, or experience, curve describes the specific cost as a function of the cumulative capacity for a given technology. It reflects the fact that some technologies may experience declining costs as a result of their increasing adoption into the society, due to the accumulation of knowledge through, among others, learning-by-doing and learning-by-using processes [2]. An experience curve can be defined as:

$$SC(C) = a * C^{-b}$$

Where:

SC: Specific cost
C: Cumulative capacity
b: Learning index
a: Specific cost of the first unit

The interaction of a number of technical, economic, environmental and social factors influences the magnitude and rate of the learning. The learning index b can be derived from the progress ratio. The progress ratio (pr) is defined as the factor by which the cost declines each time the cumulative production doubles. It can be expressed as a function of the learning index as:

$$pr = 2^{-b}$$

This parameter is a key assumption of the problem as it defines the speed of learning for the technology.

3 THE MIXED INTEGER PROGRAMMING FORMULATION

The nonlinear formulation of the experience curves produces a non-convex nonlinear programming problem, for which it is not possible to guarantee a global optimal solution. The Mixed Integer Programming (MIP) approach provides a linearisation of the problem, consisting in a piece-wise approximation of the cumulative cost curve where integer variables are required to control the sequence of segments along the curve. The MIP alternative, although more computer intensive, enables to find a global optimum. Endogenisation of experience curves in energy system models using the MIP approach has been reported by [3] for the model MESSAGE and [4] for GENIE.

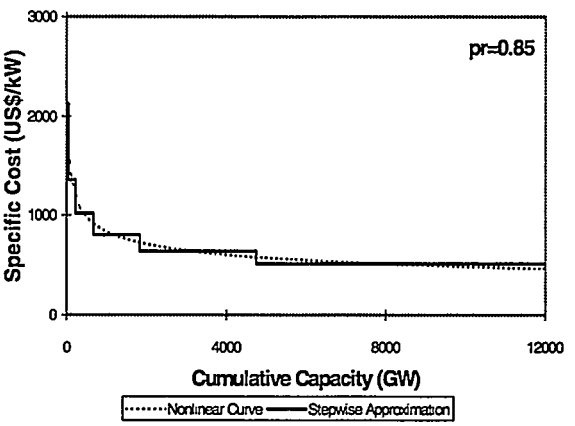

Fig. 6: Comparison between nonlinear and piecewise experience curve.

A number of parameters affects the accuracy of the piece-wise linear representation. Of particular importance are the maximum cumulative capacity allowed, the number of segments and the segmentation pattern. Procedures were defined to obtain an adequate approximation [1].

4 SOME RESULTS

The comparative results for the MARKAL Model presented here illustrate the impact of technological learning in the structure of the simplified global electricity generation system used as example. The demand corresponds to the IIASA scenario B [1]. Six learning technologies were considered: Gas Combined Cycle, Wind Turbine, Solar PV, New Nuclear, Gas Fuel Cell and Advanced Coal. A reference development and a CO_2 stabilisation scenario (constant 5 % reduction relative to 1990 levels from 2010 onwards) are presented in Figure 2 and Figure 3. Comparisons are made between the Linear Programming (LP) and learning MIP solutions. The LP solution assumes static values for the investment costs of the technologies.

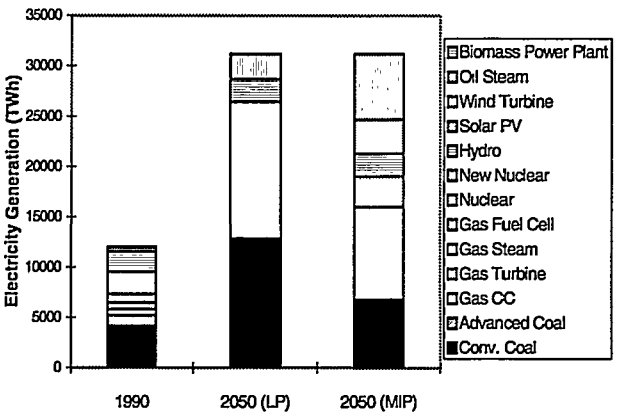

Fig. 7: Contribution to electricity generation by various technologies. Reference scenario.

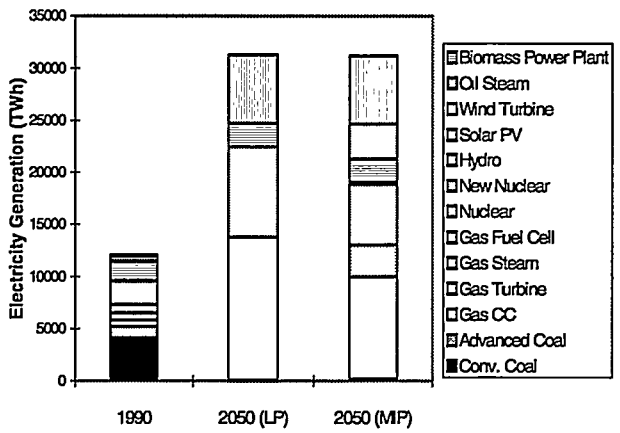

Fig. 8: Contribution to electricity generation by various technologies. CO_2 stabilisation scenario.

New, innovative technologies, such as Gas Fuel Cell and Solar PV, hardly considered by the standard LP model, are introduced when learning effects are incorporated. Also, in this case, with a learning Gas CC becoming more competitive than the gas turbine.

5 SOME REMARKS AND CONCLUSIONS

The technological learning concept helps to assess possibilities and requirements for new energy technologies. The consideration of learning in the decision models influences significantly the structure of the resulting systems. New technologies may be introduced to the solution as a consequence of the endogenous cost evolution accounted for in the MARKAL model. The marginal costs of emissions abatement are lower for the learning case. The results reveal the need for early investments on sustainable technologies, both in R&D and niche markets, in order to ensure they move along their learning curves and achieve long run competitiveness.

As uncertainty is deeply rooted in the technological evolution processes [2], the learning rate remains one of the most sensitive and difficult assumptions. A careful technology characterisation and the study of the main driving factors of technological change in specific sectors have to be done, in order to support the assumptions and complement the analysis.

6 ACKNOWLEDGEMENTS

This study is financed by the Swiss Federal Office of Education and Science (BBW) as part of the TEEM Project - EC-JOULE III of the European Union.

7 REFERENCES

[1] International Institute for Applied Systems Analysis (IIASA)/World Energy Council (WEC). *Global Energy Perspectives,* Cambridge University Press (1998).

[2] A. Grübler, *Endogenous Technological Change,* Proceedings of the IIASA Workshop on Modelling Technological Learning, IIASA, Laxenburg, Austria (1998).

[3] S. Messner, *Endogenised Technological Learning in an Energy Systems Model,* Journal of Evolutionary Economics, **7**, 291-313 (1997).

[4] N. Mattsson, *Internalising Technological Development in Energy Systems Models,* Thesis, Degree of Licenciate of Engineering, Chalmers University of Technology, Sweden (1997).

[5] S. Kypreos, L. Barreto, *Mixed Integer Programming for Learning Curves in the ERIS Prototype Model,* TEEM Project of Joule-III, The ERIS Prototype Model, Switzerland (1998).

GLOBAL POST-KYOTO SCENARIO ANALYSES AT PSI

S. Kypreos

Scenario analyses are described here using the Global Markal-Macro Trade (GMMT) model to study the economic implications of the Kyoto Protocol to the UN Convention on Climate change. Some conclusions are derived in terms of efficient implementations of the Post-Kyoto extensions of the Protocol.

1 INTRODUCTION

Quite a few models already exist to assess the implication of CO_2 mitigation policy. GMMT [1] is a combination of the top-down and the bottom-up method based on a further development of Merge [2]. It is a set of regional sub-models hard-linked through the global welfare function, the global use of resources, the international trade and the specification of sustainable levels of greenhouse gas concentrations. The model provides a better representation of the individual types of technologies for CO_2 mitigation.

2 DESCRIPTION OF SCENARIOS

Five world regions are explicitly defined in the model. The USA, other OECD, the former Soviet Union, China and the rest of the world (ROW). USA is modelled using the Markal-Macro model [3] of the International energy Agency (Project ETSAP) while all other regions are defined as in the Merge model of A. Manne and R. Richels. The analysed cases are:

The *Business as Usual* case (*BaU*): The database of GMMT is updated in order to include the assumptions and reproduce the emissions of the IPCC reference case (no policy, IS92a) [4]. The case assumes a world population level of 10 billion by the year 2050. Most of the population growth takes place in the region "Rest of the World" while China is stabilising its population to a level of approximately 1.5 billion inhabitants. The economic output increases by a factor of 4.3, the primary energy use by a factor of 2.9 and the CO_2 emissions by 2.4. Most of the growth takes place in the less developed countries while the regional differences in the energy-GDP ratios are decreasing.

The *Kyoto Forever* case (*KF*): This case assumes for 2010 a 7 % CO_2 reduction for the USA and a 5 % reduction for the other OECD regions. Emissions for the former USSR regions remain as in the levels of 1990. This scenario extents the Kyoto Protocol assuming after 2010 a decrease of emissions with a flat rate of 5 % per decade for all Annex 1 regions.

The *Kyoto Global Reduction* case (*KG*)*:* This case is imposing emission reduction targets to all the world regions similar to Kyoto forever case but the less developed countries start also with their commitments in the year 2020. It is an extension of the Kyoto Protocol to the global level.

Case *20G*: A global CO_2 reduction of 20 % below the emissions in the year 1990 is assumed to be obtained by the year 2050. This case is an example that serves the understanding of the consequences of drastic CO_2 reduction policy.

All the cases above are analysed assuming first a situation without trade and then a case with maximum possible flexibility where trade across all the world regions is allowed. Only the KF case assumes a partial trade restricted in the Annex 1 regions.

3 SOME RESULTS AND CONCLUSIONS

This study shows that the marginal CO_2 control cost of the Protocol can be reduced to $58 per ton of Carbon when a market of permits is going to be established by 2010 to Annex 1 regions (Figure 2, KF-AN1). This low costs and consequently the economic implications of the Protocol could be further reduced if the policy flexibility foreseen is fully used. This refers to the reduction of all other greenhouse gases, the possibility to enhance CO_2 sinks, and the introduction of JI actions and the Clean Development Mechanism (CDM) between Annex 1 countries and the rest of the world. Extending for example the trade of CO_2 permits to all world regions reduces the marginal cost to $34 per ton (Figure 2, KF-ALL). On the contrary to the conclusions valid for the first decade, the Kyoto forever case has high marginal costs after 2010 when the trade of permits is restricted to Annex 1 regions.

The Kyoto Protocol must be seen as the first step of policy actions. In the future, policy developments should establish safe GHG concentrations in the atmosphere and avoid dangerous interference with the climate. Although nobody knows what safe GHG concentrations exactly means, significant reductions of today's global CO_2 emissions are expected. The cost of this policy is also significant and rather high. The 20 % CO_2 reduction case by 2050 (that extrapolates to a 50 % reduction by 2100) estimates costs of $550 per ton C (Figure 2).

The study confirms the well known fact that only when the less developed countries commit themselves in reducing their CO_2 emissions in the future, the global emissions can be reduced below the level of 1990 (compare the KF and the KG cases in Figure 1). Also, if a system of global emission trade is implemented, the post-Kyoto scenarios become economically *effi-*

cient, in the sense that they give minimum GDP losses for a given CO_2 target. Therefore, the participation of the LDCs is a pre-requisite to establish successful post-Kyoto policy options. The global trade of permits is also known as the *where* flexibility since it allows to regions with high marginal costs to purchase permits from regions with low cost, thus harmonising the marginal control costs across regions.

Another fact concerns *equity* considerations. It is well known that the allocation of initial endowments of emission rights per region and the global trade define the share of mitigation burdens. If some general rules for fairness in burden sharing can be established this will increase the acceptance of the Protocol. The study examines a distribution rule for the initial endowments based on equal pollution rights per capita in the long term.

The next point of difference in the climate change debate concerns the distribution of intergenerational equity, or the intertemporal transfers of carbon emission rights; the so-called *when* flexibility. It is a well known fact that most of the USA research teams are opposing early actions against global warming, for two main reasons. First, a policy that follows the natural capital stock turnover will not result to a premature retirement of long lived plants and equipment. Second, time is necessary to develop low-cost, low-carbon alternatives to the fossil fuels used now. For example, Manne and Richels are very sceptical with the Kyoto forever case as a scenario that departs from the WRE550, the well known least cost case calculated by Wigley, Richels and Edmonds [5]. On the contrary, some European research groups claim that an earlier introduction of low-carbon alternatives will help to establish the technology dynamics needed to reduce the cost of these technologies by accumulation of experience.

PSI is developing a method to include endogenous technological change in GMMT for answering the question stated above. Preliminary results with a prototype model indicate that when the proper R&D policy is selected to support innovative technologies that assume high progress ratio and potential, like solar PV, advanced nuclear and fuel cells, the cost of CO_2 control can be significantly reduced in the future.

However, one should stress out that uncertainty is the prevailing characteristic of the climate change issue. Two policy facts are known with certainty; first, efficient CO_2 control policy can only take place under the ideal situation of international cooperation and trade among all world regions and second, the appropriate R&D policy for new and innovative technologies can significantly reduce mitigation cost.

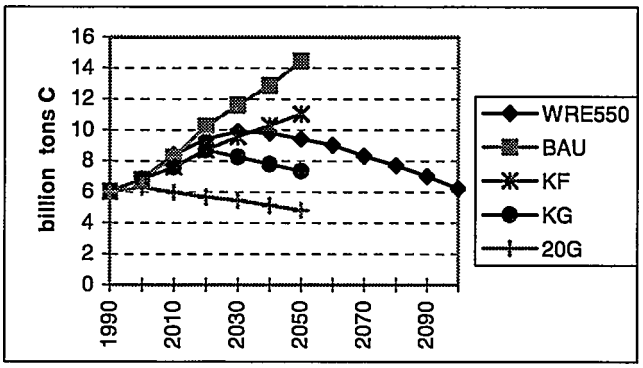

Fig. 1: CO_2 emission development per scenario.

The Kyoto Global Case (KG) is a scenario that departs from the WRE550 least cost case and obtains the same level of emission reduction 40 years earlier.

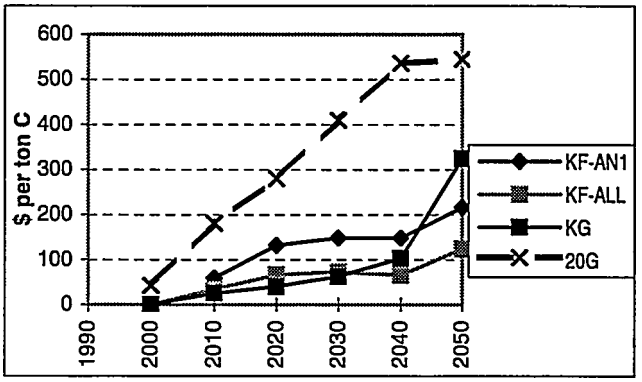

Fig. 2: CO_2 marginal costs for the cases analysed.

The marginal cost of the Kyoto forever (KF) case varies between \$34 to \$68 per ton C, in the year 2010 and is approaching \$100 per ton C later on while the costs for the 20 % reduction case are extremely high.

4 REFERENCES

[1] S. Kypreos, *GMMTM a global trade model for studying CO_2 mitigation options*, PSI F5, Annual report (1997).

[2] A.S. Manne, R. Mendelsohn, R.G. Richels, *MERGE: a Model for Evaluating Regional and Global Effects of GHG Reduction Policies*, Energy Policy **3** (1) (1993).

[3] A.S. Manne, C. Wene, *MARKAL-MACRO: a Linked Model for Energy-Economy Analysis*, Brookhaven National Laboratory, Upton, NY, BNL-47161 (1992).

[4] IPCC *Climate Change 1994*, Cambridge University Press (1994).

[5] T.M.L. Wigley, R. Richels, J.A. Edmonds, *Economic and Environmental Choices in the Stabilisation of Atmospheric CO_2 Concentrations*, Nature **379**, 240-243 (1996).

APPENDIX

PROJECT COLLABORATIONS WITH EXTERNAL PARTNERS

ALLIANCE FOR GLOBAL SUSTAINABILITY

Projektleiter: M.K. Eberle, A. Wokaun
Sustainable Mobility:
Background Systems and Novel Technologies that Made Urban Transportation Work

Projektleiter: S. Kypreos
Mobility in a CO_2-Constrained World

Projektleiter: S. Stucki, A. Wokaun
Biomass and Wastes as Renewable Fuels for Processes and Transportation

BBW

Projektleiter: W.K. Graber
VOTALP: Vertical Ozone Transport in the Alps
EU-Projekt, teilweise BBW-unterstützt

Projektleiter: W.K. Graber
ECOMONT: Ecological Effects on Land Use Change on European Terrestrial Mountain Ecosystems
EU-Projekt, teilweise BBW-unterstützt

Projekleiter: S. Kypreos
GEM-E3-ELITE: European Emission Mitigation Policy and Technical Evolution
EU-Projekt

Projekleiter: S. Kypreos
TEEM: Energy Technology Dynamics and Advanced Energy System Modelling
EU-Projekt

Projektleiter: S. Müller
ELZA: Development of Electrically Rechargeable Zinc-Air Batteries
EU Projekt

Projektleiter: G.G. Scherer
Second Generation PEFC - Development of a Commerciable Viable Stack
EU Projekt

Projektleiter: R.T.W. Siegwolf, PSI
Co-Projektleiter: Prof. Dr. J. Fuhrer, University of Bern
EUROSILVA - HARVA

Projektleiter: R.T.W. Siegwolf
ICAT-Impact of elevated CO_2 and Airpollution on Tree Physiology

BFE

Projektleiter: I. Alxneit, M. Sturzenegger, H.R. Tschudi
Direkte Umwandlung von konzentrierter Sonnenenergie in chemische Energieträger

Projektleiter: W. Durisch
Testmessungen am ICEC-Hybridkollektor

Projektleiter: T. Gerber
Investigation of Soot and NO Production in Spray Combustion of Acetal/Diesel Mixtures

Projektleiter: T. Gerber
Thermochemische Charakterisierung und spektroskopischer Nachweis von Sauerstoffverbindungen im Zusammenhang mit der Verbrennung von sauerstoffhaltigen Brennstoffen

Projektleiter: W.K. Graber
WINDBANK 3: Windbank mittleres Aaretal
HSK-Projekt, teilweise BFE-unterstützt

Projektleiter: W. Hubschmid
Laserspektroskopische Methoden zur Analyse von Flammen und Brennstoff-Sprays

Projektleiter: W. Hubschmid,
Teilprojektleiter PSI: A. Inauen
Mischung und Verdampfung von Brennstoffsprays in Gasturbinen-Vormischbrennern
ABB Corp. Research

Projektleiter: M. Koebel
NO_x-Reduktion mit Harnstoff-SCR

Projektleiter: J.C. Mayor
Experimentelle und numerische Untersuchung der Kopplung von heterogener und homogener Tieftemperaturverbrennung bei hohen Drücken und turbulenten Strömungsbedingungen

Projektleiter: S. Müller
Entwicklung eines 12V/20 Ah Zink-Luft-Moduls
Projekt und Studienfonds der Elektrizitätswirtschaft (PSEL), Zürich

Projektleiter: P. Novák
Wiederaufladbare Lithium-Ionen-Batterie

Projektleiter: R. Palumbo, A. Steinfeld
Solar Thermal Production of Zinc

Projektleiter: G.G. Scherer
Material- und Strukturaspekte von Polymerelektrolyt Brennstoffzellen

Projektleiter: G.G. Scherer
Entwicklung, Konstruktion und kostengünstige Herstellung eines 300 W PEFC Powerpacks für Lernzwecke

Projektleiter: Th.H. Schucan, E. Newson
Hydrogen Supply from Liquid Energy Carriers

Projektleiter: Th.H. Schucan
Leitung der Subtask A/Annex 11 des IEA-Wasserstoff-Programms

Projektleiter: A. Steinfeld
SolarPACES: Solar Power and Chemical Energy Systems

Projektleiter: S. Stucki
Vergasung von Abfallbiomasse

BUWAL

Projektleiter: A.S.H. Prévôt
Vertikalsondierungen während des LOOP-Feldexperimentes Mailand-Tessin

ETH-RAT

Projektleiter: R. Kötz
Supercapacitors
PPM/WF Schwerpunktprogramm Werkstoffforschung

Projektleiter: R.T.W. Siegwolf
ICAT-Impact of elevated CO_2 and Airpollution on Tree Physiology

ETHZ

Projektleiter: A. Wokaun, M. Meier
Brennstoffzellenstapel

FOGA

Projektleiter: W. Durisch
Thermophotovoltaische Wärme- und Stromerzeugung

GAZ DE FRANCE

Projektleiter: E. Newson
Low Temperature Catalytic Ignition of Methane/ Hydrogen/Air Mixtures

IEA

Projekleiter: S. Kypreos
Activities Implemented Jointly to Curb CO_2 Emissions
IEA-ETSAP / Annex VI

INDUSTRY

Projektleiter: W. Durisch
Charakterisierung von GPV-Modulen
TEMTEC Solartechnik, Schöftland

Projektleiter: S. Müller
Entwicklung eines 12V/20 Ah Zink-Luft-Moduls
Electrona SA, Akkumulatorenfabrik, Boudry NE
Larag AG, Lastwagen-Reparatur AG, Wil

Projektleiter: S. Müller
Übersichtsartikel "Zinc/Air and Zinc/Nickel Batteries and their Application in Portable Electric Equipment and Electric Vehicles"
International Lead Zinc Research Organization (ILZRO), USA

Projektleiter: P. Novák
Entwicklung eines Messverfahrens zur Charakterisierung von Lithium-Interkalationsoxiden
BASF/EMTEC AG, Ludwigshafen

Projektleiter: P. Novák
Untersuchungen an Grafitelektroden für Lithium-Ionen-Batterien
TIMCAL AG, Sins

Projektleiter: J.-C. Panitz
Entwicklung von Nanokompositen
Von Roll Isola, Breitenbach SO

Projektleiter: G.G. Scherer
Membranen für die Direkt-Methanol-Brennstoffzelle
Automobilindustrie

Projektleiter: G.G. Scherer
Mikrostrukturierte Elektroden

KTI

Projektleiter: J. Dommen
Limitation of oxidant production (LOOP)

Projektleiter: J. Dommen
Flugtauglicher Sensor für die schnelle simultane Messung von speziierten Stickoxiden und Ozon

Projektleiter: J. Keller
Environmental Impacts of Ozone due to Swiss Energy Systems

SCHWEIZERISCHER NATIONALFONDS

Projektleiter: R. Kötz
Nanoscale Intercalation into Graphite and Metaloxides
NFP 36

Projektleiter: U. Krähenbühl, University of Bern
Co-Projektleiter: R.T.W. Siegwolf, PSI
Reconstruction of Anthropogenic Pollution by S- and N-Bearing Compounds: Isotopic Signatures Since the Turn of the Century through Study of Environmental Archives

Projektleiter: S. Stucki
Thermische Abfallbehandlung
Schwerpunktprogramm Umwelt (IP Abfall)

Projektleiter: A. Wokaun
Laser-Photopolymer Interaction of a Micrometer Scale; Photochemical Reaction Mechanisms, Microspectroscopy, and Structuring by Laser Ablation

VSE

Projekleiter: S. Hirschberg
Dezentral (GaBE)

TEACHING ACTIVITIES

University Level Teaching

Dr. W.K. Graber
Messung und Modellierung der Austauschprozesse in Composite Landscapes
Lehrveranstaltung Universität Innsbruck, Austria, SS 1998.

PD Dr. Th.H. Schucan
Sonnenenergie und Energiespeicherung
Universität Basel, SS 1998.

PD Dr. Th.H. Schucan
Energie und Umwelt
Universität Basel, WS 1998/99.

Dr. R.T.W. Siegwolf, Dr. M. Saurer
Einführung zur Isotopenanalytik in der Ökologie und Physiologie der Pflanzen
Vorlesung und Praktikum, Universät Basel, Pflanzenbiologie, WS 1997/98, January 15-29, 1998.

Dr. R.T.W. Siegwolf
Einführung zur Isotopenanalytik in der Ökologie und Pflanzenphysiologie
Vorlesung, Universität Innsbruck, Austria, Ökologie der Pflanzen, SS 1998.

PD Dr. P. Talkner
Stochastische Resonanz und Brownsche Motoren: Neues aus der Nicht-Gleichgewichts Statistischen Mechanik
University of Basel, WS 1997/98.

PD Dr. P. Talkner
Hydrodynamik
University of Basel, WS 1998/99.

Prof. Dr. A. Wokaun
Erneuerbare Energien
ETH Zürich, SS 1998.

Prof. Dr. A. Wokaun
Physikalisch-chemische Aspekte der Energienutzung
ETH Zürich, WS 1998/99.

Lecture Courses at Other Schools

Dr. J. Dommen
Chemie und Werkstoffe
Zürcher Hochschule Winterthur, WS 1997/98.

Dr. F. Gassmann
Umweltethik
FH Brugg-Windisch, Interdisziplinärer Wahlfachkurs, WS 1997/98.

Contributions to Courses at Universities, FHL and Other Institutes

Dr. M. Bärtsch, F. Holzer
Festelektrolyte für Zink-Luft-Batterien
Semesterarbeit, Fachhochschule Burgdorf, April 27 - September 21, 1998.

Dr. O. Bahn
Coopérations Internationales, dans l'Optique du Protocole de Kyoto, pour Réduire les Emissions de Gaz à Effet de Serre
Formation Continue en "Gestion de l'Environnement et Entreprise", University of Geneva, June 4, 1998.

Dr. R. Bombach
LIF und Raman
Beitrag zur Vorlesung "Numerische und experimentelle Methoden in der Verbrennungsforschung" ETH Zürich, April 22 and 29, 1998.

Dr. W. Durisch
Invited Series of Seminar and Laboratory Sessions on Applied Photovoltaics
University of Bahrain, Department of Electrical Engineering, May 10-13, 1998.

Dr. W. Durisch
Photovoltaik - Strom aus Sonnenlicht
Energietechnische Ausbildung für nichttechnische Führungskräfte, ABB Technikerschule, Baden, May 25, 1998.

Dr. W. Durisch
Photovoltaik-Praktikum für Studenten des Zentralschweizerischen Technikums Luzern, ZTL
September 1, 1998.

Dr. W. Durisch
Strom aus Solarkraftwerken
Energietechnisches Seminar (im Rahmen der Vorlesung 'Kraftwerkstechnik'), Institut für Energietechnik, ETH Zürich, Prof. G. Yadigaroglu, WS 1998/99.

Dr. W. Durisch
Strom aus Solarzellen
Fachhochschule Zürich, 4. Quartal 1998.

Dr. F. Gassmann
Bis zu welchen Grenzen können komplexe Systeme verstanden werden?
Beitrag zur Vertiefungsvorlesung "Grundzüge des Verbrennungsmotors", ETH Zürich, January 19, 1998.

Dr. F. Gassmann
Die wichtigsten Erkenntnisse zum Treibhaus-Problem
Beitrag zur Vorlesung "Ökologische Aspekte der individuellen Mobilität", ETH Zürich, May 22, 1998.

Dr. F. Gassmann
CO_2-Emissionen und Klimaproblematik
Beitrag zur Vorlesung "Erneuerbare Energien", ETH Zürich, June 30, 1998.

Dr. W.K. Graber
Modelle zur Ausbreitung in der Atmosphäre
im Rahmen der Vorlesung "Einführung in die Aerobiologie", Inst. für Pflanzenwissenschaften, ETH Zürich, May 20,1998.

Dr. P. Griebel
Verbrennung in Fluggasturbinen
Beitrag zur Vorlesung "Gemischbildung und Energieumsetzung in Verbrennungskraftmaschinen", ETH Zürich, June 23, 1998.

Dr. O. Haas
Elektrochemische Energiespeicherung und Umwandlung
Beitrag zur Vorlesung "Physikalisch-chemische Aspekte der Energienutzung", Prof. A. Wokaun, ETH Zürich, WS 1998.

Dr. O. Haas
Brennstoffzellen und Elektrochemische Energiespeicherung
Fachhochschule Burgdorf, Nachdiplomstudium/ Energietechnik, 2. Quartal 1998.

Dr. B. Hemmerling
Nonlinear Optical Methods
Beitrag zur Vorlesung "Numerische und experimentelle Methoden in der Verbrennungsforschung", ETH Zürich, April 29, 1998.

Dr. W. Hubschmid
Einführung in die Spektroskopie
Beitrag zur Vorlesung "Numerische und experimentelle Methoden in der Verbrennungsforschung", ETH Zürich, April 22, 1998.

Dr. M. Koebel
Messung stabiler Abgaskomponenten mittels konventioneller Emissionsmesstechniken
Beitrag zur Vorlesung "Numerische und experimentelle Methoden in der Verbrennungsforschung", ETH Zürich, SS 1998.

Dr. I. Mantzaras
Turbulence Modelling
Beitrag zur Vorlesung "Numerische und Experimentelle Methoden in der Verbrennungsforschung", ETH Zürich, April 15, 1998.

S. Müller, Dr. O. Haas
Praktikum: Brennstoffzellen und Batterien
Fachhochschule Burgdorf, Nachdiplomstudium Energietechnik, 2. Quartal 1998.

S. Müller
Teil I: Aufbau und Charakterisierung elektrochemischer Zellen
Teil II: Entwicklungsschritte zur Realisierung der elektrisch wiederaufladbaren PSI Zink-Luft-Batterie
Beitrag zur Vorlesung "Elektrochemie", Prof. R. Weber, Fachhochschule Burgdorf, February 17, 1998.

PD Dr. P. Novák
Elektrochemische Energiespeicherung und Umwandlung
Beitrag zur Vorlesung "Physikalisch-chemische Aspekte der Energienutzung", Prof. A. Wokaun, ETH Zürich, WS 1998.

Dr. G.G. Scherer
Brennstoffzellen
Beitrag zur Vorlesung "Physikalisch-chemische Aspekte der Energienutzung", Prof. A. Wokaun, ETH Zürich, WS 1998.

Dr. G.G. Scherer
Elektromembranprozesse
Beitrag zur Vorlesung "Membrantechnik", PD Dr. W. Heinzelmann, Dr. W. Schirg, ETH Zürich, WS 1998.

Dr. G.G. Scherer
Elektromembranverfahren
Membrantrenntechnik ETH Zürich, June 3, 1998.

Dr. R.T.W. Siegwolf
Einsatz stabiler Isotope in der Ökologie und Physiologie der Pflanzen
Nachdiplomkurs in angewandten Erdwissenschaften der Abteilung Erdwissenschaften, Leitung: Dr. Björn Olsson, ETH Zürich, May 15, 1998.

Dr. R.T.W. Siegwolf
Auswirkungen von Veränderungen von Umweltfaktoren auf die Isotopenfraktionierung in Pflanzen
Beitrag zur Proseminarreihe „Stressphysiologie der Pflanzen", Universität Bern, April 21, 1998.

PUBLICATIONS

Books

P. Talkner, E. Pollak*, A.M. Berezhkovskii**, Guest Editors
Dynamical Processes in Condensed Phases
Chemical Physics **235**, Special Issue (1998).
* Weizmann Institute, Rehovot, Israel
** Karpov Institute, Moscow, Russia

Peer Reviewed Papers

S. Andreani-Aksoyoglu, J. Keller
Short-Term Impacts of Air Pollutants in Switzerland: Model Evaluation and Preliminary Scenario Calculations for Selected Swiss Energy Systems
In C.A. Brebbia, C.F. Ratto, H. Power (Eds.), Air Pollution **VI**, Computational Mechanics Publications, 799-808 (1998).

R. Badii, P. Talkner
Two-Scale Analysis of Intermittency in Fully-Developed Turbulence
Europhys. Lett. **43**, 284-289 (1998).

O. Bahn, E. Fragnière*, S. Kypreos
Swiss Energy Taxation Options to Curb CO_2 Emissions
European Environment **8**, 94-101 (1998).
* HEC-Lausanne

O. Bahn, A. Haurie*, S. Kypreos, J.-P. Vial*
Advanced Mathematical Programming Modeling to Assess the Benefits from International CO_2 Abatement Cooperation
Environmental Modeling and Assessment **3**, 107-115 (1998).
* HEC-Geneva

A.R. Bandy*, T.S. Bates**, D.R. Blake***, S. Businger****, F.L. Eisele*****, B.J. Huebert****, J.E. Johnson**, G.L. Kok*****, C. Mari******, R.Lee Mauldin III*****, A.S.H. Prévôt, R. Rosset******, R.D. Schillawski, K. Suhre******, D.J. Tanner*****, D.C. Thornton*, Q. Wang*******
Physico-Chemical Modelling of the First Aerosol Characterization Experiment (ACE 1) Lagrangian B. 1. A Moving Column Approach
Journal of Geophys. Res. **103,** D13, 16433-16455 (1998).
* Drexel University, Philadelphia, Pennsylvania, USA
** Pacific Marine Environmental Lab., NOAA, Seattle, Washington, USA
*** University of California at Irvine, USA
**** University of Hawaii at Mãnoa, USA
***** National Center for Atmospheric Research, Boulder, Colorado, USA
****** UMR CNRS/ Université Paul Sabatier, Toulouse, France
******* Naval Postgraduate School, Monterey, California, USA

P. Beaud, P. Radi, D. Franzke, H.-M. Frey, B. Mischler, A.-P. Tzannis, T. Gerber
Picosecond Investigation of the Collisional Deactivation of OH A2Sigma in an Atmospheric-Pressure Flame
Appl. Opt. **37**, 3345-3367 (1998).

K.U.M. Bengtsson*, P. Benz**, C.E. Frouzakis ***, R. Schären
N_yO_X Formation in Lean Premixed Combustion of Methane in a High-Pressure Jet-Stirred Reactor
27th International Symposium of Combustion, Boulder, USA, August 2-7 (1998).
* now ABB, Baden
** now Von Roll, Zürich
*** ETH Zürich

S. Borella*, M. Leuenberger*, M. Saurer, R.T.W. Siegwolf
Reducing Uncertainties in $\delta^{13}C$ Analysis of Tree Rings: Pooling, Milling, and Cellulose Extraction
J. Geophys. Research **103(D16),** 19519-19526 (1998).
* University of Bern

J. Bucher*, D. Tarjan*, R.T.W. Siegwolf, M. Saurer, H. Blum**, G. Hendrey***
Growth of a Deciduous Tree Seedling Community in Response to Elevated CO_2 and Nitrogen Supply
Chemosphere IUFRO 17th Int. Meeting for Specialists in Air Pollution on Forest Ecosystems, Florence, September 14-19, 1996; Chemosphere **36,** 777-782 (1998).
* WSL, Birmensdorf
** ETH Zürich
*** Brookhaven National Laboratory, USA

A. Drozdov*, P. Talkner
Path Integrals for Fokker-Planck Dynamics with Singular Diffusion: Accurate Factorization of the Time Evolution Operator
J. Chem. Phys. **109**, 2080-2091 (1998).
* University of Sevilla, Spain

W. Durisch, S. Leutenegger*, D. Tille**
Comparison of Small Inverters for Grid-Independent Photovoltaic Systems
Renewable Energy **15**, 585-589 (1998).
* LEC, Küsnacht
** Technical College Ulm, Germany

P. Egli*, S. Maurer, M.S. Günthardt-Goerg*, C. Körner**
Effects of Elevated CO_2 and Soil Quality on Leaf Gas Exchange and Above-Ground Growth in Beech-Spruce Model Ecosystems
New Phytologist **140**, 185-196 (1998).
* WSL, Birmensdorf
** University of Basel

D. Franzke*, J. Kritzenberger**, E. Ortelli, A. Baindl***, O. Nuyken***, A. Wokaun
Photolysis and Thermolysis of Diaryl(pentazadiene) Compounds in Solid Matrix Investigated by Infrared Spectroscopy
J. Photochem. Photobiol. A **112**, 63-72 (1998).
* now Gretag Imaging AG, Regensdorf
** now Diehl-Glaeser, Hiltl & Partner, Munich, Germany
*** TU Munich, Garching, Germany

W.K. Graber, R.T.W. Siegwolf, M. Furger
Exchange of CO_2 and Water Vapour between a Composite Landscape and the Atmosphere in the Alps
K. Kovar, U. Tappeiner, N.E. Peters, R.G. Craig: Hydrology, Water Recources and Ecology in Headwaters. Oxfordshire, 107-114 (1998).

B. Gupta*, G.G. Scherer, J.G. Highfield**
Thermal Stability of Proton Exchange Membranes Prepared by Grafting of Styrene Into Pre-Irradiated FEP Films and the Effect of Crosslinking
Angew. Makromol. Chem. **256**, 81-84 (1998).
* now Indian Institute of Technology, New Delhi, India
** now Osaka National Research Institute, Ikeda, Osaka, Japan

P. Häring, R. Kötz, G. Repphun*, O. Haas, H. Siegenthaler*
In Situ Scanning Probe Microscopy Investigations of Electroactive Films
Appl. Phys. **A 66**, 481-486 (1998).
* University of Bern

Ch. Hahn, I. Gagel*, C. Thunig*, G. Platz*, A. Wokaun
Investigation of the Photo-Induced Optical Anisotropy of Azo Dye Mesophases
Langmuir **14**, 6871-6878 (1998).
* University of Bayreuth, Germany

Ch. Hahn, Th. Kunz, U. Dahn*, O. Nuyken*, A. Wokaun
Developing Novel Photoresists: Microstructuring of Triazene Containing Copolyester Films
Appl. Surf. Sci. **127-129**, 899-904 (1998).
* TU München, Garching, Germany

A.M. Hering*, J. Stähelin*, U. Baltensperger, A.S.H. Prévôt, G.L. Kok**, R.D. Schillawski**, A. Waldvogel*
Airborne Measurements of Atmospheric Aerosol Particles and Trace Gases during Photosmog Episodes over the Swiss Plateau and the Southern Pre-Alpine Region
Atmospheric Environment **32**, 3381-3392 (1998).
* ETH Zürich
** National Center for Atmospheric Research, Boulder, Colorado, USA

R. Imhof, P. Novák
In Situ Investigation of the Electrochemical Reduction of Carbonate Electrolyte Solutions at Graphite Electrodes
J. Electrochem. Soc. **145**, 1081-1087 (1998).

F. Joho, P. Novák, O. Haas, A. Monnier*, F. Fischer*
Influence of Graphite Surface Modifications on Lithium Intercalation Properties
Mol. Cryst. Liq. Cryst. **310**, 383-388 (1998).
* Timcal AG, Sins

P. Kaufmann*, R.O. Weber
Directional Correlation Coefficient for Channeled Flow and Application to Wind Data over Complex Terrain
J. Atmos. Oceanic Technol. **15**, 89-97 (1998).
* Schweizerische Meteorologische Anstalt

M. Koebel, M. Elsener
Selective Catalytic Reduction of NO over Commercial DeNOx-Catalysts: Experimental Determination of Kinetic and Thermodynamic Parameters
Chem. Eng. Sci. **53**, 657-669 (1998).

M. Koebel, M. Elsener
Selective Catalytic Reduction of NO over Commercial DeNOx-Catalysts: Comparison of the Measured and Calculated Performance
Ind. Eng. Chem. Res. **37**, 327-335 (1998).

M. Koebel, M. Elsener
Oxidation of Diesel-Generated Volatile Organic Compounds in the Selective Catalytic Reduction
Process. Ind. Eng. Chem. Res. **37**, 3864-3868 (1998).

G.L. Kok*, A.S.H. Prévôt, R.D. Schillawski*, J. Johnson**
Atmospheric Carbon Monoxide Measurements from 76° N to 59° S and over the South Tasman Sea
J. Geophys. Res. **103**, NO.D13,16731-16736 (1998).
* National Center for Atmospheric Research, Boulder, Colorado, USA
** NOAA/PMEL, Seattle, USA

A.P. Kouzov*, D.N. Kozlov*, B. Hemmerling
CARS Studies of Bending States of CO_2: Evidence of Collisional Rotational Transitions with Odd ΔJ
Chem. Phys. **236**, 15-24 (1998).
* General Physics Institute, Moscow

J. Kritzenberger*, D. Franzke**, Th. Kunz, A. Lang***, O. Nuyken***, A. Wokaun
Isomerization and Decomposition of a Poly(alkylaryldiazosulfide): Comparison of Thermolytically and Photolytically Induced Reactions
Angew. Makromol. Chem. **254**, 17-26 (1998).
* now Diehl-Glaeser, Hiltl & Partner, Munich, Germany
** now Gretag Imaging AG, Regensdorf
*** TU Munich, Garching, Germany

Th. Kunz, J. Stebani*, J. Ihlemann**, A. Wokaun
Photoablation and Microstructuring of Polyestercarbonates and their Blends with a XeCl-Excimer Laser
Appl. Phys. A **67**, 347-352 (1998).
* Bayer AG, Leverkusen, Germany
** Laser Laboratorium Göttingen, Germany

Th. Kunz, Ch. Hahn, A. Wokaun
Photochemical Properties of Poly(arylazophosphonates)
Adv. Mater. **10**, 786-789 (1998).

R. Lamprecht, D. Berlowitz
Evaluation of Diagnostic and Prognostic Flow Fields over Prealpine Complex Terrain by Comparison of the Lagrangian Prediction of Concentrations with Tracer Measurements
Atmos. Environ. **32**, 1283-1300 (1998).

Th. Lippert*, Th. Kunz, Ch. Hahn, A. Wokaun
Polymers Designed for UV-Laser Applications
"Recent Research Developments in Macromolecules Research", Research Signpost **2**, 121-125 (1998).
* Los Alamos National Laboratory, USA

Th. Lippert*, J.T. Dickinson**, S.C. Langford**, H. Furutani***, H. Fukumura***, H. Masuhara***, Th. Kunz, A. Wokaun
Photopolymers Designed for Laser Ablation - Photochemical Ablation Mechanism
Appl. Surf. Sci. **127-128**, 117-121 (1998).
* Los Alamos National Laboratory, USA
** Washington State University, Pullman, USA
*** Osaka University, Osaka, Japan

M. Lugauer, U. Baltensperger, M. Furger, H.W. Gäggeler, D.T. Jost, M. Schwikowski, H. Wanner*
Aerosol Transport to the High Alpine Sites Jungfraujoch (3454 m asl) and Colle Gnifetti (4452 m asl)
Tellus **50B**, 76-92 (1998).
* University of Bern

R. Matyssek*, M.S. Günthardt-Goerg**, P. Schmutz**, M. Saurer, W. Landolt**, J.B. Bucher**
Response Mechanisms of Birch and Poplar to Air Pollutants
Journal of Sustainable Forestry **6**, 3-22 (1998).
* University of Munich, Germany
** WSL, Birmensdorf

R.L. Mauldin III*, G.J. Frost*, G. Chen, D.J. Tanner*, A.S.H. Prévôt, D.D. Davis***, F.L. Eisele*
OH Measurements during the First Aerosol Characterization Experiment (ACE 1): Observations and Model Comparisons
J. of Geophys. Res. **103, D13**, 16713-16729 (1998).
* NCAR/ACD, Boulder, Colorado, USA
** Nat. Oceanic and Atmospheric Admininstration, Boulder, Colorado, USA
*** Georgia Inst. of Technology, Atlanta, USA

P. Mizsey, N.T. Hau*, N. Benko*, I. Kalmar*, Z. Fonyo*
Process Control for Energy Integrated Distillation Schemes
Computers Chem. Engng. **22 Suppl.**, 427-434 (1998).
* Technical University of Budapest, Hungary

S. Müller, O. Haas, C. Schlatter*, C. Comninellis*
Development of a 100 W Rechargeable Bipolar Zinc/Oxygen Battery
J. Appl. Electrochem. **28**, 305-310 (1998).
* Swiss Federal Institute of Technology, Lausanne

S. Müller, F. Holzer, O. Haas
Optimized Zn Electrode for the Rechargeable Zinc-Air Battery
J. Appl. Electrochemistry **28**, 895-898 (1998).

E. Newson, Th. Haueter, P. Hottinger, F. von Roth, G.W.H. Scherer, Th.H. Schucan
Seasonal Storage of Hydrogen in Stationary Systems with Liquid Organic Hydrides
Int. J. Hydrogen Energy **23**, 905-909 (1998).

O. Nuyken*, U. Dahn*, A. Wokaun, Th. Kunz, Ch. Hahn, V. Hessel**, J. Langsiedel**
Excimer Laser Ablation of Triazene-Containing Polyesters with Different Topologies
Acta Polym. **49**, 427-432 (1998).
* TU München, Garching, Germany
** Institut für Mikrotechnik Mainz, Germany

E.E. Ortelli, J.M. Weigel, A. Wokaun
Methanol Synthesis Pathway over Cu/ZnO_2 Catalysts: A Time Resolved DRIFT ^{13}C Labelling Experiment
Catal. Lett. **54**, 41-48 (1998).

R. Palumbo, J. Lédé*, O. Boutin*, E. Elorza Ricart*, A. Steinfeld, S. Moeller, A. Weidenkaff, E.A. Fletcher**, J. Bielicki***
The Production of Zn from ZnO in a High-Temperature Solar Decomposition Quench Process—I. The Scientific Framework for the Process
Chem. Eng. Sci. **53**, 2503-2517 (1998).
* CNRS-ENSIC, Nancy, France
** University of Minnesota, USA
*** Valparaiso University, USA

J.-C. Panitz, A. Wokaun
Raman Microprobe Study of Silicon Infiltrated Silicon Carbide
Appl. Spectr. **52**, 1252-1254 (1998).

J.-C. Panitz, F. Geiger
Leaching of the Anthraquinone Dye Solvent Blue 59 Incorporated into Organically Modified Silica Xerogels
J. Sol-Gel Sci. Technol. **13**, 473-477 (1998).

M.-C. Pham*, B. Piro*, E. A. Bazzaoui*, M. Hedayatullah*, J.-C. Lacroix*, P. Novák, O. Haas
Anodic Oxidation of 5-Amino-1,4-Naphthoquinone (ANQ) and Synthesis of a Conducting Polymer (PANQ)
Synt. Metals **92**, 197-205 (1998).
* Université Paris 7, CNRS-URA 34, Paris, France

B. Piro*, M.-C. Pham*, E.A. Bazzaoui*, M. Hedayatullah*, J.-C. Lacroix*, P.-C. Lacaze*, P. Novák, O. Haas
Un Nouveau Film Conducteur Poly(aminoquinone) pour le Stockage de l Énergie
J. Chim. Phys. **95**, 1522-1525 (1998).
* Université Paris 7, CNRS-URA 34, Paris, France

H. Ries*, H.R. Tschudi, W. Spirkl**
On the Stability of Solar Chemical Particle Receivers
J. Sol. Energy Engineering **120**, 96-100 (1998).
* Optics and Energy Consulting, Munich, Germany
** University of Munich, Germany

B. Roduit*, A. Baiker*, A. Wokaun
3-D Modeling of SCR of NO_x by NH_3 on Vanadia Honeycomb Catalysts
A. I. Chem. **44**, 2731-2744 (1998).
* ETH Zürich

B. Roduit*, A. Wokaun, A. Baiker*
Global Kinetic Modeling of Reactions Occurring during Selective Catalytic Reduction of NO by NH_3 over Vanadia / Titania-Based Catalysts
Ind. Eng. Chem. Res. **37**, 4577-4590 (1998).
* ETH Zürich

R. Rozenfeld*, J. Luczka*, P. Talkner
Brownian Motion in a Fluctuating Medium
Phys. Lett. A **249**, 409-414 (1998).
* Silesian University, Katowice, Poland

M. Saurer, K. Aellen*, R.T.W. Siegwolf
Correlating $\delta^{13}C$ and $\delta^{18}O$ in Cellulose of Trees
Plant, Cell and Environment **20**, 1543-1550 (1997).
* University of Basel

M. Saurer, I. Robertson*, R.T.W. Siegwolf, M. Leuenberger **
Oxygen Isotope Analysis of Cellulose: An Inter-Laboratory Comparison
Analytical Chemistry **70**, 2074-2080 (1998).
* Cambridge Isotope Laboratory, UK
** University of Bern

M. Saurer, R.T.W. Siegwolf, S. Borella*, F. Schweingruber**
Environmental Information from Stable Isotopes in Tree Rings
The Impacts of Climate Variability on Forests (eds. M. Beniston, J.L. Innes). Springer Verlag, Berlin, Heidelberg, 241-253 (1998).
* University of Bern
** WSL, Birmensdorf

D. Schläpfer, C. Borel, J. Keller, K. Itten*
Atmospheric Precorrected Differential Absorption Technique to Retrieve Columnar Water Vapor
Remote Sensing of Environment **65**, 353-366 (1998).
* University of Zürich

M.E. Spahr*, P. Novák, W. Scheifele, O. Haas, R. Nesper**
Electrochemistry of Chemically Lithiated NaV_3O_8: A Positive Electrode Material for Use in Rechargeable Lithium-Ion Batteries
J. Electrochem. Soc. **145**, 421-427 (1998).
* Timcal AG, Sins
** ETH Zürich

M.E. Spahr*, P. Novák, B. Schnyder, O. Haas, R. Nesper**
Characterization of Layered Lithium Nickel Manganese Oxides Synthesized by a Novel Oxidative Coprecipitation Method and Their Electrochemical Performance as Lithium Insertion Electrode Materials
J. Electrochem. Soc. **145**, 1113-1121 (1998).
* Timcal AG, Sins
** ETH Zürich

L. Sigg*, K.-U. Goss*, S. Haderlein*, H. Harms*, S.H. Hug*, Ch. Ludwig
Sorption Phenomena at Environmental Solid Surfaces
Chimia **51**, 893-899 (1997).
* EAWAG, Dübendorf

V.I. Srdanov*, I. Alxneit, C.M. Reaves*,
S.B. DenBaars*, G.D. Stucky*
Optical Properties of GaAs Confined in the Pores of MCM-41
J. Phys. Chem. **B102,** 3341-3344 (1998).
* University of California, Santa Barbara, USA

A. Stampanoni-Panariello, B. Hemmerling,
W. Hubschmid
Temperature Measurements in Gases Using Laser-induced Electrostrictive Gratings
Appl. Phys. **B67**, 125-130 (1998).

G. Stefanicki, P. Talkner, R.O. Weber
Frequency Changes of Weather Types in the Alpine Region since 1945
Theor. Appl. Climatol. **60,** 47-61 (1998).

A. Steinfeld, P. Kuhn, A. Reller*, R. Palumbo,
J. Murray**, Y. Tamaura***
Solar-Processed Metals as Clean Energy Carriers and Water-Splitters
Int. J. Hydrogen Energy, **23**, No. 9, 767-774 (1998).
* University of Hamburg, Germany
** Portland State University, USA
*** Tokyo Institute of Technology, Japan

A. Steinfeld, M. Brack, A. Meier, A. Weidenkaff,
D. Wuillemin
A Solar Chemical Reactor for Co-Production of Zinc and Synthesis Gas
Energy **23**, 803-814 (1998).

A. Steinfeld, I. Spiewak*
Economic Evaluation of the Solar Thermal Co-Production of Zinc and Synthesis Gas
Energy Conv. Mgmt. **39**, 1513-1518 (1998).
* Institute for Prospective Technological Studies, EC Joint Research Centre, Spain

A. Steinfeld, S. Sanders*, R. Palumbo
Design Aspects of Solar Thermochemical Engineering
J. Solar Energy **65**, 43-53 (1999).
* Valparaiso University, USA

S. Stucki, G.G. Scherer, S. Schlagowski*,
E. Fischer**
PEM Water Electrolyzers: Evidence for Membrane Failure in 100 kW Demonstration Plants
J. Appl. Electrochem. **28**, 1041-1049 (1998).
* Solar Wasserstoff Bayern GmbH, Neunburg vorm Wald, Germany
** Aare-Tessin AG für Elektrizität, Olten

S. Stucki, A. Jakob
Thermal Treatment of Incinerator Fly Ash: Factors Influencing the Evaporation of $ZnCl_2$
Waste Management **17**, 231-236 (1997).

P. Talkner, E. Pollak*, A.M. Berezhkovskii**
Binary Collision Theory for Thermal and Nonisothermal Relaxation and Reaction of Polyatomic Molecules
Chem. Phys. **235**, 131-146 (1998).
* Weizmann Institute, Rehovot, Israel
** Karpov Institute, Moscow, Russia

R.O. Weber
Climatology of Regional Flow Patterns Around Basel
Theor. Appl. Climatol. **59**, 13-27 (1998).

R.O. Weber
Estimators for the Standard Deviation of Lateral, Longitudinal and Vertical Wind Components
Atmos. Environ. **32**, 3639-3646 (1998).

R.O. Weber, P. Kaufmann
Relationship of Ambient Winds and Complex Terrain Flows during the MISTRAL Field Experiment
J. Appl. Meteor. **37**, 1486-1496 (1998).

A. Weidenkaff, A. Steinfeld, A. Wokaun,
B. Eichler, A. Reller*
The Direct Solar Thermal Dissociation of ZnO: Condensation and Crystallisation of Zinc in the Presence of Oxygen
Solar Energy **65**, 59-69 (1999).
* University of Hamburg, Germany

M. Winter*, J.O. Besenhard*, M.E. Spahr**, P. Novák
Insertion Electrode Materials for Rechargeable Lithium Batteries
Adv. Materials **10**, 725-763 (1998).
* Technical University of Graz, Austria
** Timcal AG, Sins

M. Winter*, P. Novák
Chloroethylene Carbonate, a Solvent for Lithium-Ion Cells, Evolving CO_2 during Reduction
J. Electrochem. Soc. **145**, L27-L29 (1998).
* Technical University of Graz, Austria

M. Winter*, P. Novák, A. Monnier**
Graphites for Lithium-Ion Cells: The Correlation of the First-Cycle Charge Loss with the Brunauer-Emmett-Teller Surface Area
J. Electrochem. Soc. **145**, 428-436 (1998).
* Technical University of Graz, Austria
** Timcal AG, Sins

J. Wochele, S. Stucki
Ähnlichkeitsgesetze zum Rohrofen als Modell des Festbettes einer Müllverbrennungsanlage
Chemie Ingenieur Technik **70,** 1572-1576 (1998).

Other Papers

A. Arnold, R. Bombach, W. Hubschmid, B. Käppeli
Optical Diagnostics in Gas Turbine Burners
ERCOFTAC Bulletin **38**, 10-19, (September 1998).

A. Arnold, R. Bombach, W. Hubschmid, B. Käppeli
Laser-Induced Fluorescence Measurements of the Mixing of Fuel with Air
Proc. 20th IEA Task Leaders Meeting 1998 on Energy Conservation and Emissions Reduction in Combustion.

J.-L. Barras*, C. Daul*, E. Deiss
First Principles Modelling of Lithium Intercalation into Graphite and Manganese Oxide for Electrodes: Where is the "bottle neck"?
Chimia **52**, 491 (1998).
* University of Fribourg

M. Bärtsch, A. Braun, R. Kötz, O. Haas
High Power Electrochemical Double-Layer Capacitor
Proc. 38th Power Sources Conference, Cherry Hill, NJ, USA, 17-20 (1998).

M. Bracht*, A. de Groot*, C.E. Gregoire Padro**, Th.H. Schucan, E. Skolnik***
Evaluation Tool for Selection and Optimization of Hydrogen Demonstration Projects. Application to a Decentralised Renewable Hydrogen System
Hydrogen Energy Progress XII, Proc. 12th World Hydrogen Energy Conference, Buenos Aires, Argentina, **2**, 1243-1253 (1998).
* Netherlands Energy Research Foundation, NL
** National Renewable Energy Laboratory, USA
*** Energetics Inc., USA

H.P. Brack, L. Bonorand*, H.G. Bührer*, G.G. Scherer
Radiation Grafting of ETFE and FEP Films: Base Polymer Film Effects
ACS Polymer Preprints **39**, 976-977 (1998).
* Technikum Winterthur, Ingenieurschule, Winterthur

H.P. Brack, L. Bonorand*, H.G. Bührer*, G.G. Scherer
Radiation Processing of Fluoropolymer Films
Polymer Preprints **39**, 897-898 (1998).
* Technikum Winterthur, Ingenieurschule, Winterthur

H.P. Brack, G.G. Scherer
Influence of Crosslinkers on the Water-Swelling Properties of Radiation-Grafted Ion-Exchange Membranes
Water-Soluble/Water-Swellable Polymers Symposium, American Chemical Society National Meeting, Boston, MA, USA, 1998, Polymer Materials Science and Engineering **79**, 457-458 (1998).

W.H. Casey*, Ch. Ludwig, B. Holmén*
Towards Understanding the Rates at Mineral Surfaces
L. Marini, G. Ottonello, eds., Proc. Rome Seminar on Environmental Geochemistry, 103-119, Pacini Editore, Pisa (1998).
* University of California, Davis, USA

A. de Groot*, M. Bracht*, C.E. Gregoire Padro**, Th.H. Schucan, E. Skolnik***
Evaluation Tool for Selection and Optimization of Hydrogen Demonstration Projects
Hydrogen Energy Progress XII, Proc. 12th World Hydrogen Energy Conference, Buenos Aires, Argentina, **1**, 75-86 (1998).
* Netherlands Energy Research Foundation, NL
** National Renewable Energy Laboratory, USA
*** Energetics Inc., USA

O. Epelly, J. Gondzio*, J.-P. Vial**
Implementation of an Interior Primal-Dual Method for Large-Scale Smooth Nonlinear Convex Programming
Logilab Internal Report, December (1998).
* University of Edinburgh, Scotland
** University of Geneva

M. Furger, L. Poggio, A.S.H. Prévôt, W.K. Graber
Wind Measurements by Scintillometer at Different Locations in an Alpine Valley
Proc. 8th Conference on Mountain Meteorology, Flagstaff, Arizona, American Meteorological Society, 197-198 (1998).

M. Furger, J. Dommen, W.K. Graber, L. Poggio, A.S.H. Prévôt, B. Neininger*
The VOTALP Valley Campaign 1996 - Results and Climatological Evaluation
Proc. 25th International Conference on Alpine Meteorology (ICAM'98), Turin, Italy, 246-249 (1998).
* MetAir AG, Illnau

W.K. Graber
Land-Use Changes and Atmosphere Exchange Processes in the Alps
Proc. VIIth International Congress of Ecology, Florence, Italy, 165-166 (1998).

M.S. Günthardt-Goerg*, S. Maurer, B. Frey*, R. Matyssek**
Birch Leaves from Trees Grown in Two Fertilization Regimes: Diurnal and Seasonal Responses to Ozone
Responses of Plant Metabolism to Air Pollution and Global Change. L.J. De Kock, I. Stulen (Eds.), Backhuys Publishers, Leiden, The Netherlands, 315-318 (1998).
* WSL, Birmensdorf
** University of Munich, Freising, Germany

O. Haas
14. PSI-Tagessymposium Elektrochemische Energiespeicherung
Chimia **52**, 505 (1998).

D. Häringer, P. Novák, O. Haas
Optimierung positiver Oxidelektroden für Lithium-Ionentransfer-Batterien
GDCh-Monographie **12**, 625 (1998).

Ch. Hahn, Th. Kunz, A. Wokaun
Materials Study for Technically Relevant Devices Fabricated by Excimer Ablation Lithography
Proc. LASE'97, SPIE, **3274**, 229-235 (1998).

V. Hermann*, S. Müller, C. Comninellis*
Oxygen Reduction on Perovskite-coated Nickel and Titanium Electrodes
The Electrochem. Soc. Proc. PV **97-28**, 159-169 (1998).
* Swiss Federal Institute of Technology, Lausanne

F. Holzer, S. Müller, O. Haas
Development and Tests of Cell Components for a 12 V/20 Ah Electrically Rechargeable Zinc/Air Battery
Proc. 38th Power Sources Conference, Cherry Hill, NJ, USA, June 8-11, 354-357 (1998).

R. Kötz, M. Carlen*
High Power Density Supercapacitor Demonstrated
PPM Materials Newsletter No. 2 (1998).
* ABB Corporate Research, Dättwil

R. Kötz, D. Alliata, C. Barbero*, M. Bärtsch, A. Braun, R. Imhof, B. Schnyder, M. Sullivan**
Characterization of Surface Layers on Glassy Carbon Formed by Constant Potential Anodization
Extended Abstract, Spring Meeting of the Electrochemical Society, San Diego, USA, **98-1**, 85 (1998).
* Universidad Nacional de Rio Cuarto, Rio Cuarto, Argentina
** University of Minnesota, Minneapolis, USA

S. Kypreos
The Global MARKAL-MACRO Trade Model
Energy Models for Decision Support: New Challenges and Possible Solutions. Proc. of the Joint ETSAP/ FEES Workshop, Berlin, 1998, IER Stuttgart, Eds.: Egbert Laege and Peter Schaumann, 99-112 (1998).

S. Kypreos, L. Barreto
Experience Curves in MARKAL and Links to Macroeconomic Models
Proc. of the Workshop on Modelling Technological Learning, IIASA, Laxenburg, March 19-21 Chapter **14**, 1-23 (1998).

S. Kypreos, L. Barreto
A Simple Global Electricity MARKAL Model with Endogenous Learning
Proc. of the Joint IEA-ALEP/ETSAP Workshop, Antalya, Turkey, October (1998).

S. Kypreos, A. Cadena
Partial and General Equilibrium Versions of MARKAL Models with Multiregional Trade: Model Specifications and Applications
Proc. of the Joint IEA-ALEP/ETSAP Workshop, Antalya Turkey, October (1998).

Th. Lippert*, J.T. Dickinson**, S.C. Langford**, H. Furutani***, H. Fukumura***, H. Masuhara***, Th. Kunz, A. Wokaun
Laser Machining of Specially Designed Photopolymers - Photochemical Ablation Mechanism
Proc. LASE'97, SPIE, **3404**, 192-199 (1998).
* Los Alamos National Laboratory, USA
** Washington State University, Pullman, USA
*** Osaka University, Osaka, Japan

Ch. Ludwig, F. Ziegler*, C.A. Johnson*
Heavy Metal Binding Mechanisms in Cement-Based Materials
J.J.J.M. Goumans, G.J. Senden, H.A. van der Sloot, eds., *Waste Materials in Construction*, Studies in Environmental Science **71**, 459-468, Elsevier (1997).
* EAWAG, Dübendorf

M. Lugauer, U. Baltensperger, M. Furger, H.W. Gäggeler, D.T. Jost, M. Schwikowski
Vertical Transport Processes in the Lower Troposphere Above the Alpine Region
Proc. 8th Conference on Mountain Meteorology, Flagstaff, Arizona, American Meteorological Society, 159-162 (1998.)

P. Mizsey, E. Mansur*, Z. Fonyo*
Rigorous Evaluation of Energy Integrated Distillation Schemes
Oral lecture on CHISA '98, Ref. No. 0174, Praha (1998).
* Technical University of Budapest, Hungary

A. Meier, A. Steinfeld
Solarchemie - Technologien fürs 21. Jahrhundert
Schweizerische Technische Zeitschrift - Technik Aktuell, **4**, 28-31 (1998).

A. Meier, A. Steinfeld, R. Palumbo
Brennstoffe aus Sonnenlicht und Wasser
Sonnenenergie **3**, 12-15 (1998).

S. Müller, F. Holzer, O. Haas
Development of a 12 V/20 Ah Electrically Rechargeable Zinc-Air Battery
The Electrochem. Soc. Proc., **PV 98-15** (1998).

E. Newson, T.B. Truong, P. Hottinger, F. von Roth, Th.H.Schucan
Optimisation of Seasonal Energy Storage in Stationary Systems with Liquid Hydrogen Carriers, Decalin and Methylcyclohexane
Hydrogen Energy Progress XII, Proc. 12th World Hydrogen Energy Conference, Buenos Aires, Argentina, **2**, 935-942 (1998).

E. Newson, E. Uenala, K. Geissler, P. Hottinger, T.B. Truong, F. von Roth
Catalyst Screening for Hydrogen Production in Mobile Systems by the Partial Oxidation of Methanol or Hydrocarbons
Hydrogen Energy Progress XII, Proc. 12th World Hydrogen Energy Conference, Buenos Aires, Argentina, **2**, 953-961 (1998).

J.-C. Panitz
Characterisation of Technical Ceramics with Raman Microscopy
Proc. 16th International Conference on Raman Spectroscopy, A. Heyns ed., 800-801, Chichester (1998).

A.S.H. Prévôt, J. Dommen, M. Bäumle*
VOC Measurements as Indicators for Valley Wind Circulation Phenomena
Proc. 8th Conference on Mountain Meteorology, Flagstaff, Arizona, 1998, American Meteorological Society, 207-208 (1998).
* MetAir AG, Illnau

A.S.H. Prévôt, M. Furger, B. Neininger*, L. Poggio, J. Dommen, W.K. Graber
1998b: Mesolcina Valley = Highly Efficient Air Pump for Vertical Transport
Proc. 8th Conference on Mountain Meteorology, Flagstaff, Arizona, 1998, American Meteorological Society, 401-403 (1998).
* MetAir AG, Illnau

A.S.H. Prévôt, J. Dommen, M. Furger
1998: Morning VOC Concentration Minima on the Mesolcina Valley Floor
Extended Abstracts of the VOTALP Open Workshop, Vienna, Austria, (1998).

A.S.H. Prévôt, J. Dommen, M. Furger, W.K. Graber, B. Neininger*, L. Poggio
1998b: Mesolcina Valley = Highly Efficient Air Pump for Vertical Transport
Extended Abstracts of the VOTALP Open Workshop, Vienna, Austria, (1998).
* MetAir AG, Illnau

M. Ruge, G.G. Scherer
Nachhaltigkeit: Brennstoffzellen für mobilen Einsatz
STZ Technik Aktuell 4, 42-45 (1998).

G.G. Scherer
Brennstoffzellen - Eine zukünftige Quelle zur Energieerzeugung
Tagungsband 56d, Energietechnische Gesellschaft des SEV 5, 5-15 (1998).

D. Schläpfer, P. Meyer*, K.I. Itten*
Parametric Geocoding of AVIRIS Data Using a Ground Control Point Derived Flightpath
Summaries of the Seventh JPL Airborne Earth Science Workshop, published on www.makalu.jpl.nasa.gov/docs/workshops/98_docs/, JPL, Pasadena (CA) (1998).
* University of Zürich

M. Schubnell, W. Durisch, B. Grob, J.-C. Mayor, J.-Ch. Panitz
Koproduktion von Wärme und Strom mit Thermophotovoltaik
gwa **4**, 248-253 (1998).

Th.H. Schucan, P. Hottinger, E. Newson, F. von Roth, T.B. Truong
Seasonal Storage of Electricity with Chemically Bound Hydrogen
EESAT '98 Proc., Chester, UK, 103-108 (1998).

Th.H. Schucan, E. Skolnik*, M. Bracht**, C.E. Gregoire Padro***
Development of Hydrogen Technology Component Models for Systems Integration
Hydrogen Energy Progress XII, Proc. 12th World Hydrogen Energy Conference, Buenos Aires, Argentina, **1**, 111-120 (1998).
* Energetics Inc., USA
** Netherlands Energy Research Foundation, NL
*** National Renewable Energy Laboratory, USA

A. Steinfeld, A. Reller*
Solar Thermochemical Production of Hydrogen Using Metal Oxide Redox Systems
Proc. 12th World Hydrogen Energy Conference, Buenos Aires, Argentina, June 21-26 (1998).
* University of Hamburg, Germany

A. Steinfeld
IEA-SolarPACES Annual Report 1997
W. Grasse ed., Chapter 3 (1998).

M. Sturzenegger
International Symposium on Solar Chemistry
Chimia **52**, 73 (1998).

M. Sturzenegger, J. Ganz, P. Nüesch, T. Schelling
Solar Hydrogen From Manganese Oxide - A New Thermochemical Cycle
Proc. 12th World Hydrogen Energy Conference - Hydrogen Energy Progress XII, Buenos Aires, Argentina, 801-805 (1998).

M. Tsuji*, M. Nezuka*, S. Yoshida*, H. Amano*, Y. Tamaura*, A. Steinfeld
Thermochemical Solar/Fossil Energy Mixing Using Metal Oxides
Proc. International Symposium on Ferrites in Asia '97, 1997, Journal of the Magnetic Society of Japan, **22**, 411-412 (1998).
* Tokyo Institute of Technology, Japan

A. Weidenkaff, S. Moeller, R. Palumbo, A. Steinfeld
Zink als Sonnenenergiespeicher
Baugarten Stiftung Forschungsbericht (1998).

J. Wochele, S. Stucki
Labor-Simulierung des Festbettes von Müllverbrennungsanlagen aufgrund der Ähnlichkeitsgesetze
VDI-Bericht 1390, zur VDI-GET Tagung, Braunschweig, Germany, 287-296 (1998).

J. Wochele, S. Stucki, Ch. Ludwig
Factors Influencing the Volatility of Heavy Metals in MSW Incinerators
Proc. WASTECON 1998, SWANA's Waste Conference / ISWA World Congress 1998, Charlotte (NC) USA, 403-408 (1998).

A. Wokaun, M.K. Eberle
Brennstoffzellen – Ende des Verbrennungsmotors?
Neue Zürcher Zeitung, Nr. 53, B11-B12, March 5, 1998.

A. Wokaun
Alternativenergien auf dem Prüfstand
Jubiläumsschrift der Liechtensteinischen Kraftwerke, May 1998.

A. Wokaun
Erneuerbare Energien auf dem Prüfstand
Schweizerische Technische Zeitschrift, 4/98, 18-21 (1998).

A. Wokaun
Brennstoffzellenfahrzeuge und Treibstoffe aus erneuerbaren Energien – Perspektiven für eine nachhaltige individuelle Mobilität
Proc. Energieinnovation und Forschung, Zweite Enquête, Technische Universität Graz, ÖVE Schriftenreihe **16**, 51-57 (1998).

DISSERTATIONS

K.U.M. Bengtsson
Experimental and Numerical Study of the NO_x Formation in High-Pressure Lean Premixed Combustion of Methane
Ph.D. Thesis, ETH Zürich, Nr. 12877, October 9,1998.

U. Dogwiler
Experimentelle und numerische Untersuchungen zur katalytisch stabilisierten Verbrennung von Methan
Ph.D. Thesis, ETH Zürich, Nr. 12648, May 11, 1998.

J.S. Füssler
On the Interaction between Atmosphere and Vegetation under Increasing Radiative Forcing: A Model Analysis
Ph.D. Thesis, ETH Zürich, Nr. 12802, August 11, 1998.

Ch. Hahn
Laser Induced Modifications of Photopolymers and Mesophases Containing Azo Chromophores
Ph.D. Thesis, ETH Zürich, Nr. 12636, April 7, 1998.

P. Häring
In Situ Scanning Probe Microscopy. Untersuchungen an elektroaktiven Materialien
Ph.D. Thesis, University of Bern, March 26, 1998.

P. Nüesch
Wasserstoff aus Sonnenenergie - Ein neuer thermochemischer Zyklus auf der Basis von Manganoxiden
Ph.D. Thesis, University of Zürich, December 1998.

L. Poggio
Use of Scintillation Measurements to Determine Fluxes in Complex Terrain
Ph.D. Thesis, ETH Zürich, Nr. 12755, July 1998.

B. Roduit
Kinetic Modeling of Honeycomb-Type Reactors for the Selective Catalytic Reduction of NO_x by NH_3
Ph.D. Thesis, ETH Zürich, Nr. 12664, April 28, 1998.

D. Schläpfer
Differential Absorption Methodology for Imaging Spectroscopy of Atmospheric Water Vapor
Ph.D. Thesis, University of Zürich, Remote Sensing Series **32**, RSL, Zürich, September 1998.

A. Scholz
Vibrationsspektroskopische Untersuchungen an WO_x / TiO_2 und WO_x-V_yO_z / TiO_2 Katalysatoren und verwendeten Precursormaterialien
Ph.D. Thesis, ETH Zürich, Nr. 12640, April 28, 1998.

C. von Scala
The Influence of Contaminants on the Gasification of Waste Wood
Ph.D. Thesis, ETH Zürich, Nr. 12665, April 28, 1998.

DIPLOMA THESES

D. Fischer
Beitrag zur Oberflächenanalytik von Kunststoff-membranen, die in Brennstoffzellen eingesetzt werden
Diplomarbeit, Zürcher Hochschule Winterthur, September 8 - October 30, 1998.

T. Frei
Untersuchungen zum Wasserhaushalt der Elektrolyt-membran in Polymerelektrolyt-Brennstoffzellen
Diplomarbeit, Fachhochschule beider Basel FHBB, October 23, 1997 - Januar 30, 1998.

D. Rüegg
Thermische Abbauprozesse an Folien für Brenn-stoffzellen
Diplomarbeit, Zürcher Hochschule Winterthur, September 8 - October 30, 1998.

F. Schaller, F. Holzer
Optimierung der Separatorschichten in der Zink-Luft-Batterie
Physiklaboranten-Facharbeit, PSI Villigen, December 1, 1997 - May 15, 1998.

Ch. Spirig
Meteorologische Einflüsse auf die Ozonverteilung in der Poebene
Diplomarbeit, ETH Zürich, April - September 1998.

TALKS

Invited Talks

R. Badii
Complexity
University of Bayreuth, January 1998.

R. Badii
Two-Scale Analysis of Intermittency in Fully-Developed Turbulence
Conference on the Physics of Turbulence, Max-Planck-Institute for the Physics of Complex Systems, Dresden, July 20 - August 7, 1998.

M. Bärtsch
High-Power Electrochemical Double-Layer Capacitor
38th Power Sources Conference, Cherry Hill, NJ, USA, June 8-11, 1998.

H.P. Brack
Development and Characterization of Membranes for Application in Fuel Cells and other Electrochemical Devices
Naval Undersea Warfare Center, Newport RI, USA, August 1-6, 1998.

H.P. Brack
Membrane Preparation at PSI Using the Radiation-Grafting Method
Dept. of Analytical Chemistry, University of Geneva, June 18, 1998.

E. Deiss
Alternative Methode zur Berechnung von Impedanz-spektren
Institut für Festkörperphysik, University of Fribourg, September 21, 1998.

W. Durisch
Interfacing a Small Thermophotovoltaic Generator to the Grid
4th NREL Conference on Thermophotovoltaic Generation of Electricity. Denver, Colorado, USA, October 11-14, 1998.

W. Durisch
- *Characterization of Photovoltaic Generators*
- *Testing of Small Sinusoidal Inverters for Photovoltaic Stand-Alone Systems*
- *Climatological Investigation for Solar Power Stations in the Swiss Alps*

7th International Energy Conference and Exhibition, Energex 98, University of Bahrain, Manama, Bahrain, November 19-21, 1998.

M. Eberle, O. Bahn
Elements of a Robust Greenhouse Gas Policy
4th International Conference on Greenhouse Gas Control Technologies, Interlaken, Switzerland, August 30 - September 2, 1998.

H.-M. Frey
Rotational Recurrences by Femtosecond Degenerate Four Wave Mixing in Gases
LASERS '98, Tucson AZ, December 7-11, 1998.

F. Gassmann
Chaos und Selbstorganisation als Grundprinzipien von Lebensphänomenen
Aargauische Naturforschende Gesellschaft, Aarau, February 11, 1998.

F. Gassmann
Sind komplexe Systeme lenkbar?
SAEE-Tagung, Bern, February 20, 1998.

F. Gassmann
Das Lorenz-System als Paradigma der nichtlinearen Dynamik
Physik-Seminar mit Experimenten, Universität Zürich-Irchel, April 30, 1998.

F. Gassmann
Luftqualität im Wechselspiel zwischen Industrieentwicklung, Verkehrsgestaltung und Erholungsraum
Symposium on Advances in Regional Climatology, Karlsruhe, October 5-7, 1998.

F. Gassmann
Treibhauseffekt und Klimaveränderungen: Sind Überraschungen zu erwarten ?
ELCO-Fachtagung, Münchenstein, October 20, 1998.

F. Gassmann
Effet de Serre: Modélisation et Observations
Société Vaudoise des Sciences Naturelles, Lausanne, November 26, 1998.

W.K. Graber
Windfeldklassen: Wie lässt sich die meteorologische Dynamik lokal systematisieren?
Seminar Atmosphärische Ausbreitung im Bereich Radioaktivität, PSI Villigen, June 9-10, 1998.

W.K. Graber
Ökologische Forschung am Paul Scherrer Institut, Schweiz
GMD First Forschungszentrum Informationstechnik, Rudower Chaussee 7, Berlin, Germany, April 14, 1998.

W. Grasse*, C. Tyner**, A. Steinfeld
International R&D Collaboration in Developing Solar Thermal Technologies For Electric Power and Solar Chemistry: The SolarPACES Program of the International Energy Agency
9th International Symposium on Solar Thermal Concentrating Technologies, Odeillo, France, June 22-26, (1998).
* SolarPACES, Gifhorn-Winkel, Germany
** SANDIA National Laboratories, Albuquerque, NM, USA

O. Haas
Development of an Experimental 1 kW PEFC Stack
49th Annual Meeting of ISE, Kitakyushu, Japan, September 13-18, 1998.

O. Haas
Leitende Polymere als Elektrodenmaterial in wiederaufladbaren Batterien und Superkondensatoren
DECHEMA-Arbeitsauschuss "Elektrochemische Prozesse", Frankfurt (Main), Germany, January 26, 1998.

O. Haas
Rechargeable 100 W Multicell Zinc/Air Battery
49th Annual Meeting of ISE, Kitakyushu, Japan, September 13-18, 1998.

B. Hemmerling
Nichtlineare optische Methoden für die Diagnostik in Hochdruckumgebungen
DLR Lampoldshausen, Germany, June 9, 1998.

B. Hemmerling
Diagnostik in Gasen mittels laserinduzierter Gitter
University of Stuttgart, Germany, October 28, 1998.

F. Holzer
Development and Tests of Cell Components for a 12 V/20 Ah Electrically Rechargeable Zinc/Air Battery
38th Power Sources Conference, Cherry Hill, NJ, USA, June 8-11, 1998.

R. Imhof
DEMS Investigation of the Electrochemical Oxidation of Organic Carbonate Electrolyte Solutions at Lithium Metal Oxide Electrodes
Invited speaker from poster sessions, 9th International Meeting on Lithium Batteries, Edinburgh, UK, July 17, 1998.

S. Müller
Development of a 12V/120 Ah Electrically Rechargeable Zinc-Air Battery
194th Meeting of ECS, Boston, MA, USA, November 1-6, 1998.

R. Palumbo
Solar Thermal Chemical Processing: Challenges and Changes
9th International Symposium on Concentrating Solar Technology, Odeillo, France, June 22-26, 1998.

R. Palumbo, A. Steinfeld, A. Weidenkaff
Solar Thermal Chemical Processing: A Renewable Energy Path for Reducing Greenhouse Gas Emissions
4th International Conference on Greenhouse Gas Control Technology, Interlaken, August 30 - September 2 (1998).

A.S.H. Prévôt
Eine photochemische Reise von Milano nach Tasmanien
Institut für Atmosphärenphysik, ETH Zürich, January 12, 1998.

A.S.H. Prévôt
Alpine Valleys, Valley Meteorology and Photochemistry
Aeronomy Laboratory, NOAA (National Oceanic and Atmospheric Administration), Boulder, Colorado, USA, August 14, 1998.

A.S.H. Prévôt
Alpentäler - Vertikaler Transport und Photochemie
Geographisches Institut der Universität Basel, December 15, 1998.

M. Saurer
$\delta^{18}O$ in Jahrringen als Klimaindikator: Neue Möglichkeiten dank On-line-Methodik
Forschungszentrum Jülich, October 29, 1998.

W. Scheifele
Batteriesysteme für Elektro- und Hybridfahrzeuge
ETH Zürich, October 29, 1998.

G.G. Scherer
Brennstoffzellen - eine zukünftige Quelle zur Stromerzeugung
ETG Tagungszyklus "Neue Wege in der Energieerzeugung", Technikum Winterthur, May 5, 1998.

G.G. Scherer
Brennstoffzellen – Stromquellen für das 21. Jahrhundert?
Hahn Meitner Institut, Berlin Wannsee, Germany, April 6, 1998.

G.G. Scherer
Das PSI-Brennstoffzellenprojekt - Eine Übersicht über neuere Ergebnisse
Fachkolloquium: PEM-Brennstoffzellen: "Aktuelle Resultate und Zukunftsperspektiven", Arbeitsgruppe Brennstoffzellen, University of Stuttgart, June 3, 1998.

G.G. Scherer
Brennstoffzellen
Seminartag "Ökologie und Ökonomie im Verkehr", ETH Zürich, October 29, 1998.

Th.H. Schucan
Wasserstoff-Technologie
Berufsbildungszentrum des Kantons Schaffhausen, Cernier, October 8, 1998.

R.T.W. Siegwolf
Auswirkungen von Umweltfaktoren auf die pflanzenphysiologischen Fraktionierungsmechanismen stabiler Isotope
Pflanzenphysiologisches Institut der Unversität Bern, January 16, 1998.

R.T.W. Siegwolf
The Stable Isotopes $\delta^{13}C$ and $\delta^{18}O$ as Climate Indicators in Treerings
Swedish University of Agricultural Sciences, Dept. Forestry Ecology, Umea Sweden, April 1, 1998.

R.T.W. Siegwolf
The Stable Isotopes $\delta^{13}C$ and $\delta^{18}O$ in Combined Use as a Tool for Plant Physiological Research
CNR, Istituto per l'Agroselvicoltura, Porano, Italy, June 9, 1998.

S. Stucki
Values from Waste - Thermochemical Recycling for Sustainable Material Management
University of Tokyo, Department of Chemical Systems Engineering, May 18, 1998.

S. Stucki
Separation of Heavy Metals from Incineration Residues
EPF Lausanne, May 29, 1998.

S. Stucki
The Volatility of Heavy Metals in Waste Incineration Processes: Environmental Hazard or Opportunity?
9th Conference on Physical Chemistry, Romanian Academy of Sciences, Galati, Romania, September 23–25, 1998.

S. Stucki
Kann Biomasse wirtschaftlich sein?
Forum für Wissenschaft und Energie, ETH Zürich, October 30, 1998.

M. Sturzenegger
Solarchemie – Einblicke in ein brandheisses Forschungsgebiet
ETHZ-Vereinigung der Chemiestudierenden, Zürich, May 6, 1998.

P. Talkner
Adiabatic Theory of Seasonal Processes
International Workshop on Fluctuations Far from Equilibrium: Noise Induced Transport, Dresden, April 19-23, 1998.

P. Talkner
Semiadiabatic Theory of Periodic Processes with an Application to Stochastic Resonance
Seminar of the Chemical Department, Weizmann Institute, Rehovot, Israel, May 6, 1998.

Z. Veziridis
Elektrochemie von Platin auf mikrostrukturierten Elektroden in Kontakt mit Nafion
Jahrestagung GDCh-Fachgruppe Angew. Elektrochemie 1998, 4. El. Grundlagen-Symposium DECHEMA, Frankfurt (Main), Germany, September 30 - October 2, 1998.

A. Wokaun
Treibstoffe aus erneuerbaren Energien und Brennstoffzellen als effiziente Wandler - Perspektiven für eine nachhaltige individuelle Mobilität
Energieinnovation und Forschung, TU Graz, Austria February 5, 1998.

A. Wokaun
Chancen der Reduktion der globalen CO_2-Emissionen
Jahrestagung Europ. Klimabündnisstädte, Luzern, June 3, 1998.

A. Wokaun
Towards Sustainable Mobility
4th International Conference on Greenhouse Gas Control Technologies, GHGT-4, Interlaken, August 30 - September 2, 1998.

A. Wokaun
Brennstoffzellenfahrzeuge und Treibstoffe aus erneuerbaren Energien – Perspektiven für eine nachhaltige individuelle Mobilität
48. Jahrestagung der Österreichischen Physikalischen Gesellschaft, Karl-Franzens-Universität Graz, Austria, September 17, 1998.

A. Wokaun
Energieforschung an der ETHZ und am PSI
SPG-Jahrestagung, Airolo, September 25, 1998.

Other Talks

D. Alliata
In-Situ Characterization of Battery Electrodes during Ion Exchange Processes with the Bathing Electrolyte
Annual Meeting of the Swiss Physical Society, Bern, February 26-27, 1998.

O. Bahn, A. Cadena, M. Jakob, S. Kypreos
Joint Implementation of CO_2 Emissions Reduction: Options for a Co-operation between Switzerland and Colombia
2nd International Conference of the European Society for Ecological Economics, Geneva, March 4-7, 1998.

O. Bahn
International CO_2 Emissions Reduction after the Kyoto Protocol: Insights from Regional Analyses
Seminar of the Swiss Nuclear Society, ETH Zürich, March 26, 1998.

O. Bahn, A. Cadena, M. Jakob, S. Kypreos
Reaching the Swiss Kyoto CO_2 Target through a Clean Development Mechanism with Colombia
International Workshop in Honour of Prof. A. Manne, University of Geneva, June 11, 1998.

O. Bahn, B. Büeler, S. Kypreos
Trade of Carbon Permits (I): The Model MARKAL-MACRO Multi-Regions
OR98 International Conference on Operations Research, ETH Zürich, August 31 - September 3, 1998.

O. Bahn, L. Barreto, B. Büeler, S. Kypreos
Trade of Carbon Permits (II): A Case Study for Three European Countries
OR98 International Conference on Operations Research, ETH Zürich, August 31 - September 3, 1998.

R. Bombach
Simultaneous Visualization of Transient Species in Flames Using Planar Laser Induced Fluorescence
ERCOFTAC Joint Annual Meeting, PSI Villigen, August 27, 1998.

H.P. Brack
- *Influence of Crosslinkers on the Water-Swelling Properties of Radiation-Grafted Ion-Exchange Membranes*
- *Radiation Grafting of ETFE and FEP Films: Base Polymer Film Effects*
- *Radiation Processing of Fluoropolymer Films*

American Chemical Society Fall Meeting, Boston, MA, USA, August 23-27, 1998.

H.P. Brack
Recent Progress in the Development of the Radiation-Grafted PSI Membrane
194th ECS Meeting, Boston MA, USA, November 1-6, 1998.

A. Braun
Investigation on Oxidized Glassy Carbon Sheets for Supercapacitor Electrodes with Small Angle X-ray Scattering and Complementary Techniques
Autumn Meeting Swiss Group of Colloid and Interfacial Science, PSI, November 26, 1998.

F.N. Büchi
In-Plane Resolved In-Situ Measurements of the Membrane Resistance in PEFCs
2nd International Symposium Proton Conduct. Membrane Fuel Cells, 194th ECS Meeting, Boston, MA, USA, November 1-6, 1998.

B. Büeler
Pricing of Greenhouse Gas Emission Rights
International Workshop in Honour of Prof. A. Manne, University of Geneva, Switzerland, June 11, 1998.

M. Corboz, I. Alxneit
Influence of Photoabsorbed O_2 on the Photoreduction of CO_2 with H_2O at the Surface of TiO_2
9th International Symposium on Solar Thermal Concentrating Technology, Odeillo, France, June 22-26 (1998).

E. Deiss
First Principles Modelling of Lithium Intercalation into Graphite and Manganese Oxide for Electrodes; where is the bottle neck?
Herbstversammlung der NSChG, ETH Zürich, October 15, 1998.

E. Deiss
Modelling of Lithium Intercalation Batteries
BFE Workshop, Bern, December 12, 1998.

W. Durisch
Thermophotovoltaische Wärme- und Stromerzeugung
Fachtagung 'Erdgas - Energie mit Zukunft'
Wädenswil, August 27, 1998.

O. Epelly
Towards an Efficient Solver for MARKAL-MACRO Models
International Workshop in Honour of Prof. A. Manne, University of Geneva, June 11, 1998.

H.-M. Frey
Femtosecond Degenerate Four Wave Mixing Applied to Molecular Beams
California Institute of Technology, Pasadena, USA, December 15, 1998.

M. Furger
Volume Fluxes over an Elevated Alpine Plateau under Varying Weather Conditions
5th Ecomont Workshop, PSI, Villigen, March 26-28, 1998.

M. Furger, J. Dommen, W.K. Graber, L. Poggio, A.S.H. Prévôt, B. Neininger*
The VOTALP Valley Campaign 1996 - Results and Climatological Evaluation
25th International Conference on Alpine Meteorology (ICAM'98), Turin, Italy, September 14-19, 1998.
* MetAir AG, Illnau

M. Furger, L. Poggio, W. K. Graber, A.S.H. Prévôt
Towards Diurnal Airmass Budgets in the Mesolcina Valley: Scintillometer and DOAS Measurements
Extended Abstracts of the VOTALP Open Workshop, Vienna, Austria, Universität für Bodenkultur, January 19-20, 1998.

F. Gassmann
Treibhauseffekt
Schweiz. Drogistenschule, Neuenburg, February 18, 1998.

F. Gassmann
Treibhauseffekt, was ist das ?
Bezirksschule Bremgarten, Bremgarten, November 10, 1998.

T. Gerber
Methylal, an Oxygenated Fuel for Use in Diesel Engines
IEA 20th Task Leader Meeting, Ottawa, Canada, July 26-29, 1998.

W.K. Graber
Exchange of CO_2 and Water Vapour between a Composite Landscape and the Atmosphere in the Alps
Headwater Conference, Merano, Italy, April 20-23, 1998.

W.K. Graber
Land-Use Changes and Atmosphere Exchange Processes in the Alps
Int. Conf. on Ecology (INTECOL), Firence, Italy July 21-25 1998.

W.K. Graber
Wasserdampfflüsse in einer Talatmosphäre
Symposium Mesoscale Alpine Programme, Airolo, September 24-25, 1998.

W.K. Graber
Windfeldmodelle für die Zonen 1 und 2 von Kernanlagen
Jahrestagung der Eidgenössischen Kommission für AC-Schutz (KOMAC) ETH Zürich, November 17, 1998.

O. Haas
Die Brennstoffzelle in der H_2-Kette
Berner Energie Apéro, Fachhochschule Burgdorf, May 7, 1998.

O. Haas
Experimental 1 kW 20 Cell PEFC Stack
2nd International Fuel Cell Workshop, Yamanashi, Japan, September 19-20, 1998.

O. Haas
Brennstoffzellen
Energie 2000, Energie Apéro in der Region Baden, ABB Baden, November 23, 1998.

D. Häringer
The Effect of Ball Milling and Temperature Treatment on Electrochemical Properties of $LiMn_2O_4$ Electrodes
194th Meeting of the Electrochemical Society, Boston, MA, USA, November 1-6, 1998.

B. Hemmerling
Generation and Temporally Resolved Detection of Laser-Induced Electrostrictive Gratings by a Single, Pulsed Nd:YAG Laser
CARS Workshop, Besançon, France, March 23, 1998.

B. Hemmerling
Diagnostics in Gases by Transient Laser-Induced Electrostrictive Gratings
ICONO'98, Moskau, Russia, July 1, 1998.

B. Hemmerling
Temperature and Mixture Fraction Measurements in Gases by Laser-Induced Electrostrictive Gratings
27th International Symposium on Combustion, University of Colorado, Boulder, USA, August 6, 1998

W. Hubschmid
Laser-Induced Fluorescence Measurements of the Mixing of Fuel with Air
IEA Task Leaders Meeting Ottawa, Canada, July 26-29, 1998.

W. Hubschmid
Gemischaufbereitung in Gasturbinen
Schweizerische Vereinigung für Verbrennungsforschung, Jahrestagung Zürich, August 28, 1998.

W. Hubschmid
Transient Rotational State Thermal Equilibrium of Laser-Induced Gratings in O_2
European Quantum Electronics Conference, Glasgow, UK, September 14-18, 1998.

R. Imhof
Elektrode/Elektrolyt Phasengrenze in Lithium-Ionen Batterien
Abteilung für Chemie, University of Bern, May 7, 1998.

A. Inauen
H-Bonded Gas-Phase Pair-Complexes of Chiral Substances
Herbstversammlung der Neuen Schweizerischen Chemischen Gesellschaft, Zürich, October 15, 1998.

J. Keller
Modelle zur Ausbreitung von Stoffen in der Atmosphäre: Übersicht und Anwendungen
Seminar "Atmosphärische Ausbreitung im Bereich Radioaktivität" der Eidgenössischen Kommission für AC-Schutz, PSI, Villigen, June 9-10, 1998.

J. Keller
Short-Term Impacts of Air Pollutants in Switzerland: Model Evaluation and Preliminary Scenario Calculations for Selected Swiss Energy Systems
- 2nd GLOREAM Workshop, Genova, Italy, September 16-18, 1998.
- 6th International Conference "Air Pollution '98", Genova, Italy, September 28-30, 1998.

R. Kötz
Characterization of Surface Layers on Glassy Carbon Formed by Constant Potential Anodization
193rd Meeting of Electrochemical Society, San Diego, USA, May 3-8, 1998.

R. Kötz
Double-Layer Capacitor Stack with Glassy Carbon Electrodes
49th ISE Meeting, Kitakyushu, Japan, September 13-18, 1998.

R. Kötz
Surface and Interface Analysis in Electrochemistry
SGCIS Meeting, PSI Villigen, November 26, 1998.

S. Kypreos
The Global MARKAL-MACRO Trade Model and the Kyoto Protocol
International Workshop in Honour of Prof. A. Manne, University of Geneva, June 11, 1998.

I. Mantzaras
Homogeneous Ignition in Catalytically Stabilized Combustion: A Theoretical and Numerical Investigation
ERCOFTAC joint annual meeting, PSI Villigen, August 27, 1998.

A. Meier, V.A. Kirillov*, G.G. Kuvshinov*, Y.I. Mogilnikh*, A. Weidenkaff, A. Steinfeld
Production of Catalytic Filamentous Carbon by Solar Thermal Decomposition of Hydrocarbons
9th International Symposium Solar Thermal Concentrating Technology, Odeillo, France, June 22-26 (1998).
* Boreskov Institute of Catalysis, Novosibirsk

A. Meier
CFD as a Design Tool for the Solar Reactor Development at PSI
NREL, Golden, Colorado, USA, September 23, 1998.

A. Meier
Hochtemperatur-Solarchemie: Brennstoffe aus Sonnenlicht und Wasser
Schaffhauser Energieapéro, Neuhausen, October 29, 1998.

A. Meier
Erdgas und Sonnenenergie in einer nachhaltigen Energietechnologie
- Fachtagung Erdgas und Sonnenenergie, Basel, June 18, 1998.
- Fachtagung Erdgas und Sonnenenergie, Olten, November 10, 1998.

P. Novák
Interactions between Graphite and Carbonate Based Electrolytes
Herbstversammlung der NSChG, ETH Zürich, October 15, 1998. Abstract in Chimia **52**, 483 (1998).

L. Poggio, M. Furger, W. K. Graber, A.S.H. Prévôt
SCIDAR/DOAS Measurements during the VOTALP Valley Experiment
European Geophysical Society 23rd General Assembly, Nice, France, April 20-24 1998.

A.S.H. Prévôt, M. Furger, B. Neininger*, L. Poggio, J. Dommen, W.K. Graber
Mesolcina Valley = Highly Efficient Air Pump for Vertical Transport
Eighth Conference on Mountain Meteorology, Flagstaff, Arizona, USA, August 3-7, American Meteorological Society, 1998.
* MetAir AG, Illnau

M. Saurer
The Use of Oxygen Isotope Analysis in Organic Matter for Ecological Research
21. Jahrestagung der Arbeitsgemeinschaft Stabile Isotope, Düsseldorf, Germany, October 5-8, 1998.

Y. Scheidegger
Characterisation of Land Use Intensity in Alpine Regions in Combination of $\delta^{13}C$, $\delta^{18}O$ and $\delta^{15}N$ Analysis
Tagung der Arbeitsgemeinschaft Stabile Isotope (ASI), Düsseldorf, Germany, October 5-7, 1998.

B. Schnyder
X-Ray Photoelectron Spectroscopy (XPS) and XPS-Imaging of Polymers Modified by Laser Ablation
10th International Conference on Quantitative Analysis (QSA 10), Birmingham, UK, August 31 - September 4, 1998.

R.T.W. Siegwolf
The Natural Isotope Variation of $\delta^{13}C$, $\delta^{15}N$, and $\delta^{18}O$ in Mountainous Meadows, as Influenced by Land Use Changes
VII International Congress of Ecology, Florence, Italy, July 19-25, 1998.

A. Stampanoni-Panariello
Diagnostics in Gases by Transient Laser-Induced Gratings
ERCOFTAC Joint Annual Meeting, PSI Villigen, August 27, 1998.

A. Steinfeld, A. Weidenkaff, M. Brack, S. Möller, R. Palumbo
Solar Thermal Production of Zinc: Program Strategy and Status of Research
9th International Symposium on Solar Thermal Concentrating Technologies, Odeillo, France, June 22-26, 1998

A. Steinfeld
Solarthermal Processing of Zinc
Electric Fuel Ltd. Headquarters, Jerusalem, Israel July 16, 1998.

A. Steinfeld
The SynMet Project
British Gas Technology Headquarters, Loughborough, UK, November 13, 1998.

A. Steinfeld
Hochtemperatur-Solarchemie: Brennstoffe aus Sonnenlicht und Wasser
Energie 2000, ABB-Baden, November 23, 1998.

S. Stucki
Biomass and Waste as Renewable Fuels
AGS Day, ETH Zürich, July 9, 1998.

S. Stucki
Waste Management and Research in Switzerland
Sino-Swiss Workshop on Solid Waste Management, Shanghai, China, May 11–15, 1998.

M. Sturzenegger, E. Steiner, A. Frei
A Kinetic Study of the Hydrogen Evolution from Fayalite and Water
GDCh, 9. Vortragstagung der Fachgruppe Festkörperchemie, Saarbrücken, Germany, September 23-25, 1998.

A.P. Tzannis
Laser-Induced Incandescence: Towards Quantitative Soot Volume Fraction Measurements
ERCOFTAC joint annual meeting, PSI Villigen, August 27, 1998.

L.L. Vant-Hull*, M.E. Izygon*, A. Imhof
Optimization of Central Receiver Fields to Interface with Applications Requiring High Flux Density Receivers
9th International Symposium on Solar Thermal Concentrating Technology: Odeillo, France, June 22-26 (1998).
* University of Houston, Houston, USA

R.O. Weber, G. Stefanicki, P. Talkner
Influence of NAO Index to Synoptic Weather Situation over Switzerland
XXIII General Assembly of the European Geophysical Society, Nice, France, April 20-24, 1998.

R.O. Weber
Identification of Flow Patterns by Means of Few Stations
Symposium on Advances in Regional Climatology, Karlsruhe, Germany, October 5-7, 1998.

A. Weidenkaff, A. Steinfeld, A. Wokaun, A. Reller*
CO_2 Abatement by Producing New Solar Energy Carriers - Product Formation in High Temperature Solar Chemistry
4th International Conference on Greenhouse Gas Control Technology, Interlaken, August 30 - September 2 (1998).
* University of Hamburg, Germany

A. Weidenkaff
Solar Thermal Chemical Processing: A Renewable Energy Path for Reducing Greenhouse Gas Emissions
4th International Conference on Greenhouse Gas Control Technology, Interlaken, August 30 - September 2, 1998.

J. Wochele
Labor-Simulierung des Festbettes von Müllverbrennungsanlagen aufgrund der Ähnlichkeitsgesetze
VDI-GET Tagung, Braunschweig, Germany, April 1-2, 1998.

J. Wochele, S. Stucki, Ch. Ludwig
Factors Influencing the Volatility of Heavy Metals in MSW Incinerators
WASTECON 1998, SWANA's Wasteconference/ ISWA World Congress 1998, Charlotte (NC) USA, October 26–29, 1998.

A. Wokaun
Erdgas und Sonnenenergie in einer nachhaltigen Energietechnologie
Fachverbund Erdgas, Bern, October 21, 1998.

A. Wokaun
Wann erhalten erneuerbare Energien eine Chance für eine nachhaltige Elektrizitätsversorgung?
Aarg. Elektrizitätswerk, Bremgarten, December 16, 1998.

A. Wokaun
Sustainable Mobility
AGS Day, ETH Zürich, December 16, 1998

POSTERS

D. Alliata, P. Häring, R. Kötz, O. Haas, H. Siegenthaler*
Electrochemical Scanning Probe Microscopy of Graphite Electrodes during Anion Intercalation Processes
5th International Conference on Nanometer-scale Science and Technology (NANO 5), Birmingham, UK, August 31 - September 4, 1998.
* University of Bern

D. Alliata, R. Kötz, O. Haas, H. Siegenthaler*
Electrochemical Scanning Probe Microscopy of Graphite Electrodes during Anion Intercalation Processes
Hasliberg 3rd Workshop on Nanoscience, Hasliberg, October 12-16, 1998.
* Univeristy of Bern

M. Bärtsch, R. Kötz, A. Braun, O. Haas
Double Layer Capacitor Stack with Glassy Carbon Electrodes
49th ISE Meeting, Kitakyushu, Japan, September 13-18, 1998.

J.-L. Barras*, L. Benco*, C. Daul*, E. Deiss
Oxides and Li-intercalated Derivatives for Lithium Intercalation Batteries
ESF-TMR Workshop on the Electronic Structure Calculations for Industry and Basic Sciences, Vienna, June 3-4, 1998.
* University of Fribourg

F.N. Büchi, C.A. Marmy, G.G. Scherer, O. Haas
Development of an Experimental 1 kW PEFC Stack
2nd International Fuel Cell Workshop, Fujiyoshida City, Japan, September 19-20, 1998.

H.P. Brack, M. Wyler*, G. Peter*, B. Schnyder, G.G. Scherer
Surface Analysis of Radiation-Grafted Films and Ion-Exchange Membranes
Amer. Chem. Society Fall Meeting, Boston, MA, USA, August 1998.
* Technikum Winterthur, Ingenieurschule, Winterthur

A. Braun, M. Bärtsch, B. Schnyder, R. Kötz, O. Haas
SAXS on Glassy Carbon with Variable Scattering Contrast
6th PSI Summer School Neutron Scattering, Zuoz, August 8-14, 1998.

M. Corboz, I. Alxneit
Molecular Oxygen - A Desirable Product of the Photoreduction of CO_2 at TiO_2 ?
12th International Conference on Photochemical Conversion and Storage of Solar Energy, IZ Berlin, Germany, August 9-14, 1998.

J. Dommen, A.S.H. Prévôt
Airborne Measurements of Ozone, Peroxides, Formaldehyde, Nitrogen Oxides and Hydrocarbons in Northern Italy with a Motorglider
American Geophysical Union Fall Meeting, San Francisco, USA, December 6-10, 1998.

W. Durisch, R. Lavric, O. Struss
Drei Netzverbund-Kleinsysteme im Vergleichstest
Nationale Photovoltaiktagung, Bern, May 5, 1998.

H.-M. Frey, P. Beaud, T. Gerber, B. Mischler, P. Radi, A.-P. Tzannis
Species Detection from Rotational Recurrences in Femtosecond Degenerate Fourwave Mixing
2nd Symposium "Towards Clean Diesel Engines", PSI Villigen, May 14-15, 1998.

H.-M. Frey, P. Beaud, T. Gerber, B. Mischler, P. Radi, A.-P. Tzannis
Femtosecond Degenerate Four-Wave Mixing in Gases at Atmospheric Pressure and in Molecular Beams
CARS Workshop, Besançon, March 1998.

M. Furger, L. Poggio, A.S.H. Prévôt, W.K. Graber
Wind Measurements by Scintillometer at Different Locations in an Alpine Valley
8th Conference on Mountain Meteorology, Flagstaff, Arizona, USA, American Meteorological Society, August 3-7, 1998.

J. Ganz, E. Steiner, M. Sturzenegger
Powder Cloud Reactors – An Attractive Concept to Run Solar High-Temperature Reactions
9th International Symposium on Solar Thermal Concentrating Technology, Odeillo, France, June 22-26, 1998.

P. Geissbühler, G. Stefanicki, R.T.W. Siegwolf
CO_2 and Water Exchange between Forest and Canopy and Atmosphere in Complex Terrain
VII International Congress of Ecology, Florence, Italy, July 19-25, 1998.

O. Haas
Dynamics of Lithium Insertion Electrodes
49th Annual Meeting of the ISE, Kitakyushu, Japan, September 13-18, 1998.

D. Häringer, E. Deiss, P. Novák, O. Haas, A. Wokaun
Untersuchung von Elektroden für Lithium-Ionen-Batterien mit Potentialsprungmessungen
Herbstversammlung der NSChG, ETH Zürich, October 15, 1998. Abstract in Chimia **52,** 489 (1998).

D. Häringer, P. Novák, E. Deiss, A. Wokaun, O. Haas
Dynamics of Lithium Insertion Electrodes
49th ISE Meeting, Kitakyushu, Japan, September 13-18, 1998.

F. Holzer, S. Müller
Secondary Zn/O_2 – Cells with Improved Zinc Electrodes
Herbstversammlung der NSChG, ETH Zürich, October 15, 1998. Abstract in Chimia **52**, 175 (1998).

J. Huslage, F. Büchi, G.G. Scherer
Conductivity Measurements on Proton-Conducting Perfluorinated Membranes
7th International Meeting on "Solid State Protonic Conduction", Bled, Slowenia, August 1998.

R. Imhof, P. Novák
DEMS Investigation of the Electrochemical Oxidation of Organic Carbonate Electrolyte Solutions at Lithium Metal Oxide Electrodes
9th International Meeting on Lithium Batteries, Edinburgh, UK, July 12-17, 1998.

R. Imhof, P. Novák
Oxidative Electrolyte Solvent Degradation in Lithium-Ion Batteries
Herbstversammlung der NSChG, ETH Zürich, October 15, 1998. Abstract in Chimia **52**, 490 (1998).

M. Jäggi, R.T.W. Siegwolf, J. Fuhrer*
^{15}N Variation in Norway Spruce in Relation to Water Uptake
21. Jahresversammlung der Arbeitsgemeinschaft Stabile Isotope, Düsseldorf, Germany, October 5-7, 1998.
* Eidg. Forschungsanstalt f. Agrikulturchemie & Umwelt, Liebefeld

F. Joho, B. Rykart, R. Imhof, P. Novák, M.E. Spahr*, A. Monnier*
Influence of Water on the Charge Loss during the First Intercalation of Lithium into Graphite
Herbstversammlung der NSChG, ETH Zürich, October 15, 1998. Abstract in Chimia **52**, 490 (1998).
* Timcal AG, Sins

F. Joho, B. Rykart, R. Imhof, P. Novák, M. E. Spahr*, A. Monnier*
Key Factors for the Cycling Stability of Graphite Intercalation Electrodes for Lithium-Ion Batteries
9th International Meeting on Lithium Batteries, Edinburgh, UK, July 12-17, 1998.
* Timcal AG, Sins

P. Kaufmann*, R.O. Weber
Characteristic Air Flow Patterns Around Basel
Symposium on Advances in Regional Climatology, Karlsruhe, Germany, October 5-7, 1998.
* Schweizerische Meteorologische Anstalt

J. Keller, D. Schläpfer
Intercomparison of Solar Radiometer and Radio Sounding Water Vapor Columns for Atmospheric Processing of Imaging Spectroscopy Data
1st EARSeL Workshop on Imaging Spectroscopy, University of Zürich, October 6-8, 1998.

J. Keller, D. Buerki, S. Andreani-Aksoyoglu
An Approach for the Estimation of Seasonal Impacts of Air Pollutants in Switzerland on the Basis of an Air Quality Classification
EUROTRAC-2 Symposium 98, Garmisch-Partenkirchen, Germany, March 23-27, 1998.

M. Koebel, M. Elsener, M. Kleemann
Urea-SCR: The Promising Aftertreatment Technique to Reduce NO_x-Emissions
2nd Symposium "Towards Clean Diesel Engines", PSI Villigen, May 14-15, 1998.

M. Koebel, M. Elsener
Formation of Carboxylic Acids in the SCR-Process Applied to Diesel Exhaust Gas
Second World Congress on Environmental Catalysis, Miami Beach, USA, November 15-20, 1998.

R. Kötz, M. Carlen*, E. Krause**
Supercapacitors
PPM Fall Meeting 1998, Bern, November 13, 1998.
* ABB Corporate Research, Dättwil
** Leclanché SA, Yverdon

A. Meier
A Predictive CFD Model for a Falling Particle Receiver/Reactor Exposed to Concentrated Sunlight
15th International Symposium on Chemical Reaction Engineering (ISCRE 15), Newport Beach, California, USA, September 13-16, 1998.

A. Meier, V.A. Kirillov*, G.G. Kuvshinov*, Y.I. Mogilnikh*, A. Reller**, A. Steinfeld, A. Weidenkaff
Solar Thermal Decomposition of Hydrocarbons and Carbon Monoxide for the Production of Catalytic Filamentous Carbon
15th International Symposium on Chemical Reaction Engineering (ISCRE 15), Newport Beach, California, USA, September 13-16, 1998.
* Boreskov Institute of Catalysis, Novosibirsk
** University of Hamburg

E.E. Ortelli, A. Wokaun
Use of Periodic Variations of Reactant Concentrations in Time Resolved FTIR Studies of Heterogeneous Catalyzed Reactions
AIRS III, Vienna, Austria, July 5-9, 1998.

P. Novák, F. Joho, R. Imhof, J.-C. Panitz, O. Haas
In-Situ Investigation of the Interaction between Graphite and Electrolyte Solutions
9th International Meeting on Lithium Batteries, Edinburgh, UK, July 12-17, 1998.

J.-C. Panitz
Characterization of Technical Ceramics with Raman Microscopy
16th International Conference on Raman Spectroscopy, Cape Town, ZA, September 6-11, 1998.

M.-C. Pham*, B. Piro*, O. Haas, P. Novák
Electrochemical and Ion Exchange Properties of Poly(5-Amino-1,4-Naphthoquinone) Film in Aqueous and Nonaqueous Media
49th Annual Meeting of ISE, Kitakyushu, Japan, September 13-18, 1998.
* Université Paris 7, CNRS-URA 34, Paris, France

A.S.H. Prévôt, M. Bäumle*, J. Dommen
Morning VOC Concentration Minima in the Mesolcina Valley during the VOTALP Experiment
Abstracts of Lectures and Posters, Ed. P. Borrell, Poster presented at the EUROTRAC-2 Conference in Garmisch-Partenkirchen, Germany, Transport and Chemical Transformation in the Troposphere, Symp'98 EUROTRAC-2, 1998.
* MetAir AG, Illnau

A.S.H. Prévôt, M. Bäumle*, J. Dommen
VOC Measurements as Indicators for Valley Wind Circulation Phenomena
8th Conference on Mountain Meteorology, Flagstaff, Arizona, USA, August 3-7, American Meteorological Society, 207-208, 1998.
* MetAir AG, Illnau

P. Radi, P. Beaud, D. Franzke, H.-M. Frey, T. Gerber, B. Mischler, A.-P. Tzannis
Femtosecond Photoionization of $(H_2O)_n$ and $(D_2O)_n$ Clusters
International Conference on Water in the Gas Phase Marne la Vallée, Paris, France, June 21-24, 1998.

M. Saurer
The Relationship between $\delta^{13}C$ and $\delta^{18}O$ in Cellulose of Trees
Uses of Stable Isotopes on Plant Ecophysiology, Orsay, France, July 22-24, 1998.

Y. Scheidegger, R.T.W. Siegwolf, M. Saurer, U. Tappeiner*
The Stable Isotopes $\delta^{13}C$, $\delta^{18}O$ and $\delta^{15}N$ as Indicators of Land Use Intensities
INTECOL (VII International Congress of Ecology), Florence, Italy, July 19-25, 1998.
* Europ. Akademie, Bozen, Italy

M. Schubnell, W. Durisch, B. Grob, J.-C. Mayor, J.-Ch. Panitz
Koproduktion von Wärme und Strom mit Thermophotovoltaik
Nationale Photovoltaiktagung, Bern, May 5, 1998.

R.T.W. Siegwolf, M. Saurer, P. Geissbühler, Y. Scheidegger, G. Stefanicki
CO_2 and H_2O-Fluxes in Heterogenic Mountainous Terrain Measured with the Stable Carbon Isotope Gradients, Eddy Covariance, Xylemsapflux and Optical Longranging Methods
GCTE-LUCC Open Science Conference on Global Change, Barcelona, Spain, March 14-18, 1998.

E. Steiner, J. Ganz, M. Sturzenegger
The Reactor Cairo – A Versatile Tool to Investigate High-Temperature Reactions
Herbstversammlung der NSChG, ETH Zürich, October 15, 1998.

R. Struis, S. Stucki, H. Armbruster, G. Heinzelmann
CO_2-Neutral, Ultra-Low Emission Vehicle Fuelled by Dimethyl Ether on the Basis of On-Board Methanol Conversion
2nd Symposium "Towards Clean Diesel Engines", PSI Villigen, May 14-15, 1998.

M. Sturzenegger, J. Ganz, P. Nüesch, T. Schelling
Solar Hydrogen from Manganese Oxide Based Thermochemical Cycle
9th International Symposium on Solar Thermal Concentrating Technology, Odeillo, France, June 22-26, 1998.

M. Sturzenegger, P. Nüesch
Solar Hydrogen From Manganese Oxide – A New Thermochemical Cycle
International Association for Hydrogen Energy, Buenos Aires, Argentina, June 28-30, 1998.

M. Sturzenegger, J. Ganz, P. Nüesch, T. Schelling
Evaluation of a Solar-Driven Process for a Sustainable Production of Hydrogen
Energieforschung in der Schweiz – Symposium der Schweizerischen Physikalischen Geschellschaft, Airolo, September 25, 1998.

M. Sturzenegger, P. Nüesch
A Study on the Reactivity of Alkali Hydroxides with Manganese Oxides and Iron Oxides under Inert Atmospheres
Herbstversammlung der NSChG, ETH Zürich, October 15, 1998.

P. Talkner
Semiadiabatic Theory of Periodic Processes
Statphys 20, Paris, France, July 20-24, 1998.

P. Talkner
Binary Collision Theory for Thermal and Nonisothermal Relaxation and Reaction of Polyatomic Molecules
Statphys 20, Paris, France, July 20-24, 1998

H.-R. Tschudi, M. Schubnell, Ch. Müller
Measuring Temperatures on Absorbers Irradiated in a Solar Furnace
- Symposium der SPG: Energieforschung in der Schweiz, Airolo, September 25,1998.
- 9th International Symposium on Solar Thermal Concentrating Technology, Odeillo, France, June 22-26, 1998.

A.-P. Tzannis, P. Beaud, H.-M. Frey, T. Gerber, B. Mischler, P. Radi, J.C. Lee*, A. Tomboulides*, K. Boulouchos*
Application of Resonant Holographic Interferometry to OH Concentration Measurements in a 2D Co-Flow H_2/Air Diffusion Flame and Comparison with Direct Numerical Simulations
26th Symposium on Combustion, Boulder, Colorado, USA, 1998.
* ETH Zürich

R.O. Weber, P. Kaufmann*
Forcing of Surface Winds in the MISTRAL/REKLIP Experiment
Symposium on Advances in Regional Climatology, Karlsruhe, Germany, October 5-7, 1998.
* Schweizerische Meteorologische Anstalt

R.O. Weber
Remarks on the Definition of Friction Velocity
XXIII General Assembly of the European Geophysical Society, Nice, France, April 20-24, 1998.

M. Winter*, G. H. Wrodnigg*, R. Imhof, F. Joho, P. Novák
FTIR and DEMS Investigation on the Electroreduction of Chloroethylene Carbonate Based Electrolyte Solutions for Lithium Ion Cells
9th International Meeting on Lithium Batteries, Edinburgh, UK, July 14, 1998.
* Technical University of Graz, Austria

PATENT APPLICATIONS

W. Durisch
Thermophotovoltaik-Generator
Modellschutz, BAGE, March 3, 1998.

P. Haueter, A. Steinfeld, S. Möller, R. Palumbo
Vorrichtung und Verfahren zur thermischen und thermochemischen Behandlung von metall- und kohlenstoffhaltigen Materialien unter Nutzung von externer Wärmestrahlung als Prozesswärme
November 18, 1998.

Ch. Ludwig, A. Schuler
Verfahren und Vorrichtung zum Überführen schwerflüchtiger Verbindungen in eine Detektionsapparatur
German Patent Application, August 24, 1998.

C. Schüler*, R. Kötz
Mehrschichtige Elektrode für elektrochemische Anwendungen
August 7, 1998.
* ABB Corporate Research, Dättwil

CONFERENCES, WORKSHOPS & EXHIBITIONS

S. Biollaz, S. Stucki
Tagung des IP Abfall; Optimale Rückstandsqualität: Schmelzen oder Sortieren?
PSI Villigen, November 4, 1998.

H.-P. Brack
Colloid and Interface Science at the PSI
Autumn Meeting of the Swiss Group for Colloid and Interface Science, PSI Villigen, November 26, 1998.

E. Cairns*, O. Haas, Z. Ogumi**, B.B. Owens*, B. Scrosati***, O. Yamamoto**
Symposium on "Battery and Energy Storage"
49th Annual Meeting of the Electrochemical Society of Electrochemistry, Kitakyushu, Japan, September 13-18, 1998.
* LBL Laboratory, Berkeley, USA
** School of Engineering, Kyoto, Japan
*** Università di Roma, Italy

W. Durisch
EWZ-Ausstellung 'Häuser für Morgen'
Exhibits 'Solarzellen-Test' and 'Thermophotovoltaik-Experimentiermodul', Zürich, August 25 - November 16, 1998.

J. Egger*, F. Fiedler**, F. Gassmann, G. Najjar***, E. Parlow****, P. Paul***
REKLIP-Symposium on Advances in Regional Climatology
University of Karlsruhe, Germany, October 5-7, 1998.
* University of Munich, Germany
** University of Karlsruhe, Germany
*** University of Strasbourg, France
**** University of Basel

B. Eliasson*, P. Riemer**, A. Wokaun
Fourth International Conference on Greenhouse Gas Control Technologies
GHGT-4, Interlaken, August 30 - September 2, 1998.
* ABB Corporate Research, Baden
** IEA GHG R&D Programme, Cheltenham, GB

W.K. Graber
Ecomont Workshop
PSI Villigen, March 26-28, 1998.

O. Haas
14. Tagessymposium Elektrochemische Energiespeicherung
PSI Villigen, July 1, 1998.

R. Palumbo
Solar Production of Zn: 1998 Status of Research
PSI Villigen, November 20, 1998.

S. Stucki, Ch. Ludwig
Botschaften und Technologietransfer im transdisziplinären Umfeld
Umsetzungsworkshop des IP Abfall, Leissigen, March 16-17, 1998.

S. Stucki, Liu Suiqing*
Sino-Swiss Workshop on Solid Waste Management
Shanghai, China, May 11–15, 1998.
* Tong-Ji University Shanghai, China

S. Stucki
Biomass and Wastes as Renewable Fuels for Processes and Transportation
AGS-Workshop PSI, August 11, 1998.

M. Sturzenegger
Solare Hochtemperatur-Prozesse
Sommerschule des Schwerpunktes 5 der AG Solar NRW: «Solare Chemie und solare Materialforschung», Geseke, Germany, July 20-21, 1998.

M. Watanabe*, S. Gottesfeld**, O. Haas, U. Stimming***
Fuel Cells for Portable and Transportation Power Sources
2nd International Workshop on Fuel Cell Technology, Yamanashi, Japan, September 19-21, 1998.
* University of Tokyo, Japan
** Los Alamos National Laboratory, USA
*** TU Munich, Garching, Germany

MEMBERSHIPS IN EXTERNAL COMMITTEES

S. Andreani-Aksoyoglu
Air Pollution 98, International Scientific Advisory Committee
Member

W. Durisch
Prüfungskommission für die Lehrlinge des Laborantenberufes des Kantons Zürich
Fachexperte

W. Durisch
International Energy Foundation, IEF
Advisory Committee

W. Durisch
Swiss Society of Engineers and Architects (SIA)
Fachgruppe für Verfahrens- und Chemieingenieur-Technik (FVC)
Delegate

W. Durisch
UNESCO, World Renewable Energy Congress
Steering Committee

H.-M. Frey
European CARS Workshop
Steering Committee

F. Gassmann
Institute for Global Environmental Issues (IGEI), Naples FL, USA
Member of the Board of Directors

F. Gassmann
Internationaler Lenkungsausschuss des trinationalen Projektes REKLIP
Member

F. Gassmann
Maturakommission für die Kantonsschulen Baden und Wohlen
Experte für Mathematik und Physik

F. Gassmann
Strategie Nachhaltigkeit ETHZ: Arbeitsgruppe NOVATLANTIS
Member

T. Gerber
Towards Clean Diesel Engines
Steering Committee

T. Gerber
IEA Implementing Agreement on Energy Conservation and Emissions Reduction in Combustion
Task Leader

T. Gerber
ERCOFTAC
Scientific Committee

W.K. Graber
Project Coordination Commitee (PCC) of the EC-Project on "Vertical Ozone Transport over the Alps (VOTALP II)"
Member

W.K. Graber
Project Coordination Commitee of the EC-Project on "Ecological Effects of Land Use Changes in European Terrestrial Mountain Ecosystems (ECOMONT)"
Member

W.K. Graber
Kommission für Klima und Atmosphärenforschung (CCA) der Schweizerischen Akademie der Wissenschaften (SANW)
Member

O.Haas
International Society of Electrochemistry ISE
Division Officer Electrochemical Energy Technology

O. Haas
Working Party on Electrochemistry of the FELS
Delegate of the New Swiss Chemical Society

O. Haas
Journal of New Materials for Electrochemical Systems
Advisory Board

G.G. Scherer
IEA Implementing Agreement on "Advanced Fuel Cells", Annex VIII, Collaborative Research and Development on Polymer Electrolyte Fuel Cells
Task Leader "Improved Single Cells"

Th.H. Schucan
IEA Implementing Agreement on Hydrogen Production and Utilisation, Annex XI, Integrated Systems
Subtask Leader "Case Studies"

Th.H. Schucan
Swiss Academy of Engineering Sciences
Member of Energy Committee

A. Steinfeld
Energy—The International Journal
Associate Editor

A. Steinfeld
Solar Chemistry News
Editor

A. Steinfeld
International Energy Agency's SolarPACES
Operating Agent

S. Stucki
Priority Programme Environment, SNF Integrated Project Waste
Coordinator

S. Stucki
TVA-Revision im Bereich der Verbrennungsrückstände
Expertengruppe des BUWAL

A. Wokaun
Deutsche Bunsen-Gesellschaft für Physikalische Chemie
Mitglied des Ständigen Ausschusses

A. Wokaun
Strategie Nachhaltigkeit des ETH-Rates
Mitglied des Leitungsausschusses

A. Wokaun
4th International Conference on Greenhouse Gas Control Technologies, GHGT-4, Interlaken, August 30 - September 2, 1998
Member, Organising and Program Committee

A. Wokaun
Molecular Physics
Advisory Board Member

AWARDS

W. Durisch et al.
Best Research Paper Award in the Field of *New Clean Energy*
On 20th November, 1998 at the 7th International Energy Conference, ENERGEX 98, Manama, Bahrain, November 19-21, 1998.

S. Moeller
EU-TMR Scholarship to the Solar Chemistry Summer School, Almeria, Spain, September 20-25, 1998.

A Weidenkaff
Recipient of SolarPACES Post-Graduate Award 1998.